Structural investigation of druggable membrane proteins via SPA cryo-EM

DISSERTATION

Zur Erlangung des

DOKTORGRADES DER NATURWISSENSCHAFTEN (DR. RER. NAT.)

der Fakultät für Biologie und vorklinische Medizin

der Universität Regensburg

vorgelegt von

Benedikt Mayer

aus Landshut

im Jahr 2024

Das Promotionsgesuch wurde eingereicht am:

Die Arbeit wurde angeleitet von:
Prof. Dr. Christine Ziegler

Unterschrift:

“I never lose. I either win or learn”

- Nelson Mandela

Table of Contents

List of abbreviations

All amino acids were abbreviated according to one- or three-letter notation.

2D	Two-dimensional
3D	Three-dimensional
A_x	Absorbance at a wavelength of x nm
Å	Angström(s)
AA	Amino Acid
AI	Artificial intelligence
AP	Alkaline Phosphatase
Approx.	Approximately
APS	Ammonium persulfate
ATP	Adenosine triphosphate
AtTPC1	Two-pore channel 1 from *Arabidopsis thaliana*
AU	Arbitrary unit (absorption unit)
BCIP	5-bromo-4-chloro-3-indolyl-phosphate
BPR	Blue-light absorbing proteorhodopsin
BSA	Bovine serum albumin
Carb	Carbenicillin
Cam	Chloramphenicol
CHS	Cholesterol hemisuccinate
CHT1	High affinity choline transporter 1
CLR	Cholesterol
CMC	Critical micelle concentration
CTF	Contrast transfer function
CV	Column volume

Da	Dalton
ddH_2O	Double-distilled water
DDM	*n*-Dodecyl-β-D-maltoside
DIBMA	Diisobutylene maleic acid
DM	Decyl β-D-maltoside
DMEM F-12	Dulbecco´s Modified Eagle´s Medium/Nutrient Mixture F-12 Ham
DMF	Dimethylformamide
DNA	Deoxyribonucleic acid
DNJ	1-Deoxynojirimycin
dNTPs	Deoxynucleotide Triphosphates
E.g.	*Exempli gratia,* for example
EM	Electron microscope/ microscopy
ET	Electron tomography
et al.	*et alia, et alii*
FBS	Fetal bovine serum
Fig.	Figure
FSC	Fourier shell correlation
Gen	Gentamycin
GDN	Glyco-diosgenin
GDP	Guanosine diphosphate
GLUT	Glucose transporter
GOI	Gene of interest
GPCR	G-protein-coupled receptor
GPR	Green-light absorbing proteorhodopsin
GTP	Guanosine triphosphate
His_x	x-fold histidine tag

IPTG	Isopropyl-β-*D*-thiogalactopyranosid
ISTA	Institute of Science and Technology Austria
JPT2	Jupiter Microtubule Associated Homolog-2
Kan	Kanamycin
LB	Lysogeny Broth
LMNG	Lauryl Maltose Neopentyl Glycol
LoG	Laplacian-of-Gaussian
LSM12	'like-Sm' protein 12
MWCO	Molecular weight cut-off
NAADP	nicotinic acid adenine dinucleotide phosphate
NBT	Nitro blue tetrazolium
NMDG	N-Methyl-D-glucamin
NMR	nuclear magnetic resonance
OD_x	Optical density at a wavelength of x
o/N	Overnight
PBS	Phosphate buffered saline
PCR	polymerase chain reaction
PDB	Protein Data Bank
Pen-Strep	Penicillin-Streptomycin
$PI(3,5)P_2$	Phosphatidylinositol 3,5-bisphosphate
POPC	1-Palmitoyl-2-Oleoyl-sn-Glycero-3-Phosphocholine
Rab7A	Ras-related protein Rab-7a
rpm	Revolutions per minute
RT	Room temperature
SARS-CoV-2	Severe acute respiratory syndrome coronavirus 2
SDS	Sodiumdodecylsulfate

SEC	Size exclusion chromatography
SGLT	Sodium–glucose cotransporter
SMA	Styrene maleic acid
SMALP	Styrene maleic-acid lipid particle
SPA	Single particle analysis
SSM	Solid-Supported Membrane
Str	Streptomycin
Tet	Tetracycline
TPC	*Two-pore channel*
Tris	2-amino-2-hydroxymethyl-propane-1,3-diol
UAc	uranyl acetate
v/v	Volume per volume
w/v	Weight per volume
wt	wildtype
x g	Acceleration of gravity
X-ray	X-radiation / Röntgen radiation
x^R	resistance to antibiotic x

List of figures

List of tables

Abstract

Single Particle Analysis (SPA) cryo-Electron Microscopy (cryo-EM) has become a powerful tool in the field of structural biology. Membrane proteins, in particular, have greatly benefited from the numerous advantages of SPA cryo-EM, including the ability to determine structures of multiple conformational states. The near-atomic resolution structures of membrane proteins, which are major drug targets, provide valuable insights for structure-guided drug design by allowing direct visualization of drug-protein interactions. This can lead to the development of more effective and safer drugs. However, the structural analysis of membrane proteins using SPA cryo-EM is a challenging task. In this study, we focused on two emerging drug targets using SPA cryo-EM. The investigation included members of the Solute Carrier 5 (SLC5) family, specifically sodium-glucose cotransporters (SGLTs) that are linked to Type II diabetes mellitus and cardiovascular diseases. Additionally, we studied Two-Pore Channel 2 (TPC2), an endolysosomal ion-selective channel implicated in cancer proliferation and viral infection.

The production of proteins in adequate quality and quantity, along with their purification, is a crucial prerequisite for SPA cryo-EM. However, these tasks can be particularly challenging for mammalian membrane proteins. These proteins exhibit poor responses to changes in the membrane environment, lack of appropriate interaction partners, and alterations in post-translational modifications during heterologous expression. The primary objective of this study was to establish optimal conditions to produce SLC5 transporters and TPC2 for biochemical and structural investigations. Various membrane-mimicking systems, including amphipols and nanodiscs, were evaluated to determine their suitability for the study of mammalian membrane proteins using a model protein, the Green-light absorbing proteorhodopsin (GPR).

While structural studies of SLC5 transporters were not possible within this thesis, the valuable experience gained in working on SLC5 transporters was instrumental to successfully solve structures of the TPC2 channel in complex with agonist and inhibitors. This was possible mainly due to the extensive screening of expression conditions for SLC5 transporters, which led to the use of lentiviral stable cell lines successfully applied to SGLT3 and TPC2, respectively. Also, experience gained due to the extensive screening of purification procedures for the SGLT homologues helped in the TPC2 project. Membrane protein purification per se is far from trivial due to their hydrophobic and fragile nature requesting either constant presence of detergent or reconstitution in a membrane mimic. In this thesis, both, detergent reconstitution as well as reconstitution into nanodiscs or amphipols was successfully applied. This was possible due to initial screening of protocols using the pentameric bacterial channel GPR, for which a SPA cryo-EM map at a resolution of 3.64 Å could be determined. Most importantly, GPR reconstitution allowed to screen parameters such as lipid-to-protein ratios, incubation times, salt concentration etc. These optimized protocols helped reconstitute the mammalian targets, for which the protein yields were too low to perform such a screening. The selection of Saposin-based nanodiscs for SGLT3 and glyco-diosgenin (GDN) for TPC2 proved to be the most effective reconstitution systems for structural studies. Notably, several high-resolution SPA cryo-EM structures for TPC2 were obtained under varying conditions, leading to the visualization and comprehension of specific agonist-antagonist interactions.

A structure of TPC2 in complex with the inhibitor naringenin revealed the pivotal role of lipids and detergent on the open state of the TPC2 channel. By a systematic comparison with a published $PI(3,5)P_2$-activated open state, it was possible to describe the key interactions of the pore blocker naringenin with one of the gating residues. A structure in complex with NAADP-mimicking agonist TPC2-A-N1 pointed towards an alternative opening mechanism distinct from the $PI(3,5)P_2$-activation. Two structures of TPC2 in complex with the agonist SGA-111 provided multiple important insights into NAADP-like activation.

Firstly, the structures shed light into the tautomer-specificity of agonist binding, which is an important step towards the development of new drugs. Secondly, SGA-111 binding triggered changes to the complex two-layered selectivity filter, which is key to the enigmatic ion selectivity switch from Na^+ to Ca^{2+} upon NAADP-activation. While in PI(3,5)P_2-activation the conformation of the selectivity filter is not altered, SGA-111 binding reveals a remodulation which most likely account for the selectivity switch. Moreover, the structural work in this thesis highlights the impact of specific lipid interactions aside of the well-known PI(3,5)P_2-interaction. Three lipids were identified as regulators for the concerted movements of the linker helices connecting the voltage-sensor domains to the pore domain. These findings show for the first time the interference of a lipophilic agonist with regulatory lipids and will initiate new strategies to develop lipophilic agonists for TPC2.

Understanding the structural interactions of lipophilic small-molecule agonists and inhibitors with TPC2 provides insights into its physiological and pathophysiological roles, but also open new strategies in drug development. In recent years, TPC2 has emerged as a promising novel drug target for various diseases, e.g. infectious diseases such as Ebola virus, SARS-CoV-2, or cholera. Inhibiting TPC2 has demonstrated efficacy in reducing cancer cell migration, and neoangiogenesis. The understanding of the different molecular activation mechanisms of TPC2 will provide important new impulses for drug development.

In summary, the results of this thesis have opened new research projects on the SLC5 transporter SGLT3 and on the GPR channel, respectively, and provided new molecular insights into the differences in activation mechanisms of TPC2.

Zusammenfassung

Die kryo-elektronenmikroskopische (kryo-EM) Einzelteilchenanalyse hat sich in den letzten Jahren zu einer leistungsstarken Methode auf dem Gebiet der Strukturbiologie entwickelt. Insbesondere die strukturelle Analyse von Membranproteinen hat enorm von den zahlreichen Entwicklungen profitiert. Atomare Strukturen von Membranproteinen, die wichtigsten biologischen Ziele für Arzneimittel, können wertvolle Erkenntnisse für Ligand-Protein-Wechselwirkungen liefern. Dies kann ein wichtiger Beitrag zur Herstellung wirksamer und sicherer Medikamente sein. Die Strukturanalyse von Membranproteinen mittels kryo-EM Einzelteilchenanalyse stellt jedoch eine anspruchsvolle Aufgabe dar. In dieser Arbeit liegt der Fokus auf der strukturellen Untersuchung zweier neuer möglicher Wirkstoffziele. Zum einen Mitglieder der Familie der „Solute Carrier 5“ (SLC5), dabei insbesondere Natrium-Glukose-Cotransporter (SGLTs), die mit Diabetes mellitus Typ II und Herz-Kreislauf-Erkrankungen in Zusammenhang stehen, sowie „Two-Pore Channel 2“ (TPC2), ein endolysosomaler, ionenselektiver Kanal, der an der Proliferation von Krebszellen als auch bei Virusinfektionen beteiligt ist. Die Herstellung von Proteinen in ausreichender Qualität und Menge sowie deren Reinigung sind eine entscheidende Voraussetzung für die kryo-EM Einzelteilchenanalyse. Allerdings stellt diese Aufgabe für Membranproteine von Säugetieren eine besondere Herausforderung dar. Der Wandel in der Membranumgebung, das Fehlen geeigneter Interaktionspartner und die Veränderungen der posttranslationalen Modifikationen während der heterologen Expression, sind hierbei problematisch. Das Hauptziel dieser Arbeit bestand darin, optimale Bedingungen für die Produktion von SLC5-Transportern und TPC2 zur biochemischen und strukturellen Untersuchung zu entwickeln. Dabei wurden verschiedene membran-nachahmende Systeme, darunter „amphipol“ und „nanodiscs“, getestet, um die Eignung für die Untersuchung von Säugetier-Membranproteinen zu bestimmen. Hierfür wurde ein bakterielles Modellprotein, das grün-absorbierende Proteorhodopsin (GPR) genutzt. Eine strukturelle Analyse von SLC5-Transportern im Rahmen dieser Arbeit war nicht möglich. Jedoch konnten die wertvollen Erkenntnisse, die bei der Arbeit an SLC5-Transportern gewonnen wurden, entscheidend für die erfolgreiche Aufklärung von TPC2-Strukturen mit Agonisten und Inhibitoren genutzt werden. Dies war vor allem durch den umfangreichen Test von Expressionsbedingungen für SLC5-Transporter möglich, welche zur erfolgreichen Nutzung lentiviraler stabiler Zelllinien für SGLT3 bzw. TPC2 führte. Auch die Erfahrungen, die durch die Untersuchung verschiedener Reinigungsverfahren für die SGLTs gewonnen wurden, waren für das TPC2-Projekt hilfreich. Die Reinigung von Membranproteinen an sich ist herausfordernd, da sie durch ihre hydrophoben Bereiche entweder die ständige Anwesenheit von Detergens oder die Rekonstitution in einer Membranumgebung benötigen. In dieser Arbeit wurde sowohl Detergens als auch die Rekonstitution in „nanodiscs“ und „amphipol“ erfolgreich genutzt. Möglich wurde dies durch einen Test der Methoden unter Verwendung des pentameren, bakteriellen Protonenkanals GPR, für welchen eine kryo-EM Struktur mit einer Auflösung von 3,64 Å erzeugt werden konnte. Dabei ermöglichte die GPR-Rekonstitution die Untersuchung von Parametern wie unter anderem Lipid-zu-Protein-Verhältnis, Inkubationszeit und Salzkonzentration. Die optimierten Protokolle wurden dann für die Rekonstitution der Säugetier-Membranproteine genutzt, da für diese die Proteinausbeuten zu niedrig waren, um ein solches Screening durchzuführen. Die Auswahl von Saposin-basierten „nanodiscs“ für SGLT3 und dem Detergens Glyco-Diosgenin (GDN) für TPC2 erwiesen sich als die effektivsten Rekonstitutionssysteme. Für TPC2 konnten somit unter verschiedenen Bedingungen hochaufgelöste kryo-EM Strukturen erzeugt werden, welche zur Darstellung und zum Verständnis spezifischer Agonisten/Antagonisten-Wechselwirkungen führten. Eine Struktur von TPC2 im Komplex mit dem Inhibitor Naringenin zeigt die entscheidende Rolle von Lipiden und Detergens im offenen Zustand des TPC2-Kanals. Durch einen systematischen Vergleich mit dem $PI(3,5)P_2$-aktivierten offenen Zustand war es möglich, die Interaktion des Porenblockers Naringenin mit einer

spezifischen Aminosäure im „gate“ von TPC2 zu beschreiben. Eine Struktur mit dem Agonisten TPC2-A-N1, welcher die NAADP-abhängige Aktivierung von TPC2 imitiert, deutet auf einen alternativen Öffnungsmechanismus hin, der sich von der $PI(3,5)P_2$-Aktivierung unterscheidet. Zwei Strukturen von TPC2 mit dem Agonisten SGA-111 lieferten mehrere wichtige Erkenntnisse zur dieser NAADP-imitierenden Aktivierung. Erstens geben die Strukturen Aufschluss über die tautomere Spezifität der Bindung des Agonisten, was einen wichtigen Schritt auf dem Weg zur Entwicklung neuer Medikamente darstellt. Zweitens löste die SGA-111-Bindung Veränderungen am komplexen zweistufigen Selektivitätsfilter aus, welcher der Schlüssel zum Wechsel der Ionenselektivität von Na^+ zu Ca^{2+} bei der NAADP-Aktivierung ist. Während bei der $PI(3,5)P_2$-Aktivierung die Konformation des Selektivitätsfilters nicht verändert wird, zeigt die SGA-111-Bindung eine Änderung, welche höchstwahrscheinlich für den Selektivitätswechsel verantwortlich ist. Darüber hinaus beschreiben die TPC2-Strukturen dieser Arbeit den Einfluss spezifischer Lipid-Wechselwirkungen neben der bekannten $PI(3,5)P_2$-Wechselwirkung. Drei Lipide wurden als Regulatoren für die konzertierten Bewegungen der „Linker Helices“ identifiziert, die die „voltage-sensor“ Domänen mit der Porendomäne verbinden. Diese Ergebnisse zeigen zum ersten Mal die Wechselwirkung eines lipophilen Agonisten mit regulatorischen Lipiden und können die Grundlage für die Weiterentwicklung dieser Agonisten sein. Das Verständnis der strukturellen Wechselwirkungen von Agonisten und Inhibitoren mit TPC2 liefert Einblicke in seine physiologischen und pathophysiologischen Rollen und eröffnet neue Strategien in der Arzneimittelentwicklung. In den letzten Jahren hat sich TPC2 zu einem vielversprechenden neuen Wirkstoffziel für verschiedene Krankheiten entwickelt, zum Beispiel Infektionskrankheiten wie Ebola, SARS-CoV-2 oder Cholera. Die Inhibierung von TPC2 hat sich als wirksam bei der Reduzierung der Krebszellmigration und der Neoangiogenese erwiesen. Das Verständnis der unterschiedlichen molekularen Aktivierungsmechanismen von TPC2 kann wichtige neue Impulse für die Wirkstoffherstellung liefern.

Die Ergebnisse dieser Arbeit haben grundlegende Erkenntnisse für neue Forschungsprojekte zum SLC5-Transporter SGLT3 bzw. zum GPR-Kanal erzielt und neue molekulare Einblicke in die unterschiedlichen Aktivierungsmechanismen von TPC2 geliefert.

1. Introduction

1.1 Single particle analysis and membrane proteins

1.1.1 Single particle analysis cryo-electron microscopy

Single particle analysis (SPA) cryo-electron microscopy (cryo-EM) is a cutting-edge structural biology technique that enables the determination of atomistic protein structures. The method involves the vitrification of biological samples, followed by imaging them with an electron microscope and the reconstruction of three-dimensional structures from the collected data (Fig. 1.1).

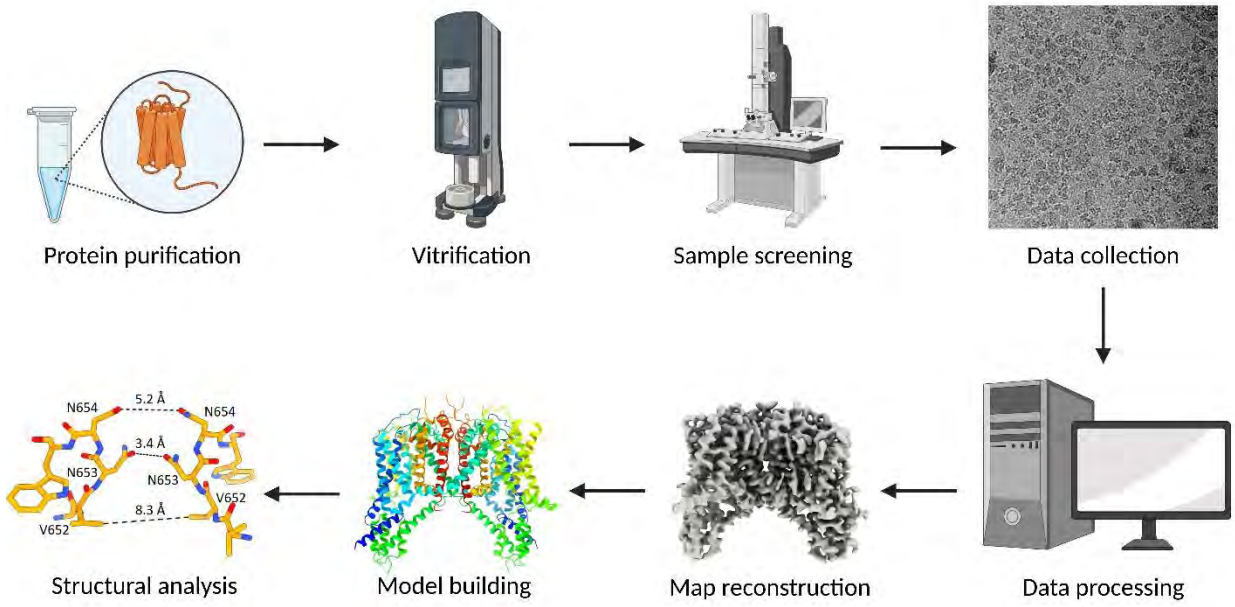

Figure 1.1: Typical workflow of structural analysis of a protein by SPA cryo-EM
The SPA cryo-EM workflow starts with protein expression and purification, followed by vitrification and sample screening. When a good sample is identified, data collection is performed, and the recorded micrographs are processes to a final 3D map. Based on this 3D map and the AA-sequence of the protein, a model is built, which then is finally used for structural analysis of the protein. Derived from Zhu *et al.*, 2023, and created with ChimeraX (2.1.2) and BioRender (2.1.2).

In contrast to other structural biology methods like X-ray crystallography and nuclear magnetic resonance (NMR), SPA cryo-EM does not require the crystallization or labeling of the target protein. In addition, relatively small amounts of protein as well as heterogenous samples are sufficient for SPA cryo-EM, making it feasible to target proteins that are difficult to produce (Bai *et al.*, 2015). Development of direct electron detectors (McMullan *et al.*, 2009) combined with algorithms that correct for beam-induced movement and specimen drift (Li *et al.*, 2013), improvements of the EM optics and powerful image processing tools (Scheres S. H., 2012; Punjani *et al.*, 2017), made SPA cryo-EM a method to solve protein structures routinely at atomic resolution. These combined technological improvements resulted in the so-called 'resolution revolution' (Kühlbrandt W., 2014). So far SPA cryo-EM is routinely used to determine structures of proteins larger than 100 kDa, at 3 Å resolution or better (Zhu *et al.*, 2023). However, the technical development of new electron optical apparatuses like energy filter (Gubbens *et al.*, 2010) and Volta phase plate (Danev *et*

al., 2014) has led to an increasing number of structures from smaller proteins, e.g. Lys-Asp-Glu-Leu receptor (23 kDa; Wu X. & Rapoport T. A., 2021) and the key cancer signaling protein KRAS (19 kDa; Castells-Graells *et al.*, 2023). With all these advantages and innovations SPA cryo-EM has revolutionized structural biology, facilitating the determination of the structures of biomolecules, such as membrane proteins (Gao *et al.*, 2016; She *et al.*, 2019; Han *et al.*, 2022) and large protein complexes (Amporndanai *et al.*, 2018; Sun *et al.*, 2018; Rapisarda *et al.*, 2019), which are biochemically difficult to handle. Thereby SPA cryo-EM made significant contributions to the understanding of fundamental cellular processes. Additionally, SPA cryo-EM has enabled structure-guided drug design for previously inaccessible targets like membrane proteins, by direct visualization of drug-protein interactions and investigation of protein dynamics and conformational changes (Niu *et al.*, 2022), possibly resulting in the development of more effective and safer drugs in the future.

However, the application of SPA cryo-EM is not without challenges, e.g. sample preparation, imaging conditions, data processing and model interpretation (Lyumkis D., 2019). Further, SPA cryo-EM presents certain technical barriers in the analysis of small proteins, targeted by many efforts including the improvement of data collection (Gubbens *et al.*, 2010; Danev *et al.*, 2014), as well as the utilization of molecules which increases the size of the target protein (e.g. nanobodies (Rasmussen *et al.*, 2011; Wu *et al.*, 2012)). Even though the best resolution to date is 1.15 Å (Yip *et al.*, 2020), most of the reported SPA cryo-EM structures are still at the 3 – 4 Å level, and therefore the structural information on drug molecule binding target sites usually needs to be combined with higher resolution protein structures obtained from X-ray crystallography (Kühlbrandt W., 2014, Bai *et al.*, 2015). Moreover, SPA cryo-EM data collection and processing need improvement in automation and data verification, enabling a higher throughput of possible drug targets and/or candidates. Hereby, the utilization of programs for automatic data collection such as SerialEM (Mastronarde D. N., 2005), the use of multigrid cartridges to enhance grid throughput and on-the-fly data processing tools like cryoSPARC live (Punjani *et al.*, 2017) that speed up the judgement on data and grid quality, are helpful benefits. Finally, artificial intelligence (AI) techniques can help to overcome those limitations of SPA cryo-EM soon. In summary, SPA cryo-EM is a powerful, fast developing tool in investigating drug-target interactions for improvement of drug effect and specificity, as well as resolving the structure of possible drug targets for structure-based drug discovery (Robertson *et al.*, 2022).

1.1.2 SPA cryo-EM studies on membrane proteins

Integral membrane proteins are involved in many biological processes, and function among others, as ion channels, transporters, and receptors. They are targets for approx. 70% of approved small-molecule drugs (Santos *et al.*, 2017), by being encoded by only 25% of the genes within the human genome (Uhlén *et al.*, 2015). This fact clearly shows their high pharmacological importance. However, revealing the structure and function of membrane proteins is very challenging (Gulezian *et al.*, 2021). Consequently, only 3.3% of all structures deposited in the PDB are membrane proteins with an average resolution of approx. 3.1 Å. This resolution is notably lower than the average achieved for all deposited protein structures, which stands at approx. 2.2 Å (Berman *et al.*, 2000; Newport *et al.*, 2019). Nevertheless, in the last years the number of cryo-EM membrane protein structures increased strongly, as well as the achieved resolutions (Fig. 1.2; Vénien-Bryan C. & Fernandes C. A. H., 2023). In the following the challenges of investigating membrane proteins by SPA cryo-EM will be explained and possible approaches will be shown.

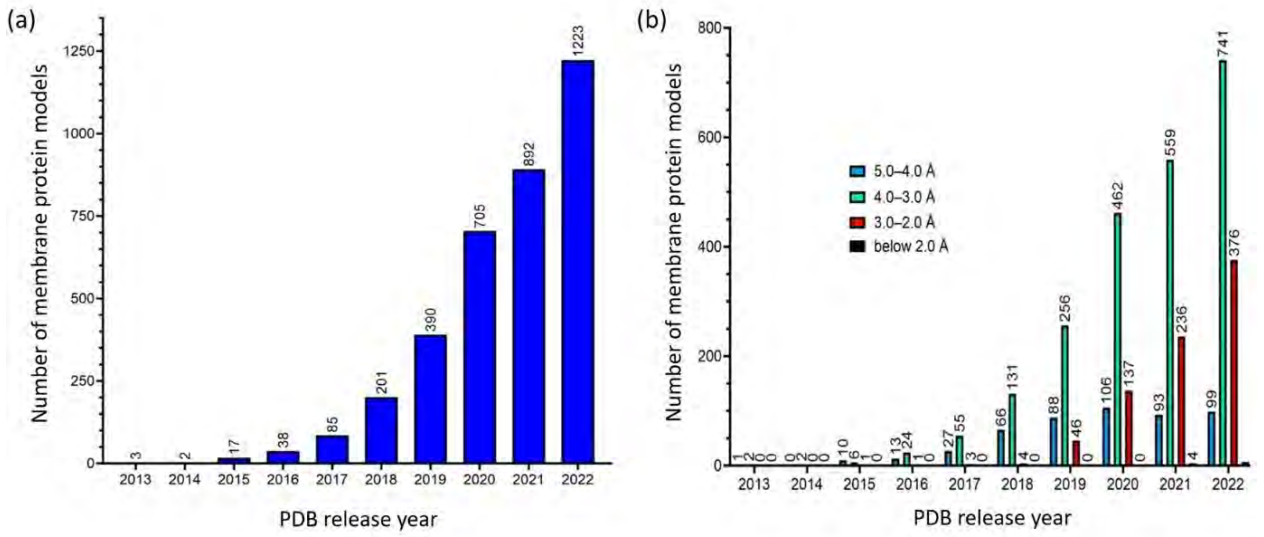

Figure 1.2: SPA cryo-EM models of membrane proteins in the PDB
The number of structures of membrane proteins deposited in the PDB solved by SPA cryo-EM. **(a)** Total number of membrane protein structures deposited per year. **(b)** Number of membrane protein structure deposits per year and per resolution range. The figure is adopted from Vénien-Bryan C. & Fernandes C. A. H., 2023.

1.1.2.1 Expression and purification

The first step in characterizing any protein is to get hands on it. This can be done by either extraction from an organism in which it occurs naturally (Amporndanai *et al.*, 2018) or heterologous expression followed by purification. Hereby the key is to balance expression yields and purification efficiencies while maintaining protein function and stability (Piper *et al.*, 2022).
As most membrane proteins cannot be obtained in sufficient amounts from their native environments, heterologous expression is used. For prokaryotic membrane proteins *E. coli* is the expression host of choice. Eukaryotic membrane proteins however require a suitable expression system, which preserves key elements in protein translation machinery and post-translational modifications. Important factors are post-translational modifications (Goth *et al.*, 2020), inefficient membrane integration (Cymer *et al.*, 2015), loss of native interaction partners (Coady *et al.*, 2017; Sun *et al.*, 2018) and a possible toxicity to the host cells (Gulezian *et al.*, 2021). Also, the design of a functional construct is decisive for proper expression as well as for purification. Affinity-tags can influence or even disturb functional folding or protein localization (Piper *et al.*, 2022). Point mutations or domain deletions, often used in the past for better crystallization behavior, can improve stability of the membrane protein during purification (Lau *et al.*, 1999), but may lead to compromised functionality. In some cases, co-expression with relevant co-factors can help stabilizing a fragile target (Niu *et al.*, 2022). For improvement of protein yield and purification output of cell organelle membrane proteins, a specific re-localization into the plasma membrane can be fruitful (Brailoiu *et al.*, 2010; She *et al.*, 2019). However, it can also lead to loss of functionality and stability because of deviant lipid composition of the different membranes. Finally, growth conditions must be adapted to contain all substances necessary for functional homeostasis of the cells as well as the expressed target protein. For instance, substrate availability is crucial for the expression of some membrane proteins (Ghezzi C. & Wright E. M., 2012). Despite this, temperature and growth time are essential. Too long expression times can generate toxicity by waste products, short times can lead to low yields. For mammalian cells, availability of carbon dioxide for regulating pH is also an influencing factor, as in suspension decent stirring is essential for proliferation and metabolism of the cells (Wang *et al.*, 2015).

For purification, membrane proteins must be extracted out of the membrane and solubilized in a suitable membrane mimic to protect the hydrophobic areas formerly interacting with membrane lipids. Therefore, the buffer must mimic the native environment of the target protein (Ghezzi C. & Wright E. M., 2012). Detergents (Fig. 1.3a+b) are most commonly used for membrane extraction (Gulezian *et al.*, 2021). These amphipathic molecules are used above their critical micelle concentration (CMC; Autzen *et al.*, 2019) to solubilize lipid bilayers and keep membrane proteins in solution by forming micelles around the hydrophobic domains (Helenius A. & Simons K., 1975). For mammalian membrane proteins, adding the cholesterol derivative cholesterol hemisuccinate (CHS; Fig. 1.3c) is crucial (She *et al.*, 2018; She *et al.*, 2019). By mimicking cholesterol (CLR) it promotes stability of mammalian membrane proteins (Mobbs *et al.*, 2021), but can also affect function by locking the protein in a specific conformation (Autzen et al., 2018). Detergents have to be present during all purification steps in the absence of another membrane mimic and their concentration has to be carefully adapted to prevent protein aggregation. Especially G-protein-coupled receptors (GPCRs), high-resolution structures (<3 Å) primarily utilize detergents like LMNG, supplemented with CHS (Liang *et al.*, 2020; Zhang X. *et al.*, 2020).

There are no 'golden rules' for selecting suitable detergents for the solubilization of a specific membrane protein. However, the non-ionic mild detergents n-dodecyl-β-d-maltoside (DDM; Fig. 1.3a) and lauryl maltose neopentyl glycol (LMNG; Fig. 1.3b) are mostly used (Ratkeviciute *et al.*, 2021). Recently, high throughput methods to optimize solubilization and stabilization conditions using a variety of detergents are available (Kotov *et al.*, 2019), as not all membrane proteins survive solubilization via DDM or LMNG (Seddon *et al.*, 2004).

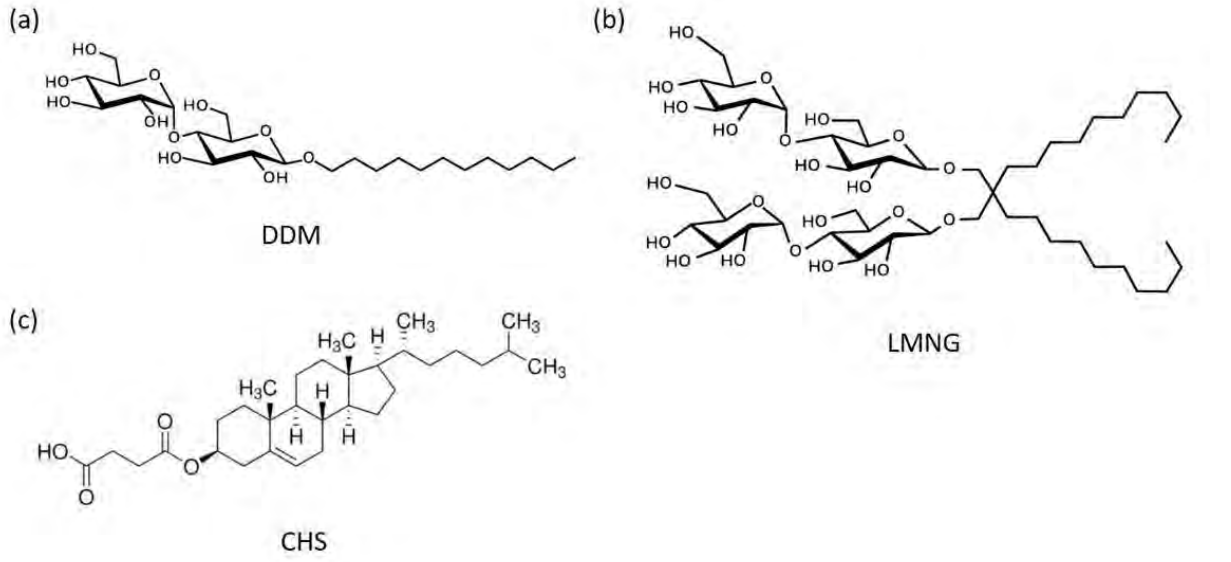

Figure 1.3: Chemical structures of typical detergents and additives
(a) Chemical structure of n-dodecyl-β-d-maltoside (DDM; Structure from anatrace.com). **(b)** Chemical structure of lauryl maltose neopentyl glycol (LMNG; Structure from anatrace.com). **(c)** Chemical structure of cholesterol hemisuccinate (CHS; Structure from sigmaaldrich.com).

In general, detergents tend striping away functionally important annular lipids and disrupt labile, multi-subunit protein complexes (Young et al., 2022), directly affecting the protein's function (She et al., 2019). Numerous detergent derivatives were recently developed via the introduction and modification of functional groups (Lee *et al.*, 2022), and also the development of completely novel detergents has

multiplied. Examples are fluorinated glucose and maltose-based detergents (Boussambe *et al.*, 2018; Wehbie *et al.*, 2021), facial amphiphiles (Das *et al.*, 2018), disulfide containing amphiphiles (Xue *et al.*, 2019), malonate-derived tetra-glucosides (Ehsan *et al.*, 2020) or oligoglycerol detergents, that maintain lipid interactions (Urner *et al.*, 2020). Another interesting class are five vitamin-E based glycoside amphiphiles consisting of a hydrophobic vitamin E based alpha-tocopherol chain and hydrophilic branched glycoside head group. They have displayed elevated stability, retention of functionality and successful purification of the human β_2-adrenergic receptor complex highlighting a potential application in SPA cryo-EM (Ehsan *et al.*, 2018). Of note are also modifications to the length of the acyl tail, which were shown to dramatically influence solubilization efficacy, while longer tails lead to lower CMC and improve extraction of membrane proteins (Matar-Merheb *et al.*, 2011). In summary, the choice of a suitable detergent for a specific membrane protein encompasses a balance between high solubilization capability out of the membrane, providing lateral stability in the micelle while only mildly solubilizing of closely associated lipids (Ehsan *et al.*, 2018). Because of this, detergents are often switched during purification, e.g. extraction is typically performed using DDM or LMNG prior to exchange into milder detergents for further purification and investigation (She *et al.*, 2019). DDM remains the first choice of detergent for solubilization accounting for approx. 50% of all membrane protein structures solved between 2010 and 2019 (Choy *et al.*, 2021).

Besides this developments, cell-free expression systems are an emerging technique. Thereby proteins are produced in vitro, what has already worked out for membrane proteins as well (Kögler *et al.*, 2019). Although this approach has not yet yielded high resolution SPA cryo-EM structures, proteins produced in this way have the potential to impact the SPA cryo-EM field in the future (Piper *et al.*, 2022).
All in all, finding the right expression and purification protocol is not trivial. It must be noted that even though many of the steps used in production of membrane proteins have been optimized yet, further optimization for every single new target is necessary. Additionally, if a protocol from a related membrane protein is available this can be used only as a starting point because the same procedure may not be adaptable to every approach or laboratory environment.

1.1.2.2 High-quality samples for SPA cryo-EM

Detergent-solubilized membrane proteins can be used for structural analysis by methods such as X-ray crystallography and SPA cryo-EM (Yamashita *et al.*, 2005; Faham *et al.*, 2008; She *et al.*, 2019; Hirschi *et al.*, 2021), as well as functional studies like receptor-ligand binding assays (Antoine *et al.*, 2016). As detergents might disrupt native protein sates (Young *et al.*, 2022; She *et al.*, 2019), there are extensive efforts towards developing new classes of detergents to minimize these dissociating and delipidating effects (Lee *et al.*, 2022) such as reconstituting detergent-solubilized proteins back into an artificial lipid environment (e.g. MSP nanodiscs (1.2.2.1) or Saposin-based nanodiscs (salipros) (1.2.2.2)) or producing native nanodiscs (e.g. SMALPs (1.2.2.3)). Nevertheless, reconstitution of detergent-solubilized membrane proteins is not always possible for fragile membrane protein complexes, which respond badly to any multi-step alterations of their hydrophobic environment (Tocilj *et al.*, 2008). Despite this, high amounts of detergent is also a problem for SPA cryo-EM. It alters the surface tension of water, might increase ice thickness and limit particle distribution on the grid (Autzen *et al.*, 2019). In addition, free detergent micelles in solution also increase the background noise in SPA cryo-EM images (Schmidt-Krey I. & Rubinstein J. L., 2011). To date high-resolution structures of membrane proteins were determined in detergents with low CMCs, like DDM (CMC = 0.17 mM) and LMNG (CMC = 0.01 mM). Steroidal detergent such as digitonin (Zhang Z. & Chen J., 2016) extracted from the purple foxglove plant *Digitalis purpurea* were also applied successfully. Because of batch-to-batch variations of digitonin and its toxic byproducts such as digitoxin and digoxin (Barrueto F.,

2005), the synthetically produced glyco-diosgenin (GDN; Fig. 1.4) is mainly used recently (She *et al.*, 2018; Singh *et al.*, 2018; She *et al.*, 2019) and has proven its advantages in stability and purification compared to other detergents (Chae *et al.*, 2012).

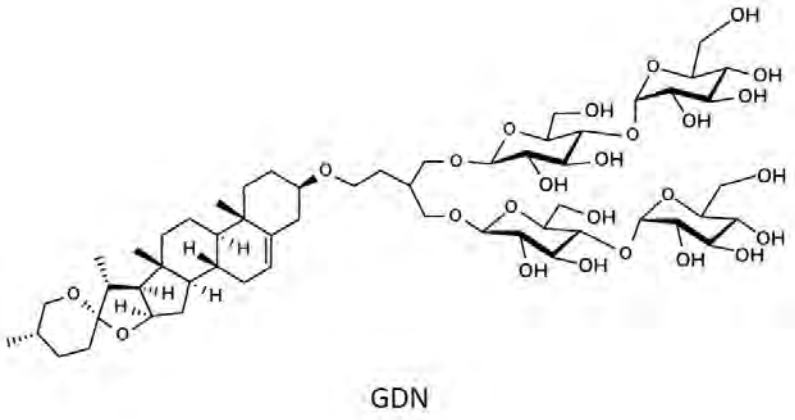

Figure 1.4: Chemical structure of GDN
Chemical structure of the synthetic, non-toxic digitonin-derivate named glyco-diosgenin (GDN; Structure from anatrace.com).

Protein size and shape play important roles in SPA cryo-EM of membrane proteins. The addition of binding partners can help to stabilize flexible domains, increase particle size, and enable the alignment of particles for 2D and 3D reconstruction by features outside of the micelle/lipid belt. Therefore, often antibody-derived "superbodies" are used. Included in this terminology are nanobodies (Rasmussen *et al.*, 2011), Fabs (fragments antigen binding; Wu *et al.*, 2012), megabodies (Uchański *et al.*, 2021) and legobodies (Wu X. & Rapoport T. A., 2021). Examples for the requirement of a Fab fragment to increase particle size and help particle alignment for SPA cryo-EM by adding a feature outside of the membrane/micelle, are the human serotonin transporter (Plenge *et al.*, 2012) or the chloriquine resistant transporter from *Plasmodium falciparum* (Kim *et al.*, 2019). Moreover, the visualization of how Fab fragments bind to proteins can also have implications for development of antibody-based therapeutics (Zhang H. *et al.*, 2012). Nonetheless, such fiducial markers need to have limited flexibility relative to the target protein to support alignment and reconstruction of the target (Piper *et al.*, 2022).
One of the most important steps in SPA cryo-EM is optimizing the vitrification conditions, e.g. by screening different grid types to optimize protein concentration and orientation in the holes. Carbon coated Quantifoil® grids is the so far mostly used grid type (Piper *et al.*, 2022), for membrane proteins however, graphene oxide shows improvement in particle numbers in the hole (Han *et al.*, 2020). Gold-coated grids can increase the final resolution (Danev *et al.*, 2021). Other factors are glow discharge and blotting conditions, blot force and blot time, and as well the use of different vitrification devices (Piper *et al.*, 2022). Also, the time interval between sample application to the grid and vitrification, has influence on the orientation of the particles in the holes (Noble *et al.*, 2018). More manageable approaches for improving the distribution of particles in the vitrified ice, are to add fluorinated detergents prior to vitrification (Wang *et al.*, 2019) or to vary salt concentrations (Kampjut *et al.*, 2021). In general, intensive screening in vitrification is necessary for every single target protein to find the best reproduceable conditions.
Despite SPA cryo-EM, there are other cryo-EM applications that can be used to determine structures of membrane proteins. One is the so called *in situ* cryo-tomography (cryo-ET) on native membranes (Chen W. & Kudryashev M., 2022). Currently, mostly large membrane protein structures are suitable for *in situ* cryo-

EM (Rapisarda *et al.*, 2019), as smaller integral membrane proteins cannot yet be solved in high-resolution. Considering the rate of progress in this area, it is only a matter of time before smaller proteins will also be resolved by *in situ* cryo-EM (Piper *et al.*, 2022).

Another currently developed workflow to solve high-resolution cryo-EM membrane protein structures in near-native environments is their structure determination in proteoliposomes (Pang *et al.*, 2019). So far, they are used for functional analysis of membrane proteins (Pitard *et al.*, 1996; Madej *et al.*, 2014). Using a combination of optimized proteoliposome isolation, cryo-sample preparation on graphene grids and an efficient particle selection strategy will be necessary to open this strategy up for smaller membrane proteins. This approach also gives insight on the functional impact of physical membrane modulations to membrane proteins (Yao *et al.*, 2020). Another very promising approach in this field is the so called 'liposomes on a streptavidin crystal'. Thereby a voltage across the liposome can be generated to determine the atomic structures of membrane proteins, particularly voltage gated ion channels, under certain membrane potentials (Wang *et al.*, 2010).

1.2 Membrane mimics

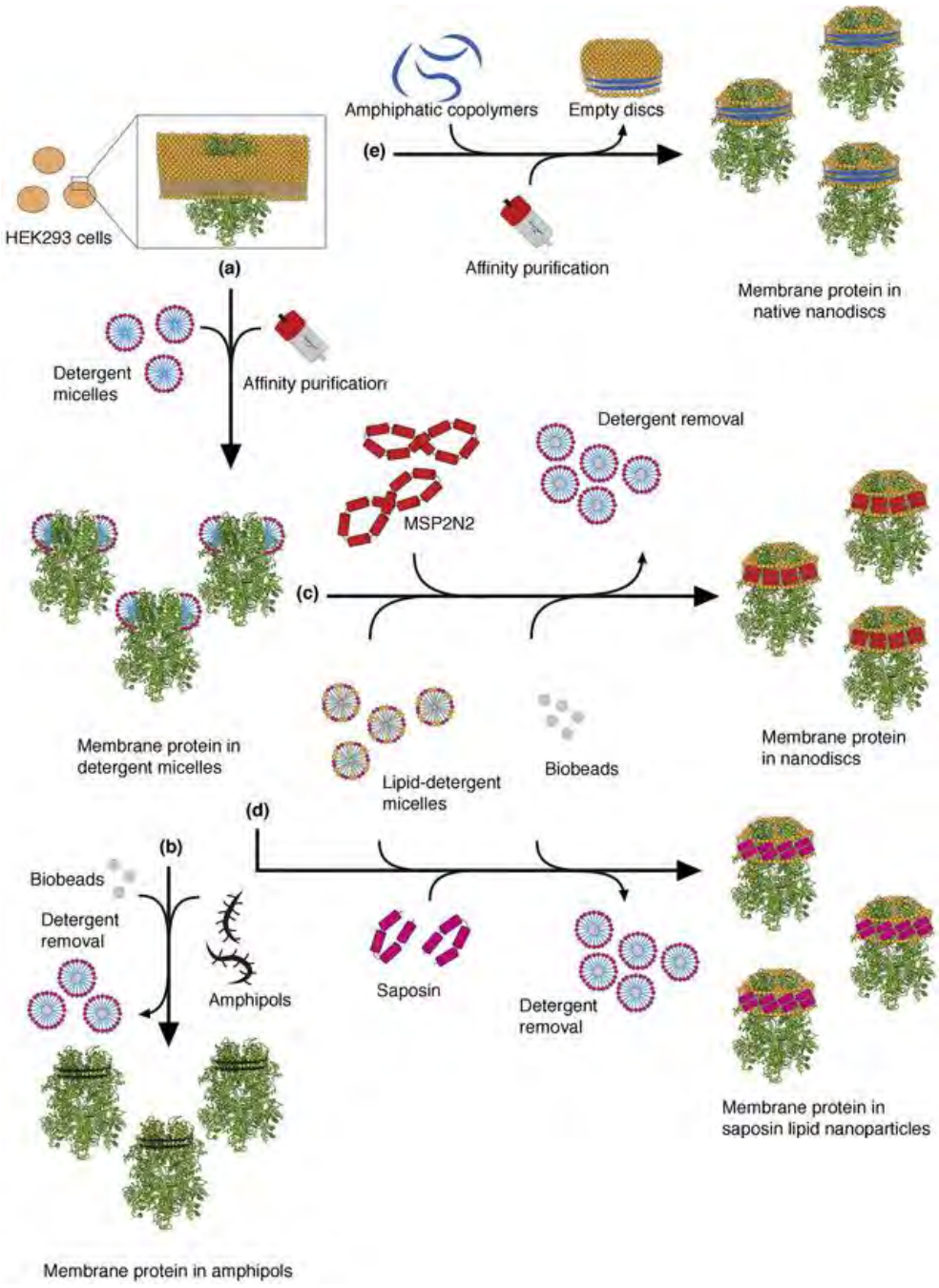

Figure 1.5: Solubilization and purification of membrane proteins for SPA cryo-EM studies
Here, TRPM4 (Autzen *et al.*, 2018) is used as an example to illustrate various approaches of solubilizing and purifying membrane proteins for SPA cryo-EM. The figure is adopted from Autzen *et al.*, 2019. **(a)** Extraction and solubilization of membrane proteins from cell membranes by detergent. **(b)** The detergent-solubilized membrane protein is exchanged into amphipols using biobeads to remove the detergent. **(c)** The detergent-solubilized membrane protein is reconstituted into MSP nanodiscs by addition of detergent-solubilized lipids, membrane scaffold proteins (MSPs) and biobeads. **(d)** The detergent-solubilized membrane protein is reconstituted into salipros, adding detergent-solubilized lipids, Saposin A and biobeads. **(e)** Instead of breaking the cells and solubilize the membrane with detergent, addition of styrene maleic acid (SMA) copolymers will extract the membrane protein as native nanodiscs, so called styrene maleic-acid lipid particles (SMALPs).

SPA cryo-EM can provide crucial insights into the native architecture as well as lipid–protein interactions (Sun *et al.*, 2018) and bilayer modulation of the protein (Yao *et al.*, 2020). Interestingly, a recent study shows that, by using nanodisc, amphipol or detergent, the amphipathic belts surrounding the extracted proteins are often of similar in size. This indicates that the use of different methods reveals similarly ordered belts around transmembrane regions after 3D reconstructions, independent of the solubilization method or protein used (Zampieri *et al.*, 2021).
In the following sections the two major categories of membrane-mimicking systems, amphipols and nanodiscs (Ratkeviciute *et al.*, 2021), will be explained in more detail.

1.2.1 Amphipols

Amphipols are amphipathic polymers specially designed to keep membrane proteins soluble (Tribet et al., 1996). They are composed of a hydrophilic backbone adorned with multiple hydrophobic groups (Fig. 1.6). Like detergents, amphipols self-assemble into well-defined particles that tightly surround transmembrane domains of the target protein (Fig. 1.5b; Tribet et al., 1996; Popot *et al.*, 2003). Unlike detergents, amphipols exhibit a higher affinity for hydrophobic transmembrane domains, ensuring a tight association without a CMC (Le Bon *et al.*, 2018). Once reconstituted into amphipol discs, the membrane protein does not require any additional amphipol in the buffer. Furthermore, their tight association has been observed to stabilize the conformation of membrane proteins (Liao *et al.*, 2013).
Membrane proteins solubilized with detergent are reconstituted into amphipols by slowly removing detergent via either nonpolar hydrophobic polystyrene beads (biobeads), that absorb the amphiphilic detergents, or by dialysis (Fig. 1.5b). Finally, the reconstituted membrane protein is subjected to size-exclusion chromatography (SEC) in detergent-free buffer to remove aggregates and and/or excess amphipols. The amphipol A8-35 is commonly used (Fig. 1.6). Membrane protein structures solved in amphipols are TRPV1 in A8-35 at a resolution of 3.4 Å (Liao *et al.*, 2013), HCN4 (Saponaro *et al.*, 2021), the STRA6 receptor (Chen *et al.*, 2016), the TRPA1 ion channel (Paulsen *et al.*, 2015) or the so far highest achieved resolution of 2.17 Å on the *bovine-bestrophin-2 anion channel* (Owji *et al.*, 2020). However, apparent sensitivity of A8-35 to pH (Gohon *et al.*, 2006) and divalent cations (Picard *et al.*, 2006) are disadvantages. Various derivates of A8-35, like non-ionic glycosylated amphipols (Sharma *et al.*, 2012), sulfonated amphipols (Dahmane *et al.*, 2011) or phosphorylcholine-based amphipols (Diab *et al.*, 2007) have been used successfully. Additionally, there are new group of amphipols, the cycloalkane-modified amphiphile polymers, which allow for direct extraction from the membrane (Marconnet *et al.*, 2020). This promising approach, making it possible to study membrane proteins in their native environment via SPA cryo-EM, shows promising first results (Higgins *et al.*, 2021) and will be investigated further.

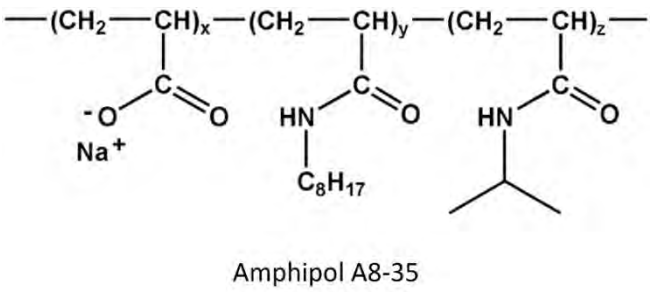

Figure 1.6: Molecular structure of amphipol A8-35
Unlabeled A8-35 is composed by three different chemical groups randomly distributed along the chain. The molar percentages of each group are x=35%, y=25% and z=40%.
The figure is derived from Gohon *et al.*, 2008

1.2.2 Nanodiscs

The term “nanodisc” describes a membrane protein inserted into a discoidal lipid bilayer section stabilized by either an amphipathic protein, peptide or polymer that act to shroud the hydrophobic lipid tails from the aqueous environment (Ratkeviciute *et al.*, 2021). Nanodiscs facilitate lipid-protein interactions in a quasi-native environment. In this paragraph, nanodisc systems stabilized by membrane scaffold proteins (MSPs; Bayburt *et al.*, 2002) or Saposin A (Frauenfeld *et al.*, 2016), as well as styrene maleic-acid lipid particles (SMALPs; Knowles *et al.*, 2009), also termed native nanodiscs, will be discussed.

1.2.2.1 Membrane scaffold protein (MSP) nanodiscs

The best-known nanodisc systems are “MSP nanodiscs”. These are discoidal lipid bilayers stabilized by two encircling, amphipathic, helical protein belts, the so called “membrane scaffold proteins” (MSPs; Bayburt *et al.*, 2002). They are constructed by one or several serially connected domains of apolipoprotein A1, the major proteinaceous component of high-density lipoprotein particles (Bayburt *et al.*, 1998). By genetic engineering of apolipoprotein A1, various MSPs have been developed, enabling modulation of nanodisc size (8-16 nm) and incorporation of a range of tags (Denisov I. G. & Sligar S. G., 2017). Alongside these linear MSPs, there is also circularized MSPs with a covalent bond between the N- and C-termini of an MSP. These circularized scaffolds form nanodiscs with greater homogeneity and diameters of up to 50 nm, what is beneficial for reconstituting large multi-subunit membrane protein complexes (Nasr *et al.*, 2017). Conveniently, all these MSPs can easily be produced in high yield and purity after expression in *E. coli* (Denisov *et al.*, 2004), enabling a rapidly screen for different reconstitution scaffolds related to the membrane protein of interest.

In the standard workflow the membrane protein in detergent is incubated with detergent-solubilized phospholipids and MSPs (Fig. 1.5c). Then detergent is slowly removed by dialysis or biobeads. The final step is size exclusion chromatography (SEC) in detergent-free buffer to remove aggregates and separate the reconstituted target protein from empty, lipid-only discs and/or excess MSPs (Alami *et al.*, 2007). To perform successful reconstitution of a membrane protein into homogenous nanodisc particles, several parameters must be elaborated for every single target. Foremost, the length of the MSP used is the most critical parameter. A second parameter is the identity and amount of lipids to include in the reconstitution mixture. Depending on the research question, pure synthetic phospholipids (Reid *et al.*, 2020) or more complex lipid extracts (Gao *et al.*, 2016) are used. This high variability makes MSP nanodiscs an attractive biochemical tool with numerous applications. MSP nanodiscs are a robust method extensively used for SPA cryo-EM for both, membrane proteins expressed in prokaryotes as well as eukaryotes. Structures determined with the help of MSP nanodiscs include various transporters (Reid *et al.*, 2020), ion channels, like the first ever MSP nanodisc SPA cryo-EM structure of rat TRPV1 (Gao *et al.*, 2016), and even GPCRs (Zhang M. *et al.*, 2021). Many of these structures have revealed new insights into membrane protein structure and function which were not evident from studies performed in detergent micelles, such as revealing the binding sites for specific lipids which modulate protein function or revealing a substrate binding site (Gao *et al.*, 2016). In addition to this, nanodiscs provide other possible advantages for SPA cryo-EM. Adding a molecular weight of more than 100 kDa to the protein of interest by reconstitution into nanodiscs, the method results in an increase of the overall size of the particle. However, the additional mass of the nanodisc will only be advantageous if their heterogeneity does not interfere with particle alignment, especially if the nanodisc is large with respect to the size of the target protein. Also studying membrane proteins that have very small extramembrane domains is challenging. Increasing the contrast by taking images with a Volta phase plate and new image-processing algorithms could be helpful in this case (Efremov *et al.*, 2017).

Beyond structural characterization of membrane proteins, nanodiscs have been used to characterize binding of soluble protein and small-molecule ligands onto membrane protein receptors (Alami *et al.*,

2007), and additionally empty, lipid-only discs have been used to monitor binding of peripheral membrane proteins onto membrane lipids (Zhang X. X. *et al.*, 2021) or to study membrane binding of antimicrobial peptides by native mass spectrometry (Kostelic *et al.*, 2021), what may be impactful for developing novel antibiotics. In general, MSP nanodiscs have a diverse potential and can be used in almost every method characterizing membrane proteins.
MSP nanodiscs also have several drawbacks. It is almost impossible to reconstitute membrane proteins solubilized and purified in detergents with very low CMCs and sometimes reconstitution cannot restore lipids striped away during reconstitution. MSP nanodisc reconstitution also adds additional time to the sample preparation, which may be harmful for fragile targets. An approach hereby is to add MSP and biobeads immediately after detergent solubilization and prior to affinity purification (Sharma S. & Wilkens S., 2017). This approach may significantly shorten the exposure to detergent but requires a considerable amount of MSP for reconstitution. Also finding the perfect disc size is not trivial as using short MSPs may generate more homogeneous nanodisc-protein particles, but with the potential risk that a too tightly bounded MSP may constrain functionally interesting conformational states.

1.2.2.2 Saposin-based nanodiscs (salipros)

Another lipid nanoparticle option is the salipro system (Fig. 1.5d). This approach is very similar to MSP nanodiscs (1.2.2.1) but utilizes Saposin A as the scaffolding protein (Frauenfeld *et al.*, 2016). The saposin protein family is composed of four (A-D) small (approx. 10 kDa), amphipathic, α-helical glycoproteins. X-ray crystallography structures of Saposins A-D have shown that they can form discoidal lipoprotein particles when incubated with unilamellar liposomes (Ahn *et al.*, 2006; Rossmann *et al.*, 2008). By exploiting these properties, Saposin A was identified to function as a scaffold to reconstitute membrane proteins within a lipid environment, forming a saposin-lipoprotein, the so called salipros (Frauenfeld *et al.*, 2016).
The workflow of salipro preparation is similar to MSP nanodiscs (1.2.2.1). A detergent-purified membrane protein of interest is incubated at a fixed ratio with phospholipids in detergent and Saposin A, following detergent removal by dialysis or biobeads and a final SEC in detergent-free buffer to separate salipros containing the protein of interest from 'empty' lipid-only discs and excess saposin (Fig. 1.5d; Frauenfeld *et al.*, 2016). Also, optimization of the suitable ratio of protein to lipid to Saposin A is necessary for every target protein (Flayhan *et al.*, 2018). Salipros are more adaptive towards membrane proteins of different sizes and shapes by using different numbers of Saposin A to form the scaffold (Lyons *et al.*, 2017). This makes screening less complex compared to MSP nanodiscs. Additionally, this highlights the big advantage of salipros, as they combine the adapting to the size of the incorporated membrane protein, like detergents and amphipols, while including a lipid environment similar to MSP nanodiscs (Kintzer *et al.*, 2018). Like MSPs, Saposin A can be expressed and purified readily from *E. coli* (Frauenfeld *et al.*, 2016).
Several structures of membrane proteins reconstituted in salipros were determined including bacterial membrane proteins like MsbA (Kehlenbeck *et al.*, 2022) and AcrB (Du *et al.*, 2020), as well as eukaryotic ones like 5HT3A serotonin receptor (Zhang Y. *et al.*, 2021) and the nicotinic acetylcholine receptor (Rahman *et al.*, 2022), or TPC1 from *Arabidopsis thaliana* (Kintzer *et al.*, 2018), underlining the wide applicability of salipros. Another high-resolution SPA cryo-EM structure, namely of the mitochondrial calcium uniporter, shows another benefit of this technique, as initially testing MSP nanodiscs proved that these are too large and flexible for the rather small transmembrane domain (Nguyen *et al.*, 2018).
However, the 3D structure of Saposin A may impose constraints on the overall shape and conformation of the target protein (Autzen *et al.*, 2019) and salipros do not rebuild the mechanical properties of a lipid bilayer. A method called 'DirectMX' enables reconstitution into salipros almost directly from native membranes (Lloris-Garcerá *et al.*, 2020). Thereby, membranes containing an affinity-tagged protein of interest are solubilized with a mild detergent, such as GDN (Fig. 1.4), and reconstitution into salipros is achieved by diluting the solubilized material in a large volume excess of aqueous buffer containing pure

Saposin A. Following a brief incubation, the protein is purified by affinity chromatography in detergent-free conditions. This approach is very similar to a method existing for MSP nanodiscs (Sharma S. & Wilkens S., 2017). A recent study on the mammalian PANX1 channel using DirectMX, shows that it can be used for high-resolution SPA cryo-EM, as well as ligand binding assays by surface plasmon resonance (Drulyte *et al.*, 2023). As the target protein is exposed to detergent for only a short time, this method is suitable for challenging human membrane proteins targets, GPCRs and ion channels, for downstream drug discovery, e.g. screening for small molecule binders or therapeutic antibodies (Dodd *et al.*, 2020). In this context, also the so called peptidiscs need to be mentioned. In this method, quite similar to DirectMX, reconstitution is achieved during affinity purification ('on-beads' reconstitution) by adding a large volume excess of detergent-free buffer supplemented with concentrated peptidisc peptide (nanodisc scaffold peptide (NSP)). Herby the detergent is diluted well below its CMC and multiple copies of the peptidisc peptide can self-assemble around the hydrophobic transmembrane region of the target protein and any co-purifying annular lipids, forming homogenous peptidiscs (Carlson *et al.*, 2018). However, no high-resolution structural data has yet been reported for a membrane protein purified in peptidiscs, and as it has been extensively applied towards bacterial membrane proteins (Young *et al.*, 2022), it has not been successfully used for eukaryotic membrane proteins by now.

1.2.2.3 SMALPs (native nanodiscs)

A significant development in nanodisc technology was the utilization of the styrene maleic acid (SMA) copolymer to form SMALPs (Fig. 1.7a; Knowles *et al.*, 2009). SMAs extract membrane proteins directly from the lipid bilayer in the absence of detergents, encapsulating them into discoidal, water-soluble particles. Due to this they have been termed native nanodiscs because they carry native lipids from the membrane in which the target protein resides, preserving certain unique characteristics of the native membrane, such as lipid composition and asymmetry of the bilayer, as well as associated protein interactors. Thus, the SMALP system is the only membrane mimetic that is truly detergent-free (Dörr *et al.*, 2016).

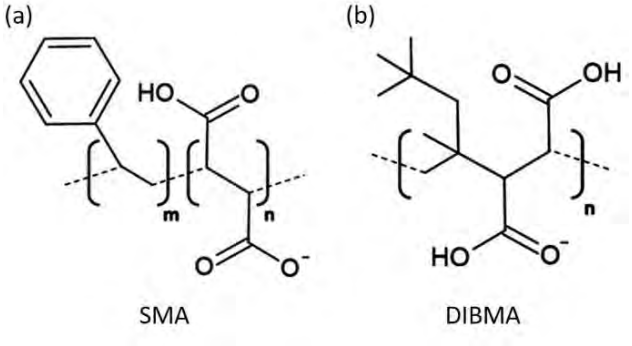

Figure 1.7: Molecular structure of SMA and DIBMA **(a)** Chemical structure of the styrene maleic acid copolymer (SMA; Ratkeviciute *et al.*, 2021). **(b)** Chemical structure of di-isobutylene maleic acid (DIBMA; Ratkeviciute *et al.*, 2021).

Practically, native membranes, or whole cells, containing the tagged protein are solubilized adding SMA, and affinity purified in detergent-free conditions. A subsequent SEC step is routinely performed to remove aggregates and/or protein contaminants (Fig. 1.5e; Dörr *et al.*, 2014).

SMALPs have been used for some membrane proteins by SPA cryo-EM, e.g. ion-channels (Yoder N. & Gouaux E., 2020; Kumar *et al.*, 2021) or a respiratory chain complex (Swainsbury *et al.*, 2023). The first reported SPA cryo-EM structure is that of the alternative complex III, which presumably captures the native lipid–protein interactions (Sun *et al.*, 2018). This structure, however, shows only a very thin layer of density around the protein, suggesting that SMA encircles the protein tightly, with only few lipids included in the nanodisc, not mimicking a real bilayer environment.

Besides the benefit of generating native nanodiscs and the successful use for structural, biophysical, and biochemical analysis of membrane proteins, SMA also has limitations. Its incompatibility to low pH (< 7.0)

and divalent cations coupled with a tendency to form populations of heterogeneous disc size, severely restricts their usage (Pollock *et al.*, 2018). In addition, SMAs interfere with affinity resin, mainly during metal affinity chromatography, due to the negative charge on the polymer (Swainsbury *et al.*, 2023). Also, the solubilization efficiency of the polymer is often lower than for detergents (Oluwole *et al.*, 2017). This low solubilization efficiency is especially problematic in the context of eukaryotic membrane proteins, which are often present at low levels. Additionally, it absorbs UV light because of its styrene moiety, interfering with spectroscopic studies (Oluwole *et al.*, 2017), and the nanodisc diameter is limited to 10-12 nm (Pollock *et al.*, 2018). Furthermore, isolation conditions with SMA copolymers are too harsh for mammalian targets, and the sample loss in the preparation process is too severe for membrane proteins with limited expression. Currently, typical approaches for using SMA co-polymers include high ionic strength buffers, such as 500 mM NaCl or L-arginine and/or 12-24 hours of incubation with affinity resins (Sun *et al.*, 2018). Such conditions may not be compatible with the typical fragility of membrane proteins, particularly of mammalian origin.

Consequently, research within the nanodisc field has centered largely upon developing polymers which may be utilized in a wider range of applications. Modifications entailed variation of the styrene to maleic acid ratio, to adjust polymer hydrophobicity or SMA polymers with ethylenediamine. Both species display greater tolerance towards salt and divalent cations (up to 200 mM) and are stable under a greater range of pH values (Ravula *et al.*, 2017). In addition, a quaternary amine containing derivative can form macro-nanodiscs of approx. 30 nm in diameter, much like an ethanolamine containing derivative, which may form macro-nanodiscs up to 60 nm in diameter (Ravula *et al.*, 2018). A positively charged copolymer displays pH stability below pH 7.8, is entirely divalent resistant and forms nanodiscs of a smaller diameter, being ideal for the solubilization of membranes and smaller proteins under acidic pHs (Hall *et al.*, 2018). To mitigate the problem of UV absorption, aliphatic polymers lacking the styrene hydrophobic group have been developed. Di-isobutylene maleic acid (DIBMA) is composed of alternating di-isobutylene and maleic acid moieties (Fig. 1.7b), forming larger nanodiscs (12-29 nm; Oluwole *et al.*, 2017). In contrast with SMA, DIBMA displays a higher tolerance to divalent cations and increase its solubilization efficacy in the presence of low millimolar concentrations of Mg^{2+} and Ca^{2+}, due to steric hindrance (Danielczak *et al.*, 2019). However, precipitation at acidic pH remains a vulnerability of DIBMA due to retention of the maleic acid carboxyl groups. To date, DIBMA has been successfully implemented in the purification of several MPs, however, when compared directly with SMA, DIBMA nanodiscs typically display reduced stability over time and provide lower protein yields of reduced purity (Gulamhussein *et al.*, 2020). In addition, the effect on the lipid acyl-chain order is not as significant as for the aromatic SMA copolymer. It was shown that the size of the DIBMA nanodisc increases with increasing lipid acyl-chain length and order, while it decreases with increasing ionic strength (Oluwole *et al.*, 2017), making it a hard to handle system.

1.3 Emerging membrane protein drug targets

The development of new pharmaceutical drugs is a complex and time-consuming process. It typically involves the identification and characterization of possible drug targets, followed by screening of large chemical libraries to identify potential drug candidates for further development. Screening methods are based on biochemical and cell-based assays, which are limited by their specificity, sensitivity, and relevance to in vivo conditions. SPA cryo-EM has emerged as a powerful and versatile technique that holds great promise for drug discovery. It can provide detailed insights into the structure of a possible drug target (Gao *et al.*, 2016; She *et al.*, 2019; Han *et al.*, 2022) as well as binding modes and conformational changes induced by drug binding (Niu *et al.*, 2022), which are crucial for understanding drug efficacy and specificity. In this work, two emerging drug targets were structurally investigated, SLC5 transporters and two-pore channels. Although no drug screening was performed, the structural work was designed for later bioinformatic drug screening.

1.3.1 The SLC5A family

The movement of glucose in and out of cells is crucial for cellular physiology. In mammals this movement is achieved by two structurally and functionally different families of membrane proteins: First, Glucose transporters (GLUTs), which operate by facilitated diffusion (Mueckler M., 1994) and second, sodium–glucose cotransporters (SGLTs), which actively transport glucose against the concentration gradient by coupling with Na^+ (Wright E. M., 2001). The SGLTs belong to the Solute Carrier 5A (SLC5A) protein family, that has twelve human genes expressed in tissues ranging from epithelia to the central nervous system. Functionally these twelve proteins can be subdivided as followed: ten are tightly coupled plasma membrane Na^+/substrate cotransporters for solutes such as sugars, myoinositol, vitamins, anions or short chain fatty acids (Wright E. M., 2013), whereas CHT1 (SLC5A7) is a Na^+/Cl^-/Choline cotransporter (Okuda T. & Haga T., 2000) and SGLT3 (SAAT1/SLC5A4) is a glucose sensor (Fig. 1.8a; Diez-Sampedro *et al.*, 2003). All members of the SLC5 family share a common structural framework, the LeuT-fold (Yamashita *et al.*, 2005), consisting of 10 to 14 transmembrane helices, divided into two domains, while the central substrate-binding site is located between these two domains, making them fully functional transporters as monomers (Fig. 1.8b; Turk *et al.*, 2000). Mechanistic insights are based on functional studies on SGLTs expressed in cells (Panayotova-Heiermann *et al.*, 1995; Ghezzi C. & Wright E. M., 2012), structural studies on the bacterial homologues vSGLT (Faham *et al.*, 2008) and SiaT (Wahlgren *et al.*, 2018), as well as the distally related LeuT (Yamashita *et al.*, 2005), and MD simulations on homology models (Adelman *et al.*, 2016). By this the functionality of SGLTs can be described as an alternating access mechanism (Fig. 1.8c). Although the mechanism is conserved, homology models on SGLTs did so far not reveal the structural basis for differences in sugar selectivity, in Na^+ to sugar stoichiometry ($2Na^+$/1 glucose for SGLT1 (Chen *et al.*, 1995) and $1Na^+$/1 glucose for SGLT2 (Hummel *et al.*, 2011)) or the selectivity and affinity of inhibitors (Dong *et al.*, 2018; Kamitori *et al.*, 2022). Another important aspect is the complex formation of SGLTs with MAP17, which is a small membrane-associated protein that stimulates SGLTs (Coady *et al.*, 2017). However, the molecular nature of MAP17-SGLTs interaction is largely unknown, it seems to represent an interesting approach towards new inhibition mechanisms.

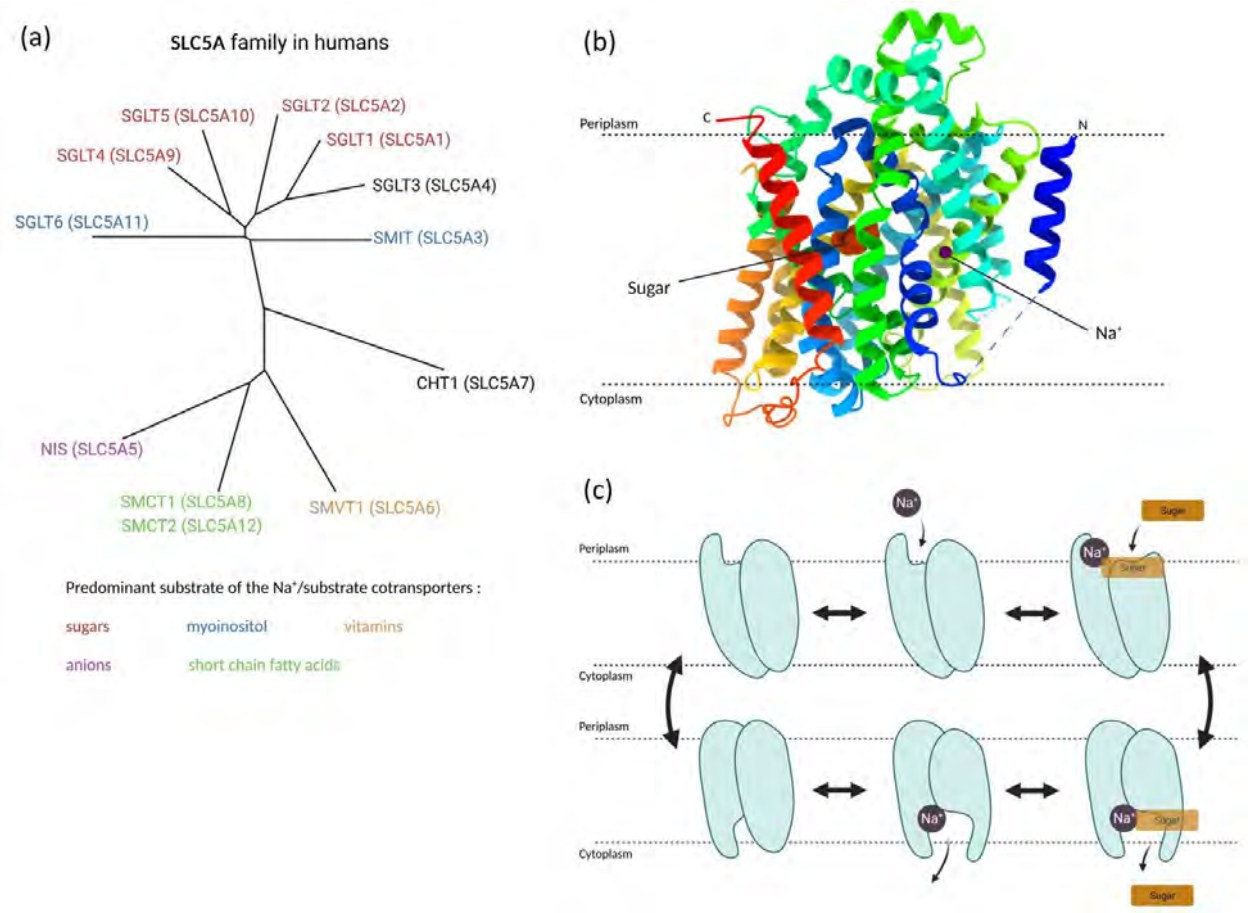

Figure 1.8: Characteristics of the SLC5A family
(a) Unrooted phylogenetic tree of the twelve human members of the SLC5A family. The tightly coupled plasma membrane Na+/substrate cotransporters are colored related to their predominant substrates, whereas the exceptions CHT1 (Na^+/Cl^-/Choline cotransporter (Okuda T. & Haga T., 2000)) and SGLT3 (glucose sensor (Diez-Sampedro et al., 2003)) are not colored. Figure is based on Wright E. M., 2013, and created with BioRender (2.1.2). **(b)** The structure of the bacterial SGLT homolog vSGLT (PDB: 3DH4). A side view of the 3-D structure of vSGLT in the membrane. The structure contains 14 transmembrane spanning helices with sugar (dark orange) and Na^+ (dark purple) bound in the center occluded from the periplasm. The structure consists of two inverted repeats with one TM helix in each repeat containing an unwound region in the middle of the membrane. Derived from Faham et al., 2008, and created with ChimeraX (2.1.2) and BioRender (2.1.2). **(c)** Model of the alternating access mechanism of SGLTs on the example of SGLT2: First Na^+ binds to an outward-facing state. This binding triggers the opening of an external gate to allow glucose to bind. By this the external gate is closed, what allows SGLTs so isomerize to the inward-facing state. Here glucose and Na^+ can be released and the protein alternates back to the outward-facing state, being ready for the next cycle. Derived from Schultz S. G., 1985, and created with BioRender (2.1.2).

The main target within the SLC5A family for drug research is sodium/glucose cotransporter 2 (SGLT2). It is mainly located in the kidney proximal convoluted tubule where it is responsible for 90% of tubular glucose absorption, while inhibition leads to urinary glucose excretion, which in turn lowers blood glucose concentration (Ghezzi C. & Wright E. M., 2012). By this the development of specific SGLT2 inhibitors such as empagliflozin was and still is of paramount interest to treat Type 2 diabetes mellitus patients, due to these existing inhibitors display side effects and limitations in efficiency (Gallo *et al.*, 2015; Steen O. & Goldenberg R. M., 2017; Chan G. C. W. & Tang S. C. W., 2018). To identify new therapeutic compounds, knowledge of the molecular determinants in SGLT2 inhibition specificity is required, which can be achieved by determination of protein structure in combination with functional studies (Niu *et al.*, 2022).

Although the SLC5A family is considered to consist of cotransporters there is one big exception. Based on its electrophysiological properties SGLT3 is a glucose sensor inhibited by the SGLT-antagonist phlorizin (Diez-Sampedro *et al.*, 2003). Supporting this glucose-sensing role is its high expression in the small intestine and skeletal muscle (Diez-Sampedro *et al.*, 2003, Chen *et al.*, 2010), where there is evidence that SGLT3 stimulates serotonin secretion to inhibit gastric emptying and food intake (Freeman *et al.*, 2006). In other tissues like the brain or the kidney SGLT3 appears to be expressed at a lower level (Nishimura M. & Naito S., 2005; Kothinti *et al.*, 2012). Additionally, to be a glucose sensor, SGLT3 can transport imino sugars, that are used to treat Type 2 diabetes mellitus and lysosomal storage disorder. This fact together with its expression in the small intestine makes it a very interesting target for research on imino sugars used as drugs (Voss *et al.*, 2007). A very interesting fact about SGLT3 is the ability to be converted from a glucose sensor into a glucose transporter only by a point mutation. The mutation E457Q transforms SGLT3 into a transporter similar to SGLT1 (Bianchi L. & Díez-Sampedro A., 2010). Getting insight into the lacking structural information of SGLT3 and the mutant E457Q, together with the existing functional data, might give hints for finding better imino sugars to treat Type 2 diabetes mellitus or even develop more potent and selective inhibitors for SGLT1.

Another subgroup of the SLC5A family is the sodium-coupled monocarboxylate transporters (SMCTs) represented by SMCT1 (SLC5A8) and SMCT2 (SLC5A12) in humans, co-transporting short chain fatty acids and Na^+ (Wright E. M., 2013). As SMCT1 is a high-affinity membrane transporter of lactate that can also mediate the uptake of other monocarboxylates such as pyruvate, butyrate, propionate, and acetate (Miyauchi *et al.*, 2004), mainly expressed in the intestinal colon and the outer kidney cortex (Ganapathy *et al.*, 2008), SMCT2 is a low-affinity membrane transporter of lactate, also transporting other monocarboxylates, including pyruvate and nicotinate (Gopal *et al.*, 2007), being present in the proximal parts of the intestinal tract and both kidney cortex and medulla (Srinivas *et al.*, 2005). SMCT1 and SMCT2 are both Na^+-coupled. SMCT1-mediated transport is electrogenic with a Na^+ to monocarboxylate stoichiometry of 2:1, whereas SMCT2-mediated transport is electroneutral (Na^+ to monocarboxylate stoichiometry of 1:1) (Sivaprakasam *et al.*, 2017). Moreover, SMCT1 has been shown to function as a tumor suppressor for tumors in the colon, thyroid, stomach, kidney, and brain (Li *et al.*, 2003; Ganapathy *et al.*, 2008). The tumor-suppressive function is related to its ability to mediate concentrative uptake of butyrate, propionate, and pyruvate, all of which are inhibitors of histone deacetylases (Chen *et al.*, 2003; Davie J. R., 2003; Myzak M. C. & Dashwood R. H., 2006). It can also transport a variety of pharmacologically relevant monocarboxylates, including salicylates, benzoate, and γ-hydroxybutyrate and is inhibited by non-steroidal anti-inflammatory drugs such as ibuprofen, ketoprofen, and fenoprofen (Itagaki *et al.*, 2006). Kidney-specific ablation of the expression of SMCT1 and SMCT2 resulted in a marked increase in urinary loss of lactate and a decrease in blood levels, indicating that these transporters might be responsible for renal lactate reabsorption. As there is a lot of functional and even structural information on SMCT1 (Han *et al.*, 2022), very little is known about the role of SMCT2. Getting insight to the missing structural and functional data of SMCT2 is of high relevance for a better understanding of drug transport in the kidney.

1.3.2 The Two-Pore Channel 2

Two-pore channels (TPCs) belong to the voltage-gated ion channel superfamily (Yu F. H. & Catterall W. A., 2004) and are present in animals (TPC1-3) and plants (TPC1). They function as a homodimer, with each subunit containing two homologous *Shaker*-like 6-TM repeats (domain I and II) each compromising a voltage sensor (S1-S4) and a pore (S5-S6) (Fig. 1.9; She *et al.*, 2018; She *et al.*, 2019; Dickinson *et al.*, 2022).

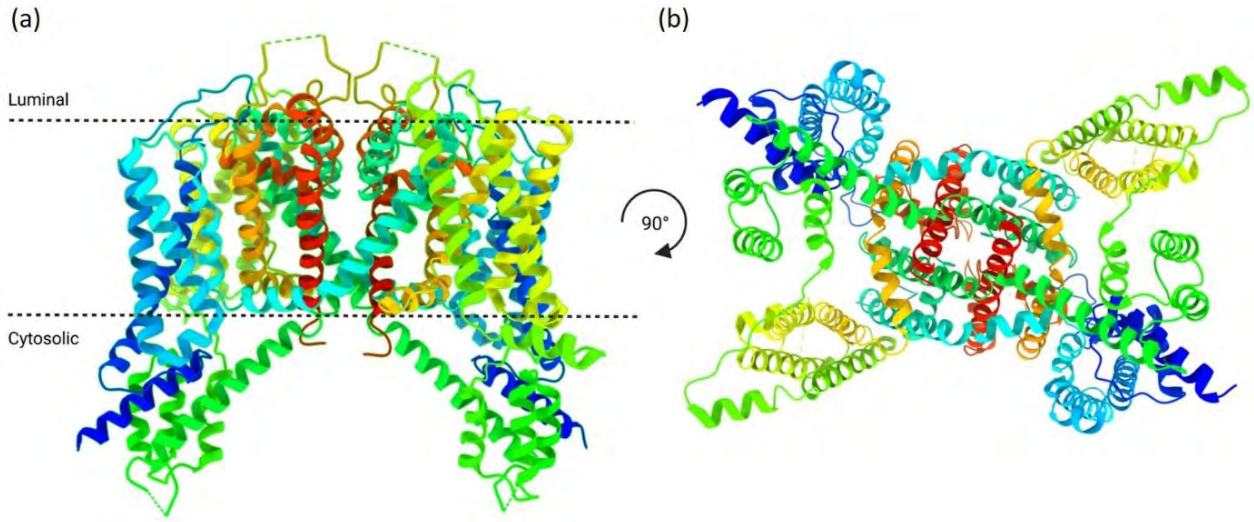

Figure 1.9: Typical homo-dimeric TPC structure
Cartoon representation of the sideview (a) and the cytosolic-view (b) of the typical TPC homo-dimer on the example of human TPC2 (PDB: 6NQ1). Figure created with ChimeraX (2.1.2) and BioRender (2.1.2).

TPCs are located in different cell compartments gated by a range of different factors. TPC1 of plants located in the vacuolar membrane is a voltage-dependent calcium (Ca^{2+})-channel (Hedrich R. & Marten I., 2011). TPCs of animals are regulating the conductance of sodium (Na^{+}; Wang *et al.*, 2012) and Ca^{2+} (Brailoiu *et al.*, 2009; Calcraft *et al.*, 2009; Zong *et al.*, 2009) through the endolysosomal membrane, activated by phosphoinositides (Wang *et al.*, 2012) via direct interaction (She *et al.*, 2018; She *et al.*, 2019), and nicotinic acid adenine dinucleotide phosphate (NAADP; Fig. 1.11c) (Brailoiu *et al.*, 2009; Calcraft *et al.*, 2009; Zong et al., 2009) via the NAADP-binding proteins Jupiter Microtubule Associated Homolog-2 (JPT2) and 'like-Sm' protein 12 (LSM12) (Gunaratne *et al.*, 2023). The activation is voltage-dependent for TPC1 (She *et al.*, 2018) and TPC3 (Cang *et al.*, 2014a), and voltage-independent for TPC2 (She *et al.*, 2019). Animal TPCs are the main influencers of intravesicular pH (Wang *et al.*, 2012; Ambrosio *et al.*, 2016), trafficking (Grimm *et al.*, 2014; Sakurai *et al.*, 2015) and excitability (Cang *et al.*, 2014b) of the endolysosome. The functions of mammalian TPC1 and TPC2 (TPC3 is absent in primates and some rodent species (Calcraft *et al.*, 2009)) are associated with various physiological processes like blood vessel formation (Favia *et al.*, 2014), mammalian target of rapamycin (mTOR) -dependent nutrient sensing (Cang *et al.*, 2013), lipid metabolism (Grimm *et al.*, 2014) and Ebola virus infection (Sakurai *et al.*, 2015; Penny *et al.*, 2019). Recent studies show that TPCs are also involved in severe acute respiratory syndrome coronavirus 2 (SARS-CoV-2) infection (Ou *et al.*, 2020; Clementi *et al.*, 2021) as well as cancer proliferation, metastasis, autophagy and angiogenesis (Favia *et al.*, 2014; Pafumi *et al.*, 2017; Müller *et al.*, 2021; Netcharoensirisuk *et al.*, 2021). Thereby TPC2 inhibitors like naringenin (Favia *et al.*, 2014; Pafumi *et al.*, 2017; Clementi *et al.*, 2021; Müller *et al.*, 2021; Netcharoensirisuk *et al.*, 2021), tetrandrine (Sakurai *et al.*, 2015; Penny *et al.*, 2019; Ou *et al.*, 2020) and

their analogues (Müller *et al.*, 2021) are promising drug candidates for preventing SARS-CoV-2 infection or cancer growth.

In this work the focus is on the human *Two-pore channel 2* (TPC2), preferentially localized in the membrane of the late endosome/lysosome (Brailoiu *et al.*, 2009; Calcraft *et al.*, 2009). Besides, TPC2 is also expressed in pigmented cells where it controls the pH and size of melanosomes, thereby regulating the tyrosinase activity required for melanogenesis and pigmentation (Ambrosio *et al.*, 2016). As described, TPC2 is involved in various physiological functions, including virus infection and cancer proliferation, as well as Parkinson´s disease (Hockey *et al.*, 2015), making it a possible drug-target of high interest.

Functionally human TPC2 is largely independent in its activity from luminal pH (Wang *et al.*, 2012) and shows an agonist-dependent ion selectivity (Fig. 1.10). Activation via the endolysosomal enriched phosphatidylinositol 3,5-bisphosphate ($PI(3,5)P_2$; Fig. 1.11a; Takasuga S. & Sasaki T., 2013) directly through a structurally-resolved binding site results in a Na^+-selective channel (Wang *et al.*, 2012; She *et al.*, 2019), while other phosphoinositides like $PI(4,5)P_2$, $PI(3,4)P_2$, PI(3)P and PI(5)P cannot activate the channel, illustrating the high ligand specificity of TPC2 (She *et al.*, 2019). Indirect activation through NAADP by associated NAADP-binding proteins JPT2 and LSM12 (Gunaratne *et al.*, 2023) creates a preferably Ca^{2+}-permeable, but also Na^+-permeable, non-selective cation channel (Calcraft *et al.*, 2009; Zong *et al.*, 2009). When a combination of both agonists is applied, Ca^{2+}-flux is increased but not Na^+-flux (Yuan *et al.*, 2022).

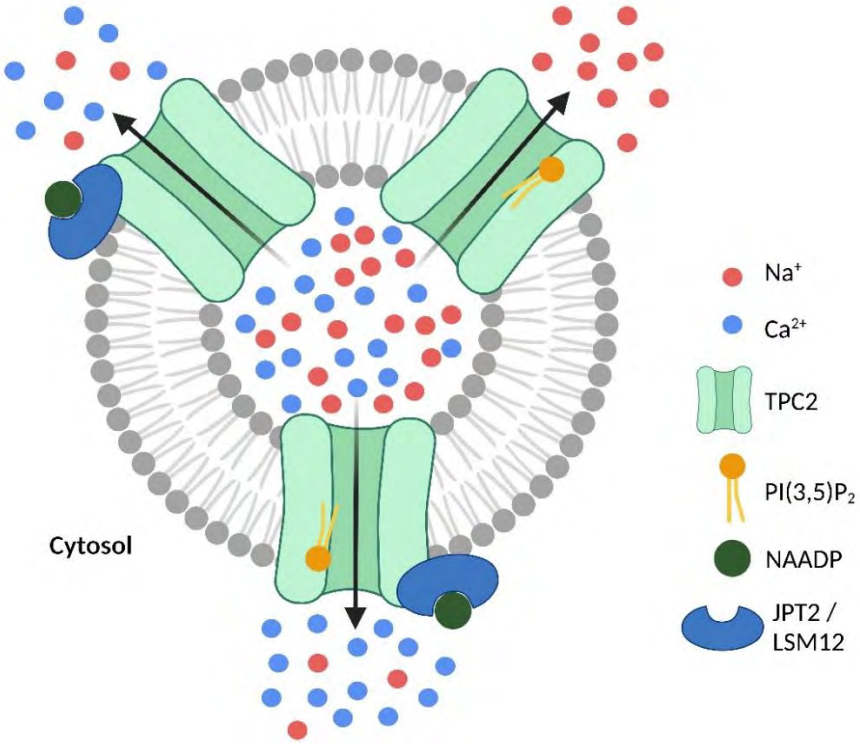

Figure 1.10: Agonist dependent ion selectivity of human TPC2
Schematic showing the influence of $PI(3,5)P_2$- and NAADP-dependent activation of human TPC2 on its Na^+- and Ca^{2+}-permeability. Created with BioRender (2.1.2).

Additional data is proposing that $PI(3,5)P_2$ may be required for NAADP signaling (Wang Q. & Zhu M. X., 2023) and manipulation of $PI(3,5)P_2$ synthesis regulates NAADP-evoked Ca^{2+}-signals (Jha *et al.*, 2014). Moreover, recent studies show that NAADP-mediated indirect activation of TPC2 requires the $PI(3,5)P_2$-binding site (Saito *et al.*, 2023). By contrast, experiments with vacuolin, which has an inhibitory effect on $PI(3,5)P_2$ synthesizing enzymes, reveal that NAADP-dependent activation is largely unaffected by $PI(3,5)P_2$

depletion, but the incubation time with vacuolin was short in that study (Ruas *et al.*, 2015). By now, there is structural evidence about the PI(3,5)P_2-activating mechanism (She *et al.*, 2019), while the NAADP-dependent mechanism is structurally not investigated yet. Molecular dynamic (MD) simulations of Na^+-flux through TPC2 suggest that accumulation of Na^+ in between the selectivity filter and the gate regulates ion flow (Milenkovic *et al.*, 2021), but structural details of the Na^+-transport through the selectivity filter are currently lacking. Besides Ca^{2+} and Na^+ also magnesium (Mg^{2+}) plays an important role in TPC2 activation, as in inhibits the NAADP-activated Ca^{2+} currents (Jha *et al.*, 2014). All in all, this data shows that TPC2 can regulate the flux of different and the channel is tightly regulated by multiple parameters, depending on the relative levels of PI(3,5)P_2 and NAADP (or synthetic agonists), the presence of regulatory proteins like NAADP-binding proteins and additional interacting proteins controlling TPC2 activity, e.g. mTOR or the GTPase *Ras-related protein Rab-7a* (Rab7A; Lin-Moshier *et al.*, 2014). These different modes of activation might affect physiological and pathophysiological states in large bandwidth.

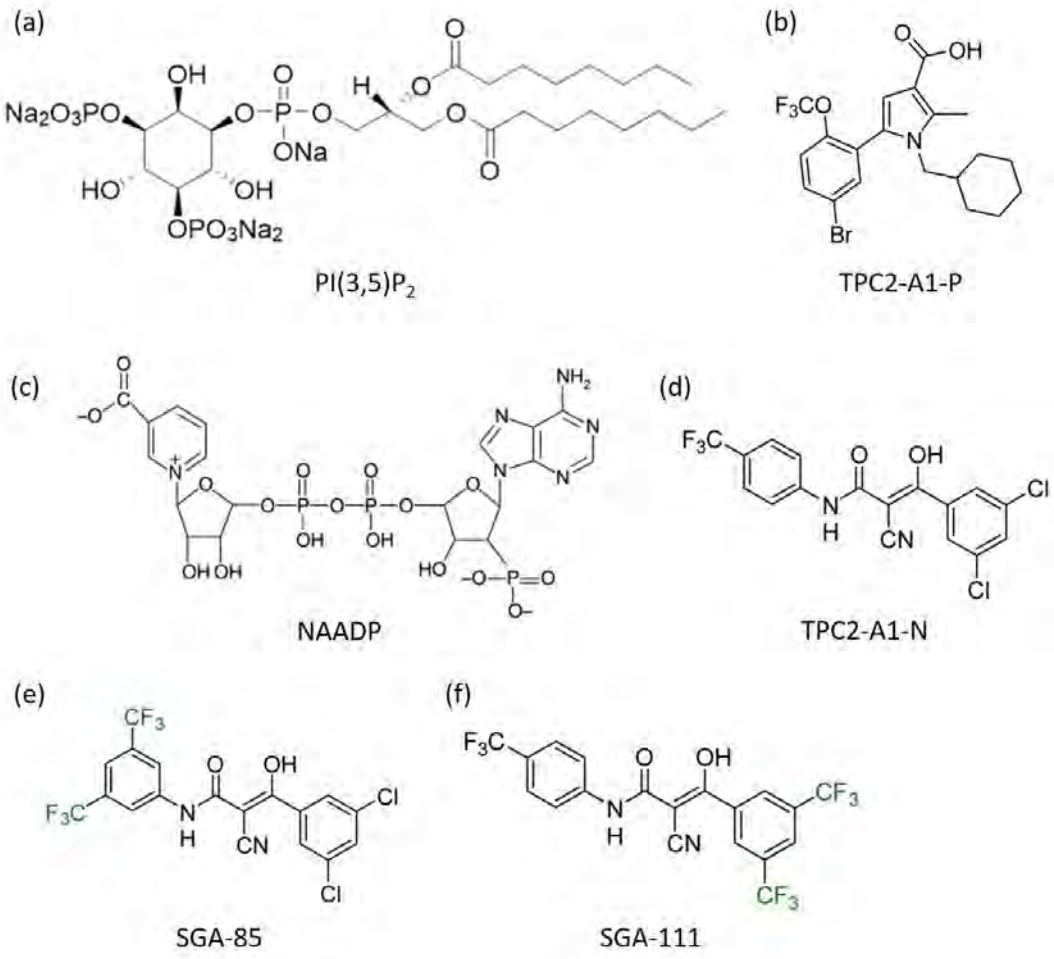

Figure 1.11: Chemical structures of human TPC2 agonists

(a) PI(3,5)P_2 diC8 (2.1.11), a synthetic dioctanoyl PI(3,5)P_2 (She *et al.*, 2019; Structure from echelon-inc.com). **(b)** Chemical structure of TPC2-A1-P (Gerndt *et al.*, 2020b). **(c)** Chemical structure of NAADP (Genazzani A. A. & Debidda M., 2013). **(d)** Chemical structure of TPC2-A1-N (enol-form; Gerndt *et al.*, 2020b). **(e)** Chemical structure of the TPC2-A1-N analogue SGA-85 (enol-form; Gerndt *et al.*, 2020b). Deviations to TPC2-A1-N are colored green. **(f)** Chemical structure of the TPC2-A1-N analogue SGA-111 (enol-form; Gerndt *et al.*, 2020b). Deviations to TPC2-A1-N are colored green.

Several lipophilic, ion selective, TPC2 agonists are reported (Gerndt *et al.*, 2020a; Gerndt *et al.*, 2020b). The first one, TPC2-A1-P (Fig. 1.11b), named so because it mimics the effect of $PI(3,5)P_2$ (Fig. 1.11a), is making TPC2 a Na^+ permeable channel despite being structurally distinct to $PI(3,5)P_2$ (Gerndt *et al.*, 2020a). The second one is TPC2-A1-N (Fig. 1.11d), directly mimicking the effect of NAADP-dependent channel activation without intermediate NAADP-binding proteins (Saito *et al.*, 2023), leading to a non-selective Na^+- and preferably Ca^{2+}-permeable state, also having a complete different chemical structure than NAADP (Gerndt *et al.*, 2020a, (Fig. 1.11c). TPC2-A1-N analogues like SGA-85 (Fig. 1.11e) and SGA-111 (Fig. 1.11f) are also promising candidates (Gerndt *et al.*, 2020a).

TPC2-A1-N and TPC2-A1-P when co-applied or sequentially applied induced larger Ca^{2+} and unchanged Na^+ currents compared to the compounds applied alone, what is also obtained when NAADP and $PI(3,5)P_2$ were co-applied (Yuan *et al.*, 2022). Thus, TPC2 activation by the combination of TPC2-A1-N and TPC2-A1-P seems to affect Ca^{2+}-permeability independently from ion selectivity (Yuan *et al.*, 2022). So far there are no structures of TPC2-A1-P or TPC2-A1-N binding sites, but several functional studies on various TPC2 mutants give a hint (Table 1.1). It is likely that TPC2-A1-P binds in the $PI(3,5)P_2$ binding pocket, though there is not much data present by now. TPC2-A1-N however might have another binding-site, as it can activate TPC2 in an NAADP-dependent way without the presence of NAADP-binding proteins and $PI(3,5)P_2$-binding but requires residues outside of the $PI(3,5)P_2$-binding site for activation, similar to NAADP (Saito *et al.*, 2023). Several tricyclic anti-depressants were also identified as agonists, inducing voltage-sensitivity and Na^+-selective currents in TPC2 (Zhang X. *et al.*, 2019). Riluzole was also identified as a Na^+-selective TPC2 agonist that operates in a voltage-insensitive manner (Zhang X. *et al.*, 2019).

Table 1.1: Functional mutations in human TPC2 and their influence on different agonists

Mutation	$PI(3,5)P_2$	TPC2-A1-P	NAADP	TPC2-A1-N
K203A	X [1]	-	-	-
K204A	X [1,3]	R [2]	X [3]	A [2,3]
K207A	R [1,3]	-	X [3]	A [3]
W211A	X [3]	-	X [3]	X [3]
L265P	-	-	X [3]	X [3]
S322A	R [1]	-	X [3]	A [3]
R329A	X [1]	-	X [3]	A [3]
R331A	X [3]	-	X [3]	X [3]
I551R	X [1]	-	-	-
R557A	X [3]	-	A [3]	X [3]

X: activity abolished to wildtype (wt); R: activity reduced to wt; A: full activity like wt; 1: She *et al.*, 2019; 2: Gerndt *et al.*, 2020a; 3: Saito *et al.*, 2023

In addition to all these agonists, there are also various inhibitors of TPC2, e.g. ATP (Cang *et al.*, 2013), GDN (She *et al.*, 2019), Ned-19 (NAADP-antagonist; Favia *et al.*, 2014), fluphenazine (Penny *et al.*, 2019), verapamil (Skelding *et al.*, 2022), raloxifene (Penny *et al.*, 2019) or tetrandrine (Fig. 1.12a; Sakurai *et al.*, 2015; Ou *et al.*, 2020). Tetrandrine is shown to suppress SARS-CoV-2 (Ou *et al.*, 2020) and Ebola virus infection (Sakurai *et al.*, 2015; Penny *et al.*, 2019). It also suppresses cancer proliferation (Skelding *et al.*, 2022), while analogues like SG-094 and SG-005 are even more potent TPC2 inhibitors and increase antiproliferative properties against cancer cells (Müller *et al.*, 2021). Another important TPC2 inhibitor is naringenin (Pafumi *et al.*, 2017) (Fig. 1.12b), a flavonoid present in high content in citruses and tomatoes. Epidemiological studies have demonstrated that a high naringenin content diet is associated with a reduced incidence of cancer and metabolic diseases (Giovannucci E., 1999; Alam *et al.*, 2014). These findings can be explained by the inhibition of TPC2 by naringenin, thereby blocking the neoangiogenesis mechanism involved in cancer (Favia *et al.*, 2014; Pafumi *et al.*, 2017), increasing antiproliferative properties (Müller *et al.*, 2021) and repressing the proliferation, migration, and invasion of melanoma cells by increasing melanin production (Netcharoensirisuk *et al.*, 2021). Additionally, inhibition of TPC2 via naringenin reduces SARS-CoV-2 infection (Clementi *et al.*, 2021). Interestingly, when applied additionally to the tricyclic anti-depressant desipramine, a TPC2 agonist, naringenin shows potentiation of the TPC2 activation (Shimomura *et al.*, 2023). These findings again show the complexity of the TPC2 gating modes. Therefore, it is important to characterize the molecular basis of the interaction between TPC2 and naringenin by structural approaches like SPA cryo-EM, because MD simulations could by now not give sufficient insights (Benkerrou *et al.*, 2019).

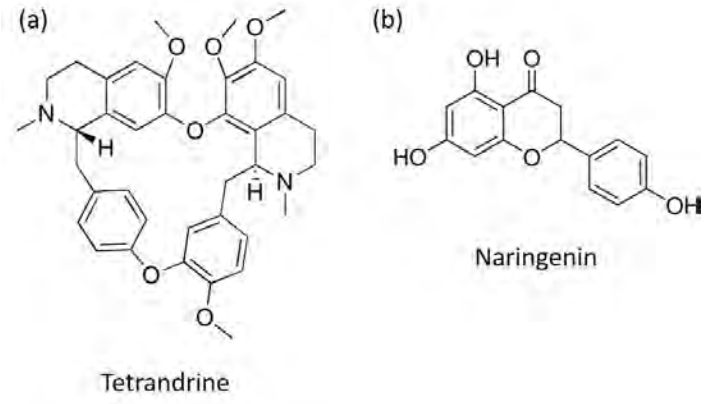

Figure 1.12: Chemical structures of human TPC2 antagonists
(a) Chemical structure of tetrandrine (Skelding *et al.*, 2022). **(b)** Chemical structure of naringenin (Skelding *et al.*, 2022).

The structure of human TPC2 was solved by SPA cryo-EM in an apo and PI(3,5)P_2-bound state (She *et al.*, 2019). While the apo structure (PDB: 6NQ1; 3.5 Å) shows the closed conformation, the PI(3,5)P_2-bound form shows both, and PI(3,5)P_2-bound open state (PDB: 6NQ0; 3.7 Å) and PI(3,5)P_2-bound closed state (PDB: 6NQ2; 3.4 Å) in a 3:5 ratio, likely representing the ligand efficacy of channel activation (She *et al.*, 2019). As the apo structure is virtually identical to the ligand-bound closed state, it is likely that the PI(3,5)P_2 binding site is readily formed without any conformational change. Overall human TPC2 shows the typical dimeric TPC-fold, as the transmembrane region is domain swapped, with the S1-S4 voltage-sensing domain (VSD) from one 6-TM interacting with the S5-S6 pore domain from the neighboring 6-TM (Fig. 1.9). The ion conduction pore of TPC2 consists of S5, S6 and two pore helices (Fig. 1.13a). L265 is essential for pore formation and L265P (pore dead mutant) results in an unfunctional channel (Brailoiu *et al.*, 2010; Saito *et al.*, 2023). There are two sets of filter residues that enclose the central ion pathway with different dimensions (She *et al.*, 2019). Filter I with T271 and A272 and a distance larger than 7 Å, and filter II with V652, N653 and N654, using their side chains to generate a much narrower pathway, as the two N653 residues of the dimer form the narrowest constriction point and play the central role in determining Na^+-selectivity (Fig. 1.13b). The pore itself consists of two pairs of residues, T308 and Y312 from IS6 and L690 and L694 from IIS6 (Fig. 1.13c). While opening, these residues rotate away from each other to open the

intracellular gate (Fig. 1.13c). The two VSDs of TPC2 are not fully functional. VSD1 contains the typical arginines, but an incomplete gating charge transfer center and a short regular alpha helix instead of a 3_{10} helix, while VSD2 has preserved most key features of a canonical voltage sensor but lacks an arginine at position R3 (I551 in TPC2, R551 in TPC1), which is identified as the key residue for voltage-dependence (She *et al.*, 2018; She *et al.*, 2019).

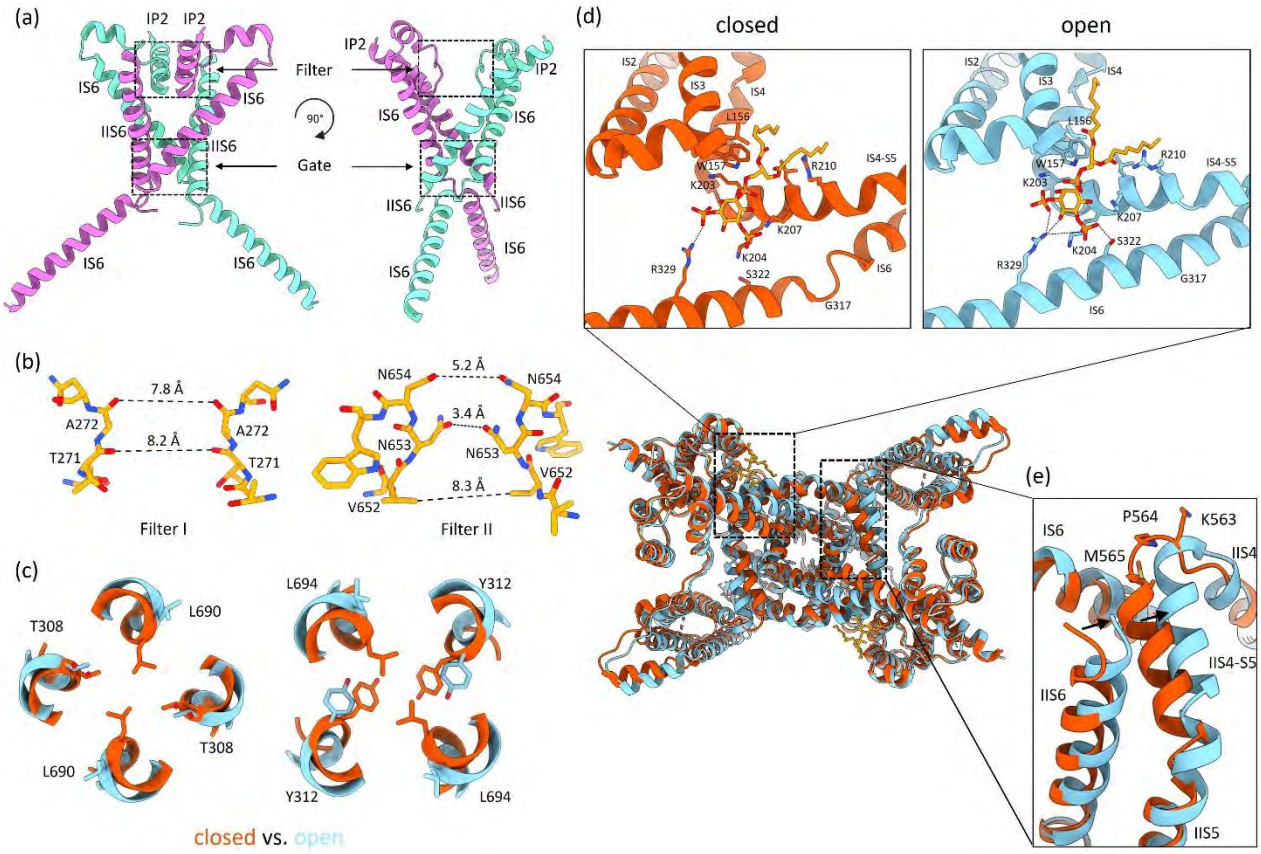

Figure 1.13: Structural overview of human TPC2

(a) The ion conduction pore of TPC2 (Apo; PDB:6NQ1) with one subunit colored in magenta and the other in cyan. The filter region and the cytosolic gate are boxed. **(b)** The selectivity filter of TPC2 (Apo; PDB:6NQ1) formed by filter I and filter II. Only one protomer is shown for clarity. **(c)** The cytosolic gate in PI(3,5)P_2-bound closed (red; PDB:6NQ2) and open (blue, PDB:6NQ0) state viewed from the cytosolic side. For better illustration it is shown in two sections: Thr308/Leu690 (left) and Tyr312/Leu694 (right). **(d)** PI(3,5)P_2 binding site of TPC2 both in the PI(3,5)P_2-bound closed (red; PDB:6NQ2) and open (blue, PDB:6NQ0) state. **(e)** Structural comparison between the PI(3,5)P_2-bound open (blue, PDB:6NQ0) and closed (red; PDB:6NQ2) state of the IIS(6)/IIS4-S5 region in TPC2. The important gating residues Lys563, Pro564 and Met565 are shown as sticks. All figures created with ChimeraX (2.1.2) and BioRender (2.1.2).

PI(3,5)P_2 binds TPC2 at the junction formed by IS3, IS4, and the IS4-S5 linker of the 6-TM I. Here the inositol 1,3,5-trisphosphate head group of PI(3,5)P_2 shows most of the ligand-protein interactions (Fig. 1.13d), while the acyl chains of PI(3,5)P_2 insert upright into the membrane. Most of the basic residues involved in PI(3,5)P_2 binding, particularly those on the IS4-S5 linker, are lysines (K203, K204, K207). Replacing these lysines by alanines reduces the effect of PI(3,5)P_2 activation (She *et al.*, 2019; Table 1.1). Additionally, R329 and S322 on IS6 show state-dependent PI(3,5)P_2 interaction, being involved in opening and closing of the pore (Fig. 1.13d). Mutation of R329A almost completely abolishes channel activity whereas the mutation of S322A reduces the channel activity (Table 1.1), indicating that R329 plays the determinant role in

channel opening and S322 has only a stabilizing effect for the open-state, what can be explained by the claimed PI(3,5)P2-dependent gating mechanism in TPC2. This presumption is also underlined by the observation that pore opening and closing is triggered by a conformational change at the IS6 helix. In the closed state, the IS6 helix breaks into two halves at Gly317, just below the cytosolic gate, while in the open state, IS6 becomes a long continuous helix (Fig. 1.13d). This is initiated by the salt bridges between R329 and $PI(3,5)P_2$ phosphate groups that pull the IS6 helix into a straight, continuous conformation and the hydrogen bond of S322 with the C5-phosphate of $PI(3,5)P_2$ that stabilizes the IS6 helix in the open conformation (Fig. 1.13d). The fact that closed and open conformations are observed in the ligand-bound structure suggests that TPC2 alternates in dynamic equilibrium between these two states in the presence of $PI(3,5)P_2$. Furthermore, the movement of IS6 from the closed to open state results in the outward dilation and rotation of T308 and Y312 as well as movement of IIS6 resulting in an outward rotation of the gating residues L690 and L694 (Fig. 1.13c). Since the IIS4-S5 linker is tightly packed with IIS6 it must swing outward along with IIS6. In the closed state there is a five-residue loop between IIS4 and the IIS4-S5 linker. Upon channel opening, the loop undergoes structural rearrangement and the three residues closest to the IIS4-S5 linker helix are restructured to be part of the linker helix (Fig. 1.13e). By this the IIS4-S5 linker can swing outward and space for outward movement of IIS6, essential for channel opening, is created. This structural change at the loop also explains the voltage-independent gating of TPC2, as I551 in IIS4 allows the outward movement of the IIS4-S5 linker without depolarization, while R551 in TPC1 does not (She *et al.*, 2018).

Remarkably, human TPC2 cDNAs used for functional studies in the past were often polymorphic variants, e.g. M484L and G734E (Calcraft *et al.*, 2009), or L564P and G734E (Brailoiu *et al.*, 2009). For structure determination of human TPC2 via cryo-EM the variant L11A/L12A, L564P and G734E was used (She *et al.*, 2019). Therefore, this same mutant construct was used and defined as the wildtype channel in this work (Fig. 1.14).

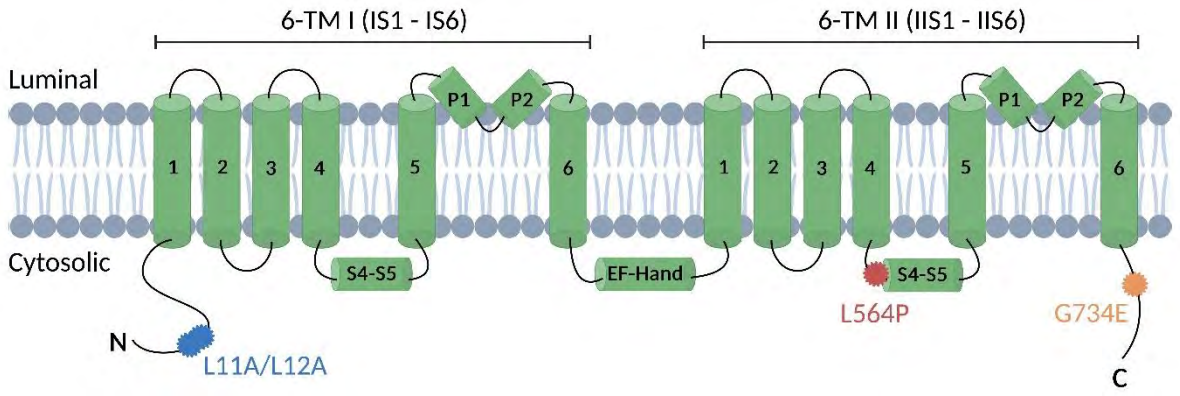

Figure 1.14: Mutations of the TPC2 construct used in this work
Topology and domain arrangement of one human TPC2 subunit, showing the localization of the mutations of the construct used in this study. Figure created with BioRender (2.1.2), derived from She *et al.*, 2019.

The double mutation L11A/L12A in the N-terminal lysosomal targeting sequence leads to trafficking of TPC2 to the plasma membrane (Brailoiu *et al.*, 2010), improving significantly TPC2 expression in HEK293 cells. L564P is the predominant TPC2 variant in humans, without having functional influence on channel function itself (Böck *et al.*, 2021). However, L564P is essential for the M484L gain-of-function effect that is associated with blond hair, and it increases bone mineral density and influences the body structure (Böck *et al.*, 2021). The point mutation G734E is the second most common mutation in European population and

has high homozygous frequency with L564P (Böck *et al.*, 2021). It effects the shift from brown to blond hair color as well as increased bone mineral density and decreased height (Böck *et al.*, 2021). G734E has no effect on activation via $PI(3,5)P_2$ but shows reduced inhibition by ATP compared to the wildtype (Chao *et al.*, 2017).

1.4 Aims of this study

The aim of this project is the structural investigation of emerging drug-targets via SPA cryo-EM. Therefore two target membrane protein classes, SLC5 transporters and two-pore channels (TPCs) were selected. Hereby, a main goal is to find expression and purification conditions suitable for high-resolution SPA cryo-EM. To do so, different expression methods will be tested to optimize protein yield, protein localization in the cell, detergent solubility, purification behavior as well as protein stability and functionality. Especially SLC5A family members are known as challenging targets for expression and purification, due to their intricate membrane topology that imparts a high degree of hydrophobicity and instability. For this reason, one main approach will be to test different reconstitution methods to mimic a proper membrane environment that is crucial for their function and stability.

Two major reconstitution methods for SPA cryo-EM studies of membrane proteins, namely amphipol (Tribet *et al.*, 1996) and salipros (Frauenfeld *et al.*, 2016), will be optimized for application on the mammalian proteins. For this optimization the *Green-light absorbing proteorhodopsin* (GPR) from marine γ-proteobacteria is used as model system, as it is colored and available in large quantities. In addition, GPR is a model system for future projects in the new established Regensburg Center for Ultrafast Nanoscopy (RUN), to adapt physical methods like atomic/scanning force microscopy (AFM) or scanning nearfield optical microscopy (SNOM) on biological samples. Parameters to test in reconstitution are lipid to protein to scaffold protein ratios (Flayhan et al., 2018), or detergent removal procedures (Allen *et al.*, 1980). Thereby a point of interest will be to investigate if the reconstitution procedure has an influence on the oligomerization of the reconstituted protein (Kruip *et al.*, 1999), which makes GPR a perfect model system, because it is known to adopt different oligomeric states (pentameric: Hirschi *et al.*, 2020; hexameric: Stone *et al.*, 2013; both: Klyszejko *et al.*, 2008). Another goal is to optimize vitrification conditions of reconstituted membrane proteins, e.g. by varying salt concentrations (Kampjut *et al.*, 2021) or adding detergent to prohibit preferred orientation of particles (Wang *et al.*, 2019), and to improve SPA cryo-EM data collection parameters at the CRYO ARM™ 200 (2.1.1).

In addition to the structural studies, functional investigation of sugar transport and sensing in SLC5A family members will be accomplished by using Solid-Supported Membrane (SSM)-Based electrophysiology. The aim of this multifaceted approach using structural and functional investigations is to contribute to a deeper understanding of the biological functions and pharmacological potential of SLC5A family members.

Finally, it is planned to solve the structure of SLC5A family members and human *Two-pore channel 2* (TPC2) in complex with known inhibitors (e.g. SGLT2 with empagliflozin) or agonists (TPC2 with TPC2-A1-N) by SPA cryo-EM. These high-resolution structural insights will offer a comprehensive understanding of critical aspects, e.g. the Na^+/glucose coupling mechanism, the regulatory processes involved in glucose transport, and the precise inhibition mechanisms of SLC5 transporters. For TPC2, functional studies accomplished by the cooperating groups of Prof. Dr. Dr. Christian Grimm (Ludwig-Maximilian-University Munich, Germany) and Prof. Sandip Patel (University College London, UK) can be supported with structural evidence.

2. Material and Methods

2.1 Materials

Standard laboratory materials, including consumables (e.g. reaction vials and cell culture dishes) are presumed to possess consistent quality across manufacturers and are therefore not detailed here. Conversely, components explicitly outlined in this section are crucial for experimental success, attributed to factors such as purity, manufacturer's quality control, or the manufacturing process itself.

2.1.1 Instruments

Instrument	Manufacturer
ÄKTA™ pure chromatography system	Cytiva, Marlborough (USA)
Superose 6 Increase 5/150 GL column	Cytiva, Marlborough (USA)
ÄKTA™ purifier chromatography system	GE Healthcare, Little Chalfont (UK)
Superose 6 Increase 10/300 GL column	GE Healthcare, Little Chalfont (UK)
Avanti J-26 XP centrifuge	Beckman Coulter, Palo Alto (USA)
Rotor JLA-8.100	Beckman Coulter, Palo Alto (USA)
Rotor JLA-16.200	Beckman Coulter, Palo Alto (USA)
BRAND® counting chamber	Merck KGaA, Darmstadt (Germany)
Cell disruptor TS 0.75	Constant Systems Ltd., Daventry (UK)
CELLSPIN spinner flask (250 ml, 1 l)	Pfeiffer Electronic Engineering GmbH, Lahnau (Germany)
CELLSPIN stirring unit	Pfeiffer Electronic Engineering GmbH, Lahnau (Germany)
Centrifuge 5415R	Eppendorf AG, Hamburg (Germany)
Centrifuge 5810R	Eppendorf AG, Hamburg (Germany)
CM12 transmission electron microscope (120 keV)	FEI Company, Hillsboro (USA)
Camera: TVIPS0124, 1k *x* 1k pixels	TVIPS GmbH, Gauting (Germany)
CRYO ARM™ 200 (200 keV)	JEOL Ltd., Akishima (Japan)
Camera: K2 Summit direct electron detector	Gatan Inc., Pleasanton (USA)
Digital sonifier 250	Branson Ultrasonics, Brookfield (USA)
Dounce homogenizer (15 m^3 or 50 m^3)	VWR GmbH, Darmstadt (Germany)

EVOS® FL Cell Imaging System	Thermo Fisher Scientific Inc., Waltham (USA)
Fastblot B33	Biometra GmbH, Göttingen (Germany)
GelDoc Go Imaging System	Bio-Rad Laboratories Inc., Hercules (USA)
Hellma® absorption cuvette (d = 10 mm; 1,4 ml)	Merck KGaA, Darmstadt (Germany)
Heraeus Pico 17 centrifuge	Thermo Fisher Scientific Inc., Waltham (USA)
Mark IV Vitrobot	Thermo Fisher Scientific Inc., Waltham (USA)
Mighty Small II Mini Vertical System	Hoefer Inc., Richmond (USA)
Mr. Frosty™ freezing container	Sigma-Aldrich®, St. Louis (USA)
NanoDrop One Spectrophotometer	Thermo Fisher Scientific Inc., Waltham (USA)
PELCO easiGlow™ Glow Discharge Cleaning System	Plano GmbH, Wetzlar (Germany)
Plasma Cleaner PDC-32G	Harrick Plasma Inc., Ithaca (USA)
SURFE^{2}R N1	Nanion Technologies GmbH, Munich (Germany)
TECAN Infinite M200 Pro plate reader	Tecan Trading AG, Männedorf (Switzerland)
Turbo Carbon Coater 208carbon	Cressington Scientific Instruments, Watford (UK)
Ultracentrifuge Optima XPN-100 Rotor 45 Ti Rotor 70 Ti Rotor SW 41 Ti	Beckman Coulter, Palo Alto (USA) Beckman Coulter, Palo Alto (USA) Beckman Coulter, Palo Alto (USA) Beckman Coulter, Palo Alto (USA)
ultrasonic cleaner (USC 300 TH)	VWR GmbH, Darmstadt (Germany)
UV-Vis Spectrophotometer (V-650)	Jasco Inc., Easton (USA)

2.1.2 Softwares

Software	Version	Used for	Reference / copyright
BioRender	-	Figures	BioRender.com
ChimeraX	1.7	Figures	Pettersen *et al.*, 2021
CLC Sequence Viewer	8.0	DNA sequence alignment	© Qiagen Bioinformatics, Venlo (NL)
Coot	0.9.8.1	SPA cryo-EM model building	Emsley *et al.*, 2010
cryoSPARC (live)	3.3.1	SPA cryo-EM data processing	cryosparc.com (Punjani *et al.*, 2017)
ExPASy - ProtParam	-	Calculation of extinction coefficient (ε_{280})	© SIB Bioinformatics Resource Portal
Igor Pro	9.0	Visualization of functional studies and evaluation of SSM-based electrophysiology (2.2.8.1)	WaveMetrics Inc., Lake Oswego (USA)
Magellan™	7.1	Evaluation of protein concentration for Bradford Assay (2.2.2.1.1)	© Tecan Trading AG, Männedorf (Switzerland)
Phenix	1.20.1	SPA cryo-EM model refinement and validation	Afonine *et al.*, 2018a Afonine *et al.*, 2018b
RELION	4.0 beta	SPA cryo-EM data processing	relion.readthedocs.io (Kimanius *et al.*, 2021)
SerialEM	4.0	SPA cryo-EM data collection	bio3d.colorado.edu/SerialEM (Mastronarde D. N., 2005)
UNICORN	7.8	Operation of ÄKTApure chromatography system	© Cytiva, Marlborough (USA)
UNICORN	5.31	Operation of ÄKTApurifier chromatography system	© GE Healthcare, Little Chalfont (UK)
wwPDB Validation System	-	Validation of the SPA cryo-EM model	Berman *et al.*, 2003

2.1.3 Consumables

Consumable	Manufacturer
400 mesh copper grids (G2400C)	Plano GmbH, Wetzlar (Germany)
96-well micro plate	Paul Boettger GmbH & Co. KG, Bodenmais (Germany)
Amicon® Ultra concentrator MWCO 3 kDa MWCO 10 kDa MWCO 50 kDa MWCO 100 kDa	Merck Millipore Ltd., Cork (Ireland)
BCA protein standard	Thermo Fisher Scientific Inc., Waltham (USA)
Bio-Beads SM-2	Bio-Rad Laboratories GmbH, Feldkirchen (Germany)
Biotin	IBA Lifesciences GmbH, Göttingen (Germany)
Bovine serum albumin (BSA)	AppliChem GmbH, Darmstadt (Germany)
Carbon rod	Cressington Scientific Instruments, Watford (UK)
Cholesterol hemisuccinate (CHS)	Anatrace Inc., Maumee (USA)
Corning® syringe filter (0.22 µm)	Merck KGaA, Darmstadt (Germany)
CryoPure tube (2 ml)	Sarstedt AG & Co. KG, Nümbrecht (Germany)
Cut Smart Buffer (10x)	New England Biolabs GmbH, Frankfurt am Main (Germany)
Deoxynucleotide Triphosphates (dNTPs)	Carl Roth GmbH, Karlsruhe (Germany)
Filter paper 595	Ted Pella Inc., Redding (USA)
FLAG® peptide	Sigma-Aldrich®, St. Louis (USA)
Graphene oxide Quantifoil® R1.2/1.3 300-mesh Cu grid	Plano GmbH, Wetzlar (Germany)
High-Fidelity Buffer (5x)	New England Biolabs GmbH, Frankfurt am Main (Germany)
Hi-Grade Mica (Grade 2)	Ted Pella Inc., Redding (USA)

Immobilon-P Transfer Membrane (pore size 0.45 µm)	Carl Roth GmbH, Karlsruhe (Germany)
MEMBRA-Cel dialysis tube (3.5 MWCO)	Serva Electrophoresis GmbH, Heidelberg (Germany)
Open-Top Thinwall Ultra-Clear Tube (13,2 ml)	Beckman Coulter, Palo Alto (USA)
Pierce™ Disposable Column with polyethylene disc (5/10 ml)	Thermo Fisher Scientific Inc., Waltham (USA)
Quantifoil® R1.2/1.3 300-mesh Cu grid	Plano GmbH, Wetzlar (Germany)
SURFE^{2}R N1 Single Sensor (3 mm)	Nanion Technologies GmbH, Munich (Germany)
T175 cell culture flask	Sarstedt AG & Co. KG, Nümbrecht (Germany)
T4 DNA Ligase Buffer (10x)	New England Biolabs GmbH, Frankfurt am Main (Germany)
Whatman GB003 papers	Cytiva, Marlborough (USA)

2.1.4 Chemicals

If not declared specifically, chemicals used in this work were purchased from AppliChem GmbH (Darmstadt, Germany), Linde GmbH (Pullach, Germany), Merck KGaA (Darmstadt, Germany), MP Biomedicals Inc. (Irvine, USA), Carl Roth GmbH (Karlsruhe, Germany), Serva Electrophoresis GmbH (Heidelberg, Germany) and Sigma-Aldrich® (St. Louis, USA).

2.1.5 Stock solutions

Substances	Stock concentration and solvent	Working concentration
Adenosine triphosphate (Sigma-Aldrich®, St. Louis, USA)	200 mM in ddH_20	2 mM
all-trans retinal (Merck KGaA, Darmstadt, Germany)	10 mg/ml in DMSO	2 µg/ml
Amphipol A8-35 (Anatrace Inc., Maumee, USA)	100 mg/ml in ddH_2O	variable
Aprotinin (Sigma-Aldrich®, St. Louis, USA)	1 mg/ml in ddH_2O	1 µg /ml

5-Brom-4-chlor-3-indoxylphosphat (BCIP) (Sigma-Aldrich®, St. Louis, USA)	50 mg/ml in DMF	0.25 mg/ml
Carbenicillin (Carb) Carl Roth GmbH (Karlsruhe, Germany)	50 mg/ml in ddH_2O	50 µg/ml
Chloramphenicol (Cam) Carl Roth GmbH (Karlsruhe, Germany)	34 mg/ml in EtOH	34 µg/ml
1-Deoxynojirimycin (DNJ) (Thermo Fisher Scientific Inc., Waltham, USA)	100 mM in ddH_2O	50 µM
Guanosine 5'-triphosphate (GTP) (Sigma-Aldrich®, St. Louis, USA)	100 mM in ddH_20	2 mM
Isopropyl-β-D-thiogalactopyranoside (IPTG) (Gerbu GmbH, Heidelberg, Germany)	1 M in ddH_2O	1 mM
Kanamycin (Kan) (Gerbu GmbH, Heidelberg, Germany)	50 mg/ml in ddH_2O	50 µg/ml
Leupeptin (Sigma-Aldrich®, St. Louis, USA)	2 mg/ml in ddH_2O	2 µg/ml
Lysozyme (from chicken egg white) (Sigma-Aldrich®, St. Louis, USA)	100 mg/ml in ddH_2O	1 mg/ml
Naringenin (Sigma-Aldrich®, St. Louis, USA)	10 mM in EtOH	0.5 mM
nitro blue tetrazolium (NBT) (Sigma-Aldrich®, St. Louis, USA)	50 mg/ml in DMF	0.5 mg/ml
Pepstatin A (Sigma-Aldrich®, St. Louis, USA)	1 mg/ml in DMSO	0.5 µg/ml
Pyranine (Sigma-Aldrich®, St. Louis, USA)	2 mM in ddH_20	0.05 mM
SGA-85 (Gerndt *et al.*, 2020a)	10 mM in DMSO	1:40 (mol:mol)
SGA-111 (Gerndt *et al.*, 2020a)	10 mM in DMSO	1:40 (mol:mol)
Sodium butyrate (Sigma-Aldrich®, St. Louis, USA)	500 mM in ddH_20	variable

Tetracycline (Sigma-Aldrich®, St. Louis, USA)	12.5 mg/ml in EtOH	12.5 µg/ml
Thrombin from human plasma (Roche Diagnostics GmbH, Mannheim, Germany)	1000 U/ml in ddH_2O	120 U/mg protein
TPC2-A1-N (Gerndt *et al.*, 2020a)	10 mM in DMSO	1:40 (mol:mol)
TPC2-A1-P (Gerndt *et al.*, 2020a)	10 mM in DMSO	1:40 (mol:mol)
Valproic acid (Sigma-Aldrich®, St. Louis, USA)	500 mM in ddH_20	variable

2.1.6 Reagent Kits

The following reagent kits were used according to manufacturer's instructions.

Reagent Kit	Manufacturer
Qiagen® Gel Extraction Kit	Qiagen, Hilden (Germany)
Qiagen® Plasmid Mini Kit	Qiagen, Hilden (Germany)
Qiagen® Plasmid Plus Giga Kit	Qiagen, Hilden (Germany)
Thrombin CleanCleave™ kit	Sigma-Aldrich®, St. Louis (USA)

2.1.7 Molecular weight markers

Molecular weight marker	Manufacturer
GeneRuler™ 1 kb Plus DNA Ladder (75-20,000 bp)	Thermo Fisher Scientific Inc., Waltham (USA)
PageRuler™ Prestained (10-180 kDa)	Thermo Fisher Scientific Inc., Waltham (USA)

2.1.8 Detergents

Detergent	Detergent class	CMC (H_2O)
Decyl β-D-maltoside (DM) (Anatrace Inc., Maumee, USA)	Nonionic maltoside	1.66 mM (0.08%)
Dodecyl-β-D-maltoside (DDM) (Anatrace Inc., Maumee, USA)	Nonionic maltoside	0.17 mM (0.0087%)
Glyco-diosgenin (GDN) (Anatrace Inc., Maumee, USA)	Nonionic glycoside	0.018 mM (0.0021%)
Fluorinated Fos-Choline 8 (Anatrace Inc., Maumee, USA)	Zwitterionic, lipid-like, fluorinated	2.9 mM (0.15%)
Lauryl Maltose Neopentyl Glycol (LMNG) (Anatrace Inc., Maumee, USA)	Nonionic neopentyl glycol	0.01 mM (0.001%)

For use, all detergents were solubilized in ddH_2O in the needed concentration (% (w/v)). To obtain detergent supplemented with CHS (2.1.3), the required amount of dry CHS was mixed with the respective, already solved, detergent, always using a ratio of 5:1 in detergent to CHS.

2.1.9 Affinity resins

Affinity resin	Manufacturer
ANTI-FLAG® M2 Affinity Gel (FLAG-Trap)	Sigma-Aldrich®, St. Louis (USA)
GFP-Trap® Agarose	ChromoTek GmbH, Planegg-Martinsried (Germany)
GFP-Trap® Magnetic Particles M-270	ChromoTek GmbH, Planegg-Martinsried (Germany)
Ni-NTA Agarose	Qiagen, Hilden (Germany)
Strep-Tactin® MacroPrep® resin (StrepII-Trap)	IBA Lifesciences GmbH, Göttingen (Germany)
Strep-Tactin®XT 4Flow® (StrepII-Trap)	IBA Lifesciences GmbH, Göttingen (Germany)
TALON® Metal Affinity resin (His-Trap)	Clontech Laboratories Inc., Mountain View (USA)

2.1.10 Enzymes and inhibitors

Enzyme / Inhibitor	Manufacturer
Antarctic Phosphatase (5,000 U/ml)	New England Biolabs GmbH, Frankfurt am Main (Germany)
DNAse I	Roche Diagnostics GmbH, Mannheim (Germany)
DpnI	New England Biolabs GmbH, Frankfurt am Main (Germany)
Phusion® High-Fidelity DNA Polymerase	New England Biolabs GmbH, Frankfurt am Main (Germany)
LR Clonase™ II enzyme mix	Life Technologies, Carlsbad (USA)
Pefabloc® SC	Roche Diagnostics GmbH, Mannheim (Germany)
Proteinase K	Life Technologies, Carlsbad (USA)
T4 DNA Ligase (400,000 U/ml)	New England Biolabs GmbH, Frankfurt am Main (Germany)

2.1.11 Lipids

Lipid	Stock concentration and solvent	Manufacturer
Brain Total Lipid Extract	4 mg/ml in 20mM Tris/HCl pH8, 150 mM NaCl, 0.05% (w/v) /0.01% (w/v) DDM/CHS	Avanti Polar Lipids, Alabaster (USA)
Diphytanoyl-sn-glycero-3-phosphocholine	7.5 µg/µl in decane	Avanti Polar Lipids, Alabaster (USA)
Phosphatidylinositol 3,5-bisphosphate diC8 ($PI(3,5)P_2$ diC8)	10 mM in ddH_20	Echelon Biosciences, Salt Lake City (USA)
1-Palmitoyl-2-Oleoyl-sn-Glycero-3-Phosphocholine (POPC)	4 mg/ml in 1% DM	Anatrace Inc., Maumee (USA)

2.1.12 Antibodies

Antibody	Manufacturer
Anti-Actin, primary, monoclonal, mouse (1 : 5.000)	Thermo Fisher Scientific Inc., Waltham (USA)
Anti-FLAG, primary, clone M2, mouse (1 : 2.000)	Sigma-Aldrich®, St. Louis (USA)
Anti-GFP, primary, monoclonal, mouse (1 : 2.000)	Sigma-Aldrich®, St. Louis (USA)
Anti-His (poly-His), primary, monoclonal, mouse (1 : 5.000)	Sigma-Aldrich®, St. Louis (USA)
Anti-Mouse IgG, secondary, rabbit, AP (1 : 5.000)	Sigma-Aldrich®, St. Louis (USA)
Anti-Rabbit IgG, secondary, goat, AP (1 : 5.000)	Abcam Ltd., Cambridge (UK)
Anti-SGLT3, primary, polyclonal, rabbit (1 : 1.000)	Biorbyt Ltd., Cambridge (UK)
Anti-TPC2, primary, polyclonal, rabbit (1 : 3.000)	Group of Prof. Dr. Dr. Christian Grimm, Ludwig-Maximilian-University Munich (Germany)

2.1.13 Media

2.1.13.1 Bacterial media

Unless precised otherwise, all chemicals for media were dissolved in ddH_2O and the pH was adjusted with NaOH or HCl.

2.1.13.1.1 LB-media and plates

LB-media (Lysogeny Broth), pH 7.0 (Bertani G., 1951)

Bacto Tryptone	1% (w/v)
Bacto Yeast Extract	0.5% (w/v)
NaCl	1% (w/v)

LB-media was autoclaved before use. For LB agar plates the autoclaved media was additionally supplemented with 1.8% (w/v) agar.

2.1.13.1.2 SOB-media

SOB-media (Super Optimal Broth), pH 7.0 (Hanahan D., 1983)

Bacto Tryptone	2% (w/v)
Bacto Yeast Extract	0.5% (w/v)
NaCl	10 mM
KCl	2.5 mM
$MgCl_2$	10 mM
$MgSO_4$	10 mM

$MgCl_2$ and $MgSO_4$ were prepared separately as 1 M stock solutions and added after autoclaving.

2.1.13.1.3 TB-media

TB-media (Terrific Broth), pH 7.0 (Tartoff K. & Hobbs C., 1987)

Bacto Tryptone	1.2% (w/v)
Bacto Yeast Extract	2.4% (w/v)
10x TB phosphate	1x

10x TB phosphates (0.17 M KH_2PO_4, 0.72 M $K_2HPO_4 \cdot 3\ H_2O$) were prepared and autoclaved separately to prevent precipitation of hardly soluble phosphates. They were added to the media just before usage.

2.1.13.2 Eukaryotic cell culture

2.1.13.2.1 Media and supplements

Media / supplement	Manufacturer
Anti-clumping agent	Thermo Fisher Scientific Inc., Waltham (USA)
Blasticidin	Thermo Fisher Scientific Inc., Waltham (USA)
Doxycycline	Sigma-Aldrich®, St. Louis (USA)
Dulbecco´s Modified Eagle´s Medium/Nutrient Mixture F-12 Ham (DMEM F-12)	Sigma-Aldrich®, St. Louis (USA)
Fetal bovine serum (FBS); tetracycline – free	Sigma-Aldrich®, St. Louis (USA)
FreeStyle™ 293 expression media	Thermo Fisher Scientific Inc., Waltham (USA)
Penicillin-Streptomycin (Pen-Strep)	Sigma-Aldrich®, St. Louis (USA)
Sf-900™ III SFM	Thermo Fisher Scientific Inc., Waltham (USA)
Trypsin-EDTA solution	Sigma-Aldrich®, St. Louis (USA)

2.1.13.2.2 Phosphate buffered saline (PBS)

Phosphate buffered saline, pH 7.3	
NaCl	137 mM
KCl	2.7 mM
Na2HPO4	6.5 mM
KH2PO4	1.5 mM

2.1.14 Cells and plasmids

2.1.14.1 *E. coli*

2.1.14.1.1 Bacterial strains

E. coli strains used in this work were either purchased from manufacturers as chemical competent cells or prepared as chemical competent cells following the corresponding protocol (2.2.1.1).

Strain	Genotype	Source	Application
BL21 (DE3)	F⁻ *ompT* *hsdS$_B$* (r_B- m_B-) *gal dcm (DE3)*	Life Technologies, Carlsbad (USA)	Expression test of Rab7A
BL21-Gold (DE3)	*F⁻ ompT hsdS(r_B- m_B-) dcm+* ***Tet^R*** *gal λ(DE3) endA Hte*	Life Technologies, Carlsbad (USA)	Expression test of Rab7A
BL21 (DE3) pLysS	*F⁻ ompT hsdSB(r_B-, m_B-) gal dcm rne131 (DE3) / pLysS (**Cam^R**)*	Life Technologies, Carlsbad (USA)	Expression test of Rab7A
BL21 (DE3) Rosetta2	*F⁻ ompT hsdSB(r_B⁻ m_B⁻) gal dcm (DE3) / pRARE2 (**Cam^R**)*	Merck KGaA, Darmstadt (Germany)	Expression of Rab7A
C43 (DE3)ΔAcrAB	*F⁻ ompT gal dcm hsdSB(r_B- m_B-) (DE3) ΔAcrAB*	Lucigen Corp., Middleton (USA)	Expression of GPR
DH10Bac™	*F⁻ mcrA Δ (mrr-hsdRMS-mcrBC) Φ80lacZΔM15 Δ lac X74 recA1 endA1 araD139 Δ(ara, leu)7697 galU galK λ - rps L nupG* / pMON14272 / pMON7124	Thermo Fisher Scientific, Waltham (USA)	Production of recombinant bacmid DNA
DH5α	*F⁻ ϕ80lacZΔM15 Δ(lacZYA-argF)U169 recA1 endA1 hsdR17 (r_k⁻ , m_k⁺) phoA supE44 thi-1 gyrA96 relA1 λ⁻*	Thermo Fisher Scientific, Waltham (USA)	Cloning and plasmid amplification
Rosetta-gami™ 2 (DE3)	Δ(*ara-leu*)*7697* Δ*lacX74* Δ*phoA* *Pvu*II *phoR araD139 ahpC galE galK rpsL* (DE3) F'[*lac*⁺ *lacI^q pro*] *gor522*::Tn*10 trxB* pRARE2 (**Cam^R**, **Str^R**, **Tet^R**)	Merck KGaA, Darmstadt (Germany)	Expression of Saposin A

2.1.14.1.2 Bacterial vectors

Plasmid	Resistance	Properties	Origin
pET27b_GPR	Kan^R	T7 promotor (IPTG-inducible), lacI, gene subcloned with NdeI and XhoI, C-terminal His_6-tag	Dr. Jagdeep Kaur, Goethe Universität, Frankfurt am Main, Germany
pET28a_Rab7A (Fig. 7.14)	Kan^R	T7 promotor (IPTG-inducible), lacI, gene subcloned with NcoI-HF and HindIII-HF, C-terminal His_6-tag	This work
pMA-RQ_Rab7A	$Carb^R$	Transport vector for Rab7A (7.4.1) flanked by NcoI-site at the N-terminus and HindII at the C-terminus	Geneart AG, Regensburg, Germany
pNIC28-Bsa4_Saposin A	Kan^R	T7 promotor (IPTG-inducible), lacI, gene subcloned with NdeI-HF and HindIII-HF, C-terminal His_6-tag	Dr. Povilas Uzdavinys, University of Regensburg, Germany

2.1.14.2 Eukaryotes

2.1.14.2.1 Eukaryotic cell lines

Cell line	Characteristics
HEK293S GnT1$^-$ (TetR$^+$) (American Type Culture Collection, Manassas, USA)	human embryonic kidney cells, stably transfected with pcDNA6-TR vector for TetR expression, grow adherent and in suspension, inactive Glucose N-acetyltransferase 1 (GnT1$^-$), limited glycosylation (Reeves *et al.*, 1996)
HEK293S GnT1$^-$-SGLT3 (Marko Roblek, Institute of Science and Technology Austria (ISTA))	human embryonic kidney cells, stably transfected with pcDNA6-TR vector for TetR expression, allowing inducible expression of SGLT3 (N-term. StrepII-mEGFP-tag followed by a Thrombin cleavage site) via doxycycline, grow adherent and in suspension, inactive Glucose N-acetyltransferase 1 (GnT1$^-$), limited glycosylation (Reeves *et al.*, 1996)
HEK293S GnT1$^-$-TPC2 (Marko Roblek, ISTA)	human embryonic kidney cells, stably transfected with pcDNA6-TR vector for TetR expression, allowing inducible expression of TPC2 (N-term. His_8-tag) via doxycycline, grow adherent and in suspension, inactive Glucose N-acetyltransferase 1 (GnT1$^-$), limited glycosylation (Reeves *et al.*, 1996)
Sf9 cells (in Sf-900™ III SFM) (Thermo Fisher Scientific Inc., Waltham, USA)	clonal isolated insect cells derived from the parental *Spodoptera frugiperda* cell line IPLB-Sf21-AE, commonly used for expression of recombinant proteins using the Baculovirus Expression System, preadapted to suspension growth in Sf-900™ III SFM

2.1.14.2.2 Eukaryotic vectors

Plasmid	Resistance	Properties	Origin
pDEST-CMV-3xFLAG-gateway-EGFP (Fig. 7.2)	$Carb^R$ Cam^R Kan^R	CMV promotor, lac operator, Gateway cloning sites attR1 and attR2, N-terminal 3xFLAG-tag, C-terminal mEGFP-tag	Addgene, Watertown (USA)
pDEST-CMV-3xFLAG-SGLT3-EGFP (Fig. 7.2)	$Carb^R$ Kan^R	CMV promotor, lac operator, SGLT3 gene subcloned with Gateway Cloning (7.1.2), N-terminal 3xFLAG-tag, C-terminal mEGFP-tag Transient expression of SGLT3	This work Similar for SGLT1, SGLT4, SGLT5 and SGLT6
pDEST-CMV-3xFLAG-SGLT3_E457Q-EGFP	$Carb^R$ Kan^R	Similar to pDEST-CMV-3xFLAG-SGLT3-EGFP, point mutation E457Q (2.2.1.7) Transient expression of SGLT3_E457Q	This work
pDEST-CMV-3xFLAG-SMCT2-EGFP	$Carb^R$ Kan^R	CMV promotor, lac operator, SMCT2 gene subcloned with Gateway Cloning (similar to SGLT3 (7.1.2)), N-terminal 3xFLAG-tag, C-terminal mEGFP-tag Transient expression of SMCT2	This work
pDONR221-SGLT3 (Fig. 7.2)	Kan^R	T7 promotor, Gateway Cloning sites attL1 and attL2, SGLT3 gene	Addgene, Watertown (USA) Similar for SGLT1, SGLT4, SGLT5, SGLT6 and SMCT2

pEGBacMam_SGLT2_3C_mEGFP_8xHis (Fig. 7.1)	$Carb^R$ Gen^R	CMV promotor, p10 promotor, SGLT2 gene subcloned with EcoRI-HF and XbaI-HF, C-term. His_8-Tag, C-term. mEGFP-Tag, 3C cleavage site Transient expression of SGLT2	Master thesis of Georg Horn, Biophysics II, University of Regensburg
pEZT-BM_TPC2 (Fig. 7.5)	$Carb^R$ Gen^R	CMV promotor, T7 promotor, p10 promotor, TPC2 gene subcloned with XhoI-HF and NheI-HF, N-term. His_8-Tag, N-term. mEGFP-Tag, Thrombin cleavage site Transient expression of TPC2	Youxing Jiang, University of Texas, Austin (USA) She *et al.*, 2019

2.1.14.2.3 Transfection reagents

Reagent	Manufacturer
Cellfectin™ II	Thermo Fisher Scientific Inc., Waltham (USA)
jetPRIME® transfection kit	Polyplus, Illkirch (France)
Lipofectamine™ 2000	Thermo Fisher Scientific Inc., Waltham (USA)
PEI 25 kDa branched	Sigma-Aldrich®, St. Louis (USA)
PEIpro®	Polyplus, Illkirch (France)

2.2 Methods

2.2.1 Molecular biological methods

2.2.1.1 Preparation of chemical competent *E. coli* cells

The following protocol was established by Dr. Pia Berlik at the chair of Biophysics II at the University of Regensburg. Thereby chemically competent *E. coli* cells are produced with the $CaCl_2$ method that increases the permeability of membranes and their ability to uptake extracellular DNA (competence) due to an excess of Ca^{2+} ions.
For preparation of the transformation buffer (Inoue *et al*., 1990), PIPES was dissolved in ddH_2O and the pH was adjusted to 6.7 with KOH. Subsequently, salts were added in the order listed below (Table 2.1) and dissolved completely. 20 ml LB-media (2.1.13.1.1) supplemented with 10 mM $MgCl_2$ was inoculated with a single colony from an agar plate (2.1.13.1.1) and incubated o/N at 37 °C, 80-100 rpm. Subsequently, 250 ml SOB-media (2.1.13.1.2) were inoculated with 1 ml of this pre-culture and incubated at 20 °C, 150 rpm up to an OD_{600} of 0.5-0.6. The cells were incubated on ice-cooled water for 10 min and centrifuged (1 min, 13,800 *x g*, 4 °C; Centrifuge 5415R (2.1.1)). The cell pellet was carefully resuspended under shaking in ice-cold transformation buffer, centrifuged again (1 min, 13,800 *x g*, 4 °C; Centrifuge 5415R (2.1.1) and finally resuspended in 20 ml ice-cold transformation buffer. The cells were supplemented with 1.5 ml DMSO and incubated on ice for additional 10 min. The chemical competent cells were aliquoted to 100 µl, frozen in liquid N_2 and stored at -80 °C.

Table 2.1: Transformation buffer for preparation of chemical competent E. coli cells

	Concentration
PIPES	10 mM
KCl	250 mM
$CaCl_2 \cdot 2\ H_2O$	15 mM
$MnCl_2 \cdot 4\ H_2O$	55 mM

2.2.1.2 Transformation of *E. coli*

A 100 µl aliquot of competent *E. coli* cells was slowly thawed on ice. 80-120 µg of plasmid DNA was added to the cells and the mixture was incubated on ice for 30 min. Subsequently, a heat shock was performed for 45 sec at 42 °C, and the cells were incubated on ice for another five minutes. 900 µl of LB-media (2.1.13.1.1) was added to the reaction, and the cells were incubated for 1 h at 37 °C and 200 rpm. Afterwards, the cells were harvested (1 min, 13,800 *x g*, RT; Heraeus Pico 17 (2.1.1)) and all but 100 µl of the supernatant was removed. After resuspending in the leftover LB-media (2.1.13.1.1), the cells were spread on a pre-warmed LB agar plate (2.1.13.1.1) containing the required antibiotics, incubated o/N at 37 °C and screened for the presence well separated *E. coli* colonies the next morning.

2.2.1.3 Isolation of plasmid DNA

To isolate Plasmid DNA, a fresh o/N culture was made with one single colony from transformed *E. coli* cells and purified with Qiagen® Plasmid Mini Kit (2.1.6) for volumes below 10 ml or Qiagen® Plasmid Plus Giga Kit (2.1.6) using a vacuum manifold for large scale plasmid preparation up to 2.5 L. The procedure was

performed according to manufacturer's instructions and plasmid DNA eluted with autoclaved ddH_2O (nuclease-free). Finally the sequence and concentration of DNA were controlled by sequencing and by absorbance at 260 nm respectively (2.1.1.4).

2.2.1.4 Determination of DNA concentration and sequence

Plasmid DNA concentration and quality was determined with a NanoDrop One Spectrophotometer (2.1.1). Here, only 1-2 µl of plasmid DNA was needed. Additionally, the DNA was sequenced via *TubeSeq Service* by Eurofins Genomics Europe Shared Services GmbH (Ebersberg, Germany) with primers listed in Table 2.2 and the accuracy of the detected sequence was checked via CLC Sequence Viewer (2.1.2).

Table 2.2: Primers used for DNA sequencing

Vector	Primer	Primer sequence
pDEST-CMV-3xFLAG-SGLT3-EGFP	CMV	5´-CGCAAATGGGCGGTAGGCGTG-3´
pDEST-CMV-3xFLAG-SGLT3_E457Q-EGFP	SGLT3_E457Q	5´-GAGAAGGAGCTGCTGATCGC-3´
pDEST-CMV-3xFLAG-SMCT2-EGFP	CMV	5´-CGCAAATGGGCGGTAGGCGTG-3´
pEGBacMam_SGLT2_3C_mEGFP_8xHis	CMV	5´-CGCAAATGGGCGGTAGGCGTG-3´
pET28a_Rab7A	T7	5´-TAATACGACTCACTATAGG-3´

2.2.1.5 Gateway cloning

Gateway® Cloning (Life Technologies, Carlsbad, USA) utilizes site-specific recombination to facilitate rapid assembly of genetic constructs (Fig. 7.2). In this work the "LR Recombination Reaction" was used, following the distributer´s protocol. The LR-reaction was set up as listed in Table 2.3., 2 µl of LR Clonase™ II enzyme mix (2.1.10) added and incubated at 25 °C for 1 h. Then 2 µl of the Proteinase K (2.1.10) solution were added and the mixture was incubated for 10 min at 37 °C. After that, the LR-reaction was transformed (2.2.1.2) into DH5α *E. coli* cells (2.1.14.1.1) and selected on the remaining antibiotic resistance of the destination vector (Carb or Kan for pDEST-CMV-3xFLAG-SGLT3-EGFP (Fig. 7.2)) on a LB agar plate (2.1.13.1.1).

Table 2.3: Setup for LR-reaction

	Volume / Mass
Entry vector (attL sites)	150 ng
Destination vector (attR sites)	150 ng
TE buffer, pH 8.0	fill up to 8 µl

For selection on positive LR-reaction, i.e. clones containing the destination vector with the gene of interest inserted, clones from the first selection were picked with a sterile toothpick and plated as followed: First a line with the toothpick on a first LB agar plate (2.1.13.1.1) containing the antibiotic of the resistance between attR sites of the destination vector was made. Then a line with the same toothpick on a second plate with the antibiotic used for initial selection was drawn. Clones having the destination vector with

positive insert did not grow on the first plate but on the second plate. For receiving the final plasmid with the gene of interest, plasmid DNA was isolated (2.2.1.3) of the positive clones (picked from second plate) and finally DNA concentration and sequence were determined (2.2.1.4).

2.2.1.6 Restriction cloning

2.2.1.6.1 Digestion

Plasmid and insert DNA were cleaved with restriction endonucleases to get linearized and prepared for ligation. The reaction setup is shown in Table 2.4. The reaction was carried out for 1 h at 37 °C. After digestion 2 µl of Antarctic Phosphatase (2.1.10) was added to nonspecifically dephosphorylate 5' and 3' ends of DNA.

Table 2.4: Setup for digestion with restriction enzymes

	Volume
Cut Smart Buffer (10x; 2.1.3)	5 µl
Restriction enzyme 1	2 µl
Restriction enzyme 2	2 µl
DNA (2-4 µg)	x µl
ddH_2O	fill up to 50 µl

2.2.1.6.2 Agarose gel electrophoresis

Cleaved vectors and inserts were analyzed by agarose gel electrophoresis. For visualization of the DNA fragments ethidium bromide was added to the agarose gel. It intercalates with the nucleotides of the DNA and can be illuminated at the excitation wavelength of 312 nm to make DNA visible in the agarose gel. For preparative agarose gel electrophoresis, 0.8% (w/v) agarose was dissolved in 1x SuperBuffer (Table 2.5). DNA samples were mixed with 6x Gel loading purple and loaded onto an agarose gel together with GeneRuler™ 1 kb Plus DNA Ladder (2.1.7). The separation of DNA samples was carried out for 20 min at 200 V. Under UV inspection the corresponding DNA bands were cut out and purified with Qiagen® Gel Extraction Kit (2.1.6) according to manufacturer's instruction. Finally, the DNA concentrations were determined (2.2.1.4).

Table 2.5: 50x SuperBuffer composition

	Volume / Mass
H_3BO_3	45 g
NaOH	8 g
ddH_2O	fill up to 400 ml

Composition of 50x SuperBuffer, pH 8.8 (Zhang *et al*., 2011). Dilute to 1x with ddH_2O before use.

2.2.1.6.3 Ligation

Ligation of digested plasmids and DNA inserts was carried out by addition of T4 DNA Ligase (2.1.10). For ligation, 50 ng of plasmid and a plasmid-insert ratio of 1:7 was used in the setup shown in Table 2.6. The reaction was carried out o/N at RT. Subsequently, the T4 DNA Ligase was heat inactivated for 10 min at 65 °C and the ligation product was transformed (2.2.1.2) in competent *E. coli* DH5α cells (2.1.14.1.1) and selected on the antibiotic resistance of the backbone of the destination vector on a LB agar plate (2.1.13.1.1). Finally, the DNA of positive clones was isolated (2.2.1.3) and controlled for successful cloning by sequencing (2.2.1.4).

Table 2.6: Mixture for ligation of digested plasmids and DNA inserts

	Volume
50 ng Plasmid DNA	x µl
Insert DNA	x µl
T4 DNA Ligase Buffer (10x; 2.1.3)	2 µl
T4 DNA Ligase (2.1.10)	1.5 µl
ddH_2O	fill up to 20 µl

2.2.1.7 Point mutation

To introduce a point mutation, site directed mutagenesis via polymerase chain reaction (PCR) was used in this work (Hemsley *et al.*, 1989). Therefore, primers were designed in back-to-back orientation, while the forward primer (F´) contained the changed nucleotide (Table 2.7) and purchased from Eurofins Genomics Europe Shared Services GmbH (Ebersberg, Germany). The PCR reaction was set up as listed in Table 2.8. The PCR consisted of an initial plasmid denaturation at 98 °C for 1 min, followed by 20 amplification cycles (Denaturation: 98°C, 30sec; Annealing: 60/62/64°C, 30sec; Extension: 72°C, 6min) and a final extension of 7 min at 72 °C. 5 µl of the final product was checked via agarose gel electrophoresis (2.2.1.6.2). The positive PCR product was mixed with 1 µl DpnI (2.1.10) and incubated for 1 h at 37 °C to cut the methylated vector used as template for the reaction. Then 1 µl T4 DNA Ligase (2.1.10) and 2 µl T4 DNA Ligase Buffer (10x; 2.1.3) was added to 17 µl of this mixture and incubated o/N at 16 °C for final ligation. The ligation product was transformed (2.2.1.2) in competent *E. coli* DH5α cells (2.1.14.1.1) and selected on the antibiotic resistance of the vector on a LB agar plate (2.1.13.1.1). Finally, the DNA from the positive clones was isolated (2.2.1.3) and checked for successful point mutation via DNA sequencing (2.2.1.4).

Table 2.7: Primer for point mutation

Mutation	Primer
SGLT3_E457Q	F´ : 5´-CCACTACACC**C**AGTCCATCTC-3´
	R´ : 5´-ATCAGCTGGCCGTTCTGGG-3´

Table 2.8: Setup PCR reaction for site directed mutagenesis

	Volume
High-Fidelity Buffer (5x; 2.1.3)	5 µl
dNTPs (10 mM; 2.1.3)	1 µl
F´ primer (10 pmol/µl)	2.5 µl
R´ primer (10 pmol/µl)	2.5 µl
vector (15 ng/µl)	1 µl
DMSO	0.75 µl
Phusion® High-Fidelity DNA Polymerase (2.1.10)	0.5 µl
ddH_2O	11.75 µl

2.2.2 Biochemical methods

2.2.2.1 Determination of protein concentration

2.2.2.1.1 (Quick) Bradford assay

Quick Bradford assay was used for fast determination of protein-containing fractions during purification. This assay is based on an absorbance shift of Coomassie Brilliant Blue dye in acidic solution from 465 nm to 595 nm by binding primarily to basic and aromatic amino acid residues (Bradford M. M., 1976). For this, 45 µl H_2O and 5 µl protein sample or 40 µl H_2O and 10 µl protein sample were mixed with 200 µl Bradford reagent and visually controlled for the blue-colored reaction to identify the protein-containing fractions.
To determine the approximate protein concentration via Bradford assays, 10 µl of BCA protein standard (2.1.3) were mixed as duplicates with 40 µl H_2O and 200 µl Bradford reagent in a 96 well micro plate (2.1.3). A quartet of 10 µl protein sample was mixed in the same plate as described before. The protein concentration was determined via the absorption of the blue colored solutions which was measured photometrically with a TECAN Infinite M200 Pro plate reader (2.1.1) and evaluated with Magellan™ software (2.1.2).

2.2.2.1.2 Photometrical determination

For final and exact concentration determination of the purified protein a NanoDrop One Spectrophotometer (2.1.1) was used. The absorption of the protein solution at a wavelength of 280 nm (A_{280}, absorption maximum of Trp and Tyr) was measured and protein concentration was estimated via Lambert Beer's Law (see below) using the extinction coefficient of the respective protein determined via ExPASy-ProtParam (2.1.2).

$$A_{280} = \lg (I_0 / I_1) = \varepsilon_{280} \times c \times d$$

I_0: Intensity of the incident light [W m^{-2}]

I_1: Intensity of the transmitted light [W m^{-2}]

A_{280}: Absorption of the material for light with a wavelength of 280 nm

ε_{280}: molar extinction coefficient [M^{-1} cm^{-1}]

c: protein concentration [M]

d: layer thickness [cm]

2.2.2.2 SDS-Polyacrylamide gel electrophoresis (SDS-Page)

To analyse protein samples under denaturing conditions SDS-Page (Table 2.9) with a Laemmli buffer system was used (Laemmli, 1970). 10% polyacrylamide gels (Table 2.10) were used for mammalian protein samples whereas for bacterial proteins 12% polyacrylamide gels (Table 2.10) were chosen. Samples were mixed with 6x loading buffer (Table 2.11). As molecular weight standard 5 µl of PageRuler™ Prestained (2.1.7) was loaded on the gel next to the protein samples.

Table 2.9: Separation and stacking gel buffer for SDS-Page

	Separation gel buffer, pH 8.8	Stacking gel buffer, pH 6.8
Tris/HCl	1.5 M	0.5 M
SDS	0.4% (w/v)	0.4% (w/v)

Table 2.10: SDS-Page gel composition (for 13 gels)

	Separation gel (10% / 12%)	Stacking gel (4.0%)
Separation gel buffer	16.25 ml	-
Stacking gel buffer	-	10 ml
Acrylamide 40% (w/v)	16.25 ml / 19.5 ml	4 ml
ddH_2O	32.5 ml / 29.25 ml	26 ml
APS 10% (w/v)	650 µl	320 µl
TEMED	65 µl	32 µl
Bromophenol blue 0.04% (w/v)	-	120 µl

Table 2.11: Laemmli running buffer and 6x loading buffer

	Laemmli running buffer, pH 8.3	6x loading buffer, pH 6.8
Tris/HCl	25 mM	62.5 mM
Glycine	9.2 M	-
Glycerol	-	10% (v/v)
SDS	0.1% (w/v)	1.5% (w/v)
β-Mercaptoethanol	-	2% (w/v)
Bromophenol blue	-	0.00025% (w/v)

The electrophoresis was performed in a Mighty Small II Mini Vertical System (2.1.1) with a current of 45 mA/gel (300 V) for 35 min. Proteins were detected by staining with staining solution (Table 2.12) for 30 min. To make protein visible the gel was incubated in destaining solution (Table 2.12) for several hours until the protein-bands were clearly visible. Finally, the gel was digitalized via GelDoc Go Imaging System (2.1.1) using the manufacturers settings for SDS-gels.

Table 2.12: Composition of staining and destaining solution for SDS-Page

	Staining solution	Destaining solution
Methanol	45% (v/v)	-
Ethanol	-	20% (v/v)
Acetic acid	9% (v/v)	10% (v/v)
Coomassie Brilliant Blue R250®	0.25% (w/v)	-

2.2.2.3 Silver Staining

To detect lower amounts of protein and to check the purity of protein more thoroughly, polyacrylamide gels (2.2.2.2) were stained with silver (nanogram quantities; Kavran J. M. and Leahy D. J., 2014) instead of Coomassie Brilliant Blue R250® (0.1-0.5 µg; Brunelle J. L. and Green R., 2014). The soaks and washes were carried out with 10-15 ml of the respective solution in a clean glass tray or beaker. Directly after electrophoresis (2.2.2.2) the gel was soaked in fixing solution (Table 2.13) for 10 minutes and washed twice for 5 min in ddH_2O. Thereafter, it was incubated for 1 min in sodium thiosulfate (Table 2.13), washed twice for 20 sec in ddH_2O and stained with silver nitrate (Table 2.13) for 10 min. After rinsing the gel again with water mixed with a small volume of developing solution (Table 2.13), it was incubated in developing solution (Table 2.13) until the desired band intensity (few seconds up to 1 min). To terminate the development, stopping solution (Table 2.13) was added for 10 min and the gel was washed repeatedly with water before being imaged with a GelDoc Go Imaging System (2.1.1) using the manufacturers settings for silver stained gels.

Table 2.13: Solutions for Silver staining

	Composition
Fixing solution	40% (v/v) methanol 13.5% (v/v) formaldehyde
Sodium thiosulfate	0.02% (w/v) $Na_2S_2O_3$ - Pentahydate
Staining solution	0.1% (w/v) $AgNO_3$
Developing solution	3% (w/v) Na_2CO_3 0.05% (v/v) formaldehyde (add fresh) 0.000016% (w/v) $Na_2S_2O_3$ – Pentahydate
Stopping solution	44% (w/v) citiric acid ($C_6H_8O_7$)

2.2.2.4 Western blot

For western blot analysis, proteins separated on a polyacrylamide gel (2.2.2.2, without staining) were transferred in a continuous buffer system to a polyvinyldifluorid membrane by electro-blotting. The transfer was carried out in a wet-blot procedure using a Fastblot B33 system (2.1.1).

Four Whatman GB003 papers (2.1.3) were soaked in transfer buffer (Table 2.14) and one Immobilon-P Transfer Membrane (2.1.3) was activated with methanol.

All components were stacked according to the prescribed order:

CATHODE

2 x Whatman GB003 paper

polyacrylamide gel

Immobilon-P Transfer Membrane

2 x Whatman GB003 paper

ANODE

The transfer was carried out with 25 V (maximum), 5 W, 200 mA (constant) for 40 min at RT. This was followed by immunodetection. To avoid unspecific binding sites the membrane was incubated at RT in blocking solution (Table 2.14) for 1 h under gentle shaking. Subsequently, the membrane was incubated for 1 h with the primary antibody solved in blocking solution, followed by washing three times for 1 min in TBS (Table 2.14) and incubated again for 1 h at RT with the appropriate secondary antibody (all with conjugated alkaline phosphatase (AP)) also diluted in blocking solution. The antibodies used and their respective concentrations are listed in 2.1.12. Finally, the membrane was washed twice with TBS for 1 min and equilibrated in developing solution (Table 2.14) for colorimetric signal detection (Blake *et al.*, 1984). When the desired band intensity was reached the addition of ddH_2O stopped the reaction and the blot was documented via GelDoc Go Imaging System (2.1.1) using the manufacturers settings for western blots.

Table 2.14: Buffer and solutions for western blot

	Composition
Transfer buffer	25 mM Tris 150 mM glycine 10% (v/v) methanol
TBS buffer	10 mM Tris/HCl pH 7.5 150 mM NaCl
Blocking solution	TBS buffer 3% (w/v) BSA (2.1.3)
AP buffer	100 mM Tris/HCl pH 9.0 150 mM NaCl 1 mM $MgCl_2$
Developing solution	AP buffer 0.5 mg/ml NBT (2.1.5) 0.25 mg/ml BCIP (2.1.5)

2.2.3 Heterologous protein expression in *E. coli*

For heterologous protein expression of GPR, Rab7A or Saposin A, different *E. coli* strains were transformed (2.2.1.2) with the associated expression vectors (Table 2.15). From the resulting transformations, one clone was transferred with a sterile loop into 50 ml LB-media (2.1.13.1.1) supplemented with the respective antibiotics. This pre-culture was incubated o/N at 37 °C, 170 rpm. The next day, 6x 1 L LB-media (2.1.13.1.1; TB-media (2.1.13.1.3) for Sapsoin A) were inoculated with the previous pre-culture at an OD_{600} = 0.1 and the corresponding antibiotics (2.1.14.1.2), and incubated at 37 °C, 170 rpm. After the culture reached OD_{600} = 0.6 expression was induced by adding 1 mM IPTG (2.1.5). For GPR additionally 2 µg/ml *all-trans* retinal (2.1.5) was added. For each protein of interest the cells were cultivated at an individual temperature and time (Table 2.15). Afterwards cells were harvested by centrifugation (15 min, 3,300 *x g*, 4 °C, Avanti J-26 XP with rotor JLA-8.100 (2.1.1)).

Table 2.15: Conditions protein expression in E. coli

Protein	Expression vector	*E. coli* strain	Temperature and growth time after induction
GPR	pET27b_GPR (2.1.14.1.2)	C43 (DE3)ΔAcrAB (2.1.14.1.1)	27 °C, o/N
Rab7A	pET28a_Rab7A (2.1.14.1.2)	BL21 (DE3) Rosetta2 (2.1.14.1.1)	30 °C, 2h
Saposin A	pNIC-Bsa4_Saposin A (2.1.14.1.2)	Rosetta-gami™ 2 (DE3) (2.1.14.1.1)	25 °C, o/N

2.2.4 Eukaryotic cell culture

2.2.4.1 Thawing of cells

Frozen cryo-stocks were quickly thawed at 37° C and immediately added to 10 ml warm DMEM F-12 (2.1.13.2.1). To remove DMSO present in the cryo-stock, the previous suspension is centrifuged for 5 min, 10 *x g*, RT. The supernatant was removed and the cell pellet was resuspended in 5 ml DMEM F-12 (2.1.13.2.1), 10% (v/v) FBS (2.1.13.2.1), 0.5% (v/v) Pen-Strep (2.1.13.2.1) and incubated at 5% CO_2, 37 °C.

2.2.4.2 Adherent cell culture

Non-transfected HEK293S GnT1$^-$ cells (2.1.14.2.1) as well as stable cell lines (2.1.14.2.1) were aseptically grown in DMEM F-12 (2.1.13.2.1), 10% (v/v) FBS (2.1.13.2.1), 0.5% (v/v) Pen-Strep (2.1.13.2.1) at 37 °C and 5% CO_2. After reaching 100% confluence, adherent cells were transferred into new flasks containing fresh media. For maintaining the cultures, PBS (2.1.13.2.2) was used to wash off dead cells and Trypsin-EDTA solution (2.1.13.2.1) was used for splitting. The cells are kept in culture until 30 passages before thawing a fresh cryo-stock.

2.2.4.3 Suspension cell culture

When a cell confluency of approx. 90% was reached in a T175 cell culture flask (2.1.3) the cells were trypsinized and seeded in a 250 ml CELLSPIN spinner flask (2.1.1) at 0.6-0.8 x 10^6 cells/ml density. The cells were grown in FreeStyle™ 293 expression media (2.1.13.2.1) containing 1% (v/v) FBS (2.1.13.2.1), 0.5% (v/v) Pen-Strep (2.1.13.2.1), 0.1% (v/v) Anti-clumping agent (2.1.13.2.1) at 37 °C, 5% CO_2 and stirred at 120 rpm on a CELLSPIN stirring unit (2.1.1). Fresh media was added every two days to keep the cell density below 2.5 x 10^6 cells/ml. Fully confluent 250 ml CELLSPIN spinner flasks (2.1.1) were transferred into 1 L CELLSPIN spinner flasks (2.1.1). If desired cell density of 1 x 10^6 cells/ml in 1 L was reached the cells were induced or transfected. A general problem in suspension cell culture was the clumping of cells, leading to poor protein expression or even cell death. To solve this problem 0.1% (v/v) Anti-clumping agent (2.1.13.2) was added to the media and the stirring speed of the used spinner flasks was increased from 70 to 120 rpm in cooperation with the Pfeiffer Electronic Engineering GmbH, Lahnau (Germany).

2.2.4.4 Protein expression via transient transfection

2.2.4.4.1 Adherent culture

For expression via transient transfection in adherent HEK293S GnT1$^-$ cells (2.1.14.2.1), the cells were grown in a 6-well plate in 2 ml DMEM F-12 (2.1.13.2.1), 10% (v/v) FBS (2.1.13.2.1), 0.5% (v/v) Pen-Strep (2.1.13.2.1) to a confluency of approx. 85%. For each well, cells were transfected with 2 µg DNA with different transfection reagents (2.1.14.2.3), respecting the manufacturers protocols. After 24 h, 5 mM sodium butyrate (2.1.5) was added. 24 h later the cells were harvested with 1 ml PBS (2.1.13.2.2), pelleted (1 min, 13,800 *x g*, RT; Heraeus Pico 17 (2.1.1)) and stored at -20°C.

2.2.4.4.2 Suspension culture

HEK293S GnT1$^-$ cells (2.1.14.2.1) in suspension culture (2.2.4.3) were transfected with 1 µg DNA/ 10^6 cells and a ratio of 1:3 (w/w) DNA:PEI 25 kDa branched (2.1.14.2.3). For 1 L culture with a total of 1000 x 10^6 cells, 1 mg DNA was diluted into 50 ml FBS-free FreeStyle™ 293 expression media (2.1.13.2.1). In parallel, 3 mg of PEI 25 kDa branched was mixed with the same volume of media. The media supplemented with PEI 25 kDa branched was added to the media containing the DNA and the mix was incubated for 20 min at RT to form DNA/PEI polyplex. The mix was added to the cells and 24 h after transfection the culture was supplemented with 5 mM sodium butyrate (2.1.5). After additional 24 h, the cells were harvested via centrifugation (30 min, 3,300 *x g*, 4 °C, Avanti J-26 XP with rotor JLA-8.100 (2.1.1) and stored at -20 °C.

2.2.4.5 Protein expression via stable cell line

Stable cell lines were generated by Marko Roblek (ISTA) via lentiviral transduction (Elegheert et al., 2018). The cryo-stocks received from Marko Roblek were transferred into pre-warmed DMEM F-12 (2.1.13.2.1), 10% (v/v) FBS (2.1.13.2.1), 0.5% (v/v) Pen-Strep (2.1.13.2.1), supplemented with 5 µg/ml blasticidin (2.1.13.2.1). Cells got cultivated as adherent stock as described in 2.2.4.2. After 3rd passage blasticidin-free media was used, and cryo-stocks were produced (2.2.4.7). Suspension cell culture of stable cell lines was executed similar to non-transfected cells (2.2.4.3). When the suspension culture reached a density of 1 x 10^6 cells/ml in 1 L protein expression was induced with 1 µg/ml doxycycline (2.1.13.2.1) and incubated for 48 hours at 37 °C, 5% CO_2, stirred at 120 rpm. Finally, cells were harvested via centrifugation (30 min, 3,300 g, 4 °C, Avanti J-26 XP with rotor JLA-8.100 (2.1.1) and stored at -20 °C.

2.2.4.6 Observation of protein expression

To observe the expression of protein in stable cell lines and transient transfected cells, two different methods were used. For constructs containing a mEGFP-coding sequence the fluorescence signal of the transfected cells was screened with the EVOS® FL Cell Imaging System (2.1.1) shortly before harvesting. Subsequently, and for all construct not containing mEFGP, 100 mg of cells were lysed in 500 µl of solubilization buffer (Table 2.16) for 1 h at 4 °C. Then the lysed cells were centrifuged (1 min, 13,800 *x g*, 4 °C; Centrifuge 5415R (2.1.1)) to separate cell debris from the solubilized parts. The supernatant was finally used to perform western blot analysis (2.2.2.4).

Table 2.16: Buffer for protein expression observation

	Composition
solubilization buffer	20 mM Tris/HCl pH 8.0 150 mM NaCl 0.01 mg/ml DNAse I (2.1.10) 1 mM Pefabloc® SC (2.1.10) 0.5 µg/ml Pepstatin A (2.1.5) 2 µg/ml Leupeptin (2.1.5) 1 µg/ml Aprotinin (2.1.5) 4% (w/v) DDM /0.8% CHS (2.1.8)

2.2.4.7 Preparation of cryo-stocks

A confluent T175 cell culture flask (2.1.3) was washed with PBS (2.1.13.2.2), the cells isolated with 3 ml Trypsin-EDTA solution (2.1.13.2.1) and filled up to 10 ml with fresh DMEM F-12 (2.1.13.2.1), 10% (v/v) FBS (2.1.13.2.1), 0.5% (v/v) Pen-Strep (2.1.13.2.1). The cells were counted with a BRAND® counting chamber (2.1.1), then sedimented at 300 × *g*, 5 min at RT and resuspended in DMEM F-12 (2.1.13.2.1), 10% (v/v) FBS (2.1.13.2.1), 0.5% (v/v) Pen-Strep (2.1.13.2.1), 10% (v/v) DMSO and aliquoted in CryoPure tubes (2.1.3). Each aliquot contained 3 x 10^6 cells in 1.8 ml. The CryoPure tubes were put in a room temperature Mr. Frosty™ freezing container (2.1.1) and placed at -80° C for 24 h. For long-term storage the vials were transferred in liquid nitrogen. One aliquot was thawed to verify viability of frozen aliquots.

2.2.5 Protein purification

Unless noted otherwise, all purification steps were performed at 4 °C.

2.2.5.1 Purification of GPR

The harvested cells containing C-terminal His_6-tagged GPR were resuspended in disruption buffer (Table 2.17) using 50 ml buffer per 1 L harvested media. Subsequently, cells were disrupted twice in a Cell disruptor TS 0.75 (2.1.1) at 1.85 kbar and 4 °C. Cell debris was removed via centrifugation (30 min, 3,300 *x g*, 4 °C, Avanti J-26 XP with rotor JLA-16.250 (2.1.1)). From the remaining supernatant, membranes were isolated via ultra-centrifugation (1 h, 88,000 *x g*, 4 °C, Ultracentrifuge Optima XPN-100 with rotor 45 Ti (2.1.1)) and afterwards resuspended in membrane buffer (Table 2.17) to a final concentration of 10 mg/ml of membrane. DDM (2.1.8) was added dropwise to a final concentration of 1.5% (w/v) and the mixture was incubated o/N at 4 °C under gentle stirring to solubilize the membranes. The next day the solubilized proteins were separated from membrane debris via ultra-centrifugation (1 h, 88,000 *x g*, 4 °C, Ultracentrifuge Optima XPN-100 with rotor 45 Ti (2.1.1)). 3ml Ni-NTA agarose (2.1.9) was washed with ddH_20 and equilibrated with 5 CV equilibration buffer (Table 2.17). The pre-equilibrated Ni-NTA agarose was incubated with the supernatant under gentle agitation for 2 h at 4 °C and thereafter the mixture was loaded into a Pierce™ Disposable Column with polyethylene disc (2.1.3). When the resin has set and the flow-through was discarded, the column was washed with 10 CV wash buffer 1 (Table 2.17) and 10 CV wash buffer 2 (Table 2.17) to remove unbound protein. Finally, GPR was eluted with 3 CV elution buffer (Table 2.17). Elution was monitored by the red color of GPR, red fractions were pooled and concentrated via an Amicon® Ultra concentrator MWCO 100 kDa (2.1.3) to 500 µl for size exclusion chromatography (SEC). This purification step allows to separate protein samples according to their hydrodynamic volumes and to check the quality of the sample according to the monodispersity of the protein peak. The protein sample was loaded on a Superose 6 Increase 10/300 GL column (2.1.1) connected to an ÄKTA™ purifier system (2.1.1, Software: UNICORN 5.31 (2.1.2)). The ÄKTA™ purifier system and the column, stored in 20% ethanol, were washed with ddH_2O and pre-equilibrated with the SEC-buffer (Table 2.17) prior to the SEC run according to the manufacturer's advice. SEC was performed at a flow rate of 0.5 ml/min and fractions of 0.5 ml were collected. The elution of protein was traced by absorption at 280 nm, 310 nm and 520 nm (*all-trans* retinal). Fractions containing GPR according to the absorption profile and red color were pooled, and protein concentration was determined photometrically (2.2.2.1.2) using the extinction coefficient of GPR (ε_{280}(GPR) = 2,788 M^{-1} cm^{-1}).

Table 2.17: Buffers for purification of GPR

	Composition
Disruption buffer	50 mM HEPES pH 7.5 5 mM $MgSO_4$ 0.01 mg/ml DNase I (2.1.10) 1 mM Pefabloc® SC (2.1.10)
Membrane buffer	50 mM HEPES pH 7.5 100 mM NaCl
Equilibration buffer	50 mM HEPES pH 7.5 300 mM NaCl 5 mM Imidazole pH 7.5 0.1% (w/v) DDM (2.1.8)
Wash buffer 1	50 mM HEPES pH 7.5 300 mM NaCl 50 mM Imidazole pH 7.5 0.1% (w/v) DDM (2.1.8)
Wash buffer 2	50 mM HEPES pH 7.5 300 mM NaCl 100 mM Imidazole pH 7.5 0.1% (w/v) DDM (2.1.8)
Elution buffer	50 mM HEPES pH 7.5 300 mM NaCl 400 mM Imidazole pH 7.5 0.1% (w/v) DDM (2.1.8)
SEC-buffer	50 mM HEPES pH 7.5 300 mM NaCl 0.1% (w/v) DDM (2.1.8)

2.2.5.2 Rab7A purification

E. coli expressing C-terminal His_6-tagged Rab7A were harvested and resuspended in solubilization buffer (Table 2.18) using 50 ml buffer per 1 L harvested media. Subsequently, cells were lysed by sonication (1 min, 60% amplitude, pulse: 3 sec on / 3 sec off, 4 °C, Digital sonifier 250 (2.1.1)) and centrifuged (30 min, 3,300 *x g*, 4 °C, Avanti J-26 XP with rotor JLA-16.250 (2.1.1)) to remove cell debris. 3 ml Ni-NTA agarose (2.1.9) was washed with ddH_20 and equilibrated with 5 CV equilibration buffer (Table 2.18). The pre-equilibrated Ni-NTA agarose was then incubated with the supernatant under gentle agitation for 2 h at 4 °C and thereafter the mixture was loaded into a Pierce™ Disposable Column with polyethylene disc (2.1.3). After the resin has set and the flow-through was discarded, the column was washed with 10 CV wash buffer (Table 2.18) to remove unbound proteins. Finally, Rab7A was eluted with 3 CV elution buffer (Table 2.18) in 500 µl fractions. The presence of protein in the elution fractions is controlled via Quick Bradford Assay (2.2.2.1.1). The positive fractions were pooled and concentrated via an Amicon® Ultra concentrator

MWCO 10 kDa (2.1.3) to 500 µl for size exclusion chromatography (SEC). SEC was performed similar to GPR (2.2.5.1), while only absorption at 280 nm for detecting protein elution, and a different SEC-buffer (Table 2.18) at RT were used. Photometrical determination (2.2.2.1.2) was used to estimate final protein concentration with the extinction coefficient of Rab7A (ε_{280}(Rab7A) = 1,083 M^{-1} cm^{-1}). Finally, the activity of Rab7A was tested (2.2.8.2).

Table 2.18: Buffers Rab7A purification

	Composition
Solubilization buffer	30 mM Tris/HCl pH 8.0 500 mM NaCl 2 mM DTT 2 mM $MgCl_2$ 0.01 mg/ml DNAse I (2.1.10) 1 mM Pefabloc® SC (2.1.10) 1 mg/ml Lysozyme (2.1.5)
Equilibration buffer	30 mM Tris/HCl pH 8.0 500 mM NaCl 2 mM DTT 2 mM $MgCl_2$ 5 mM Imidazole pH 8.0
Wash buffer	30 mM Tris/HCl pH 8.0 500 mM NaCl 2 mM DTT 2 mM $MgCl_2$ 50 mM Imidazole pH 8.0
Elution buffer	30 mM Tris/HCl pH 8.0 500 mM NaCl 2 mM DTT 2 mM $MgCl_2$ 100 mM Imidazole pH 8.0
SEC-buffer	30 mM Tris/HCl pH 8.0 500 mM NaCl 2 mM DTT 2 mM $MgCl_2$

2.2.5.3 Purification of Saposin A

The harvested *E. coli* expressing C-terminal His_6-tagged Saposin A were resuspended in resuspension buffer (Table 2.19) using 30 ml buffer for 1 L harvested media. Then cells were lysed by sonication (3 min, 65% amplitude, pulse: 2 sec on / 2 sec off, 4 °C, Digital sonifier 250 (2.1.1)), boiled for 10 min at 85 °C and afterwards centrifuged (45 min, 20,000 *x g*, 4 °C, Ultracentrifuge Optima XPN-100 with rotor 45 Ti (2.1.1)) to remove debris and denatured proteins. 3ml Ni-NTA agarose (2.1.9) was washed with ddH_20 and equilibrated with 5 CV equilibration buffer (Table 2.19). The pre-equilibrated Ni-NTA agarose was then

incubated with the supernatant under gentle agitation for 1 h at 4 °C and thereafter the mixture was loaded into a Pierce™ Disposable Column with polyethylene disc (2.1.3). After the resin has set and the flow-through was discarded, the column was washed with 15 CV wash buffer (Table 2.19) to remove unbound protein. Finally, Saposin A was eluted with 5 CV elution buffer (Table 2.19) in 500 µl fractions. The presence of protein in the elution fractions is controlled via A Quick Bradford Assay (2.2.2.1.1) and the positive fractions were pooled. Then they were dialyzed in a MEMBRA-Cel dialysis tube (3.5 MWCO, 2.1.3) against dialysis buffer (Table 2.19) for 24 h to remove imidazole. Meanwhile the dialysis buffer was changed three times. Bradford Assay (2.2.2.1.1) was used to estimate protein concentration and protein was concentrated to a final concentration of 20 mg/ml via an Amicon® Ultra concentrator MWCO 3 kDa (2.1.3).

Table 2.19: Buffers Saposin A purification

	Composition
Resuspension buffer	20 mM HEPES pH 7.5 150 mM NaCl 20 mM Imidazole pH 7.5 0.01 mg/ml DNAse I (2.1.10) 1 mM Pefabloc® SC (2.1.10) 1 mg/ml Lysozyme (2.1.5)
Equilibration buffer	20 mM HEPES pH 7.5 150 mM NaCl 5 mM Imidazole pH 7.5
Wash buffer	20 mM HEPES pH 7.5 150 mM NaCl 40 mM Imidazole pH 7.5
Elution buffer	20 mM HEPES pH 7.5 150 mM NaCl 400 mM Imidazole pH 7.5
Dialysis buffer	20 mM HEPES pH 7.5 150 mM NaCl

2.2.5.4 Affinity-purification of SGLT2

The pelleted HEK293S GnT1$^-$ cells (2.1.14.2.1) expressing C-terminal mEGFP-His_8-tagged SGLT2 was resuspended in 5 ml solubilization buffer (Table 2.20) per 1 g cells, lysed with a Dounce homogenizer (2.1.1) and 2% (w/v) /0.2% (w/v) LMNG /CHS (2.1.8) was added to solubilize membranes under gentle stirring at 4 °C for 2 h. Then the mixture was homogenized again via a Dounce homogenizer (2.1.1) and centrifuged (1 h, 70,000 *x g*, 4 °C, Ultracentrifuge Optima XPN-100 with rotor 45 Ti (2.1.1)) to remove not-solubilized cell components. 1 ml Ni-NTA agarose (2.1.9) was washed with ddH_20 and equilibrated with 5 CV equilibration buffer (Table 2.20). The pre-equilibrated Ni-NTA resin was incubated with the supernatant under gentle agitation for 2 h at 4 °C and thereafter the mixture was loaded into a Pierce™ Disposable Column with polyethylene disc (2.1.3). After letting the resin set and discarding the flow-through, the

column was washed with 10 CV wash buffer 1 (Table 2.20) and 10 CV wash buffer 2 (Table 2.20) to remove unbound protein. Finally, SGLT2 was eluted with 5 CV elution buffer (Table 2.20) in 250 µl fractions. The presence of protein in the elution fractions is controlled via a Quick Bradford Assay (2.2.2.1.1).

Table 2.20: Buffers SGLT2 purification

	Composition
Solubilization buffer	50 mM Tris/HCl pH 8.0 200 mM NaCl 0.01 mg/ml DNAse I (2.1.10) 1 mM Pefabloc® SC (2.1.10) 0.5 µg/ml Pepstatin A (2.1.5) 2 µg/ml Leupeptin (2.1.5) 1 µg/ml Aprotinin (2.1.5)
Equilibration buffer	50 mM Tris/HCl pH 8.0 200 mM NaCl 5 mM imidazole pH 8.0 0.01% (w/v) /0.001% (w/v) LMNG/CHS (2.1.8)
Wash buffer 1	50 mM Tris/HCl pH 8.0 200 mM NaCl 25 mM imidazole pH 8.0 0.01% (w/v) /0.001% (w/v) LMNG/CHS (2.1.8)
Wash buffer 2	50 mM Tris/HCl pH 8.0 200 mM NaCl 50 mM imidazole pH 8.0 0.01% (w/v) /0.001% (w/v) LMNG/CHS (2.1.8)
Elution buffer	50 mM Tris/HCl pH 8.0 200 mM NaCl 300 mM imidazole pH 8.0 0.01% (w/v) /0.001% (w/v) LMNG/CHS (2.1.8)

2.2.5.5 Purification of SGLT3

2.2.5.5.1 StrepII-Tag purification

The harvested HEK293S GnT1$^-$-SGLT3 cells (2.1.14.2.1) expressing N-terminal mEGFP-StrepII-tagged SGLT3 were resuspended in 5 ml solubilization buffer (Table 2.21) per 1 g cells, lysed with a Dounce homogenizer (2.1.1) and 1% (w/v) /0.2% (w/v) DDM/CHS (2.1.8) was added to solubilize membranes under gentle stirring at 4 °C. After 2 h the mixture was homogenized again with a Dounce homogenizer (2.1.1) and centrifuged (1 h, 70,000 *x g*, 4 °C, Ultracentrifuge Optima XPN-100 with rotor 45 Ti (2.1.1)) to remove not-solubilized cell components. 1ml Strep-tactin®XT 4Flow® (2.1.9) was filled into a Pierce™ Disposable Column with polyethylene disc (2.1.3), washed with dd$H_2$0 and equilibrated with 10 CV wash buffer (Table 2.21). Then the supernatant was loaded onto the pre-equilibrated Strep-tactin®XT 4Flow® twice and the column washed with 20 CV wash buffer (Table 2.21) to remove unbound protein. Finally, SGLT3 was eluted

with 5 CV elution buffer (Table 2.21) in 250 µl fractions. The presence of protein in the elution fractions is controlled by a Quick Bradford Assay (2.2.2.1.1). The positive fractions were pooled and concentrated via an Amicon® Ultra concentrator MWCO 50 kDa (2.1.3) to 50 µl for size exclusion chromatography (SEC).

Table 2.21: Buffers SGLT3 purification via StrepII-Tag

	Composition
Solubilization buffer	20 mM Tris/HCl pH 8.0 150 mM NaCl 0.01 mg/ml DNAse I (2.1.10) 1 mM Pefabloc® SC (2.1.10) 0.5 µg/ml Pepstatin A (2.1.5) 2 µg/ml Leupeptin (2.1.5) 1 µg/ml Aprotinin (2.1.5)
Wash buffer	20 mM Tris/HCl pH 8.0 150 mM NaCl 1 mM EDTA pH 8.0 0.05% (w/v) /0.01% (w/v) DDM/CHS (2.1.8)
Elution buffer	20 mM Tris/HCl pH 8.0 150 mM NaCl 1 mM EDTA pH 8.0 0.05% (w/v) /0.01%(w/v) DDM/CHS (2.1.8) 50 mM Biotin (2.1.3)
SEC-buffer	20 mM Tris/HCl pH 8.0 150 mM NaCl 0.05% (w/v) /0.01% (w/v) DDM/CHS (2.1.8)

The protein sample was separated on a Superose 6 Increase 5/150 GL column (2.1.1) connected to an ÄKTA™ pure system (2.1.1, Software: UNICORN 7.8 (2.1.2)) at RT. The ÄKTA™ pure system and the column stored in 20% ethanol were washed by ddH_2O and pre-equilibrated with the SEC-buffer (Table 2.21) prior to the SEC run according to the manufacturer's advice. SEC was performed at a flow rate of 0.2 ml/min and fractions of 75 µl were collected. The elution of protein was traced by absorption at 280 nm. Fractions containing SGLT3 according to the absorption profile were pooled. At the end, the protein concentration was photometrically determined (2.2.2.1.2) using the extinction coefficient of SGLT3 (ε_{280}(SGLT3) = 1,482 M^{-1} cm^{-1}).

2.2.5.5.2 GFP-Trap binding of SGLT3

Harvested HEK293S GnT1$^-$-SGLT3 cells (2.1.14.2.1) were homogenized, solubilized and cell debris was removed as described in 2.2.5.5.1. The supernatant was then loaded on 500 µl GFP-Trap® Agarose (2.1.9), respectively 500 µl GFP-Trap® Magnetic Particles M-270 (2.1.9), both pre-equilibrated with 5 CV wash buffer (Table 2.22). The mixtures were then incubated under gentle agitation for 1 h at 4 °C. Then, the unbound material was removed and the beads were washed with 5 CV wash buffer (Table 2.22). Next, the beads were resuspended in 1x loading buffer (6x loading buffer (Table 2.11) mixed 1:5 (v/v) with wash buffer (Table 2.22)) and boiled for 5 min at 95 °C to detach the protein from the beads for further analysis.

Table 2.22: Buffers SGLT3 purification via GFP-Trap

	Composition
Wash buffer	20 mM Tris/HCl pH 8.0 150 mM NaCl 0.05% (w/v) /0.01% (w/v) DDM/CHS (2.1.8)

2.2.5.6 SMCT2 purification

The pelleted HEK293S GnT1$^-$ cells (2.1.14.2.1) expressing N-terminal 3x FLAG- and C-terminal mEGFP-tagged SMCT2 was resuspended in 5 ml solubilization buffer (Table 2.23) for 1 g cells, lysed with a Dounce homogenizer (2.1.1) and 1% (w/v) /0.1% (w/v) LMNG/CHS (2.1.8) was added to solubilize membranes under gentle stirring at 4 °C. After 2 h, the mixture was homogenized again via a Dounce homogenizer (2.1.1) and centrifuged (1 h, 70,000 *x g*, 4 °C, Ultracentrifuge Optima XPN-100 with rotor 45 Ti (2.1.1)) to remove not-solubilized cell components. 1 ml ANTI-FLAG® M2 Affinity Gel (2.1.9) was filled into a Pierce™ Disposable Column with polyethylene disc (2.1.3), washed with dd$H_2$0 and equilibrated with 5 CV wash buffer (Table 2.23). Then the supernatant was loaded onto the pre-equilibrated ANTI-FLAG® M2 Affinity Gel twice and the column washed with 10 CV wash buffer (Table 2.23) to remove unbound protein. Finally, SMCT2 was eluted with 7 CV elution buffer (Table 2.23) in 500 µl fractions. The presence of protein in the elution fractions is controlled by a Quick Bradford Assay (2.2.2.1.1). The positive fractions were pooled and concentrated via an Amicon® Ultra concentrator MWCO 50 kDa (2.1.3) to 50 µl for size exclusion chromatography (SEC). The protein sample was separated on a Superose 6 Increase 5/150 GL column (2.1.1) connected to an ÄKTA™ pure system (2.1.1, Software: UNICORN 7.8 (2.1.2)) at RT. The ÄKTA™ pure system and the column stored in 20% ethanol were washed with ddH_2O and pre-equilibrated with the SEC-buffer (Table 2.23) prior to the SEC run according to the manufacturer's advice. SEC was performed at a flow rate of 0.2 ml/min and fractions of 75 µl were collected. The elution of protein was traced by absorption at 280 nm. Fractions containing SMCT2 according to the absorption profile were pooled. At the end protein concentration was photometrically determined (2.2.2.1.2) using the extinction coefficient of SMCT2 (ε_{280}(SMCT2) = 1,661 M^{-1} cm^{-1}).

Table 2.23: Buffers SMCT2 purification

	Composition
Solubilization buffer	20 mM HEPES pH 7.0 150 mM NaCl 0.01 mg/ml DNAse I (2.1.10) 1 mM Pefabloc® SC (2.1.10) 0.5 µg/ml Pepstatin A (2.1.5) 2 µg/ml Leupeptin (2.1.5) 1 µg/ml Aprotinin (2.1.5)
Wash buffer	20 mM Tris/HCl pH 8.0 150 mM NaCl 0.02% (w/v) /0.002% (w/v) LMNG/CHS (2.1.8)
Elution buffer	20 mM Tris/HCl pH 8.0 150 mM NaCl 0.02% (w/v) /0.002% (w/v) LMNG/CHS (2.1.8) 200 µg/ml FLAG® peptide (2.1.3)
SEC-buffer	20 mM Tris/HCl pH 8.0 150 mM NaCl 0.02% (w/v) /0.002% (w/v) LMNG/CHS (2.1.8)

2.2.5.7 TPC2 purification

Harvested HEK293S GnT1$^-$-TPC2 cells (2.1.14.2.1) containing N-terminal His_8-tagged TPC2 were resuspended in 5 ml solubilization buffer (Table 2.24) per 1 g cells, homogenized with a Dounce homogenizer (2.1.1) and 1% (w/v) /0.2% (w/v) DDM/CHS (2.1.8) was added to solubilize membranes under gentle stirring at 4 °C. After 2 h further stirring the mixture was homogenized again via a Dounce homogenizer (2.1.1) and centrifuged (1 h, 20,000 *x g*, 4 °C, Ultracentrifuge Optima XPN-100 with rotor 45 Ti (2.1.1)) to remove not-solubilized cell components. 3 ml TALON® Metal Affinity resin (2.1.9) was washed with ddH_20 and equilibrated with 10 CV equilibration buffer (Table 2.24). The pre-equilibrated TALON® Metal Affinity resin was incubated with the supernatant under gentle agitation for 2 h at 4 °C and thereafter the mixture was loaded into a Pierce™ Disposable Column with polyethylene disc (2.1.3). After letting the resin set and discarding the flow-through, the column was washed with 10 CV wash buffer 1 (Table 2.24) and 10 CV wash buffer 2 (Table 2.24) to remove unbound protein. Finally, TPC2 was eluted with 5 CV elution buffer (Table 2.24) in 250 µl fractions. The presence of protein in the elution fractions is controlled by a Quick Bradford Assay (2.2.2.1.1). The positive fractions were pooled and concentrated via an Amicon® Ultra concentrator MWCO 100 kDa (2.1.3) to 50 µl for size exclusion chromatography (SEC). The protein sample was separated on a Superose 6 Increase 5/150 GL column (2.1.1) connected to an ÄKTA™ pure system (2.1.1, Software: UNICORN 7.8 (2.1.2)) at RT. The ÄKTA™ pure system and the column stored in 20% ethanol were washed with ddH_2O and pre-equilibrated with SEC-buffer (Table 2.24) prior to the SEC run according to the manufacturer's advice. SEC was performed at a flow rate of 0.2 ml/min and fractions of 75 µl were collected. The elution of protein was traced by absorption at 280 nm. Fractions containing TPC2 according to the absorption profile were pooled. The final protein concentration was photometrically determined (2.2.2.1.2) using the extinction coefficient (ε_{280}(TPC2) = 1,750 M^{-1} cm^{-1}).

Table 2.24: Buffers TPC2 purification

	Composition
Solubilization buffer	20 mM Tris/HCl pH 8.0 150 mM NaCl 0.01 mg/ml DNAse I (2.1.10) 1 mM Pefabloc® SC (2.1.10) 0.5 µg/ml Pepstatin A (2.1.5) 2 µg/ml Leupeptin (2.1.5) 1 µg/ml Aprotinin (2.1.5)
Equilibration buffer	20 mM Tris/HCl pH 8.0 150 mM NaCl 5 mM Imidazole pH 8.0 0.06% (w/v) GDN (2.1.8)
Wash buffer 1	20 mM Tris/HCl pH 8.0 150 mM NaCl 20 mM Imidazole pH 8.0 0.06% (w/v) GDN (2.1.8)
Wash buffer 2	20 mM Tris/HCl pH 8.0 150 mM NaCl 50 mM Imidazole pH 8.0 0.06% (w/v) GDN (2.1.8)
Elution buffer	20 mM Tris/HCl pH 8.0 150 mM NaCl 200 mM Imidazole pH 8.0 0.06% (w/v) GDN (2.1.8)
SEC-buffer	20 mM Tris/HCl pH 8.0 150 mM NaCl 0.06% (w/v) GDN (2.1.8)

2.2.6 Reconstitution methods

Unless noted otherwise, all reconstitution steps were performed at 4 °C.

2.2.6.1 Reconstitution of GPR into amphipol

Amphipols are amphipathic polymers that biochemically stabilize membrane proteins, thereby keep them soluble in a detergent-free environment and preserve the protein's functionality (1.2.1). In this work the amphipol A8-35 is used (Fig. 1.6).
After purification (2.2.5.1) the total amount of GPR (in mg) was calculated. Amphipol A8-35 (2.1.5) was added at a 3-fold excess to GPR (w/w) and the mixture was incubated on a rotary shaker for 4 h. In the meantime, Bio-Beads SM-2 (2.1.3) were activated by washing them with methanol followed by a wash with SEC buffer (Table 2.25). To remove the detergent approx. 30 mg activated Bio-Beads SM-2 (2.1.3) per

milliliter of protein-amphipol mixture were added and incubated on a rotary shaker o/N. The next day, biobeads were added in the same way as described and incubated again on a rotary shaker for 1 h. Subsequently, the Bio-Beads were removed and the sample was concentrated via an Amicon® Ultra concentrator MWCO 100 kDa (2.1.3) to 50 µl for size exclusion chromatography (SEC). The protein sample was fractionated on a Superose 6 Increase 5/150 GL column (2.1.1) connected to an ÄKTA™ pure system (2.1.1, Software: UNICORN 7.8 (2.1.2)) at RT. The ÄKTA™ pure system and the column stored in 20% ethanol were washed with ddH_2O and pre-equilibrated with the SEC-buffer (Table 2.25) prior to the SEC run according to the manufacturer's advice. SEC was performed at a flow rate of 0.2 ml/min and fractions of 75 µl were collected. The elution of protein was traced by absorption at 280 nm, 310 nm and 520 nm (*all-trans* retinal). Fractions containing GPR according to the absorption profile and red color were checked on successful reconstitution via SDS-Page (2.2.2.2). Those fractions showing positive evidence were pooled for further use.

Table 2.25: SEC buffer for reconstitution of GPR

	Composition
SEC-buffer	50mM HEPES pH7.5 100mM NaCl

2.2.6.2 Reconstitution of GPR into salipros

Salipros (1.2.2.2) are a form of nanodiscs (1.2.2), describing a membrane protein inserted into a discoidal lipid bilayer section stabilized by the scaffold protein Saposin A (Fig. 1.5d). Salipros enable to keep membrane proteins soluble in a detergent-free buffer and design a native like environment as the type of lipids added for reconstitution can be adopted to the respective membrane protein. Thereby, this reconstitution method is well-suited for functional, but also structural studies.
First the total amount of purified GPR (2.2.5.1) in mg was calculated. For reconstitution a membrane protein to lipid to Saposin A ratio of 1 : 3 : 8 (w/w) was used. 1 mg of purified GPR (2.2.5.1) was mixed with 3 mg POPC (2.1.11) and the mixture was incubated on a rotary shaker for 15 min at RT. Then 8 mg purified Saposin A (2.2.5.3) were added, and the mixture was incubated the same way for 30 min. Meanwhile, Bio-Beads SM-2 (2.1.3) were activated by washing with methanol followed by a wash with SEC buffer (Table 2.25). In addition, the total amount of detergent (in mg) in the mixture was determined. For detergent removal a 20-fold excess of activated Bio-Beads SM-2 (2.1.3) was added to the protein-lipid-Saposin A mixture in the following steps. In two steps, respectively 20% of the total Bio-Beads SM-2 amount was added and the mixture was incubated on a rotary shaker for 1 h at RT. Next, 40% of the total Bio-Beads SM-2 amount was added and the mixture was incubated on a rotary shaker o/N at 4 °C. Finally, the remaining 20% of activated Bio-Beads SM-2 (2.1.3) were added and the mixture was incubated on a rotary shaker for 1 h at RT. After removing the Bio-Beads, the sample was concentrated with an Amicon® Ultra concentrator MWCO 100 kDa (2.1.3) to 50 µl for size exclusion chromatography (SEC). The protein sample was separated on a Superose 6 Increase 5/150 GL column (2.1.1) connected to an ÄKTA™ pure system (2.1.1, Software: UNICORN 7.8 (2.1.2)) at RT. The ÄKTA™ pure system and the column stored in 20% ethanol were wash with ddH_2O and pre-equilibrated with the SEC-buffer (Table 2.25) prior to the SEC run according to the manufacturer's advice. SEC was performed at a flow rate of 0.2 ml/min and fractions of 75 µl were collected. The elution of protein was traced by absorption at 280 nm, 310 nm and 520 nm (*all-trans* retinal). Fractions containing GPR according to the absorption profile and red color were checked on successful reconstitution by SDS-Page (2.2.2.2). The fractions showing positive evidence were pooled for further analysis.

2.2.6.3 Reconstitution of SGLT3 into salipros

For reconstitution into salipros (1.2.2.2), SGLT3 was purified in DDM/CHS without the final SEC step (2.2.5.5.1) and the protein concentration was photometrically determined (2.2.2.1.2) using the extinction coefficient of SGLT3 (ε_{280}(SGLT3) = 1,482 M^{-1} cm^{-1}). 1 mg of purified SGLT3 (2.2.5.5.1) was mixed with 3 mg Brain Total Lipid Extract (2.1.11) and 8 mg Saposin A (2.2.5.3) as described for GPR (2.2.6.2). Also, the removal of detergent was performed as for GPR (2.2.6.2). The Bio-Beads were removed, and the mixture was further purified via the His_6-Tag of Saposin A to obtain SGLT3 reconstituted into salipros. Therefore, 1 ml Ni-NTA agarose (2.1.9) was washed with ddH_20 and equilibrated with 5 CV equilibration buffer (Table 2.26) and the sample was incubated with the pre-equilibrated Ni-NTA agarose under gentle agitation o/N at 4 °C. Thereafter the mixture was loaded into a Pierce™ Disposable Column with polyethylene disc (2.1.3). After the resin has set and the flow-through was discarded, the column was washed with 10 CV wash buffer 1 (Table 2.26) and 10 CV wash buffer 2 (Table 2.26) to remove unbound protein. Finally, SGLT3 in salipros was eluted with 5 CV elution buffer (Table 2.26) in 250 µl fractions. The presence of protein in the elution fractions is controlled by a Quick Bradford Assay (2.2.2.1.1). The positive fractions were pooled and concentrated with an Amicon® Ultra concentrator MWCO 100 kDa (2.1.3) to 50 µl for size exclusion chromatography (SEC). The protein sample was fractionated on a Superose 6 Increase 5/150 GL column (2.1.1) connected to an ÄKTA™ pure system (2.1.1, Software: UNICORN 7.8 (2.1.2)) at RT. The ÄKTA™ pure system and the column stored in 20% ethanol were washed with ddH_2O and pre-equilibrated with the SEC-buffer (Table 2.26) prior to the SEC run according to the manufacturer's advice. SEC was performed at a flow rate of 0.2 ml/min and fractions of 75 µl were collected. The elution of protein was traced by absorption at 280 nm. Fractions containing protein according to the absorption profile were checked on successful reconstitution via SDS-Page (2.2.2.2). Those fractions showing positive evidence were pooled for further use.

Table 2.26: Buffers for reconstitution of SGLT3 in salipros

	Composition
Equilibration buffer	20 mM Tris/HCl pH 8.0 150 mM NaCl 5 mM Imidazole pH 8.0
Wash buffer 1	20 mM Tris/HCl pH 8.0 150 mM NaCl 20 mM Imidazole pH 8.0
Wash buffer 2	20 mM Tris/HCl pH 8.0 150 mM NaCl 50 mM Imidazole pH 8.0
Elution buffer	20 mM Tris/HCl pH 8.0 150 mM NaCl 400 mM Imidazole pH 8.0
SEC-buffer	20 mM Tris/HCl pH 8.0 150 mM NaCl

2.2.7 Electron microscopy

2.2.7.1 Negative Stain

2.2.7.1.1 Preparation of uranyl acetate staining solution

Aqueous solutions of uranyl acetate (UAc) were used for negative staining of protein samples. Deionized ddH_2O was pre-warmed to 60 °C to improve solubility of the staining reagent. UAc powder was added to a final concentration of 2% (w/v) and dissolved by gentle stirring. Two to five drops of acetic acid were added to the UAc solution to improve solubility and stability. The final pH of the staining solution should be pH 4.0. Ready-made solutions were filtered through a Corning® syringe filter (2.1.3) to remove precipitates and stored at 4 °C in dark environment to prevent degradation.

2.2.7.1.2 Preparation of carbon films

Home-made continuous carbon films were used as sample support for negative staining. The carbon film was prepared by thermal evaporation in a Turbo Carbon Coater 208carbon (2.1.1). Therefore, a sheet of Hi-Grade Mica (2.1.3) was freshly cleaved with a razor blade to generate two clean and even surfaces. The Mica sheets were fixed on a glass slide, inserted to the carbon evaporator and the evaporator chamber was evacuated. The film was created on the Mica surface by evaporating material from a carbon rod (2.1.3) at a voltage of 2.6 V. The thickness of the generated films was adjusted to 10-15 nm by variation of the evaporation time. The films were left for settling o/N and stored dust-protected for further use.

2.2.7.1.3 Preparation of carbon-coated grids

Carbon-coated grids were used for negative staining of protein samples. A home-made floating device was used for coating. Freshly glow-discharged (Plasma Cleaner PDC-32G (2.1.1), Low Power setting 6.8 W, 30 sec) 400 mesh copper grids (2.1.3) were lined on a piece of filter paper, placed below water level (ddH_2O) in the floating device. The prepared carbon film (2.2.7.1.2) was floated off the Mica support on the water surface. By lowering the water level, the film was evenly applied to the grids. Carbon-coated grids were baked at 120 °C for at least 3 h.

2.2.7.1.4 Negative staining

Negative staining was used for quality control of both protein purification and reconstitution. UAc staining solution was centrifuged (30 min, 13,800 x g, RT; Heraeus Pico 17 centrifuge (2.1.1)) prior to usage. For negative staining, 3 µL of protein sample (concentration: 10-20 mAU according to SEC) were applied on a freshly glow-discharged, carbon coated grid (2.2.7.1.3) and incubated for 30 sec. After adsorption of the sample to the carbon film, the droplet was gently blotted away with filter paper from the edge of the grid. 3 µL of UAc staining solution (2.2.7.1.1) were applied immediately as a short washing step. Again, the droplet was blotted from the edge of the grid. 3 µL of UAc staining solution (2.2.7.1.1) were applied and incubated on the grid for 1 min for staining. The grid was blotted dry from the bottom and stored in a grid box for further investigation.

2.2.7.1.5 Negative stain image acquisition

For initial investigation of negatively stained samples (2.2.7.1.4), a CM12 transmission electron microscope (2.1.1) was used. Images were recorded at a 22,000x magnification. This setup was used to screen the protein samples on their quality, characterized mainly by particle size, aggregation, uniformity and shape.

2.2.7.2 SPA cryo-EM

2.2.7.2.1 Vitrification

Vitrification is the state-of-the-art preparation method for SPA cryo-EM and was established by 2017 Nobel laureate Jacques Dubochet and co-workers (Dubochet *et al.*, 1988). For vitrification, the protein solution is applied to a grid, blotted with a filter paper, and the remaining, thin layer of liquid is frozen rapidly in liquid ethane. This results in the proteins embedded in vitrified ice, since this fast freezing-process circumvents the formation of ice crystals in the sample. Artifacts caused by crystalline ice, or the presence of staining agents are thereby avoided, and the method is suitable to preserve the hydrated state of proteins, ensuring their structural and functional integrity for high-resolution imaging.
The SPA cryo-EM grids were prepared by applying 3.5 µl of protein sample to the holey carbon film of a fresh glow-discharged (PELCO easiGlow™ Glow Discharge Cleaning System (2.1.1), 15mA, 100 sec) Quantifoil® R1.2/1.3 300-mesh Cu grid (2.1.3). Right after, the grids were blotted with Filter paper 595 (2.1.3) for 5.0 - 6.0 s, with a blot force set to zero, under 100% humidity at 4 °C before being plunged into liquid ethane using a Mark IV Vitrobot (2.1.1). To obtain the agonist/antagonist-bound structures for TPC2, the protein sample was supplemented with the regarding agonist/ antagonist (Table 3.8) for 30 min on ice before vitrification. The prepared grids were transferred to a cryo-grid box and stored in liquid nitrogen until further usage.

2.2.7.2.2 Grid loading and data screening

To check the quality of the vitrified grids (2.2.7.2.1), they were clipped and loaded into a CRYO ARM™ 200 microscope (2.1.1). After initial microscope checks and beam alignment, a 'grid atlas' was created via SerialEM (2.1.2). This `grid atlas´ is a brief overview of the grid at 80x magnification. When holes of the carbon film were visible, test images were recorded at 60.000x magnification in random holes. In case, these images were showing well distributed, not-aggregated particles in various orientations, SPA data collection (2.2.7.2.3) was set up.

2.2.7.2.3 SPA Data collection

Micrographs of grids that passed the quality check (2.2.7.2.2) were acquired on a CRYO ARM™ 200 microscope (2.1.1) operated at 200 kV with a K2 Summit direct electron detector (2.1.1), using a slit width of 20 eV on an in-column Omega energy filter. The automatic data collection process is initiated, following the parameters set for multi-hole imaging pattern of 3 x 3. Images were recorded automatically using SerialEM script (2.1.2) in the nominal pixel size of 0.7891 Å. Due to operating properties, the actual pixel size differed between 0.7934 Å and 0.8141 Å in the TPC2 data sets (Table 3.9). The target defocus range was set from -0.5 µm to -2.5 µm. Each movie in was dose-fractionated to 47 frames under a dose rate of 5.22 e^-/pixel/s, with a total exposure time of 6.58 s, resulting in a total exposure dose of approx. 55 e^-/ $Å^2$. During image recording the quality of the movies was checked via cryoSPARC live (2.1.2) to validate if it is worth to continue data collection or optimize the microscope settings. Thereby, the main quality criteria

were the recognizability of secondary protein features in 2D classes and the presence of different orientations. In addition, data collection parameters like astigmatism, contrast transfer function (CTF) max resolution fit, defocus values and relative ice thickness were considered to judge the microscope performance and the grid quality.

2.2.7.2.4 Image processing

Analysis of SPA cryo-EM datasets was performed following the brief outline given below, using the indicated software packages and tools. The individual workflows are visualized in the supplements (7.). The pre-processing was mainly performed with RELION (2.1.2). After importing the movies, the movie frames were aligned using MotionCor2 in the patch mode 5 x 5 with the gain reference. Subsequently, the CTF was estimated using CTFFIND4 and micrographs with an estimated resolution beyond 8 Å and an astigmatism above 500 Å were excluded. Form a subset of the remaining micrographs particle coordinates were initially picked by LoG-based auto-picking in the diameter from 100-160 Å to generate templates via 2D classification for template picking in RELION (2.1.2). For datasets with the same protein, also templates from previous datasets were used for template picking. Incorrectly template picked particles like false positives or junk particles were discarded during several subsequent rounds of 2D classification in RELION (2.1.2) or cryoSPARC (2.1.2). The quality of 2D class averages was judged by the presence of well-defined secondary structure features. Also, the presence of different orientations of the particles in the dataset was considered during 2D classification. Based on the 2D classified particles, a 3D initial model was reconstructed in RELION (2.1.2). To investigate structural heterogeneity in the datasets, 3D classification in RELION (2.1.2) was performed. Particles contributing to low-resolution, featureless classes/volumes were again discarded. The remaining particles were 3D auto refined with C1 symmetry. CTF refinement was estimated to adjust each particle's defocus value and correct higher-order CTF terms (beam-tilt, trefoil, etc.) and Bayesian polishing was performed. All these steps were done with RELION (2.1.2). Additionally, for GPR in salipros, after 3D auto refine, a mask was created to remove the Saposin A density and the particles were post-processed in C1 symmetry. After transferring the polished particles to cryoSPARC (2.1.2) another round of 2D classification was performed, followed by ‘ab initial reconstruction’ or ‘hetero refinement’ into 2-4 classes. Again, particles contributing to low-resolution, featureless classes/volumes were again discarded. The final maps in C1 symmetry and the respective protein symmetry (C5 for GPR, C2 for TPC2) were generated via ‘non-uniform refinement’ with the CTF refinement for ‘per particle defocus’, ‘per group CTF parameter’ and ‘Ewald sphere correction’. For the validation of the quality of SPA cryo-EM density maps, the ‘gold-standard’ Fourier shell correlation (FSC) curve is essential. Therefore, two half-maps are independently generated and refined from two randomly split halves of the dataset. The quality of these maps is assessed based on the shape of their FSC, and the global resolution of the respective map was obtained according to the FSC = 0.143 cut-off criterion. Analysis of the local resolution distribution throughout the map was performed based on results generated with cryoSPARC (2.1.2). However, also a critical visual inspection of the density map in ChimeraX (2.1.2) was considered necessary to exclude reconstruction artifacts caused by e.g. too tight masking during refinement or post-processing.

2.2.7.2.5 Model building and validation

Model building was conducted in Coot (2.1.2). An existing suitable template (Table 2.27) was rigid-body-fitted into the cryo-EM density map and refined manually. Amino acid assignments were also confirmed by the clearly defined densities for bulky residues (Phe, Trp, Tyr, and Arg). Lipid molecules and ligands were added manually into unambiguously identified densities and adjusted. Ligand restraint files were created using eLBOW (Moriarty *et al.*, 2009; included in Phenix (2.1.2)). Real space model refinement (Afonine *et*

al., 2018a) and validation (Afonine *et al.*, 2018b) were performed in Phenix (2.1.2). Thereby, several adjustment-refinement cycles were performed, until satisfactory results could be obtained. Residues that are disordered were not modeled. Finally, the model was validated via the wwPDB Validation System (2.1.2). All figures were prepared using the software Chimera X (2.1.2).

Table 2.27: Templates for SPA cryo-EM model building

SPA cryo-EM map	Template
GPR in salipros	PDB: 7B03 (Hirschi *et al.*, 2020)
TPC2 (apo)	PDB: 6NQ1 (She *et al.*, 2019)
TPC2 supplemented with SGA-111	PDB: 6NQ1 (She *et al.*, 2019)
TPC2 supplemented with naringenin + $PI(3,5)P_2$	PDB: 6NQ0 (She *et al.*, 2019)

2.2.8 Functional studies

2.2.8.1 SSM-based electrophysiology

SSM-based electrophysiology is a technique used to electrically characterize membrane proteins such as transporters and ion channels. Unlike patch-clamp measurements, it does not require living cells. Instead, it relies on native or artificial membrane vesicles, such as proteoliposomes or membrane preparations from organelles, cells, or tissue samples (Schulz et al., 2008; Bazzone et al., 2022). These vesicles, containing the membrane protein of interest, are adsorbed onto the SSM, which consists of a lipid monolayer atop a thiolated gold-coated sensor chip. This results in stable adsorption of the added membranes to the SSM and the formation of a capacitively coupled compound membrane (Schulz et al., 2008; Bazzone et al., 2022). A substrate gradient, established by rapid solution exchange, serves as the primary driving force, with the transport of charged substrates or ions into the liposomes or vesicles generating a membrane potential (Schulz et al., 2008; Bazzone et al., 2022). The potential can be detected via capacitive coupling between the membrane and the SSM on the gold layer of the sensor. Once the membrane potential equals the chemical driving force, the transport process halts, explaining why any current measured with SSM-based electrophysiology is transient, while the peak current amplitude reflects the transporter activity under steady-state conditions (Bazzone et al., 2022). This technique offers new possibilities where conventional electrophysiology falls short, such as with transporters or ion channels from bacteria and intracellular compartments. Furthermore, its setup and automation render it suitable for drug screening (Schulz et al., 2008).

2.2.8.1.1 Plasma membrane purification

In this work plasma membrane fragments containing the membrane protein of interest were used for SSM-based electrophysiology. Therefore, SGLT3 was expressed (2.2.4.5) via HEK293S GnT1$^-$-SGLT3 cells (2.1.14.2.1) and the harvested cells were resuspended in 5 ml disruption buffer (Table 2.28) for 1 g cells. Then, cells were lysed by sonication (3x 1 min, 10% amplitude, pulse: 1 sec on / 1 sec off, 4 °C, Digital sonifier 250 (2.1.1)) followed by two low-spin centrifugation steps (i.: 15 min, 4,000 *x g*, 4 °C; ii.: 20 min, 6,000 *x g*, 4 °C; Avanti J-26 XP with rotor JLA-16.250 (2.1.1) was used for both steps) to remove cell debris.

Membranes were finally harvested via ultra-centrifugation (30 min, 100,000 *x g*, 4 °C, Ultracentrifuge Optima XPN-100 with rotor 70 Ti (2.1.1)). To separate the plasma membrane containing SGLT3 from cell organelle membranes, a sucrose gradient was used. The harvested membranes were resuspended in a total of 1 ml 10 mM Tris/HCl pH 7.5 and mixed with 70% (w/v) sucrose to a final sucrose concentration of 51% (w/v). The sucrose solutions were filled into an Open-Top Thinwall Ultra-Clear Tube (2.1.3) from the bottom to the top with the highest to the lowest concentrated solution (Fig. 2.1). Next the gradient was ultra-centrifuged (18 h, 100,000 *x g*, 4 °C, Ultracentrifuge Optima XPN-100 with rotor SW 41 Ti (2.1.1)) to generate separation of the different membranes by their density. Finally, the plasma membrane fraction, appearing between 31% (w/v) and 45% (w/v) sucrose, was extracted, mixed with 8 ml storing buffer (Table 2.28), ultra-centrifuged (30 min, 100,000 *x g*, 4 °C, Ultracentrifuge Optima XPN-100 with rotor 70 Ti (2.1.1)) to remove sucrose and resuspended in 1 ml storing buffer (Table 2.28). The presence of SGLT3 in the plasma membrane fractions was checked by western blot analysis (2.2.2.4), the concentration was determined via Bradford Assay (2.2.2.1.1) and the final concentration was adjusted to 10 mg/ml of plasma membranes in storing buffer (Table 2.28).

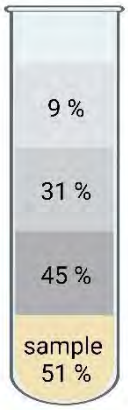

Figure 2.1: Sucrose gradient
Set up of the sucrose gradient used for plasma membrane purification. First the sample in 51% (w/v) sucrose was filled into the centrifugation tube. Then 9 ml of 45% (w/v) sucrose was added, followed by 9 ml of 31% (w/v) sucrose and topped by 9% (w/v) sucrose. Mixing of the different layers needs to be avoided. Figure created with BioRender (2.1.2).

Table 2.28: Buffers for plasma membrane preparation

	Composition
Disruption buffer	10 mM Tris/HCl pH 7.5 250 mM Sucrose 0.01 mg/ml DNAse I (2.1.10) 1 mM Pefabloc® SC (2.1.10) 0.5 µg/ml Pepstatin A (2.1.5) 2 µg/ml Leupeptin (2.1.5) 1 µg/ml Aprotinin (2.1.5)
Storing buffer	30 mM Tris/HCl pH 7.5 3 mM EDTA 1 mM EGTA 250 mM NMDG 150 mM KCl 0.2 mM DTT 5% (w/v) Glycerol

2.2.8.1.2 Sensor preparation

To investigate the function of the membrane proteins in the purified plasma membrane (2.2.8.1.1), they need to be loaded onto a SURFE^{2}R N1 Single Sensor (2.1.3) using the manufacturer's instructions. First 50 µl of 1-Octadeacethiol (0.5 mM in isopropanol) was loaded on a SURFE^{2}R N1 Single Sensor (2.1.3) and incubated for 2 h at RT. The remaining solution was shaken off and the sensor was washed three times with isopropanol and three times with ddH_2O. Then 3.5 µl Diphytanoyl-sn-glycero-3-phosphocholine (2.1.11) was added, immediately followed by 50 µl non-activating buffer (Table 2.29) to form the SSM. The plasma membrane was sonicated (3x 10 s; ultrasonic cleaner (2.1.1)) and 500 µg were added on the sensor. Finally, the sensor was put into a 50 ml falcon tube and centrifuged (30 min, 2,500 *x g*, 4 °C, Centrifuge 5810R (2.1.1)) to settle the plasma membrane on the SSM. Prior to use, the quality of the sensor was determined by verifying its conductance (approx. 5 nS) and capacity (15-30 nF) on the SURFE^{2}R N1 (2.1.1). When the quality of the sensor was approved, SSM-based electrophysiology of SGLT3 (2.2.8.1.3) was performed.

2.2.8.1.3 Imino sugar transport by SGLT3

The Na^+-dependent imino sugar (DNJ) transport of SGLT3 was investigated via SSM-based electrophysiology using a SURFE^{2}R N1 (2.1.1). A self-developed protocol with a measurement time of 2 s and flow rate of 200 µl/s was used. During measurement, the sensor was first rinsed with 400 µl non-activating buffer (Table 2.29), followed by 400 µl activating buffer (Table 2.29) and a final rinse with 400 µl non-activating buffer (Table 2.29). For each Na^+-concentration (0, 50, 100, 200, 300 mM) three measurements were accomplished. The mean values and standard deviations of the measured peak currents and the translocated charge during the rinse with activating buffer were determined, plotted against the respective Na^+-concentration (0, 50, 100, 200, 300 mM) and fitted with the Michaelis-Menten equation in Igor Pro (2.1.2) to generate the final graph.

Table 2.29: Buffers for SSM-based electrophysiology of SGLT3

	Composition
Non-activating buffer	30 mM Tris/HCl pH 7.5 3 mM EDTA 1 mM EGTA 50 µM DNJ (2.1.5) 0-300 mM Choline
Activating buffer	30 mM Tris/HCl pH 7.5 3 mM EDTA 1 mM EGTA 50 µM DNJ (2.1.5) 0-300 NaCl

2.2.8.2 Rab7A activity assay

To determine if the purified Rab7A (2.2.5.2) is functional, its activity was tested using a self-developed assay. Thereby, the pH-dependent absorbance intensity of pyranine at 455 nm (7.4.3) was used. As Rab7A is a GTPase (Lin-Moshier *et al.*, 2014), it hydrolyses GTP to GDP in aqueous solutions. This reaction creates a free phosphate group and a free proton, which leads to a decrease in pH of the solution. This decrease in pH can be made visible by adding pyranine to the solution, as the absorbance of pyranine is decreasing relative to the decrease of the pH (Fig. 2.2).
The assay was executed using a UV-Vis Spectrophotometer (2.1.1) to trace the absorption of pyranine at 455 nm under constant stirring over time. First Tris/HCl pH 7.5, $MgCl_2$, pyranine (2.1.5) and the required volume of ddH_2O (Table 2.30) were mixed in a Hellma® absorption cuvette (2.1.1). After 30 s measuring the absorbance at 455 nm, GTP or ATP (Table 2.30) was added, and the absorbance was traced for additional 470 s to ensure stable pyranine absorbance and to avoid artefacts of time-dependent ATP-/GTP-hydrolysis. Then Rab7A was quickly added and the pyranine absorbance at 455 nm was traced for additional 500 s. To investigate the activity of Rab7A, GTP was used. To verify that Rab7A is a GTPase, the same measurement was conducted with ATP. And to clarify, that time-dependent ATP-/GTP-hydrolysis in aqueous solutions does not influence the measurement, GTP without Rab7A was used as negative control. To visualize the results, the detected absorbance of pyranine at 455 nm was plotted against the respective time with Igor Pro (2.1.2).

Table 2.30: Setup Rab7A activity assay

	Concentration/Volume
Tris/HCl pH 7.5	5 mM
$MgCl_2$	2 mM
Pyranine (2.1.5)	0.05 mM
GTP/ATP (2.1.5)	2 mM
Rab7A (2.2.5.2)	10 µM
ddH_2O	fill up to 1 ml

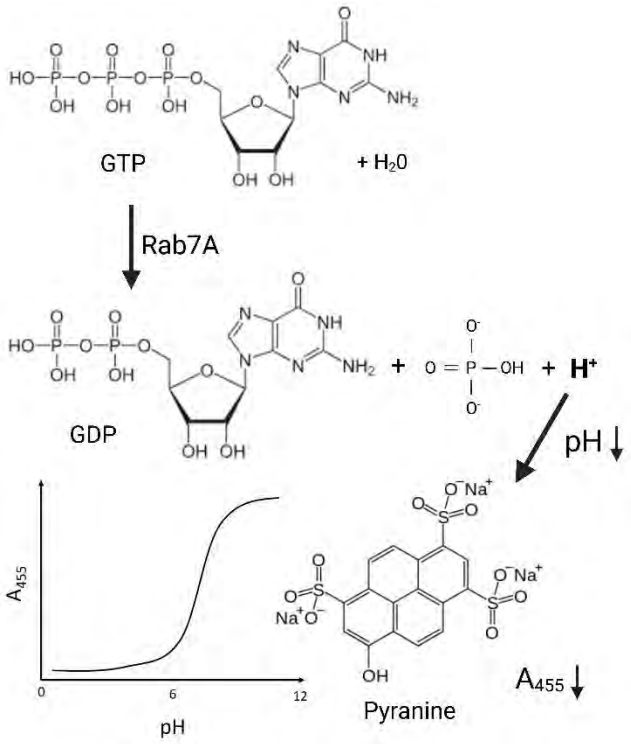

Figure 2.2: Rab7A activity assay
The hydrolysis of GTP in aqueous solutions catalyzed by Rab7A results in GDP, a free phosphate group and a proton. This reaction leads to a decrease of the pH in the surrounding solution. The pH change can be detected by the absorbance of pyranine at 455 nm, as pyranine is showing the best pH dependent absorbance at this wavelength (7.4.3). The image was created with BioRender (2.1.2).

3. Results

3.1 Expression and purification test of selected SLC5A family members

3.1.1 Na^+/glucose symporters SGLT1-6

Several constructs suitable for the Bac-Mam expression system were screened for transient expression in adherent HEK293S GnT1$^-$ cells for membrane localization, expression yield and detergent solubility by fluorescence microscopy and western blot analysis against either the GFP-tag or the respective affinity tag (Fig. 3.1). Only for the most promising candidate, pEGBacMam_SGLT2_3C_mEGFP_8xHis (2.1.14.2.2), expression was optimized by testing different transfection reagents, expression time and additives to boost protein expression (e.g. sodium butyrate or valproic acid) again in adherent cells (Table 3.1). Many expression conditions were screened, however SGLT2 always showed indications of in-cell aggregation (Fig. 3.2a). Solubilization efficiency of DDM/CHS (2.1.8) versus LMNG/CHS (2.1.8) was compared, with 2% (w/v) /0.4% (w/v) LMNG/CHS showing the best efficiency. Based on that, affinity purification of SGLT2 with Ni-NTA agarose was performed (2.2.5.4). Hereby, SGLT2 partly degraded, presumably during washing or elution steps (Fig. 3.2b). Consequently, the expression strategy was switched on the Bac-to-Bac® Expression System (Fig. 3.3).

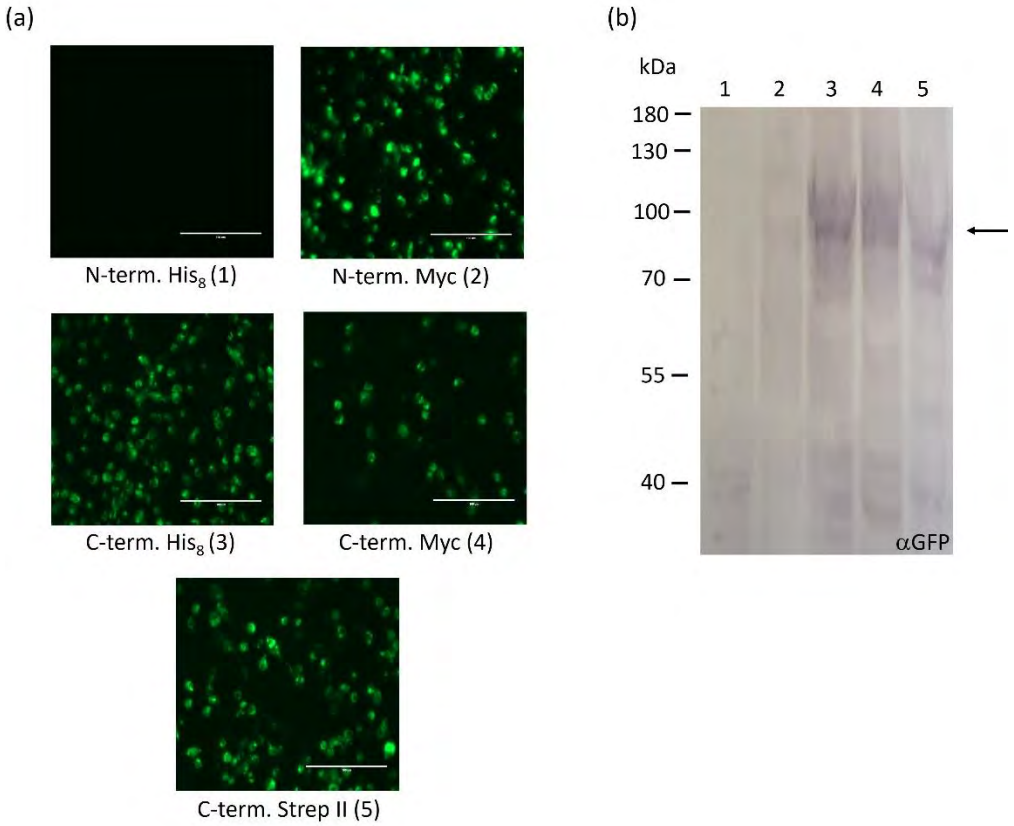

Figure 3.1: Expression check and purification of SGLT2
(a) Expression testing of five different pEGBacMam_SGLT2 constructs varying in affinity tags, visualized by the fluorescence of the mEGFP fusion protein **(b)** Western blot to check the SGLT2 expression of the different constructs. 20 µl of supernatant from lysed cells was applied to a 10% polyacrylamide gel (Table 2.10) and western blot analysis (2.2.2.4) was performed with a primary anti-GFP antibody (2.1.12). The thick bands below 100 kDa (arrow) represent SGLT2, indicating a good expression for all C-term. tagged constructs.

Table 3.1: Attempts for transient expression of SGLT2

Condition	Experimental work	Conclusion
Transfection reagents	Transfection (2.2.4.4.1) of pEGBacMam_SGLT2_3C_mEGFP_8xHis (2.1.14.2.2) in adherent HEK293S GnT1$^-$ cells (2.1.14.2.1) via jetPrime® (2.1.14.2.3), Lipofectamin™ 2000 (2.1.14.2.3) and PEIpro® (2.1.14.2.3) harvested after 48h followed by western blot analysis (2.2.2.4)	All reagents show SGLT2 expression, PEIpro® showed strongest expression PEIpro® is used for SGLT2 expression
Expression time	HEK293S GnT1$^-$ cells (2.1.14.2.1) transfected (2.2.4.4.1) with pEGBacMam_SGLT2_3C_mEGFP_8xHis (2.1.14.2.2) via PEIpro® (2.1.14.2.3), harvested 24h, 48h and 72h after transfection, followed by western blot analysis (2.2.2.4)	Weak expression after 24h, no difference in expression after 48h or 72h Harvest cells after 48h (in exceptional cases after 72h)
Additives to boost expression	HEK293S GnT1$^-$ cells (2.1.14.2.1) transfected (2.2.4.4.1) with pEGBacMam_SGLT2_3C_mEGFP_8xHis (2.1.14.2.2) via PEIpro® (2.1.14.2.3), adding 5/10 mM sodium butyrate (2.1.5) or 2/4/6 mM valproic acid (2.1.5) after 24h, harvested after 48h, followed by western blot analysis (2.2.2.4)	Neither sodium butyrate, nor valproic acid showed increased expression yield

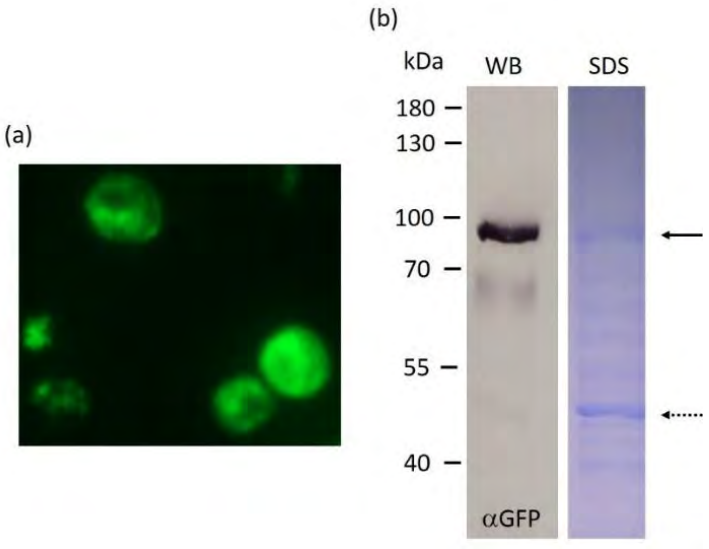

Figure 3.2: Expression and purification of SGLT2

(a) Expression of SGLT2 visualized by the fluorescence of the mEGFP fusion protein, indicating in-cell aggregation. **(b)** Western blot (WB) and SDS-Page (SDS) to check the SGLT2 purification in 2% (w/v) /0.4% (w/v) LMNG/CHS. 20 µl of an elution fraction was applied to a 10% polyacrylamide gel (Table 2.10). Western blot analysis (2.2.2.4) was performed with a primary anti-GFP antibody (2.1.12). The bands below 100 kDa (arrow) represent SGLT2 and the bands below 55 kDa.

The Bac-to-Bac® Expression System (Fig. 3.3) is an efficient system to generate baculovirus for high-level expression of recombinant proteins. Following the manufacturer´s protocol (including the troubleshooting protocol) was only partially successful for the pEGBacMam_SGLT2_3C_mEGFP_8xHis vector (Table 3.2). Although Sf9 cells showed GFP-fluorescence after transfection with bacmid DNA, virus production was neither detected by lysed Sf9 cells nor viral titer determination for SGLT2.

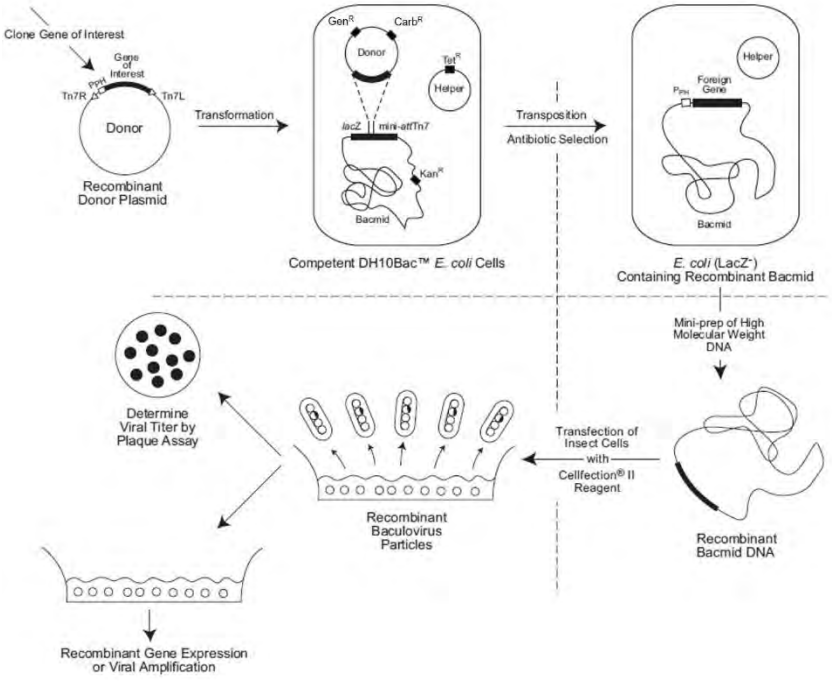

Figure 3.3: The Bac-to-Bac® Expression System
Here pEGBacMam_SGLT2_3C_mEGFP_8xHis (2.1.14.2.2) was used as donor plasmid. After transfection into DH10Bac™ *E. coli* cells the GOI is inserted into the bacmid DNA and cells with successful transposition are cultivated under antibiotic selection. Afterwards, the recombinant bacmid DNA is isolated and Sf9 cells are transfected with this DNA via Cellfectin™ II. Finally, the insect cells produce recombinant baculovirus particles that can be used for gene expression or viral amplification. Figure is derived from Thermo Fisher Scientific Inc., Waltham (USA).

Table 3.2: Establishing the Bac-to-Bac® Expression System

Step	Experimental work	Conclusion
Production of recombinant bacmid DNA	Transformation of DH10Bac™ *E. coli* cells (2.1.14.1.1) with pEGBacMam_SGLT2_3C_mEGFP_8xHis (2.1.14.2.2) and DNA extraction via isopropanol precipitation	Transformation and transposition were successful Low amount of recombinant bacmid DNA after extraction
Production of recombinant baculovirus	Transfection of Sf9 cells (2.1.14.2.1) with Cellfectin™ II (2.1.14.2.3)	*Sf9* cells did not produce baculovirus: no fluorescence and no lysis of Sf9 cells 72 h after transfection

Other members of the SLC5 family were screened on expression under similar conditions. SGLT1, SGLT3, SGLT4, SGLT5 and SGLT6 were cloned into pDEST-CMV-3xFLAG-gateway-mEGFP vector (2.1.14.2.2) via Gateway cloning (2.2.1.5) and the proteins were transiently expressed (2.2.4.4.1; PEIpro® (2.1.14.2.3)) in adherent HEK293S GnT1$^-$ cells (2.1.14.2.1). Protein expression was quantified via mEGFP-fluorescence (Fig. 3.4a) and western blot analysis (Fig. 3.4b). SGLT1, SGLT3, SGLT4 and SGLT6 showed strong expression while SGLT5 expressed at lower levels. SGLT3 showed highest expression evaluated from fluorescence microscopy. Based on these results and its high sequence identity with SGLT2 (Fig. 1.8a), SGLT3 was chosen for further studies.

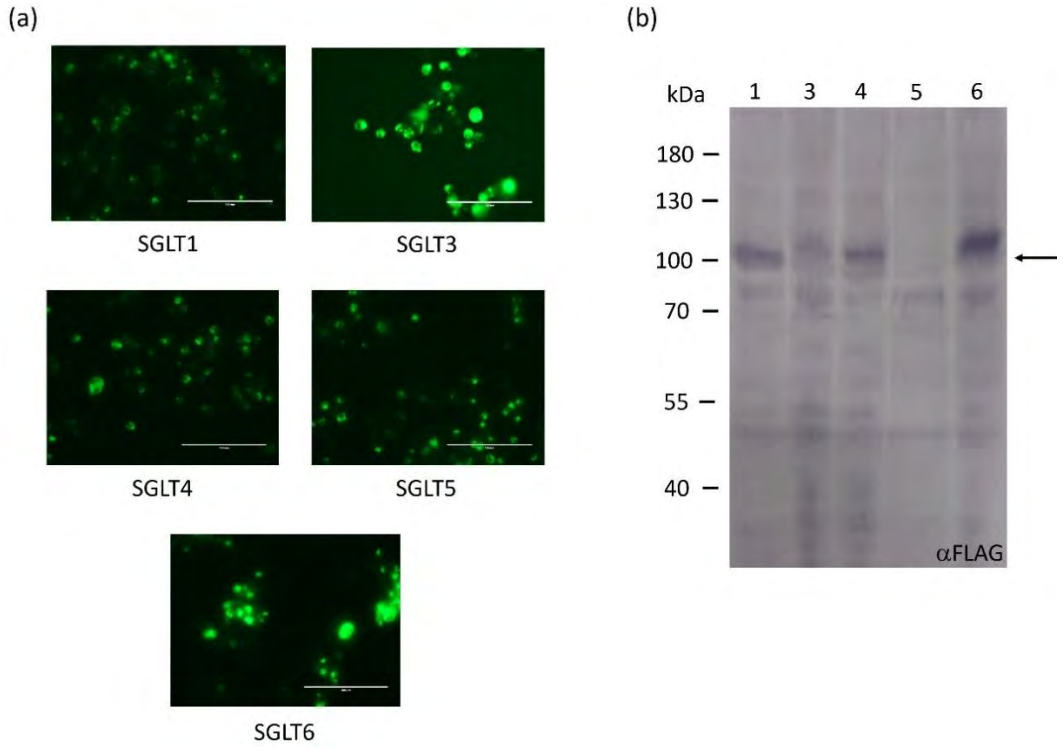

Figure 3.4: Expression of SGLT isoforms
(a) Expression of the SGLT isoforms visualized by the fluorescence of the mEGFP fusion protein. SGLT3 and SGLT6 showed strongest fluorescence. **(b)** Western blot to check expression of SGLTs. 20 µl of supernatant from lysed cells was applied to a 10% polyacrylamide gel (Table 2.10) and western blot analysis (2.2.2.4) was performed with a primary anti-FLAG antibody (2.1.12). The thick bands at 100 kDa (arrow) represent the SGLTs, indicating a good expression for SGLT1, SGLT3, SGLT4 and SGLT6.

As SGLT3 also showed tendencies for in in-cell aggregation in transient expression (Fig. 3.5a), a stable cell line HEK293S GnT1$^-$-SGLT3 (2.1.14.2.1) was produced using the lentivirus transfection system (Elegheert *et al.*, 2018) by our cooperation partner Marko Roblek (ISTA). The construct comprised a N-terminal StrepII-tag followed by a mEGFP and a Thrombin cleavage site (7.1.3), and a doxycycline-inducible promotor for SGLT3 expression. In suspension cells (Table 3.3), a high protein yields (Fig. 3.5b) of SGLT3 localized in the membrane was detected (Fig. 3.5a).

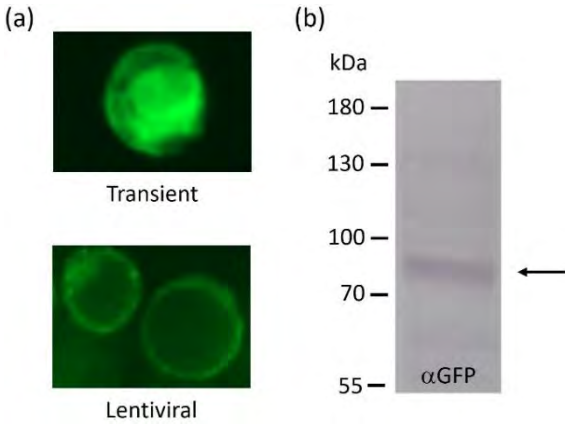

Figure 3.5: Expression of SGLT3
(a) Expression of SGLT3 via transient transfection (left) and lentiviral stable cell line (right) visualized by the fluorescence of the mEGFP fusion protein, indicating in-cell aggregation by transient expression and proper membrane localization in lentiviral expression. **(b)** Western blot analysis of SGLT3 expression via stable cell line (2.2.4.5) using HEK293S GnT1$^-$-SGLT3 cells (2.1.14.2.1). 20 µl of supernatant from lysed cells were applied to a 10% polyacrylamide gel (Table 2.10) and western blot analysis (2.2.2.4) was performed with a primary anti-GFP antibody (2.1.12). The band below 100 kDa (arrow) represents SGLT3, indicating high-yield protein expression.

Table 3.3: Attempts for expression of SGLT3 via lentiviral stable cell line

Condition	Experimental work	Conclusion
Amount of inducing reagent	Induction of SGLT3 expression in HEK293S GnT1$^-$-SGLT3 cells (2.1.14.2.1) via 0.5/1/2/3 or 4 mg/ml doxycycline (2.1.5), harvested 48 h after induction, followed by western blot analysis (2.2.2.4)	1 mg/ml doxycycline gives best result regarding protein quantity and cell death
Growth time	HEK293S GnT1$^-$-SGLT3 cells (2.1.14.2.1) induced with 1 mg/ml doxycycline (2.1.5), harvested 24h, 48h and 72h after induction, followed by western blot analysis (2.2.2.4)	Weak expression after 24h, no difference in expression after 48h or 72h Harvest cells after 48h (in exceptional cases after 72h)
Additives to boost expression	HEK293S GnT1$^-$-SGLT3 cells (2.1.14.2.1) induced with 1 mg/ml doxycycline (2.1.5), adding 5/10 mM sodium butyrate (2.1.5) or 2/4/6 mM valproic acid (2.1.5) 24h after induction, harvested after 48h, followed by western blot analysis (2.2.2.4)	No increase in protein yield by addition of sodium butyrate nor valproic acid No use of additives

3.1.2 Preliminary SPA cryo-EM analysis of SGLT3 in detergent and salipros

HEK293S GnT1$^-$-SGLT3 cells (2.1.14.2.1) were solubilized with 1% (w/v) /0.2% (w/v) DDM/CHS and purified via Strep-Tactin-affinity chromatography (2.2.5.5.1) using the Strep-Tactin® MacroPrep® resin (2.1.9) and 0.05% (w/v) /0.01% (w/v) DDM/CHS in all purification buffers (Fig. 3.6a,b,c). Remaining impurities were further characterized via mass spectroscopy (Fig. 3.6c) by Dr. Astrid Bruckmann (University of Regensburg, Germany) and identified as carboxylases containing a biotin acceptor domain that also binds Strep-Tactin resin (Fig. 3.6c; Pos *et al.*, 1994). An alternative GFP-trap purification (2.2.5.5.2) using the N-terminal mEGFP-tag and two different GFP-Trap resins was also not successful (Fig. 3.6d). However, SGLT3 in DDM/CHS was vitrified on Quantifoil® R1.2/1.3 300-mesh Cu grids (2.1.3; blotting time: 6.0 s) as the impurities could be excluded in 2D classification. 2D-classes were blurry without showing any protein features (Fig. 3.6e), most likely originating from the detergent micelle surrounding the protein. Because of this, reconstitution of purified SGLT3 into salipros (2.2.6.3), to remove the disturbing detergent, was tested.

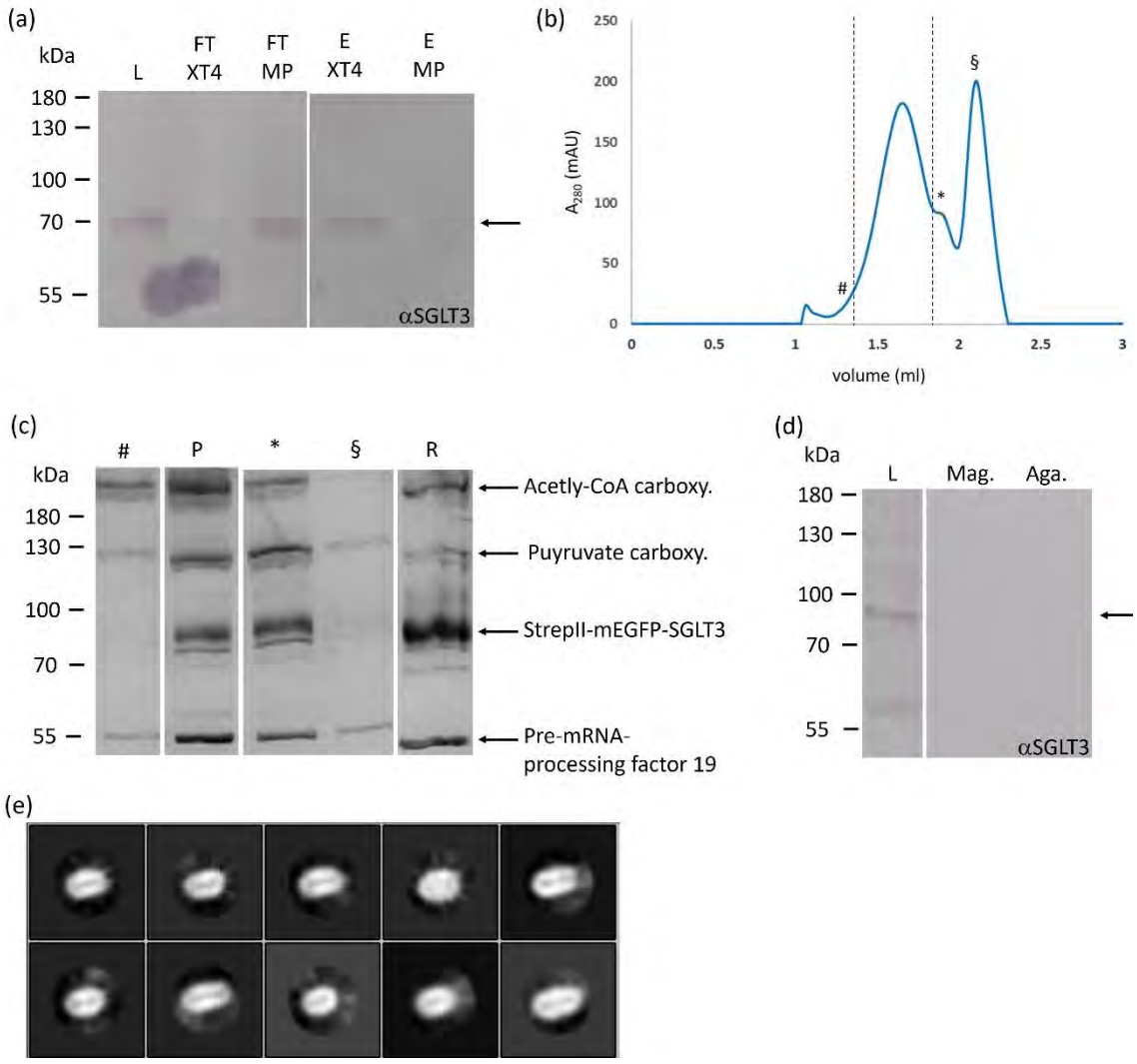

Figure 3.6: Purification of SGLT3 in DDM/CHS

(a) Western blot analysis of SGLT3 purification via Strep-Tactin®XT 4Flow® resin (XT4; 2.1.9) and Strep-Tactin® MacroPrep® resin (MP; 2.1.9). 20 µl of sample were applied to a 10% polyacrylamide gel (Table 2.10) and western blot analysis (2.2.2.4) was performed with a primary anti-SGLT3 antibody (2.1.12). The band at 70 kDa (arrow) represents SGLT3, showing successful purification with XT4, while SGLT3 did not bind to MP. L: load; FT: flow through; E: elution. **(b)** SEC elution profile of SGLT3 purification (2.2.5.5.1). The absorbance at 280 nm is plotted against the elution volume. A Superose 6 Increase 5/150 GL column (2.1.1) was used. The fractions between the dotted lines (first peak) were pooled for further use. #: fraction before pooled fractions; *: shoulder after first peak; §: second peak. **(c)** Silver stained SDS-Page of SEC fractions. 10 µl of sample was loaded on a 10% polyacrylamide gel (Table 2.10) and silver stained (2.2.2.3) for protein detection, showing impurities in all SEC fractions as well as on the resin after elution. The single bands were characterized via mass spectroscopy by Dr. Astrid Bruckmann (University of Regensburg, Germany). #: fraction before pooled fractions; P: polled main peak fractions; *: shoulder after first peak; §: second peak; R: XT4 flow resin after elution. **(d)** Western blot analysis of the GFP-trap purification (2.2.5.5.2). 10 µl of the samples were applied to a 10% polyacrylamide gel (Table 2.10) and western blot analysis (2.2.2.4) was performed with a primary anti-SGLT3 antibody (2.1.12). The band above 70 kDa (arrow) represents SGLT3, showing no binding of StrepII-mEGFP-tagged SGLT3 to the two different GFP-Trap resins. L: fraction loaded onto the GFP-trap resins; Mag: sample removed from GFP-Trap® Magnetic Particles M-270 (2.1.9). Aga: sample removed from GFP-Trap® Agarose (2.1.9). **(e)** SPA cryo-EM 2D classes of SGLT3 purified in DDM/CHS after processing (7.1.4) in RELION (2.1.2).

SGLT3 was reconstituted together with Brain Total Lipid Extract (2.1.11) in salipros (2.2.6.3). SGLT3 was successfully purified in DDM/CHS and eluted from the Ni-NTA resin after reconstitution in Saposin A (Fig. 3.7a). SEC runs revealed a main peak containing reconstituted SGLT3 (Fig. 3.7b,c,d) . Negative stain images (2.2.7.1) showed a homogenous particle size (Fig. 3.7e), indicating a successful purification and reconstitution of small quantities of SGLT3 in salipros.

SGLT3 in salipro will be investigated by SPA cryo-EM in future, however, this investigation was no longer pursued for several reasons. Firstly, a 3D structure of SGLT2 and SGLT1 was published in 2022 (Niu *et al.*, 2022; Han *et al.*, 2022). Second, while optimizing the cell culture conditions for SLC5A remained very challenging, expression and purification of TPC2 was more successful and the focus of the thesis was shifted to TPC2 structure analysis (3.3).

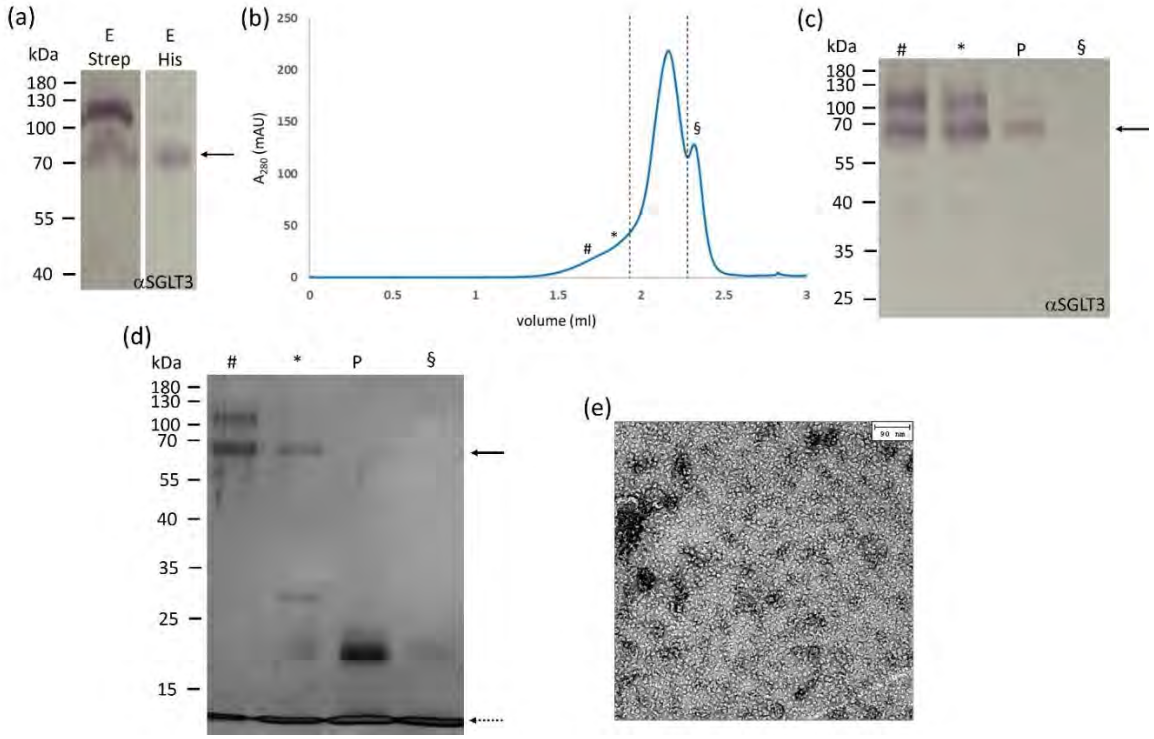

Figure 3.7: Reconstitution of SGLT3 in salipros

(a) Western blot analysis of affinity chromatography elution fractions. 20 µl of elution fractions were applied to a 10% polyacrylamide gel (Table 2.10) and western blot analysis (2.2.2.4) was performed with a primary anti-SGLT3 antibody (2.1.12). The band above 70 kDa (arrow) represents SGLT3, showing successful purification via Strep-Tactin-affinity chromatography in 1% (w/v) /0.2% (w/v) DDM/CHS (E Strep) and elution from Ni-NTA resin after reconstitution in salipros (E His). **(b)** SEC elution profile of SGLT3 reconstituted in salipros (2.2.6.3). The absorbance at 280 nm is plotted against the elution volume. A Superose 6 Increase 5/150 GL column (2.1.1) was used. The fractions between the dotted lines (first peak) were pooled. # and *: fractions before main peak; §: shoulder after main peak. **(c)** Western blot analysis of the SEC. 10 µl of the fractions were applied to a 10% polyacrylamide gel (Table 2.10) and western blot analysis (2.2.2.4) was performed with a primary anti-SGLT3 antibody (2.1.12). The band at 70 kDa (arrow) represents SGLT3, showing elution of SGLT3 mainly in the fractions before the main peak, as well as little amounts in the main peak. # and *: fractions before main peak; P: polled main peak fractions; §: shoulder after main peak. **(d)** Silver stained SDS-Page of SEC fractions. 10 µl of sample was loaded on a 10% polyacrylamide gel (Table 2.10) and silver stained (2.2.2.3) for protein detection, showing that the fractions before the main peak contain SGLT3 (below 70 kDa (arrow)), while the peak fraction consist of a smaller, unknown protein. All fractions contain Saposin A (dotted arrow). # and *: fractions before main peak; P: pooled main peak fractions; §: shoulder after main peak. **(e)** Negative stain image (2.2.7.1) of SGLT3 reconstituted in salipros (fraction *), showing a homogenous particle size.

3.1.3 Transport of imino sugars by SGLT3 and the SGLT3E457Q variant

SGLT3 is characterized as glucose sensor (Diez-Sampedro *et al.*, 2003) and imino sugar transporter (Voss *et al.*, 2007). To study the Na^+-dependent transport of imino sugars of SGLT3 via SSM-based electrophysiology, the protein was expressed in HEK293S GnT1$^-$-SGLT3 (2.1.14.2.1), followed by membrane preparation via sucrose gradient (2.2.8.1.1). The obtained fractions (Fig. 3.8a) were analyzed by western blot analysis (Fig. 3.8b; 2.2.2.4), and the fraction containing SGLT3 was used for sensor preparation (2.2.8.1.2). SSM-measurements (2.2.8.1.3) were performed with 50 µM of the imino sugar 1-Deoxynojirimycin (DNJ; 2.1.5) using 0-300 mM NaCl in the activating buffer.

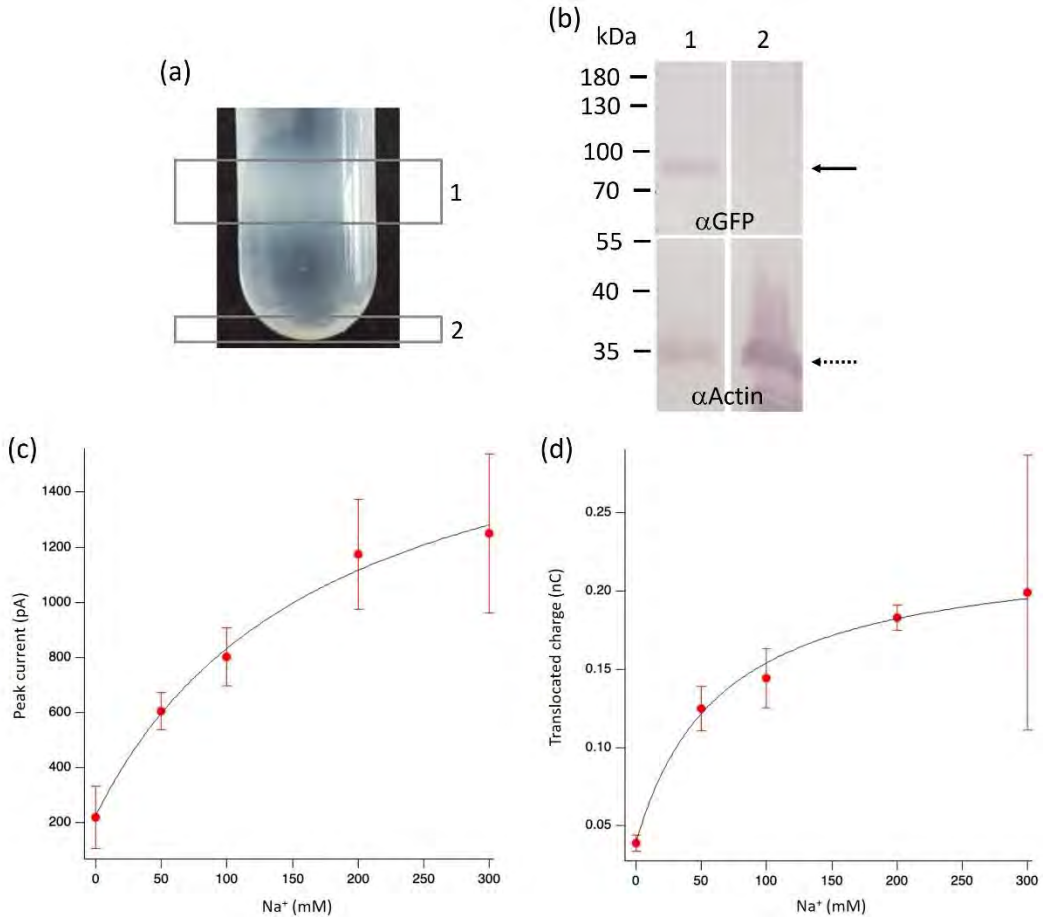

Figure 3.8: Transport of 1-Deoxynojirimycin by SGLT3

(a) Sucrose gradient of HEK293S GnT1$^-$ membranes expressing SGLT3. Two fractions occurred after centrifugation, one between 31% and 45% sucrose (1) and the second below 45% sucrose (2). **(b)** Western blot analysis of the sucrose gradient fractions. 20 µl of sample were applied to a 10% polyacrylamide gel (Table 2.10) and western blot analysis (2.2.2.4) was performed with a primary anti-GFP antibody (2.1.12), as well as a primary anti-Actin antibody (2.1.12) for loading control. The band below 100 kDa (arrow) represents SGLT3, showing that fraction 1 contains SGLT3, while fraction two shows no signal for SGLT3. The band at 35 kDa (dotted arrow) represents Actin, confirming proper sample application for western blot analysis. **(c)** Peak currents of Na^+-dependent transport of DNJ (50 µM) recorded on a 3 mm sensor plotted against the used Na^+-concentrations of 0-300 mM. To generate the final graph, the measured values were fitted with the Michaelis-Menten equation. **(d)** Integral of the measured currents of Na^+-dependent transport of DNJ (50 µM) recorded on a 3 mm sensor plotted against the used Na^+-concentrations of 0-300 mM. To generate the final graph, the measured values were fitted with the Michaelis-Menten model in Igor Pro (2.1.2).

Hereby, preliminary saturation-kinetics for Na^+-dependent transport of DNJ by SGLT3 were observed (Fig. 3.8c,d). We observed deviations in the peak current and translocated charge in duplicate measurements. Moreover, a negative control with membranes from HEK293S GnT1$^-$ cells not expressing SGLT3 is missing. Nevertheless, the data indicate that SGLT3 transports the imino sugar DNJ and that SGLT3 (2.1.14.2.1), but additional measurements are required.

The point mutation E457Q converts SGLT3 from a glucose sensor (Diez-Sampedro *et al.*, 2003) facilitating transport of imino sugars (Voss *et al.*, 2007) into a glucose transporter similar to SGLT1 (Bianchi L. & Díez-Sampedro A., 2010). To investigate sugar transport in SGLT3_E457Q, expression was induced by transient transfection in adherent HEK293S GnT1$^-$ cells (Fig. 3.9a,b), using a pDEST-CMV-3xFLAG-SGLT3_E457Q-EGFP vector (2.1.14.2.2). Similar results to the SGLT3 wt were obtained in suspension cells regarding membrane localization of the protein in the plasma membrane (Fig. 3.9c) and the protein yield (Fig. 3.9d).

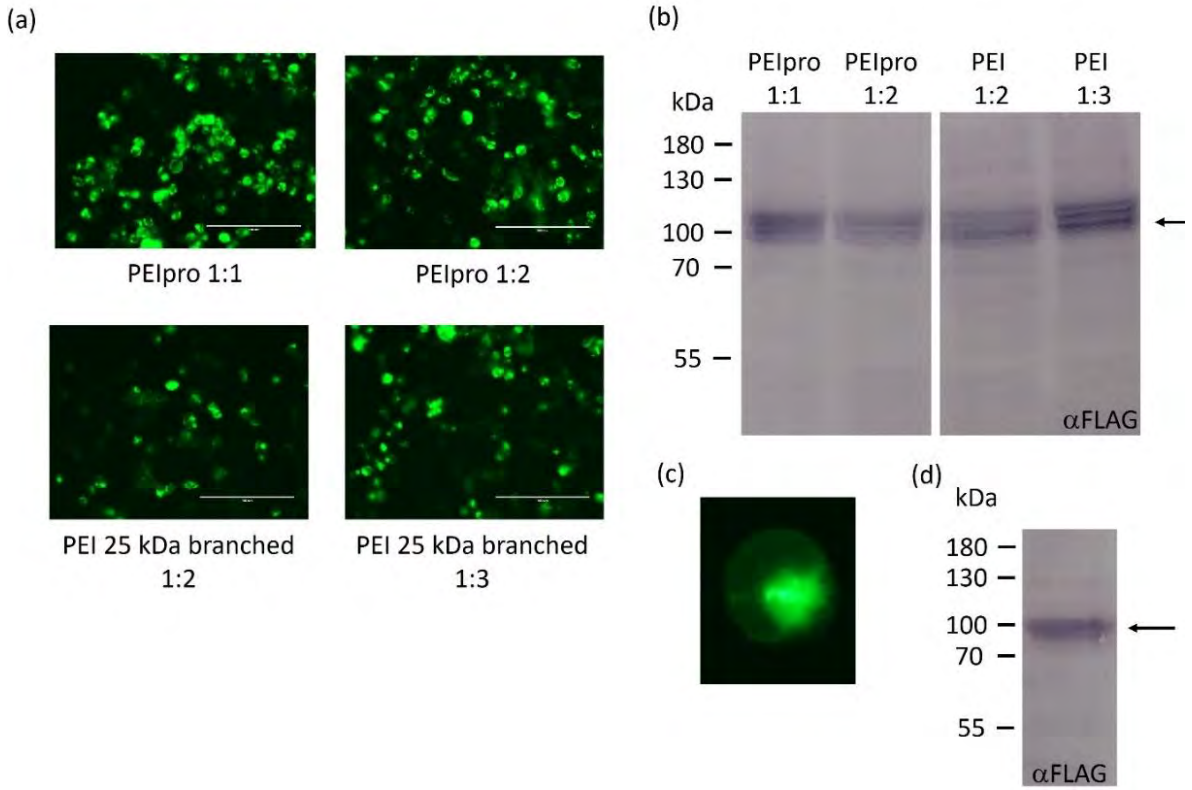

Figure 3.9: Expression of SGLT3_E457Q

(a) Expression test of SGLT3-E457Q via transient transfection of adherent HEK293S GnT1$^-$ cells (2.1.14.2.1) using PEIpro® (2.1.14.2.3) and PEI 25 kDa branched (2.1.14.2.3) in different DNA:PEI ratios, visualized by the fluorescence of the mEGFP fusion protein, indicating expression for all four approaches. **(b)** Western blot analysis of SGLT3_E457Q expression test. 20 µl of supernatant from lysed cells were applied to a 10% polyacrylamide gel (Table 2.10) and western blot analysis (2.2.2.4) was performed with a primary anti-FLAG antibody (2.1.12). The band at 100 kDa (arrow) represents SGLT3_E457Q, with the highest yield for PEI 25 kDa branched (2.1.14.2.3) in a DNA:PEI ratio of 1:3 (w/w). **(c)** Expression of SGLT3_E457Q in suspension HEK293S GnT1$^-$ cells via transient transfection with PEI 25 kDa branched (2.1.14.2.3) in a DNA:PEI ratio of 1:3 (w/w), visualized by the fluorescence of the mEGFP fusion protein, indicating little in-cell aggregation, but also proper membrane localization of the protein. **(d)** Western blot analysis of SGLT3_E457Q expression in suspension cells via transient transfection with PEI 25 kDa branched (2.1.14.2.3) in a DNA:PEI ratio of 1:3 (w/w). 20 µl of supernatant from lysed cells were applied to a 10% polyacrylamide gel (Table 2.10) and western blot analysis (2.2.2.4) was performed with a primary anti-FLAG antibody (2.1.12). The band at 100 kDa (arrow) represents SGLT3_E457Q, indicating a high-yield protein expression.

SGLT3 wt and SGLT3_E457Q will be investigated by SSM-based electrophysiology in future. Thereby, the transport of other imino sugars and glucose are of interest. In addition, sugar binding can be addressed as already done for SGLT1 (Bazzone et al., 2022). Liposomes with defined lipid composition can be used to characterize the influence of the lipid environment on the protein function. Revealing more precise insight into substrate specificity of SGLT3 can help to develop new imino sugars usable as Type II diabetes mellitus drugs. However, this investigation was no longer pursued within this thesis due to the focus on TPC2 structure analysis (3.3).

3.1.4 Expression and purification of SMCT2

The other group of the SLC5A family besides the SGLTs investigated in this work are the sodium-coupled monocarboxylate transporters (SMCTs). Because the structure of human SMCT1 is already solved to 3.5 Å (Han *et al.*, 2022), the focus was on human SMCT2.

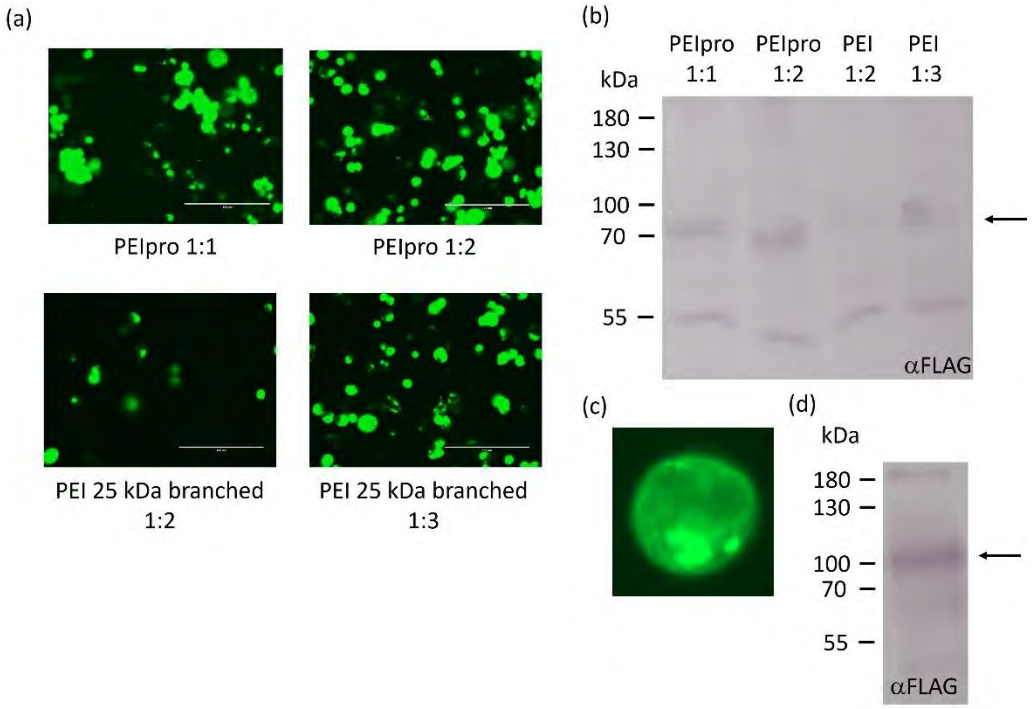

Figure 3.10: Expression of SMCT2
(a) Expression test of SMCT2 via transient transfection of adherent HEK293S GnT1$^-$ cells using PEIpro® (2.1.14.2.3) and PEI 25 kDa branched (2.1.14.2.3) in different DNA:PEI ratios, visualized by the fluorescence of the mEGFP fusion protein, indicating expression for all four approaches. **(b)** Western blot analysis of SMCT2 expression test. 20 µl of supernatant from lysed cells were applied to a 10% polyacrylamide gel (Table 2.10) and western blot analysis (2.2.2.4) was performed with a primary anti-FLAG antibody (2.1.12). The band below 100 kDa (arrow) represents SMCT2, with the highest yield for PEIpro® (2.1.14.2.3) in a DNA:PEI ratio of 1:2 (w/w). **(c)** Expression of SMCT2 in suspension HEK293S GnT1$^-$ cells via transient transfection with PEI 25 kDa branched (2.1.14.2.3) in a DNA:PEI ratio of 1:3 (w/w), visualized by the fluorescence of the mEGFP fusion protein, indicating in-cell aggregation, but also membrane localization of the protein. **(d)** Western blot analysis of SMCT2 expression in suspension cells via transient transfection with PEI 25 kDa branched (2.1.14.2.3) in a DNA:PEI ratio of 1:3 (w/w). 20 µl of supernatant from lysed cells were applied to a 10% polyacrylamide gel (Table 2.10) and western blot analysis (2.2.2.4) was performed with a primary anti-FLAG antibody (2.1.12). The band at 100 kDa (arrow) represents SMCT2, indicating a high-yield protein expression.

For protein production SMCT2 was cloned into an expression vector via Gateway cloning (2.2.1.5) resulting in pDEST-CMV-3xFLAG-SMCT2-mEGFP (2.1.14.2.2). After validation of successful cloning by DNA-sequencing (2.2.1.4), expression in adherent HEK293S GnT1$^-$ cells (2.1.14.2.1) was established (Fig. 3.10a,b), showing best expression of SMCT2 by transient transfection via PEIpro® (2.1.14.2.3) in a DNA:PEI ratio of 1:2 (w/w). Due to cost reasons and the fact that 25 kDa branched (2.1.14.2.3) using a DNA:PEI ratio of 1:3 (w/w) and 1 mg DNA per 10^6 cells also showed good results (Fig. 3.10a,b), this approach was transferred to expression in suspension cells where it showed tendencies of in-cell aggregation combined with membrane localization of the protein in the plasma membrane (Fig. 3.10c), but a sufficient protein yield (Fig. 3.10d). First purification tests were based on the method used for SMCT1 (Han *et al.*, 2022). After solubilization in 1% (w/v) /0.2% (w/v) LMNG/CHS (2.1.8) the target protein was purified via its N-term. FLAG-tag using ANTI-FLAG® M2 Affinity Gel (2.1.9), followed by a final SEC on a Superose 6 Increase 5/150 GL column (2.1.1). While western blot analysis (2.2.2.4) of the SEC run confirmed the presence of SMCT2 after purification (Fig 3.11b), silver stained SDS-Page (2.2.2.3) revealed impurities and low SMCT yields (Fig 3.11c) and negative stain images of the SEC peak containing the most SMCT2 showed a heterogenous particle size combined with aggregations (Fig. 3.11d).

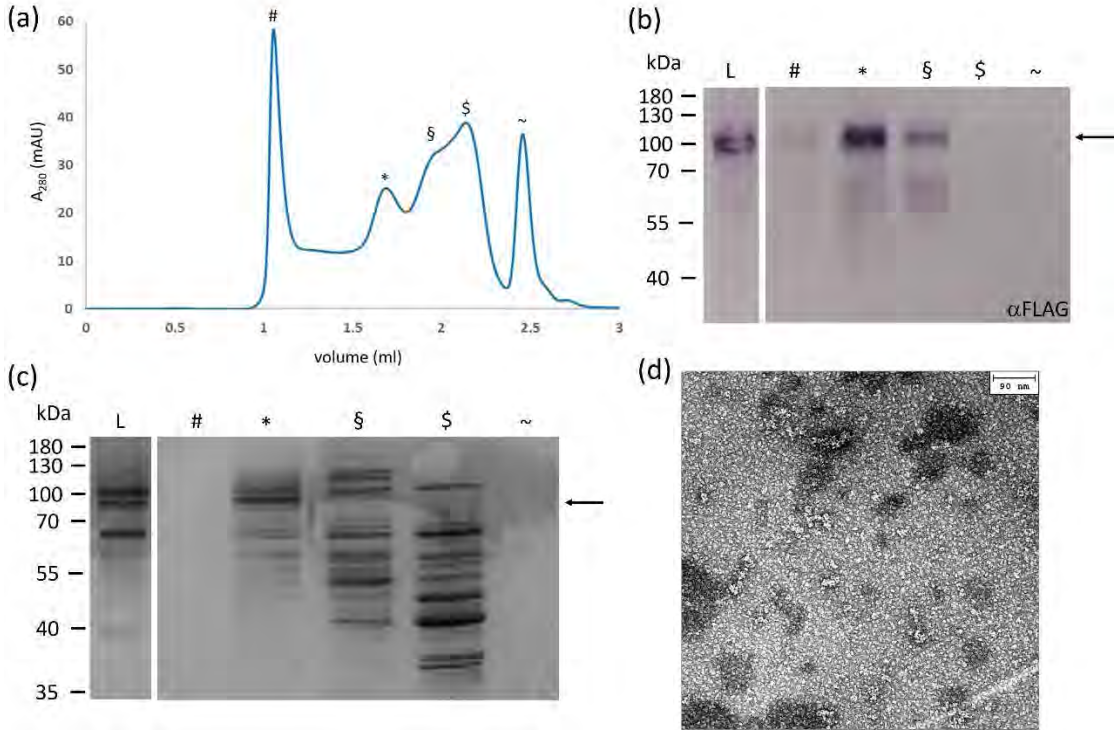

Figure 3.11: Purification of SMCT2 in LMNG/CHS

(a) SEC elution profile of SMCT2 purification (2.2.5.6). The absorbance at 280 nm is plotted against the elution volume. A Superose 6 Increase 5/150 GL column (2.1.1) was used. #: aggregate peak; *: first peak; §: shoulder before second peak; $: second peak; ~: third peak. **(b)** Western blot analysis of the SEC. 10 µl of the fractions were applied to a 10% polyacrylamide gel (Table 2.10) and western blot analysis (2.2.2.4) was performed with a primary anti-FLAG antibody (2.1.12). The band at 100 kDa (arrow) represents SMCT2, showing SMCT2 mainly occurs in the first peak. L: load SEC; #: aggregate peak; *: first peak; §: shoulder before second peak; $: second peak; ~: third peak. **(c)** Silver stained SDS-Page of SEC fractions. 10 µl of sample was loaded on a 10% polyacrylamide gel (Table 2.10) and silver stained (2.2.2.3) for protein detection, showing impurities in all SEC fractions as well as in the load, indicating impurities occurring already after FLAG-affinity chromatography. L: load SEC; #: aggregate peak; *: first peak; §: shoulder before second peak; $: second peak; ~: third peak. **(d)** Negative stain image (2.2.7.1) of the first SEC peak (*) showing a heterogenous particle size and protein aggregation.

Due to the low protein yield, protein aggregation and impurities, further improvements in expression and purification of SMCT2 are necessary for future investigations. The protocol used for SMCT1 SPA cryo-EM might be a valuable reference (Han *et al.*, 2022).

3.1.5 Summary on the studies of SLC5 transporters

Comprehending the structural and functional characteristics of SLC5A family members is of great importance in the fields of physiology, pharmacology, and drug development. This task is inherently challenging as these proteins pose difficulties in expression and purification, by unifying several attributes of ambitious samples, e.g. their membrane topology (Turk E. & Wright E. M., 1997) or stabilizing protein-protein interactions (Coady *et al.*, 2017). Expression and purification of SLC5A family members is a challenging task. The expression poses various challenges due to their complex structure and functions. Especially, the low protein yield and stability issues during purification of SMCT2 and SGLT2 presented a significant hurdle in this study. Apparently, these proteins are vulnerable to denaturation, aggregation, and degradation, especially when expressed in the HEK293S GnT1$^-$ cell. Possible reasons for this instability, are the lack of the interaction partner MAP17 (Coady *et al.*, 2017), or the lack of substrate during expression (Ghezzi C. & Wright E. M., 2012). Based on this, approaches to add sucrose in the expression media and to generate a construct co-expressing SGLT2 and Map17 were planned, but not executed.
Despite these challenges, the studies in this thesis have shown promising results in the expression and purification of SGLT3. Improved strategies, such as the use of specific detergents, chaperones, and expression systems, have enhanced the yield and quality of purified SGLT3 protein. These advancements have facilitated the elucidation of SGLT3's distinct physiological functions and regulatory mechanisms and will be pursued in future.

3.2 Reconstitution of GPR in various membrane mimics

E. coli C43 (DE3)ΔAcrAB (2.1.14.1.1) expressing GPR (Fig. 3.12a,b; 2.2.3) were solubilized in 1.5% (w/v) DDM (2.1.8) and purified in a final DDM concentration of 0.1% (w/v) via His-Tag affinity chromatography (Fig. 3.12c) and SEC (Fig. 3.12d). Purity of the protein was checked via SDS-Page (Fig. 3.12e; 2.2.2.2) and the final protein concentration was determined photometrically (2.2.2.1.2). Expression in 12 l LB-media (2.1.13.1.1) resulted in total of approx. 50 mg purified GPR, which was finally used to test reconstitution into amphipol (2.2.6.1) and salipros (2.2.6.2).

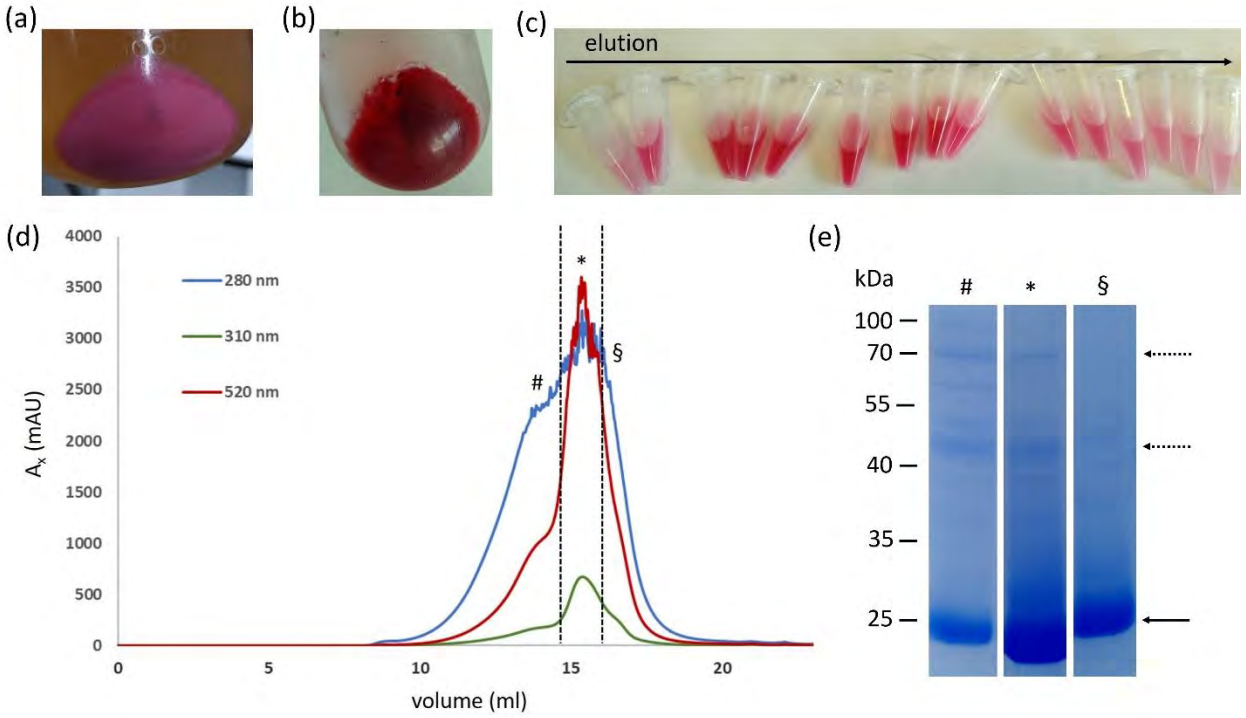

Figure 3.12: Production of GPR

(a) Harvested *E. coli* C43 (DE3)ΔAcrAB (2.1.14.1.1) from 1 l LB-media (2.1.13.1.1) indicating the expression of GPR (2.2.3) by the pink color. **(b)** Cell membranes containing GPR. **(c)** Elution fractions from His-Tag affinity chromatography of GPR (2.2.5.1). First fraction on the left, last fraction on the right. **(d)** SEC elution profile of GPR purification (2.2.5.1). The absorbance at 280 nm, 310 nm and 520 nm (all-*trans* retinal) are plotted against the elution volume. A Superose 6 Increase 10/300 GL column (2.1.1) was used. #: shoulder before main peak; *: main peak; §: end of main peak. **(e)** SDS-Page of SEC fractions. 10 µl of sample was loaded on a 12% polyacrylamide gel (Table 2.10) and stained with staining solution (Table 2.12) for protein detection, showing GPR monomer (23 kDa, arrow) in all SEC fractions as well as higher oligomers (46 kDa and 69 kDa, dotted arrows) in fraction # and *. #: shoulder before main peak; *: main peak; §: end of main peak.

For amphipol reconstitution (2.2.6.1) the most common amphipol type A8-35 (Fig. 1.6) was used in a protein to amphipol ratio of 1:3 (w/w). The final SEC run with 100 mM NaCl showed a monodisperse peak (Fig. 3.13a) and SDS-Page (2.2.2.2) confirmed the presence of GPR in the main peak (Fig. 3.13b). After vitrification on Quantifoil® R1.2/1.3 300-mesh Cu grids (2.1.3; blotting time: 6.0 s) the sample was screened on a CRYO ARM™ 200 (2.2.7.2.2). The A8-35 reconstituted GPRs formed strings with preferred side view orientation (Fig. 3.13c). Based on the findings of Kampjut *et al.*, 2021, the salt concentration was

increased to diminish this artificial oligomerization. A second SEC run, using a buffer with 150 mM NaCl revealed two peaks (Fig. 3.13d), indicating two different oligomeric states of GPR. The vitrified sample (2.2.7.2.1; Quantifoil® R1.2/1.3 300-mesh Cu grids (2.1.3); blotting time: 5.5 s) again showed string formation and mainly side views (Fig. 3.13e). When adding fluorinated Fos-Choline 8 (2.1.8) to the 150 mM NaCl sample before vitrification (2.2.7.2.1; Quantifoil® R1.2/1.3 300-mesh Cu grids (2.1.3); blotting time: 6.0 s) to reduce the preferred side view orientation of the particles, failed, since there were only particles at the edge of the grid holes, still forming strings (Fig. 3.13f).

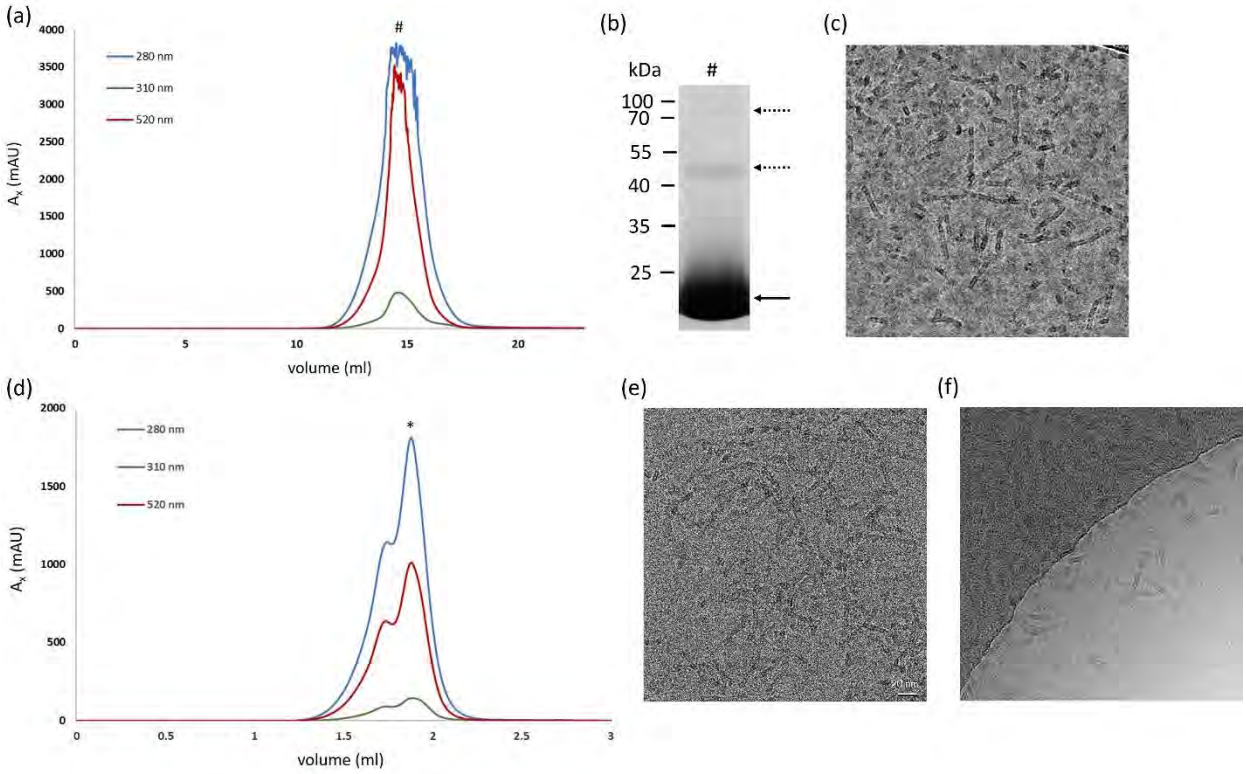

Figure 3.13: Reconstitution of GPR into A8-35

(a) (First) SEC elution profile of GPR reconstituted in Amphipol A8-35 (2.1.5) using a SEC-buffer (Table 2.25) containing 100 mM NaCl. The absorbance at 280 nm, 310 nm and 520 nm (all-*trans* retinal) are plotted against the elution volume. A Superose 6 Increase 10/300 GL column (2.1.1) was used. #: main peak **(b)** SDS-Page of SEC main peak. 10 µl of sample was loaded on a 12% polyacrylamide gel (Table 2.10) and stained with staining solution (Table 2.12) for protein detection, showing GPR monomer (23 kDa, arrow) as well as higher oligomers (46 kDa and 69 kDa, dotted arrows). #: main peak. **(c)** SPA cryo-EM image (2.2.7.2) of the SEC main peak (#) showing string formation and side view orientation of the particles. **(d)** (Second) SEC elution profile of GPR in A8-35 using a SEC-buffer (Table 2.25) containing 150 mM NaCl. The absorbance at 280 nm, 310 nm and 520 nm (all-*trans* retinal) are plotted against the elution volume. A Superose 6 Increase 5/150 GL column (2.1.1) was used. *: main peak. **(e + f)** SPA cryo-EM image (2.2.7.2) of the second SEC main peak (*) showing string formation and side view orientation of the particles (e), and addition of 1 mM fluorinated Fos-Choline 8 (2.1.8) before vitrification, shows particles only at the edge of the grid holes as well as string formation and preferred side view orientation (f).

For reconstitution in salipros (2.2.6.2) 1 mg of purified GPR was mixed with 3 mg POPC (2.1.11) and 8 mg Saposin A, followed by slow detergent removal via Bio-Beads SM-2 (2.1.3) and a final SEC run. The SEC profile (Fig. 3.14a) shows three peaks, aggregates (1,0 – 1,2 ml), reconstituted GPR (1,8 – 2,1 ml) and free Saposin A (2,2– 2,5 ml; Fig. 3.14a), as confirmed by SDS-Page (Fig. 3.14b). The middle peak was vitrified

(2.2.7.2.1) on Graphene oxide Quantifoil® R1.2/1.3 300-mesh Cu grids (2.1.3; blotting time: 5.0 s). The sample was screened on a CRYO ARM™ 200 (2.2.7.2.2) where GPR-salipro particles showed good distribution, no preferred orientation, and no aggregation (Fig. 3.14c).

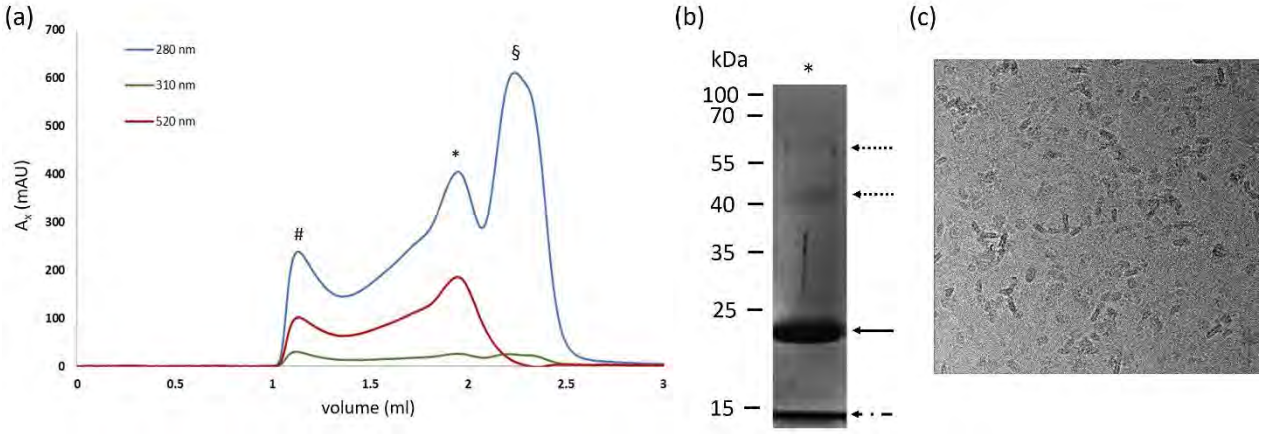

Figure 3.14: Reconstitution of GPR into salipros

(a) SEC elution profile of GPR reconstituted in salipros with POPC (2.2.6.2). The absorbance at 280 nm, 310 nm and 520 nm (all-*trans* retinal) are plotted against the elution volume. A Superose 6 Increase 5/150 GL column (2.1.1) was used. #: aggregate peak; *: main peak; §: free, not reconstituted Saposin A. **(b)** SDS-Page (2.2.2.2) of SEC main peak. 10 µl of sample was loaded on a 12% polyacrylamide gel (Table 2.10) and stained with staining solution (Table 2.12) for protein detection, showing GPR monomer (23 kDa, arrow) as well as higher oligomers (46 kDa and 69 kDa, dotted arrows). The lowest band (15 kDa, incontinuous arrow) represents Saposin A, attesting a successful reconstitution of GPR in Saposin A. #: main peak. **(c)** SPA cryo-EM image (2.2.7.2) of the SEC main peak (*) showing good particle distribution without aggregation nor preferred orientation.

Data were collected (2.2.7.2.3) for the GPR-salipro sample. The 1,530 recorded movies (Fig. 3.15a) were processed (7.2.1), resulting in final maps containing 52.981 particles (Fig. 3.15b), with a resolution of 4.23 Å applying C1 symmetry and 3.64 Å in C5 symmetry (Fig. 3.15c). For the C5 map in addition the local resolution was calculated, revealing high resolution in the core of the pentamer and a decrease of resolution towards the outer, especially the extra-membrane, parts (Fig. 3.15d). The pentameric symmetry for refining the final map was chosen on the fact that final 2D classes show only pentameric GPR (Fig. 3.15b). This underlines the previous findings that GPR has a pentameric assembly (Hirschi *et al.*, 2020), while earlier studies also claimed a hexameric state (Stone *et al.*, 2013; Klyszejko *et al.*, 2008). However, the 2D classes of the particles in the final maps also show blurry particles or some without secondary features, indicating the need of improvement in reconstitution, final purification, and vitrification, as well as data processing. Regardless to this, the final C5 map was compared with the published pentameric SPA cryo-EM structure of GPR (PDB: 7B03; Hirschi *et al.*, 2020), showing similarity in the overall structure as well as in density of the retinal, depicting an *all-trans* isoform (Fig. 3.15e).

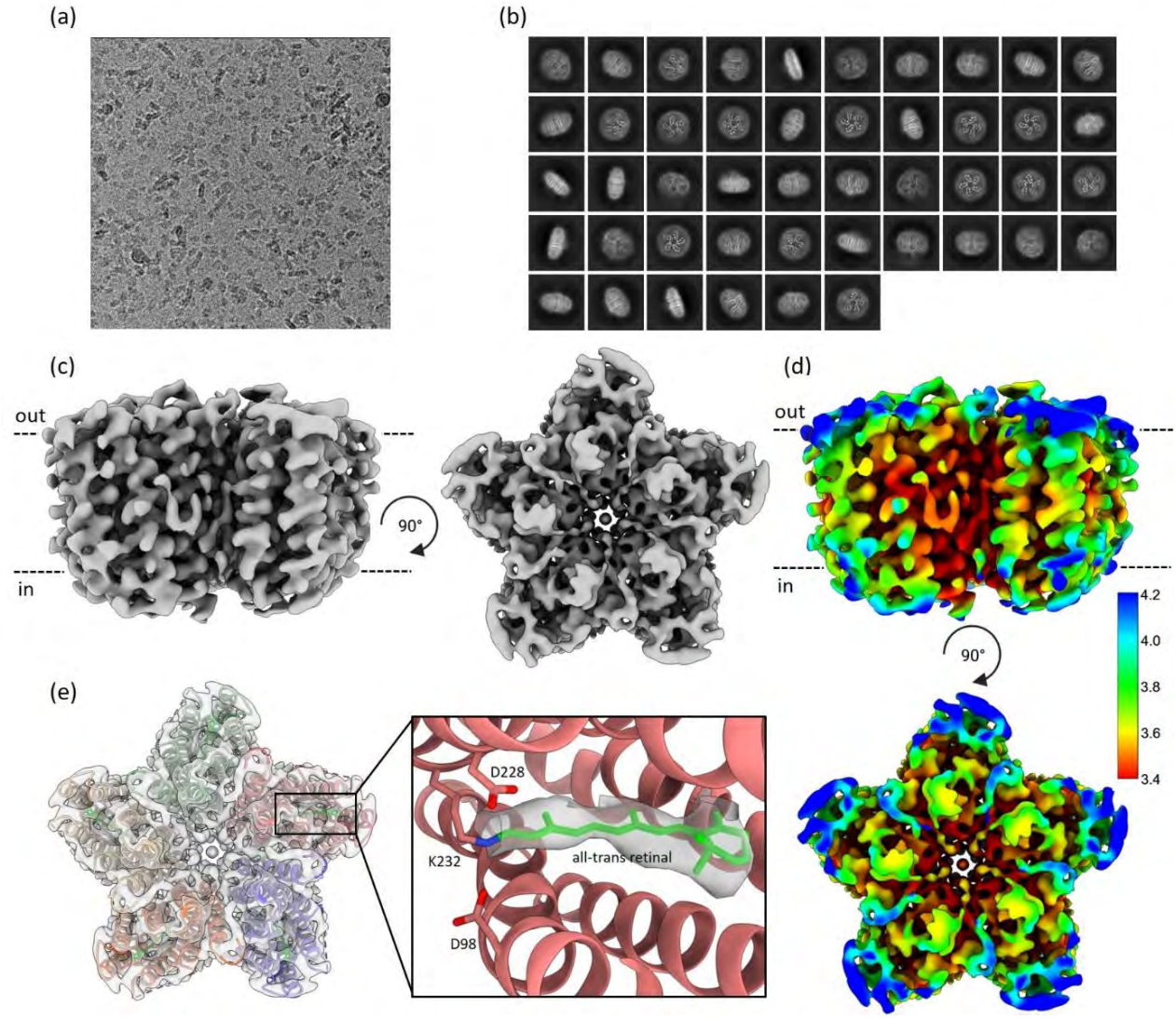

Figure 3.15: The SPA cryo-EM map of GPR in salipros

(a) Example SPA cryo-EM image (2.2.7.2) of GPR in salipros. **(b)** 2D classes of particles used for final SPA cryo-EM maps of GPR in salipros. The 2 classes show top/bottom views, side views and tilted views, indicating good SPA cryo-EM data quality (2.2.7.2.2), suitable for 3D reconstruction. However, some classes show blurry particles, or some are without secondary features. **(c)** Side view (left) and periplasmic view (right) of the GPR-salipro C5 map (3.64 Å). The densities of the surrounding lipids and Saposin A's are excluded. Dotted lines in the side view are indicating the lipid bilayer. **(d)** Side view (up) and periplasmic view (down) of the local resolution of the GPR-salipro C5 map. The densities of the surrounding lipids and Saposin A's are excluded. Dotted lines in the side view are indicating the lipid bilayer. **(e)** Periplasmic view of the GPR-salipro C5 map superimposed with the published pentameric SPA cryo-EM structure of GPR (PDB: 7B03; Hirschi et al., 2020). The density of the retinal is shown enlarged, depicting the *all-trans* retinal form.

3.3 TPC2

3.3.1 Expression and purification

To establish a protocol for expression and purification of TPC2, various attempts, based on She *et al.*, 2019, were tested to find a suitable workflow. Transient expression using the construct pEZT-BM_TPC2 (2.1.14.2.2; She *et al.*, 2019) was tested using different transfection reagents, growth times, amounts of DNA, DNA to transfection reagent ratios and additives to boost protein expression (e.g. sodium butyrate or valproic acid) in adherent cells (Table 3.4).

Table 3.4: Attempts for transient expression of TPC2

Condition	Experimental work	Conclusion
Transfection reagents	Transfection of pEZT-BM_TPC2 (2.1.14.2.2) in adherent HEK293S GnT1$^-$ cells (2.1.14.2.1) via jetPrime® (2.1.14.2.3), Lipofectamin™ 2000 (2.1.14.2.3), PEIpro® (2.1.14.2.3) and PEI 25 kDa branched (2.1.14.2.3), harvested after 48 h followed by western blot analysis (2.2.2.4)	All reagents show TPC2 expression, PEIpro® and PEI 25 kDa branched show strongest expression PEI 25 kDa branched is used due to cost reasons
Growth time	HEK293S GnT1$^-$ cells (2.1.14.2.1) transfected with pEZT-BM_TPC2 (2.1.14.2.2) via PEI 25 kDa branched (2.1.14.2.3), harvested 24 h, 48 h and 72 h after transfection, followed by western blot analysis (2.2.2.4)	Weak expression after 24 h, no difference in expression after 48 h or 72 h Harvest cells after 48 h (in exceptional cases after 72 h)
DNA amount	HEK293S GnT1$^-$ cells (2.1.14.2.1) transfected with 0.5-3 µg pEZT-BM_TPC2 (2.1.14.2.2) per 10^6 cells via PEI 25 kDa branched (2.1.14.2.3), harvested after 48 h, followed by western blot analysis (2.2.2.4)	No expression for 0.5 µg DNA, no difference in expression from 1.0 µg to 3.0 µg DNA Use 1 µg DNA per 10^6 cells
DNA to PEI 25 kDa branched ratio	HEK293S GnT1$^-$ cells (2.1.14.2.1) transfected with 1 µg pEZT-BM_TPC2 (2.1.14.2.2) per 10^6 cells via PEI 25 kDa branched (2.1.14.2.3), using ratios of 1:1 to 1:5 (w/w) harvested after 48 h, followed by western blot analysis (2.2.2.4)	Weak expression with ratios 1:1 and 1:2, no difference in expression from 1:3 to 1:5 Use a DNA to PEI 25 kDa branched ratio of 1:3
Additives to boost expression	HEK293S GnT1$^-$ cells (2.1.14.2.1) transfected with 1 µg pEZT-BM_TPC2 (2.1.14.2.2) per 10^6 cells via PEI 25 kDa branched (ratio 1:3; 2.1.14.2.3), adding 5/10 mM sodium butyrate (2.1.5) or 2/4/6 mM valproic acid (2.1.5) after 24 h, harvested after 48h, followed by western blot analysis (2.2.2.4)	Addition of 5 mM sodium butyrate 24 h after transfection increased expression yield Add 5 mM sodium butyrate 24 h after transfection

Optimized conditions for transient expression of TPC2 in adherent cells (Table 3.4), were transferred to suspension culture with similar results. In parallel to the expression conditions also purification of TPC2 was tested. Different detergents were screened for solubilization (Table 3.5), followed by testing resins for affinity chromatography. Also, thrombin cleavage to remove the N-terminal mEGFP-His_8-tag was addressed (Table 3.5).

Table 3.5: Purification test of TPC2

Step	Experimental work	Conclusion
Detergent screen	Lysis of cells with various detergents (2.1.8). All detergents were supplemented with CHS (2.1.8)	1% (w/v) /0.2% (w/v) DDM/CHS and 1% (w/v) /0.2% (w/v) LMNG/CHS show best solubilization efficiency Based on She *et al.*, 2019, 1% (w/v) /0.2% (w/v) DDM/CHS is used
Affinity resin	Testing TALON® Metal Affinity resin (2.1.9) and Ni-NTA Agarose (2.1.9) for the affinity purification step of the N-terminal mEGFP-His_8-tagged TPC2	Both resins show good protein binding, as TALON® Metal Affinity resin has better elution properties Use TALON® Metal Affinity resin
Thrombin cleavage	Testing the Thrombin CleanCleave™ kit (2.1.6), and Thrombin from human plasma (2.1.5) in batch and on column before the elution step of His-tag affinity purification, to cleave the mEGFP-His_8-tag	No successful thrombin cleavage observed

Low expression yields and thrombin cleavage were the bottleneck in the TPC2 purification. The cooperation partner Marko Roblek (ISTA) generated a stable cell line for TPC2 (HEK293S GnT1$^-$-TPC2 (2.1.14.2.1) using the lentivirus transfection system (Elegheert *et al.*, 2018). Expression conditions like growth times, additives and amount of inducing agent were optimized for suspension culture (Table 3.3) and turned out to be similar to the SGLT3 stable cell line conditions. The new construct (N-terminal His_8-tag, no Thrombin cleavage site) allowed to use the already established purification protocol without the thrombin cleavage step.

TPC2 expression was always monitored by western blot analysis (Fig. 3.16a). 30 g of cells were solubilized with 1% DDM / 0.2% CHS and N-terminal His_8-tagged TPC2 was purified via affinity chromatography using TALON® Metal Affinity resin (2.2.5.7). Peak fractions of the subsequent SEC run on a Superose 6 Increase 5/150 GL column (Fig 3.16b) were pooled and concentrated to a final concentration of approx. 1.5 mg/ml for vitrification. All these steps were additionally analyzed via silver stained SDS-Page (Fig. 3.16c).

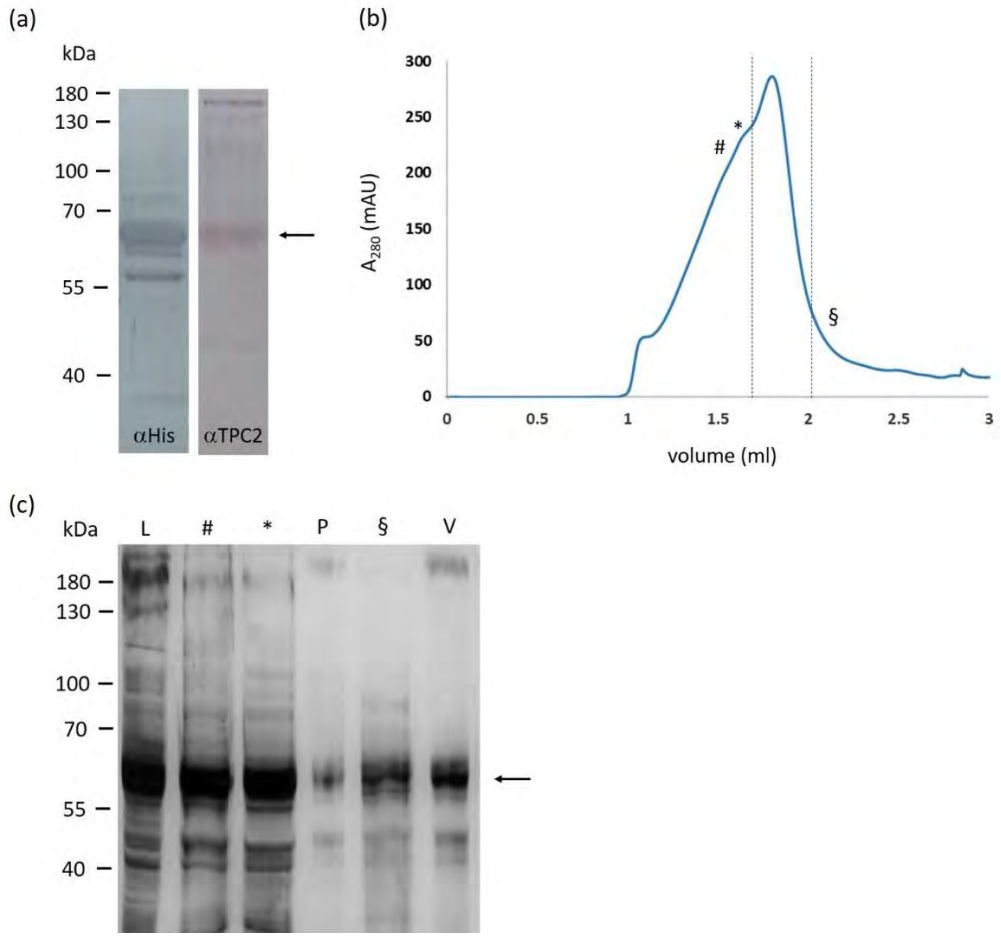

Figure 3.16: Expression and purification of TPC2
(a) Western blot to check the expression of TPC2 via stable cell line. 20 µl of supernatant from lysed cells was applied to a 10% polyacrylamide gel (Table 2.10) and western blot analysis (2.2.2.4) was performed with a primary anti-His (left; 2.1.12) and a primary anti-TPC2 antibody (right; 2.1.12). The thick bands below 70 kDa (arrow) represent TPC2. **(b)** SEC elution profile of TPC2. The absorbance at 280 nm is plotted against the elution volume. A Superose 6 Increase 5/150 GL column (2.1.1) was used. The fractions between the dotted lines (Peak fractions) were pooled for further use. # and *: fractions before main peak; §: fraction after main peak. **(c)** Silver stained SDS-Page of TPC2 samples. 10 µl of sample was loaded on a 10% polyacrylamide gel (Table 2.10) and silver stained (2.2.2.3) for protein detection. L: load SEC; # and *: fractions before main peak; P: polled main peak fractions; §: fraction after main peak; V: vitrified sample.

3.3.2 TPC2-Rab7A complex

The GTPase Rab7A is a postulated interaction partner of TPC2 (Lin-Moshier *et al.*, 2014). Rab7A was expressed in *E. coli* using the vector pET28a_Rab7A (2.1.14.1.2). Different *E. coli* at various growth times and temperatures were tested (Table 3.6), to optimize protein yield. Rab7A is anchored to the membrane via its C-terminus (Magee T. and Newman C., 1992). Consequently, a solubilization buffer was developed based on Wu *et al.*, 2005 (Table 3.6). In addition, His-tag purification was established by screening resins and imidazole concentrations for elution (Table 3.6).

Table 3.6: Attempts for Rab7A expression and purification

Condition	Experimental work	Conclusion
E. coli strain	Transformation of pET28a_Rab7A (2.1.14.1.2) into BL21 (DE3) (2.1.14.1.1), BL21-Gold (DE3) (2.1.14.1.1), BL21 (DE3) pLysS (2.1.14.1.1) and BL21 (DE3) Rosetta2 (2.1.14.1.1), growth in LB-media (2.1.13.1.1), induction via 1 mM IPTG (2.1.5) at OD_{600} = 0.6, incubated at 170 rpm, RT for 18 h, followed by western blot analysis (2.2.2.4)	All cell strains showed expression, while BL21 (DE3) Rosetta2 showed highest protein quantity BL21 (DE3) Rosetta2 cells are used
Growth time and temperature	Transformation of pET28a_Rab7A (2.1.14.1.2) into BL21 (DE3) Rosetta2 (2.1.14.1.1), growth in LB-media (2.1.13.1.1), induction via 1 mM IPTG (2.1.5) at OD_{600} = 0.6, incubated at 170 rpm, 20 °C for 18 h, 23 °C for 18 h, 30°C for 18 h, 23 °C for 6 h, 26 °C for 6 h, 30 °C for 2 h and 37 °C for 2h, followed by western blot analysis (2.2.2.4)	Short expression times combined with low temperature showed best Rab7A expression Grow cells at 30 °C for 2 h after induction
Solubilization buffer	Resuspending harvested cells in 50 ml solubilization buffer (Table 2.18), with and without 1 mg/ml lysozyme (2.1.5), per 1 l harvested culture, sonication (1 min, 60% amplitude, pulse: 3 sec on / 3 sec off, 4 °C, Digital sonifier 250 (2.1.1)), centrifugation (30 min, 3,300 g, 4 °C, Avanti J-26 XP with rotor JLA-16.250 (2.1.1)), followed by western blot analysis (2.2.2.4) of supernatant	Rab7A only present in supernatant of cells solubilized in the presence of lysozyme Use 1 mg/ml lysozyme for Rab7A solubilization
Affinity resin	Testing TALON® Metal Affinity resin (2.1.9) and Ni-NTA Agarose (2.1.9) for the affinity purification step of the His_6-tagged Rab7A	No protein binding to TALON® Metal Affinity resin, good binding and elution properties with Ni-NTA Agarose Use Ni-NTA Agarose
Imidazole concentration for elution	Elution of protein from Ni-NTA Agarose (2.1.9) via imidazole gradient 50/100/200/300/400 and 500 mM imidazole pH 8, followed by western blot analysis (2.2.2.4) of elution fractions	No elution at 50 mM, most protein eluted at 100 mM, all the rest eluted with 200 mM imidazole pH 8 Use 100 mM imidazole pH 8 for elution and 50 mM imidazole pH 8 for wash step

Finally, Rab7A was expressed in 12 l LB-media (2.1.13.1.1), cells lysed via sonication and Rab7A purified via His_6-tag affinity chromatography (2.2.5.2). The second CV of the elution was pooled and purified further via SEC on a Superose 6 Increase 10/300 GL column (Fig. 3.17a; 2.2.5.2). The peak fractions were pooled and analyzed by SDS-Page (2.2.2.2), showing some minor impurities (Fig. 3.17b). In total approx. 9 mg of Rab7A were purified out of the cells expressed in 12 l LB-media.

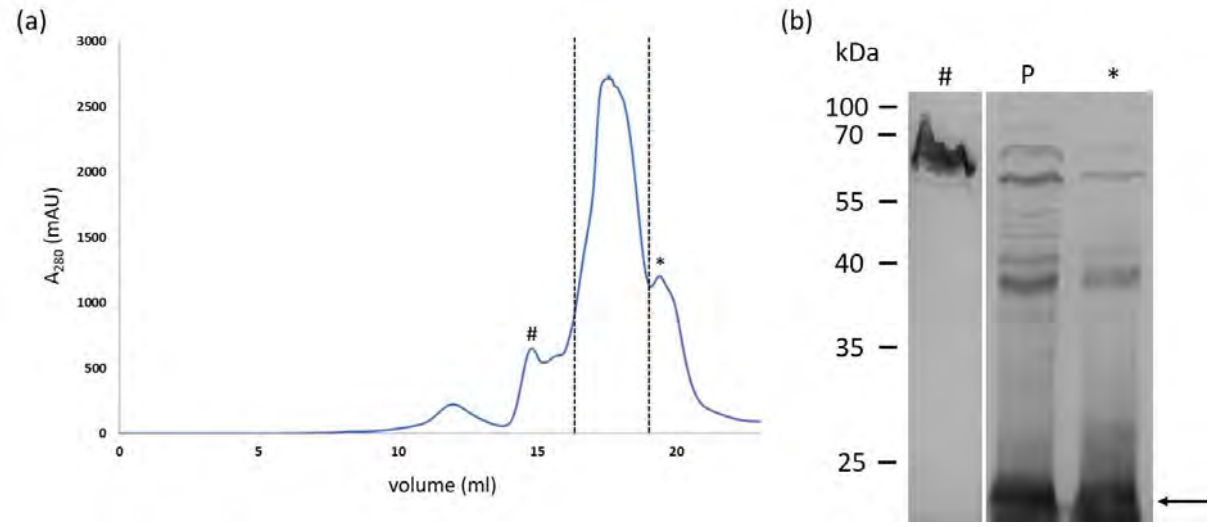

Figure 3.17: Purification of Rab7A

(a) SEC elution profile of Rab7A. The absorbance at 280 nm is plotted against the elution volume. A Superose 6 Increase 10/300 GL column (2.1.1) was used. The main peak (between the dotted lines) was polled and used for further steps. #: shoulder before main peak; *: shoulder after main peak. **(b)** SDS-Page of SEC fractions. 10 µl of sample was loaded on a 12% polyacrylamide gel (Table 2.10) and stained with staining solution (Table 2.12) for protein detection, showing Rab7A (23 kDa, arrow) in the main peak and the second shoulder. #: shoulder before main peak; P: pooled main peak; *: shoulder after main peak.

Catalytic activity of Rab7A was tested via its ability to hydrolyze GTP to GDP. By this reaction a free phosphate group as well as a proton is released (Fig. 3.18a), leading to a decrease of pH in the solution. This pH change was detected by measuring the absorbance of the fluorescent pH indicator pyranine at 455 nm (Fig. 3.18b; 2.2.8.2). To test the selectivity of Rab7A on GTP the same assay was performed using ATP instead of GTP, showing no pH change. Additionally, a negative control without protein was executed. In summary, this assay demonstrated that Rab7A was purified in a functional form.

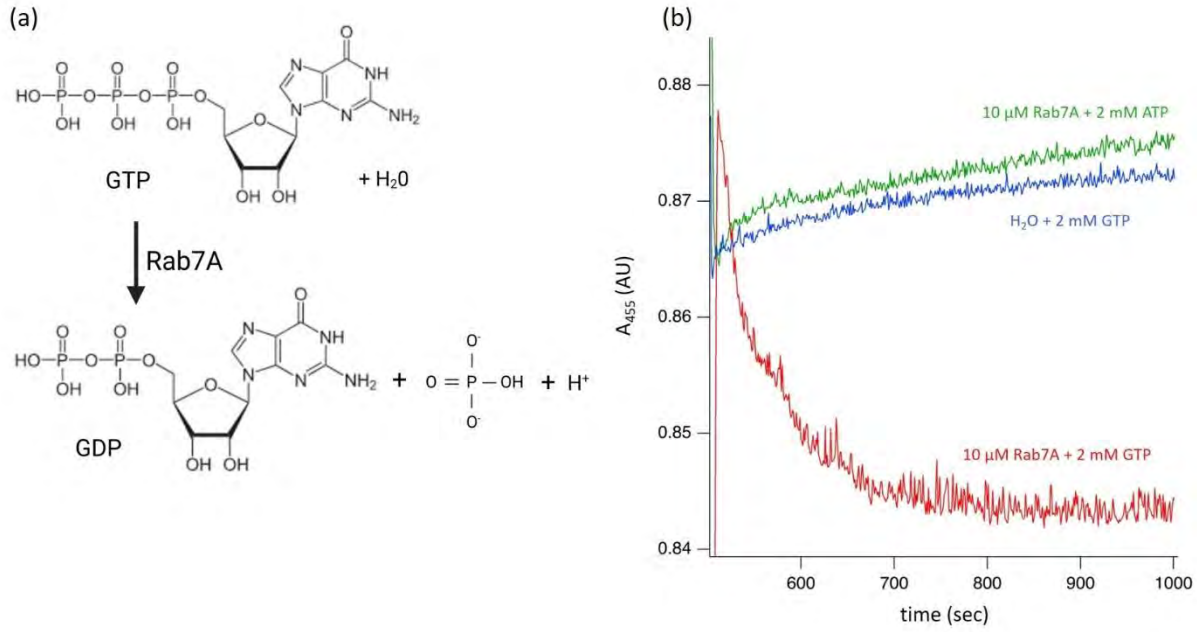

Figure 3.18: Catalytic activity of Rab7A

(a) Hydrolysis of GTP by Rab7A. The hydrolysis of GTP in aqueous solutions catalyzed by Rab7A results in GDP, a free phosphate group and a proton. The image was created with BioRender (2.1.2). **(b)** Absorbance of pyranine at 455 nm in presence of 10µM Rab7A (3.3.2) mixed with 2 mM GTP (red line; 2.1.5), 10 µM Rab7A (3.3.2) mixed with 2 mM ATP (green line; 2.1.5) and 2 mM GTP (2.1.5) without Rab7A (blue line) fitted against the time. Purified Rab7A was added 500 sec after starting the measurement to avoid artefacts of time-dependent ATP-/GTP-hydrolysis and stabilize the pyranine absorbance. Each measurement was performed in 5 mM Tris/HCl pH 8, 2 mM $MgCl_2$ with 0.05 mM pyranine (2.1.5) in final volume of 1 ml for 500 sec. Rab7A with GTP (red line) indicates a decrease of pH, relating to hydrolysis of GTP by Rab7A. Rab7A with ATP (green line) shows no decrease in pyranine absorbance, showing that Rab7A does not hydrolyze ATP, underlining the selectivity of Rab7A for GTP. GTP without Rab7A (blue line) is showing similar increasing pH characteristics like Rab7A with ATP, manifesting the Rab7A dependency of the measurements.

To analyze a possible TPC2-Rab7A complex, various attempts of binding Rab7A to TPC2 and analyzing this complex SEC were made (Table 3.7). Addition of GTP is generating the active form of Rab7A (Fig. 3.18), which was suspected to bind TPC2. The same assumption was made for TPC2, that only the $PI(3,5)P_2$-bound state (She *et al.*, 2019) can bind Rab7A. Additionally, the whole complex was reconstituted into salipros, as a membrane-like environment might be required for TPC2-Rab7A interaction. Unfortunately, none of the attempts resulted in a stable binding of purified Rab7A (Fig. 3.17) to TPC2 purified in GDN (Fig. 3.16).

Table 3.7: Overview attempts of TPC2-Rab7A complex formation for SPA cryo-EM

Condition	Experimental work	Conclusion
TPC2 + Rab7A	Mix 1.5 mg purified TPC2 (3.3.1) and purified Rab7A (3.3.2) in a ratio of 1:10 (mol:mol; TPC2:Rab7A), incubate on ice for 30 min and perform SEC (Superose 6 Increase 5/150 GL column (2.1.1)) in TPC2 SEC-buffer (Table 2.24)	Two separate elution peaks, being identified as TPC2 and Rab7A No stable complex formation
TPC2 + Rab7A + GTP	Mix purified Rab7A (3.3.2) with 2 mM GTP (2.1.5) and 2 mM $MgCl_2$, add purified TPC2 (3.3.1) in a ratio of 1:10 (mol:mol; TPC2:Rab7A), incubate on ice for 30 min and perform SEC (Superose 6 Increase 5/150 GL column (2.1.1)) in TPC2 SEC-buffer (Table 2.24)	Two separate elution peaks, being identified as TPC2 and Rab7A No stable complex formation
TPC2 + Rab7A + GTP + $PI(3,5)P_2$ diC8	Mix purified Rab7A (3.3.2) with 2 mM GTP (2.1.5) and 2 mM $MgCl_2$, add purified TPC2 (3.3.1), premixed with 0.5 mM $PI(3,5)P_2$ diC8 (2.1.11), in a ratio of 1:10 (mol:mol; TPC2:Rab7A), incubate on ice for 30 min and perform SEC (Superose 6 Increase 5/150 GL column (2.1.1)) in TPC2 SEC-buffer (Table 2.24)	Two separate elution peaks, being identified as TPC2 and Rab7A No stable complex formation
TPC2 + Rab7A + GTP + $PI(3,5)P_2$ diC8 in salipros	Mix purified Rab7A (3.3.2) with 2 mM GTP (2.1.5) and 2 mM $MgCl_2$, add purified TPC2 (3.3.1), premixed with 0.5 mM $PI(3,5)P_2$ diC8 (2.1.11), in a ratio of 1:10 (mol:mol; TPC2:Rab7A), reconstitute the mixture into salipros (similar to GPR (2.2.6.2)), but perform the final SEC (Superose 6 Increase 5/150 GL column (2.1.1)) in TPC2 SEC-buffer (Table 2.24) without GDN	Three separate elution peaks, being identified as TPC2, Rab7A and Saposin A No stable complex formation

3.3.3 Cryo-EM SPA of TPC2

For cryo-EM SPA, TPC2 samples were vitrified (2.2.7.2.1) on Quantifoil® R1.2/1.3 300-mesh Cu grids (2.1.3). To obtain the respective agonist/antagonist-bound structure, the protein sample was incubated with the agonist/ antagonist (Table 3.8) for 30 min on ice directly before vitrification (2.2.7.2.1).

Table 3.8: Overview of TPC2 SPA cryo-EM grid preparation

Condition	Antagonist/Agonist concentration	TPC2 concentration (mg/ml)
Apo	-	1.23
TPC2-A1-P	1:40 (mol:mol) TPC2 : TPC2A1-P (2.1.5)	1.61
TPC2-A1-N	1:40 (mol:mol) TPC2 : TPC2A1-N (2.1.5)	1.61
SGA-85	1:40 (mol:mol) TPC2 : SGA-85 (2.1.5)	1.61
SGA-111	1:40 (mol:mol) TPC2 : SGA-111 (2.1.5)	1.68
TPC2-A1-N + $PI(3,5)P_2$	1:40 (mol:mol) TPC2 : TPC2A1-N (2.1.5) 0.5 mM $PI(3,5)P_2$ diC8 (2.1.11)	1.28
Naringenin	0.5 mM Naringenin (2.1.5)	1.93
Naringenin + $PI(3,5)P_2$	0.5 mM Naringenin (2.1.5) 0.5 mM $PI(3,5)P_2$ diC8 (2.1.11)	1.93

After vitrification the grids were screened on quality (2.2.7.2.2) and movies were recorded (2.2.7.2.3) on good quality grids at a nominal pixel size of 0.7891 Å. Due to operating properties, the actual pixel size differed between 0.7899 Å and 0.8141 Å in the different data sets (Table 3.9). During image recording the quality of the data was checked in parallel via cryoSPARC live (2.1.2). After data collection the micrographs were processed (7.3.3) to final SPA cryo-EM maps with applied C1- or C2-symmerty (Table 3.9) used for model building (2.2.7.2.4). As the apo, SGA-111 and $PI(3,5)P_2$-naringenin conditions were the only ones with resolutions < 4 Å, just for those conditions models were built. The C2 maps of the other conditions were analyzed on open or closed conformation, using the published $PI(3,5)P_2$-bound open state (PDB: 6NQ0; She *et al.*, 2019) and apo/closed (PDB: 6NQ1; She *et al.*, 2019) human TPC2 structures as references (Fig. 3.19).

Table 3.9: Overview of TPC2 SPA cryo-EM datasets

Condition	Pixel size (Å)	Micrographs	Particles in final map	Resolution C1 (Å)	Resolution C2 (Å)
Apo	0.8141	8,539	119,218	3.78	3.55
TPC2-A1-P	0.8089	1,367	23,830	5.19	4.44
TPC2-A1-N	0.8076	2,770	23,586	4.62	4.42
SGA-85	0.8036	5,212	31,467	7.52	6.12
SGA-111	0.7891	8,418	107,627	3.67	3.58
TPC2-A1-N + $PI(3,5)P_2$	0.7934	10,035	47,105	5.28	4.71
Naringenin	0.8058	4,294	17,541	5.22	4.32
Naringenin + $PI(3,5)P_2$	0.8104	5,206	107,955	4.12	3.81

Agonist TPC2-A1-P (Fig. 1.11b), functionally mimicking the effect of $PI(3,5)P_2$ (Gerndt *et al.*, 2020a), showed a closed conformation (Fig. 3.19b). Also, the agonists TPC2-A1-N (Fig. 1.11d) and SGA-85 (Fig. 1.11e), functionally mimicking the effect of NAADP (Gerndt *et al.*, 2020a), revealed closed conformations of TPC2 (Fig. 3.19d,f). When adding $PI(3,5)P_2$ additionally to TPC2-A1-N, TPC2 revealed the $PI(3,5)P_2$-bound open conformation regarding the IS6 helix, with linker helix IIS4-S5 in an intermediate state (Fig. 3.19h). The typical $PI(3,5)P_2$-headgroup density at the $PI(3,5)P_2$-binding site (Fig. 3.19h) underlines that $PI(3,5)P_2$ leads to this characteristic state of IS6, while TPC2-A1-N most likely is responsible for the intermediate state of IIS4-S5. Addition of the inhibitor naringenin (Fig. 1.12b) however resulted in closed conformation (Fig. 3.19j). For more profound analysis of the effects of these agonists/inhibitors on TPC2, high-resolution information is missing.

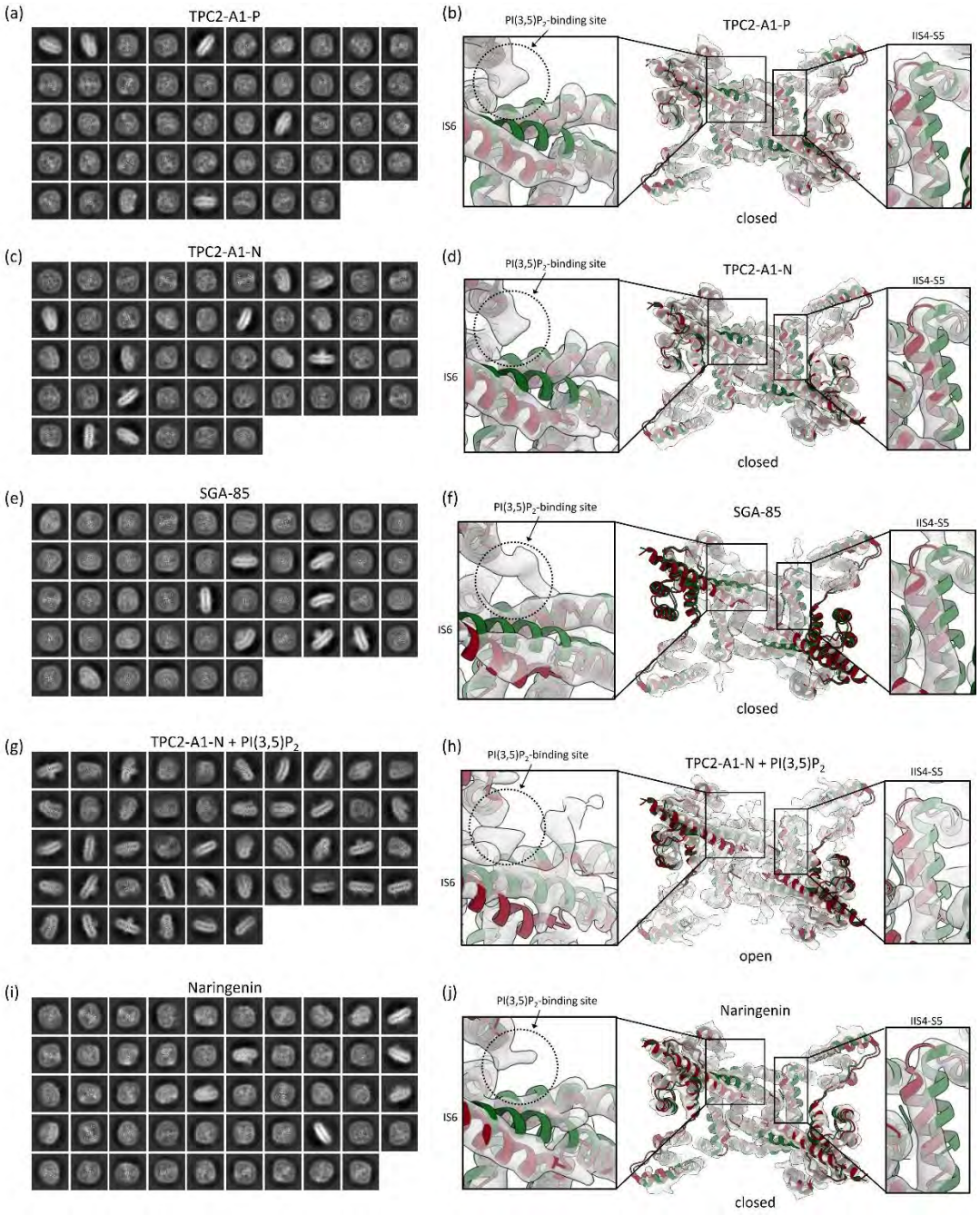

Figure 3.19: Conformation of the SPA cryo-EM maps of TPC2

2D classes of particles used for final SPA cryo-EM maps of TPC2 with various agonists/inhibitors, and the regarding maps with a resolution below 4 Å. SPA cryo-EM maps are superimposed with the TPC2 PI(3,5)P_2-bound open state (green, PDB: 6NQ0; She *et al.*, 2019) and TPC2 apo/closed (red, PDB: 6NQ1; She *et al.*, 2019) structures, to visualize the open or apo/closed conformation of TPC2 with the respective agonist/inhibitor. The PI(3,5)P_2-binding site is marked with a dotted circle. The alignments are shown from the cytosolic side. The figures showing the maps superimposed with the structures were prepared with ChimeraX (2.1.2). **(a,b)** TPC2 with the agonist TPC2-A1-P. The map shows a closed conformation and no density at the PI(3,5)P_2-binding site (b). **(c,d)** TPC2 with the agonist TPC2-A1-N. The map is in a closed conformation and no density at the PI(3,5)P_2-binding site (d). **(e,f)** TPC2 with the agonist SGA-85. The map has a closed conformation and no density at the PI(3,5)P_2-binding site (f). **(g,h)** TPC2 with the agonist TPC2-A1-N and the TPC2-activating lipid PI(3,5)P_2. The map shows an open conformation a typical PI(3,5)P_2-headgroup density at the PI(3,5)P_2-binding site (h). **(i,j)** TPC2 mixed with the inhibitor Naringenin. The map shows a closed conformation and no density at the PI(3,5)P_2-binding site (j).

3.3.4 Apo-structure of TPC2

The apo-structure of TPC2 was determined as following. 3.5 µl of the purified protein in GDN (1.23 mg/ml) were applied to a Quantifoil® R1.2/1.3 300-mesh Cu grid (2.1.3), blotted for 5.0 s and vitrified (2.2.7.2.1). 8,539 micrographs (Fig. 3.20a) were acquired (2.2.7.2.3) and processed (7.3.3.1) to a final C2 map with a resolution of 3.55 Å (Fig. 3.20c). Additionally, the local resolution of the map was calculated, showing high resolution in the protein core and lower resolutions in the flexible parts like the VSDs and the cytosolic domains (Fig. 3.20d). Comparison of the TPC2-apo C2 map with the published PI(3,5)P_2-bound open state (PDB: 6NQ0; She *et al.*, 2019) and the apo (PDB: 6NQ1; She *et al.*, 2019) TPC2 structure, revealed apo conformation (Fig. 3.20e).

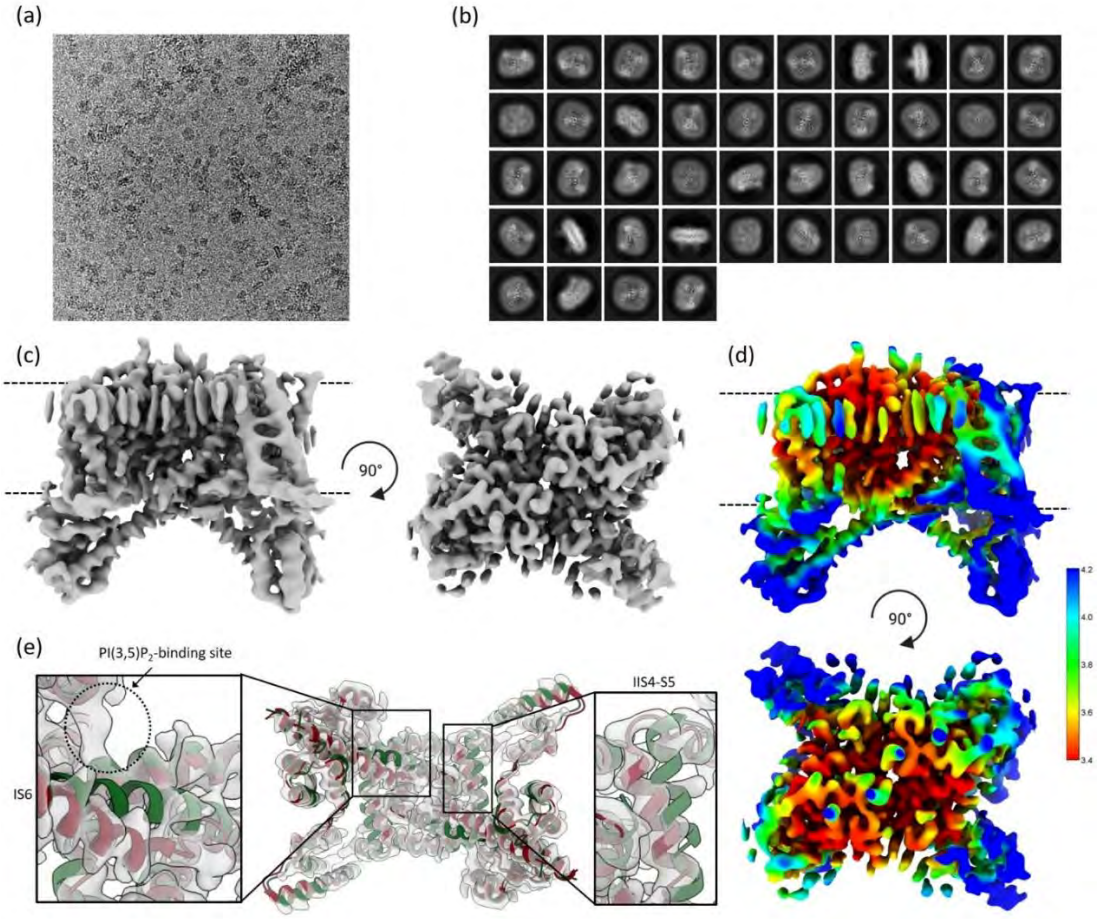

Figure 3.20: The SPA cryo-EM apo-map of TPC2 in GDN
(a) Example SPA cryo-EM image (2.2.7.2) of TPC2-apo (Table 3.9). **(b)** 2D classes of particles used for final TPC2-apo SPA cryo-EM maps. The 2D classes show top/bottom views, side views and tilted views, indicating good SPA cryo-EM data quality (2.2.7.2.2), suitable for 3D reconstruction. The GDN-micelle, surrounding the intermembrane part of TPC2, is clearly visible. **(c)** Side view (left) and luminal view (right) of the TPC2-apo C2 map (3.55 Å). The densities of the surrounding detergent are excluded. Dotted lines in the side view are indicating the lipid bilayer. **(d)** Side view (up) and luminal view (down) of the local resolution of the TPC2-apo C2 map (c). The densities of the surrounding detergent are excluded. Dotted lines in the side view are indicating the lipid bilayer. **(e)** SPA cryo-EM map of TPC2-apo superimposed with the TPC2 PI(3,5)P_2-bound open state (green, PDB: 6NQ0; She *et al.*, 2019) and TPC2 apo/closed (red, PDB: 6NQ1; She *et al.*, 2019) structures, to visualize the open or apo conformation. The PI(3,5)P_2-binding site is marked with a dotted circle. The alignment is shown from the cytosolic side.

The apo model (Fig. 3.21a) was built (2.2.7.2.4), based on the published apo structure (PDB: 6NQ1; She *et al.*, 2019). Residues 1-38, 241-251, 347-353, 526-538, 609-619, 702-752 are disordered and were not modeled. Detergent (GDN-headgroup (Fig. 3.23e)) and lipids were added into elongated non-protein densities. The final model was validated (2.2.7.2.4), showing sufficient parameters (Fig. 3.21b).

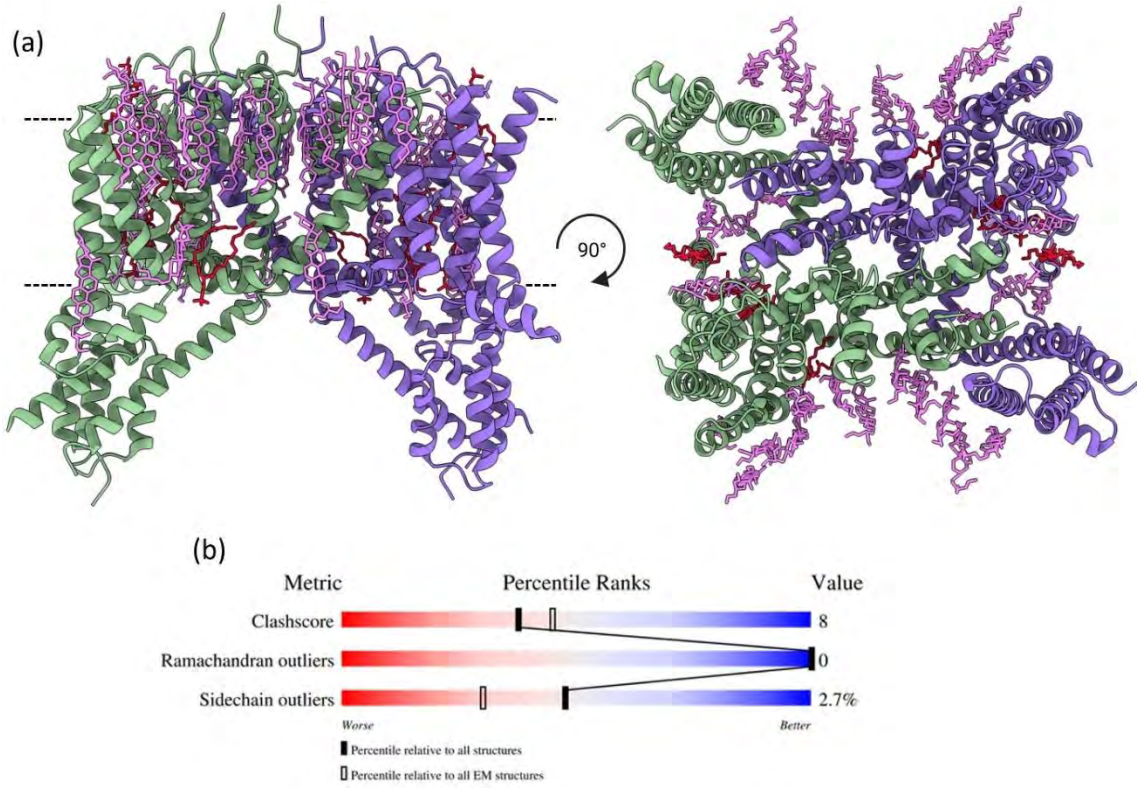

Figure 3.21: Apo-structure of TPC2
(a) Side view (left) and luminal view (right) of the TPC2-apo structure based on the TPC2-apo C2 map (Fig. 3.20c). One subunit is colored in green, the other in blue, GDN-headgroups (Fig. 3.23e) in violet and lipids in red. Dotted lines in the side view are indicating the lipid bilayer. **(b)** Validation report of the TPC2-apo structure (a) gained with the wwPDB Validation System (2.1.2).

The quality of the TPC2-apo model was additionally verified by structural alignment with the published apo model (proteins without ligands; PDB: 6NQ1; She *et al.*, 2019) showing only marginal differences with a root-mean-square deviation (rmsd) of 1.83 Å. The main deviation is in the IIS1 helix, and the other cytosolic parts. These differences originate from the high flexibility of these domains, resulting in a poor local resolution (Fig. 3.20d). In addition, the pore diameter of the two structures was investigated using the `HOLE´ tool in Coot (2.1.2). This stated that both structures have uniform pore diameters, with only minor deviations (Fig. 3.22b). Together with the identical overall structure, similar quality of both structures was proven. Consequently, the apo-structure of this work (Fig. 3.21a) will be used as initial state of TPC2 from now on.

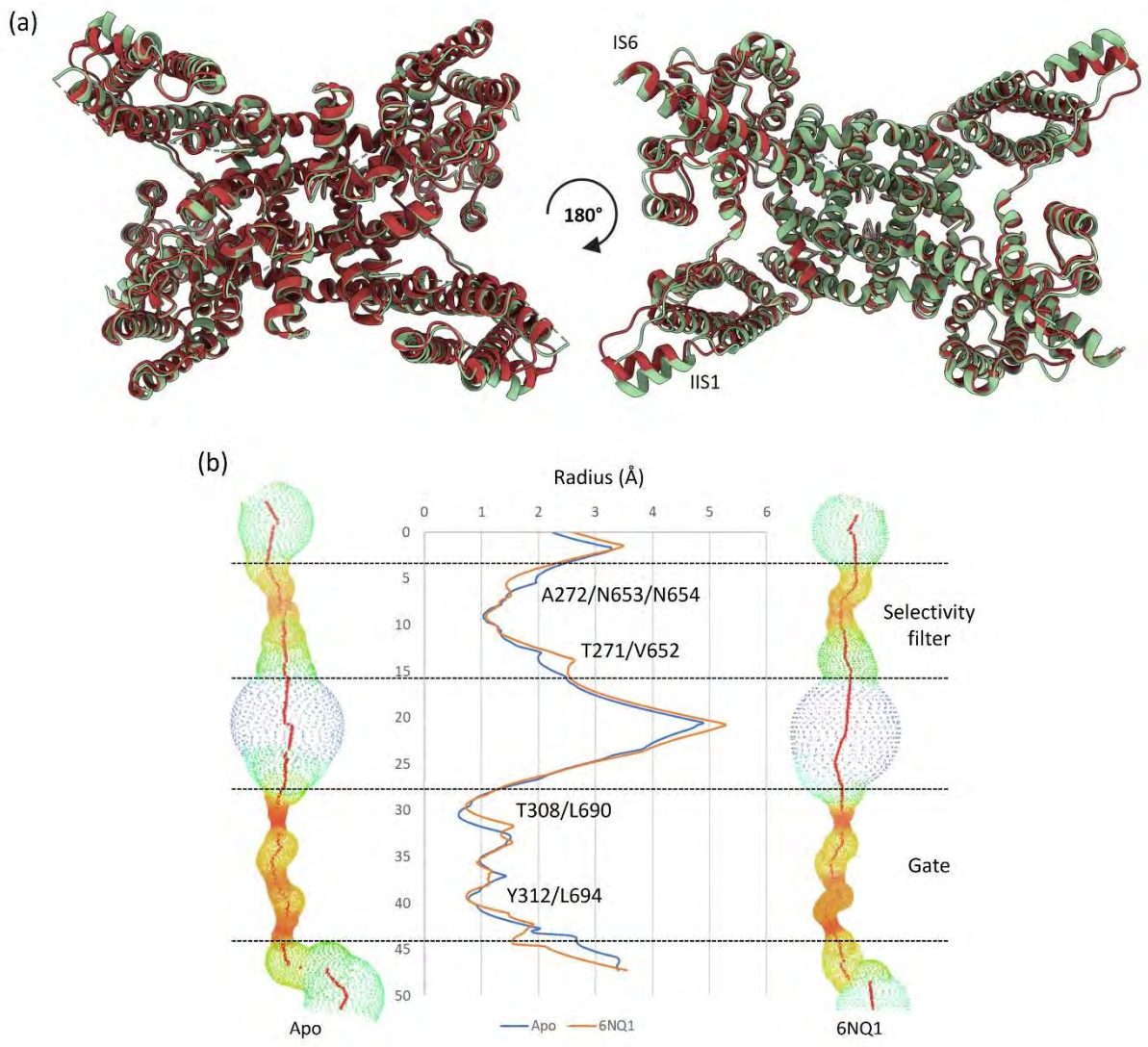

Figure 3.22: Structural alignment of TPC2-apo models
(a) Luminal view (left) and cytosolic view (right) of the TPC2-apo structure (Fig. 3.21a; green; without detergent and lipids), superimposed with the published TPC2-apo structure (red, PDB: 6NQ1; She *et al.*, 2019). **(b)** HOLE profiles of the TPC2-apo structure (left) and the published TPC2-apo structure (right) created in Coot (2.1.2). For better comparison the pore radius was plotted against the respective position in the path. Additionally, the position of the selectivity filter and gate residues are denoted.

The TPC2 map shows a strong belt of GDN surrounding the luminal part, while there is less on the cytosolic side (Fig. 3.21a; Fig. 3.23a). Thereby, especially the space between the VSD1 (IS1-S4) and VSD2 of the same subunit, respective VSD2 of the other subunit is filled with the GDN headgroups (Fig. 3.21a, Fig. 3.23a). In the cavity between VSD1 and VSD2 of the second monomer, there are additionally three lipids (Fig. 3.23a). Two of them sit in the space between IS1 and IIS5 (Fig. 3.23d) and form an interaction via R580, IS4-S5 (S200) and R 84, building a connection between the two S4-S5 linker helices from both subunits. In the same cavity a third lipid is modeled on the luminal side close to the loop linking IP2 and IS6 adjoined by two GDNs (Fig. 3.23c). In addition, another lipid occupies the PI(3,5)P_2-binding site together with a GDN headgroup (Fig. 3.23b), elucidating the importance of this site for lipid-protein interaction.

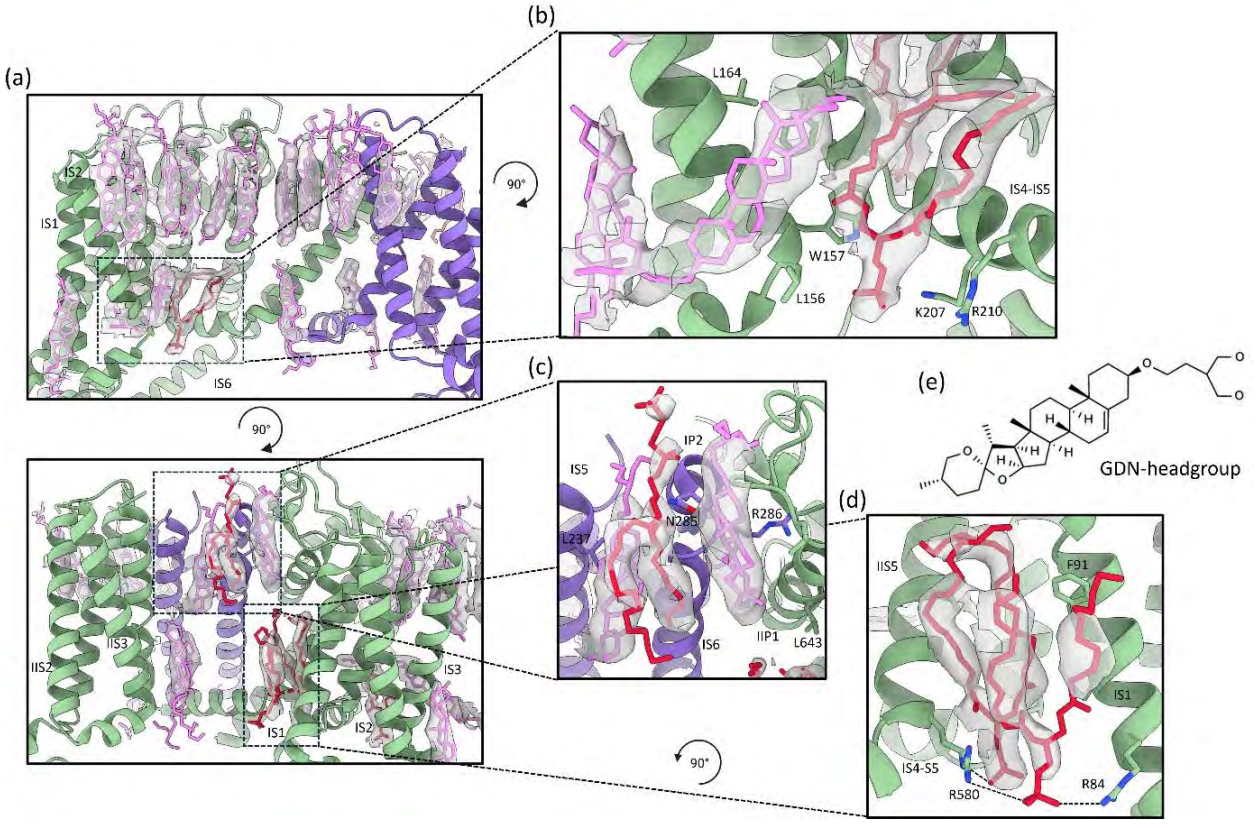

Figure 3.23: Detergent and lipids in apo TPC2

(a) Side views of the cavities between VSD1 (IS1-S4) and VDS2 (IIS1-S4) of the second subunit (up) respective VSD2 of the same subunit (down). First subunit is colored in green, the second in blue, GDN-headgroups in violet and lipids in red. **(b)** One lipid and a GDN-headgroup (violet) located at the PI(3,5)P_2-binding site with the headgroup close to K207. **(c)** One lipid (red) and two GDN-headgroups (violet) at the IP1-IS6 loop (N285). **(d)** Two lipids (red) between IS1 and IIS5. **(e)** Chemical structure of the GDN-headgroup.

3.3.5 Inhibition with naringenin in presence of PI(3,5)P_2

Purified TPC2 in GDN (1.93 mg/ml) was mixed with 0.5 µM PI(3,5)P_2 and incubated on ice for 5 min before adding 0.5 µM naringenin followed by an additional 30 min on ice incubation. 3.5 µl of the mixture was applied to a Quantifoil® R1.2/1.3 300-mesh Cu grid (2.1.3), blotted for 6.0 s under 100% humidity at 4 °C before plunged into liquid ethane using a Mark IV Vitrobot (2.2.7.2.1). 5,206 micrographs (Fig. 3.24a) were acquired on a CRYO ARM™ 200 microscope (2.2.7.2.3) and processed (7.3.3.8) to a final C2 map with a resolution of 3.81 Å (Fig. 3.24c). Additionally, the local resolution of the map was calculated, showing high resolution in the protein core and lower resolutions in the flexible parts like the VSDs and the cytosolic domains (Fig. 3.24d). Comparison of the C2 map with the published PI(3,5)P_2-bound open state (PDB: 6NQ0; She *et al.*, 2019) and the apo structure (Fig. 3.21a), shows an open conformation and a typical PI(3,5)P_2-headgroup density at the PI(3,5)P_2-binding site (Fig. 3.24e).

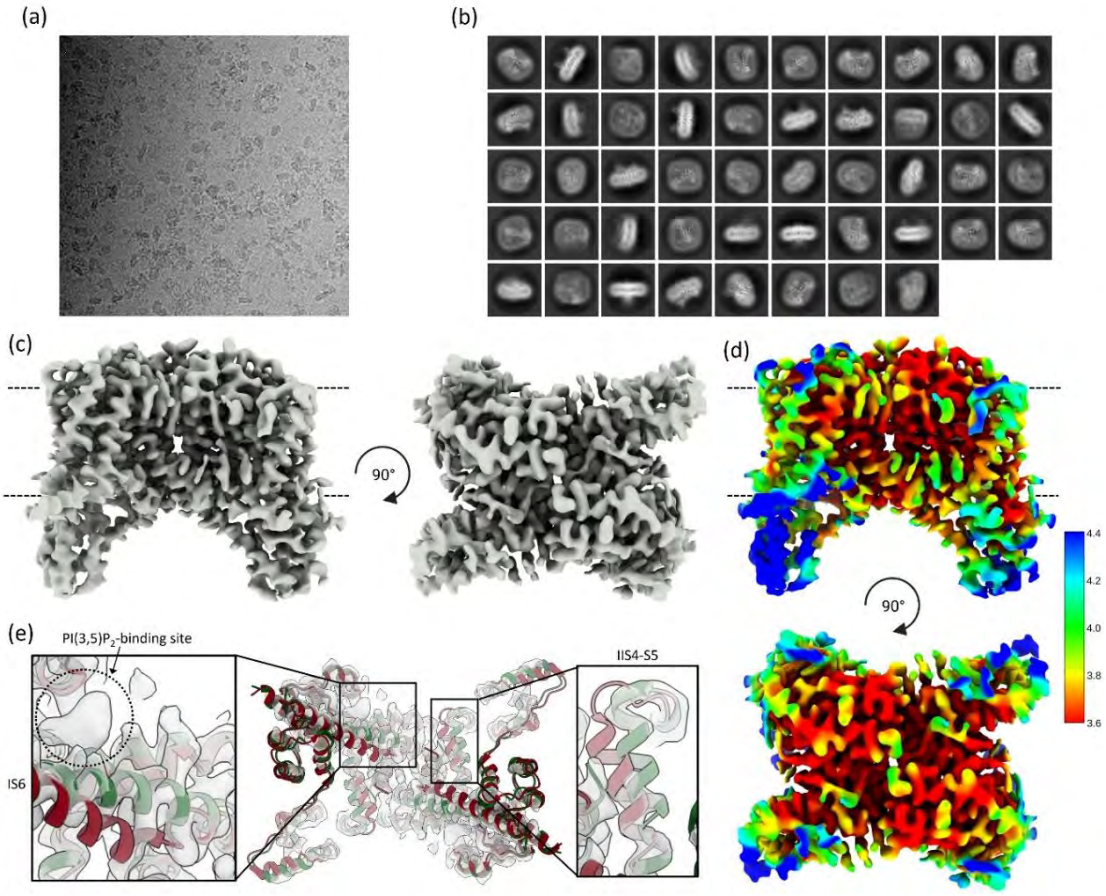

Figure 3.24: The SPA cryo-EM map of TPC2 supplemented with PI(3,5)P_2 and naringenin
(a) Example SPA cryo-EM image (2.2.7.2) of TPC2 with PI(3,5)P_2 and naringenin (Table 3.9). **(b)** 2D classes of particles used for final SPA cryo-EM maps. The 2D classes show top/bottom views, side views and tilted views, indicating good SPA cryo-EM data quality (2.2.7.2.2), suitable for 3D reconstruction. At the side views the GDN-micelle, surrounding the intermembrane part of TPC2, is clearly visible. **(c)** Side view (left) and luminal view (right) of the C2 map (3.81 Å). The densities of the surrounding detergent are excluded. Dotted lines in the side view are indicating the lipid bilayer. **(d)** Side view (up) and luminal view (down) of the local resolution of the C2 map (c). The densities of the surrounding detergent are excluded. Dotted lines in the side view are indicating the lipid bilayer. **(e)** C2 SPA cryo-EM map superimposed with the PI(3,5)P_2-bound open state (green, PDB: 6NQ0; She *et al.*, 2019) and the apo structure (Fig. 3.21a, red), to visualize the open or closed conformation. The PI(3,5)P_2-binding site is marked with a dotted circle. The alignment is shown from the cytosolic side.

Consequently, the model of TPC2 with PI(3,5)P_2 and naringenin (Fig. 3.25a) was built (2.2.7.2.4), based on the PI(3,5)P_2-bound open structure (PDB: 6NQ0; She *et al.*, 2019). Residues 1-38, 241-251, 347-353, 525-538, 609-619, 702-752 are disordered and were not modeled. The PI(3,5)P_2-headgroup density at the PI(3,5)P_2-binding site was used to model the lipid (Fig. 3.25b). Naringenin was modeled into the two densities inside the channel pore close to the gate (Fig. 3.25d). Detergent and lipids were also added and the final model was validated (Fig. 3.25c; 2.2.7.2.4). Improvement of the model quality is necessary for more detailed interpretation and future publications.

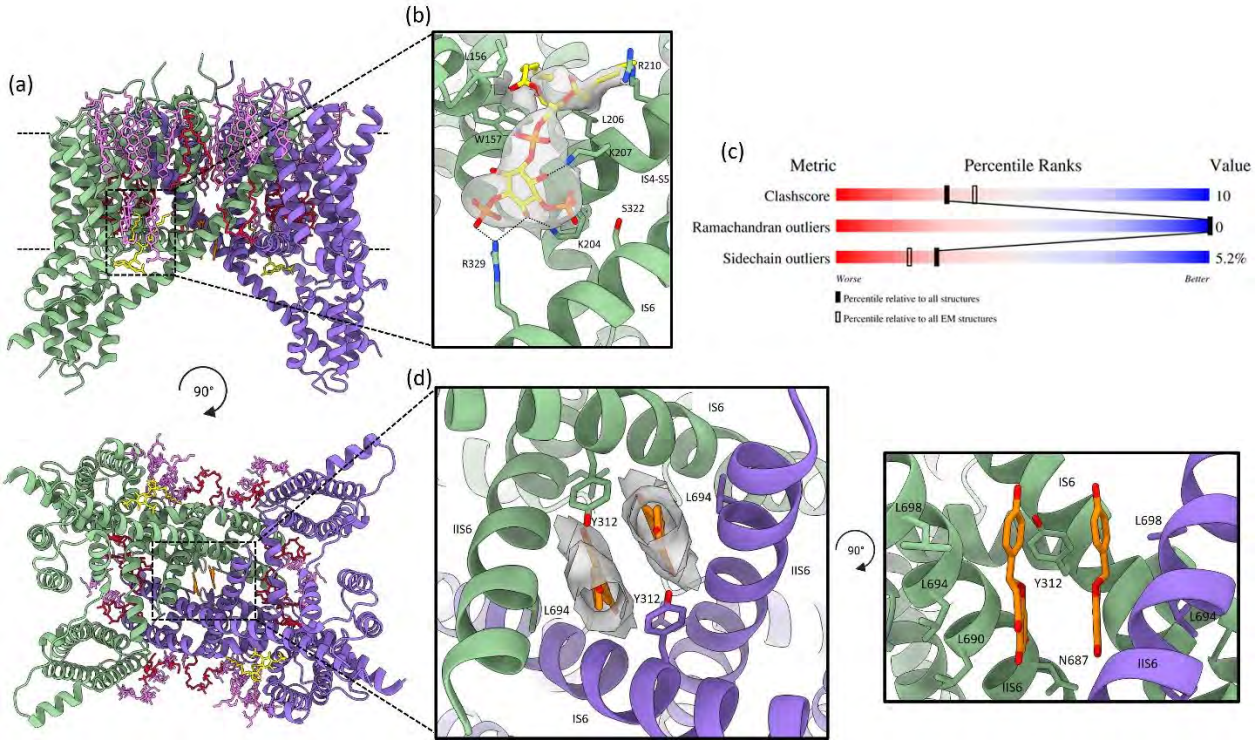

Figure 3.25: Model of TPC2 with PI(3,5)P_2 and naringenin

(a) Side view (left) and cytosolic view (right) of the structure of TPC2 supplemented with PI(3,5)P_2 and naringenin based on the C2 map (Fig. 3.24c). One subunit is colored in green, the other in blue, GDN-headgroups (Fig. 3.23e) in violet and lipids in red. PI(3,5)P_2 is highlighted in yellow and naringenin in orange. Dotted lines in the side view are indicating the lipid bilayer. **(b)** PI(3,5)P_2-binding site. PI(3,5)P_2 is highlighted in yellow and coordination with neighboring residues is marked with dotted lines. Additionally, the PI(3,5)P_2-density is shown in grey. Surrounding GDN-headgroups are removed for better visualization. **(c)** Validation report of the TPC2 structure with PI(3,5)P_2 and naringenin (a) without detergent and lipids, gained with the wwPDB Validation System (2.1.2). **(d)** Localization of naringenin. Naringenin is highlighted in orange. The upper image shows a cytosolic view and the density of naringenin in grey. The lower image shows a side view of the naringenin localization with helix IS6 of one subunit removed for better visualization.

The model was additionally validated by structural alignment with the published PI(3,5)P_2-bound open state (proteins without ligands; PDB: 6NQ0; She *et al.*, 2019). Again the models were practically identical with a rmsd of 1.82 Å and only a small deviation in the IIS1 helix (Fig. 3.26a). Also the localization and orientation of PI(3,5)P_2 is identical. Furthermore, the pore diameter of the two structures was investigated using the `HOLE´ representation tool in Coot (2.1.2). This comparison stated that both structures show a closed selectivity filter and an open gate (Fig. 3.26b), while the selectivity filter at the residues A271/V652

and the gate at Y312/L694 are more closed in the PI(3,5)P_2 and naringenin structure. The PI(3,5)P_2- and naringenin-bound state reveals an overall open state similar to the published PI(3,5)P_2-bound open state (PDB: 6NQ0; She *et al.*, 2019). The two main deviations are most likely resulting from the presence of naringenin, which is located close to Y312 (Fig. 3.25d).

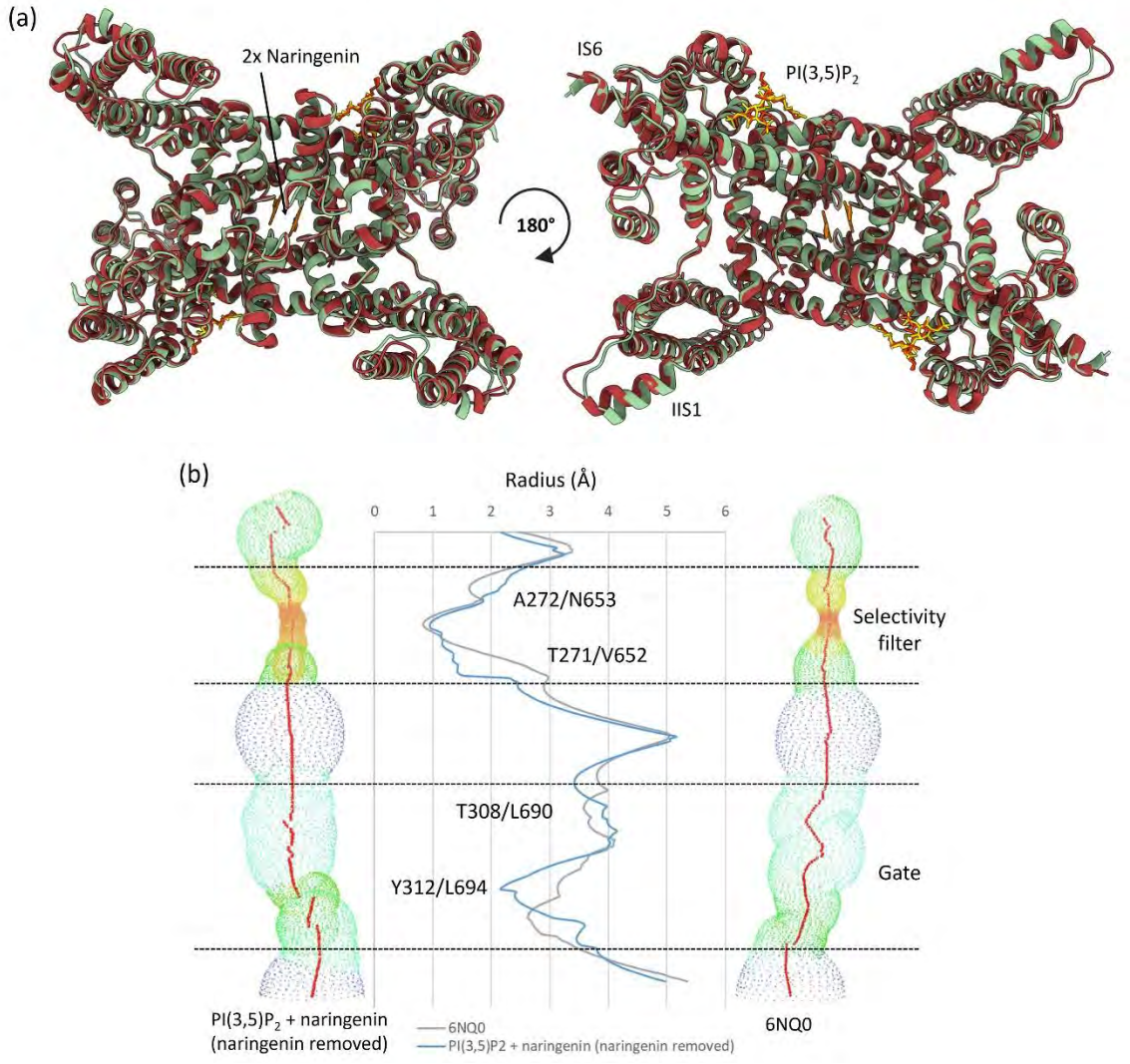

Figure 3.26: Structural alignment of TPC2 PI(3,5)P_2-bound open states
(a) Luminal view (left) and cytosolic view (right) of the TPC2 structure with PI(3,5)P_2 and naringenin (Fig. 3.25a; green; only with PI(3,5)P_2 and naringenin), superimposed with the published PI(3,5)P_2-bound open structure (red, PDB: 6NQ0; She *et al.*, 2019). PI(3,5)P_2 is highlighted in yellow (this work), respective light red (6NQ0), and naringenin in orange. **(b)** HOLE profiles of the TPC2 structure with PI(3,5)P_2 and naringenin (left) and the published PI(3,5)P_2-bound open state (right) created in Coot (2.1.2). For comparison of the actual pore diameter, naringenin molecules were deleted from the PI(3,5)P_2 and naringenin structure and the pore radius was plotted against the respective position in the path. Additionally, the position of the selectivity filter and gate residues are denoted.

When comparing the pores of the PI(3,5)P_2 and naringenin structure and the apo state (Fig. 3.25a), the diameter of the gates is very similar, as naringenin is blocking the channel. Interestingly, the blockage results in a pore diameter nearly identical with that of the apo structure.

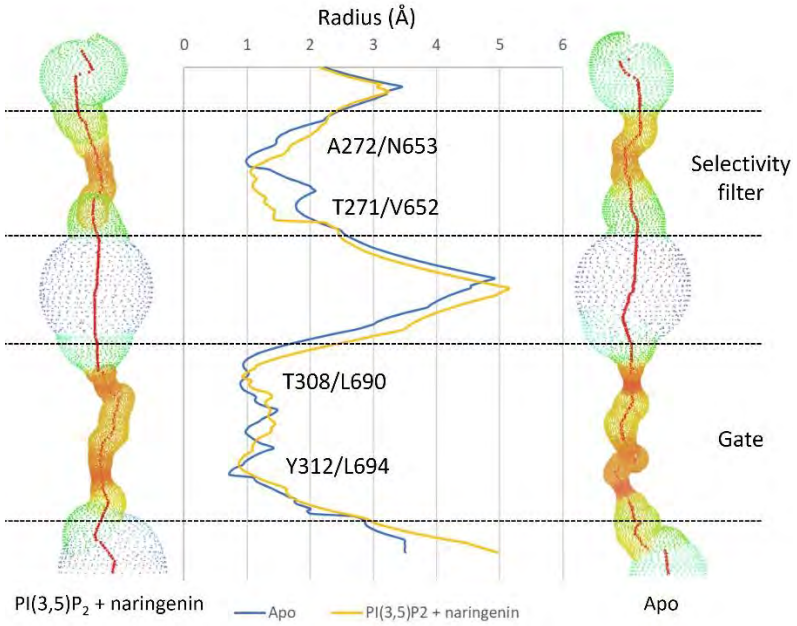

Figure 3.27: Pore of the PI(3,5)P_2 and naringenin state compared with the apo state
HOLE profiles of the TPC2 structure with PI(3,5)P_2 and naringenin (left) and the apo state (right; Fig. 3.25a) created in Coot (2.1.2). For comparison the pore radius was plotted against the respective position in the path. Additionally, the position of the selectivity filter and gate residues are denoted.

The PI(3,5)P_2- and naringenin-bound state again shows the GDN-headgroup belt surrounding the luminal side (Fig. 3.28a), but there is a difference in lipid localization and orientation compared to the apo state. One lipid is located at W669 of IIS6 on the luminal side between VSD1 and VSD2 of the second subunit (Fig. 3.28b), which is not present in the apo structure (Fig. 3.23a), while the lipid at IP2 is missing (Fig. 3.23c). What is striking is the proximity of the lipids to pore-forming domains (IP2 in apo; IIS6 in open), which could suggest a role in the stabilization of the closed/open state. However, the function of these lipids needs further investigation. On the cytosolic side a lipid close to the loop between IIS4 and IIS4-S5 (Fig. 3.28c) is present, which is a GDN-headgroup in the apo structure (Fig. 3.23a). This difference might be related to the movement of IIS4-S5 for channel opening (Fig. 1.13e) that creates the space for the lipid, which might then stabilize the open conformation. In the cavity between VSD1 and VSD2 of the same subunit lipids seem to switch coordination. In the closed apo structure two lipids link IS4-S5 with IIS4-S5 (Fig. 3.23d). In the open structure there is only one lipid, while two lipids are located along IIS4-S5 (Fig. 3.28d). From the two lipids located closest to VSD1, the fatty acid tails are rotated away from the protein pore, most likely by the outward movement of helix IIS4-S5 and IIS6 in channel opening. Further, the headgroup of the lipid located close to R84, S200 and R580 is shifted in contrast to the apo state, which might result from nearby PI(3,5)P_2-binding at IS4-S5 (Fig. 3.28d). The declared differences in lipid localization and lipid-protein interaction between the closed and open state are simple descriptions of the observed changes and need further studies to verify the precise role of the lipids in the respective protein conformation.

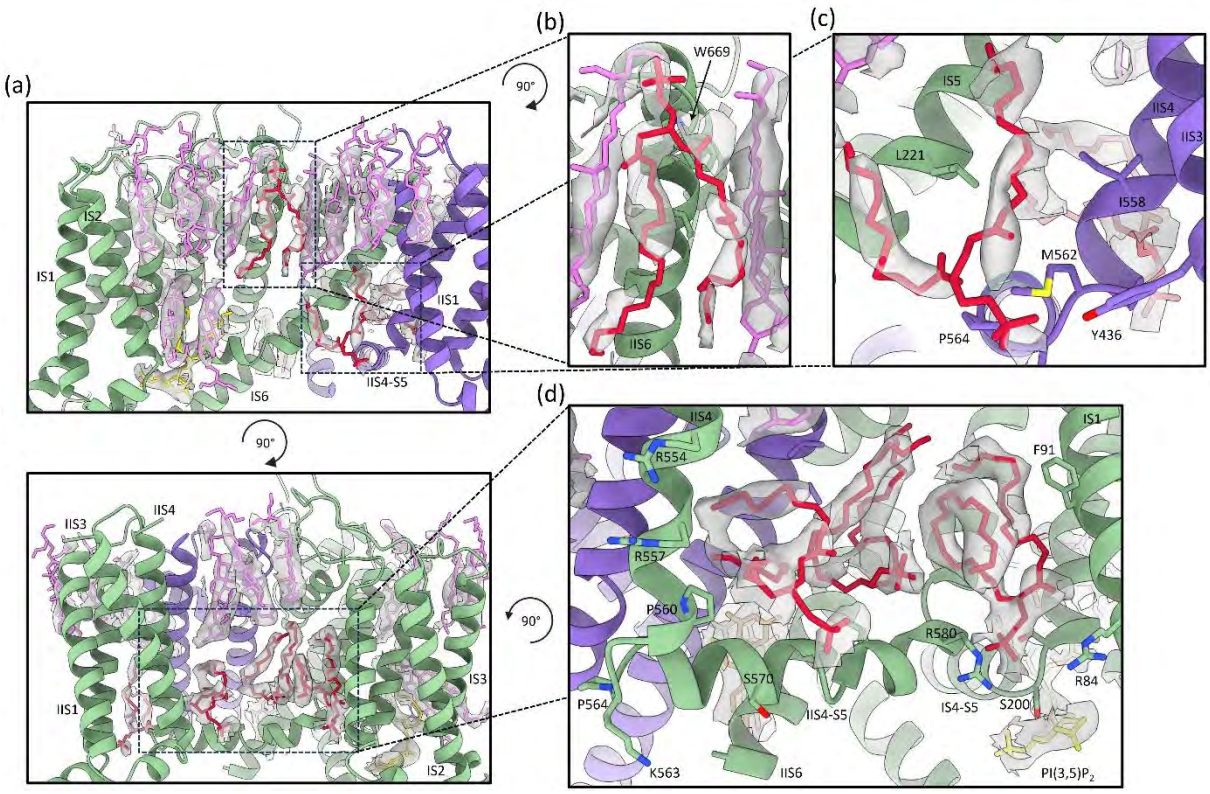

Figure 3.28: Detergent and lipids in TPC2 bound with PI(3,5)P_2 and naringenin

(a) Side views of the cavities between VSD1 (IS1-S4) and VSD2 (IIS1-S4) of the second subunit (up) respective VDS2 of the same subunit (down). First subunit is colored in green, the second in blue, GDN-headgroups in violet, lipids in red and PI(3,5)P_2 in yellow. **(b)** Lipid (red) and two GDN-headgroups (violet) at the begin of IIS6 (W669). **(c)** Lipid (red) at IS6 and the loop between IIS4 and IIS4-S5. **(d)** Three lipids (red) between IS1 and IIS4, along the IIS4-S5 linker helix. Sugar tails are twisted away from the protein center. Helix IIS3 is removed for better visualization of helix IIS4.

3.3.6 The agonist SGA-111

For the SGA-111-bound TPC2 structure the purified protein in GDN (1.68 mg/ml) was mixed with SGA-111 in a molar ratio of 1:40 (TPC2 : SGA-111), incubated on ice for 30 min and vitrified (Quantifoil® R1.2/1.3 300-mesh Cu grid (2.1.3), blotting time: 5.5 s; 2.2.7.2.1). After screening for a high-quality grid (2.2.7.2.2), 8,418 micrographs (Fig. 3.29a) were acquired on a CRYO ARM™ 200 microscope (2.2.7.2.3) and processed (7.3.3.5) to a final C2 map with a resolution of 3.58 Å (Fig. 3.29c). Additionally, the local resolution of the map was calculated, showing high resolution in the protein core and lower resolutions in the flexible parts like the VSDs and the cytosolic domains (Fig. 3.29d).

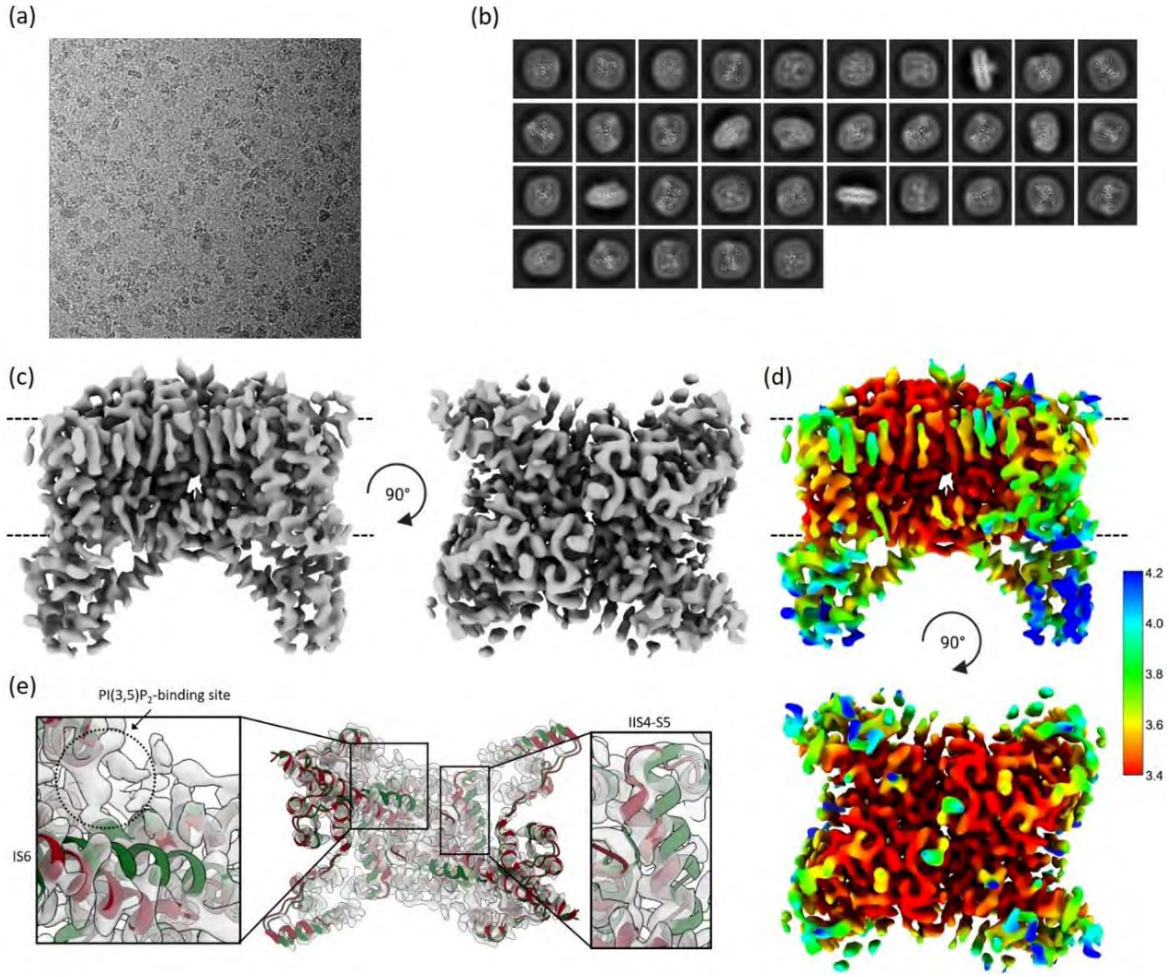

Figure 3.29: The SPA cryo-EM map of TPC2 in the presence of SGA-111
(a) Example SPA cryo-EM image (2.2.7.2) of TPC2 supplemented with SGA-111 (Table 3.9). **(b)** 2D classes of particles used for final TPC2-SGA-111 SPA cryo-EM maps. The 2D classes show top/bottom views, side views and tilted views, indicating good SPA cryo-EM data quality (2.2.7.2.2), suitable for 3D reconstruction. At the side views the GDN-micelle, surrounding the intermembrane part of TPC2, is clearly visible. **(c)** Side view (left) and luminal view (right) of the TPC2-SGA-111 C2 map (3.58 Å). The densities of the surrounding detergent are excluded. Dotted lines in the side view are indicating the lipid bilayer. **(d)** Side view (up) and luminal view (down) of the local resolution of the TPC2-SGA-111 C2 map (c). The densities of the surrounding detergent are excluded. Dotted lines in the side view are indicating the lipid bilayer. **(e)** SPA cryo-EM map of TPC2- SGA-111 superimposed with the TPC2 PI(3,5)P_2-bound intermediate state (green, PDB: 6NQ0; She *et al.*, 2019) and the apo structure (Fig. 3.21a, red), to visualize the intermediate or closed conformation. The PI(3,5)P_2-binding site is marked with a dotted circle. The alignment is shown from the cytosolic side.

Comparison of the TPC2-SGA-111 C2 map with the published PI(3,5)P_2-bound open state (PDB: 6NQ0; She *et al.*, 2019) and the apo structure (Fig. 3.21a), shows a mixed conformation (Fig. 3.29e). As the density of helix IS6 clearly fits with the apo, closed structure, helix IIS4-S5 shows an intermediate state, where especially the area of the important gating residues Lys563, Pro564 and Met565 (Fig. 1.13) is shifted towards the open state. In addition, the map shows a non-protein density in the PI(3,5)P_2-binding site (Fig.3.29e) neither present in the apo (Fig.3.20e), nor in the PI(3,5)P_2-bound state (Fig.3.23e), indicating SGA-111 is bound in this area.

Due to the mixed conformation of the map, the final particles were further analyzed on `3D variability´ to identify different states (intermediate/closed) of TPC2 supplemented with SGA-111. For that, the 107,627 particles included in the final maps were hetero-refined in cryoSPARC (2.1.2), using the published PI(3,5)P2-bound open state (EMD-0477; She et al., 2019) and apo (EMD-0478; She et al., 2019) maps as references, resulting in two classes containing 60,757 particles respectively 46,870 particles (Fig. 3.30). The two classes were further processed separately by `non-uniform refinement´ (2.2.7.2.4) in C1- and C2-symmetry, to gain the final maps (Fig. 3.30).

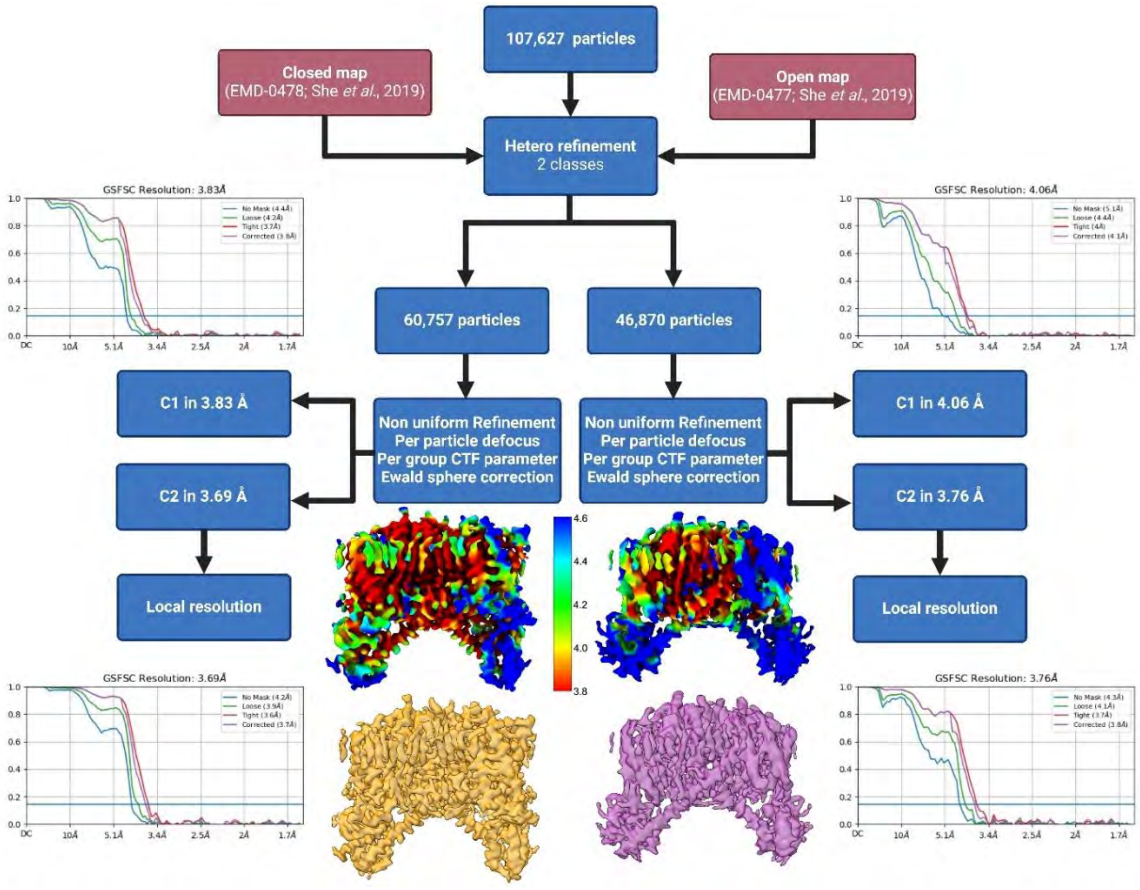

Figure 3.30: Processing workflow identifying 3D variations in TPC2 supplemented with SGA-111

SPA cryo-EM image processing workflow to detect structural deviations in the particles of the final map of TPC2 supplemented with SGA-111 (Fig. 3.29c). The 107,627 particles (Fig. 3.29b) were hetero-refined with the published PI(3,5)P_2-bound open state (EMD-0477; She et al., 2019) and apo (EMD-0478; She et al., 2019) maps as references. This resulted in two classes containing 60,757 particles respectively 46,870 particles. Non-uniform refinement of each class was performed separately. The 60,757 particles resulted in a C1 map with a final resolution of 3.83 Å and a C2 map with 3.69 Å (yellow), whereas the 46,870 particles resulted in a C1 map with a final resolution of 4.06 Å and a C2 map with 3.76 Å (purple). For the C2 maps, also the local resolution was determined. The image was created with BioRender (2.1.2).

Alignment of these maps shows different conformations (Fig. 3.31). As the intra-membrane and luminal parts of the two maps are similar, the C2 map resulting from the 46,870 particles exhibits more densely packed and upwards shifted cytosolic domains (Fig. 3.31). Also, helix IS6 is shifted upwards (Fig. 3.31), away from the channels pore, indicating a closed (60,757 particles) and an intermediate state (46,870 particles) of TPC2 in a ratio of 2:3 (intermediate : closed) when supplemented with SGA-111.

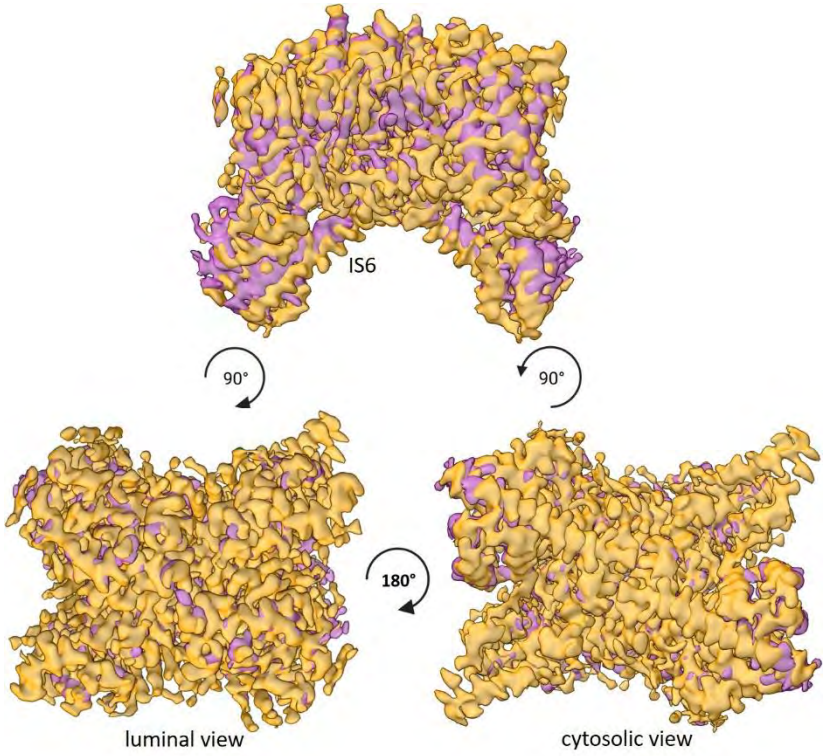

Figure 3.31: Alignment of the TPC2-SGA-111 maps
Comparison of the final SPA cryo-EM maps of TPC2 supplemented with SGA-111. The two maps received from hetero-refinement of the cleaned 107,627 particles with intermediate and closed TPC2-templates, are aligned to identify differences. The C2 map derived from the 60,757 particles (3.69 Å) is colored in yellow, the C2 map from the 46,870 (3.76 Å) is colored in purple.

Comparison with the published PI(3,5)P2-bound open state (PDB: 6NQ0; She et al., 2019) and the apo structure (Fig. 3.21a) indicates that the map consisting of 60,757 particles, shows a closed conformation with IS6 and IIS4-S5 in similar orientation than in the apo state (Fig. 3.32a) denominated as closed SGA-111-bound TPC2. The second map, consisting of 46,870 particles, shows a state with IS6 in similar orientation than the apo state, but shifted more towards the membrane (Fig. 3.32b). Helix IIS4-S5 shows a weak density, hinting similar orientation than in the apo state (Fig. 3.32b). Resuming these findings, the map shows a conformation of TPC2 different from the already described states denominated intermediate SGA-111-bound TPC2.

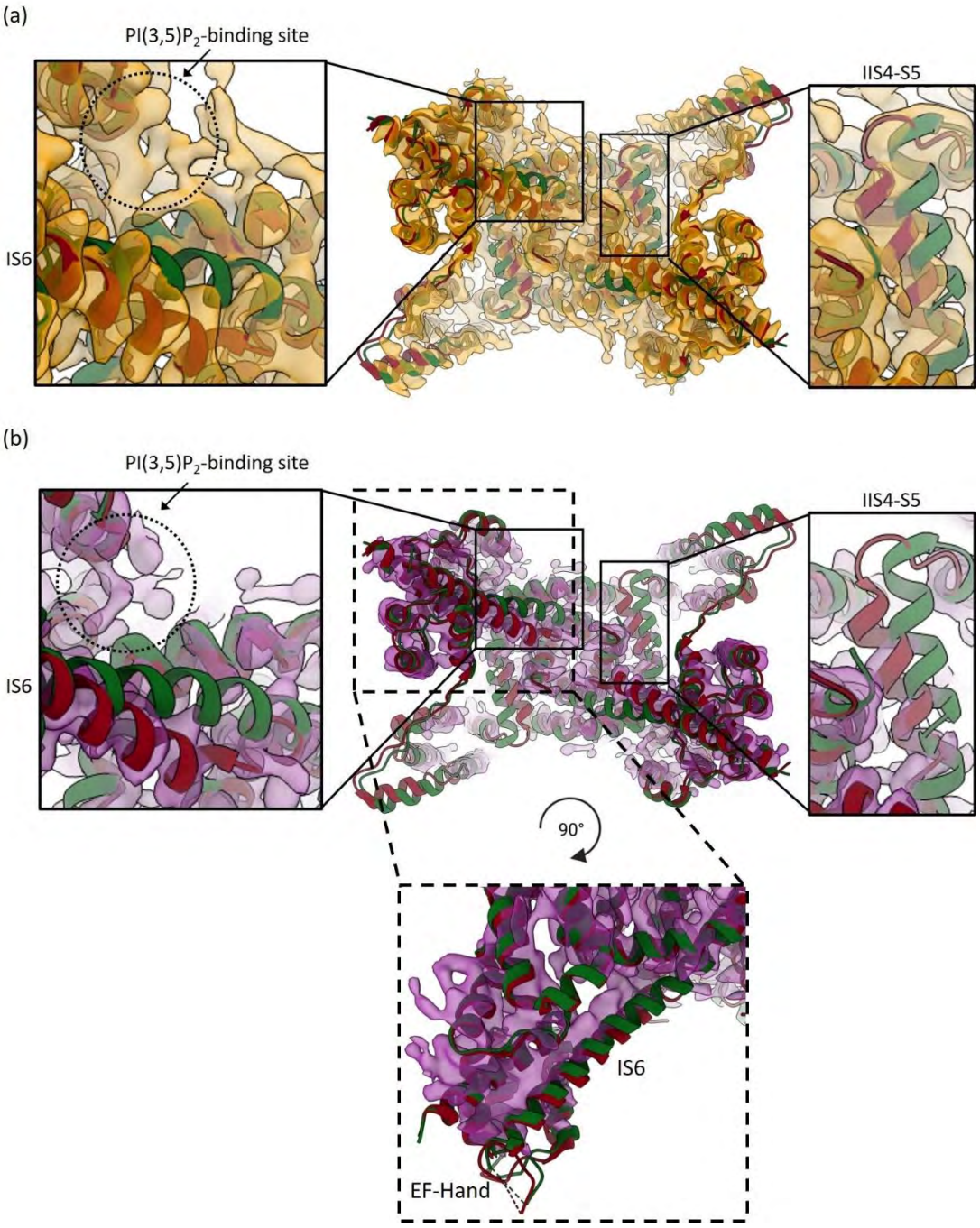

Figure 3.32: The SPA cryo-EM closed structure of TPC2 with SGA-111
(a) Closed SPA cryo-EM map of TPC2-SGA-111 (Fig. 3.30 (yellow)) superimposed with the TPC2 PI(3,5)P_2-bound open state (green, PDB: 6NQ0; She *et al.*, 2019) and the apo structure (Fig. 3.21a, red), to visualize the intermediate or closed conformation. The PI(3,5)P_2-binding site is marked with a dotted circle. The alignment is shown from the cytosolic side. **(b)** Intermediate SPA cryo-EM map of TPC2-SGA-111 (Fig. 3.30 (purple)) superimposed with the TPC2 PI(3,5)P_2-bound open state (green, PDB: 6NQ0; She *et al.*, 2019) and the apo structure (Fig. 3.21a, red), to visualize the intermediate or closed conformation. The PI(3,5)P_2-binding site is marked with a dotted circle. The alignment is shown from the cytosolic side. Additionally, one cytosolic domain is shown as sideview.

The final model for the closed conformation (Fig. 3.33a) was built, based on the apo structure (Fig. 3.21a). Residues 1-38, 241-251, 347-353, 526-538, 609-619, 702-752 are disordered in the closed map and were not modeled and the final validation (2.2.7.2.4) gave sufficient parameters (Fig. 3.33b). The ligand SGA-111 was placed in a density close to the PI(3,5)P_2-binding site. Detergent and lipids were also added into non-protein densities, resulting in the similar GDN-belt around the luminal part as in all other TPC2 models (Fig. 3.21a, Fig. 3.25a).

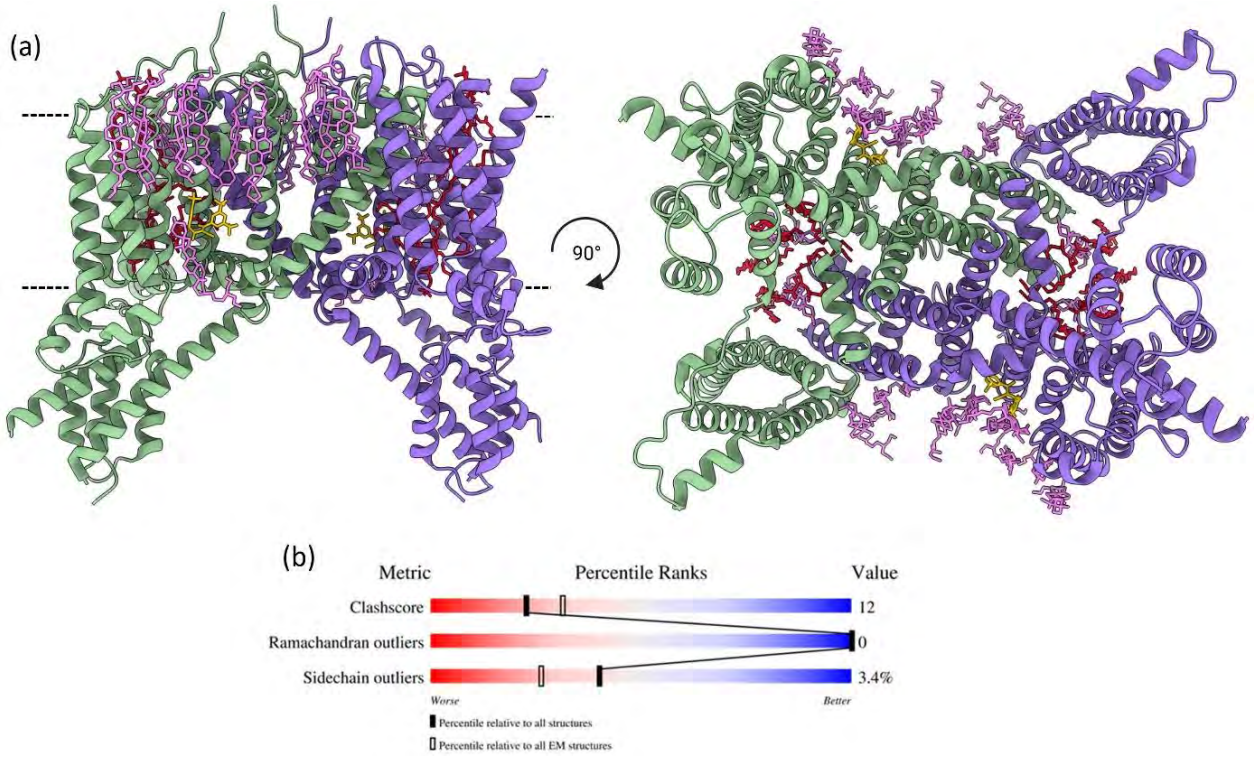

Figure 3.33: SPA cryo-EM closed structure of TPC2 with SGA-111
(a) Side view (left) and cytosolic view (right) of the closed TPC2-SGA-111 model based on the closed SPA cryo-EM map of TPC2-SGA-111 (Fig. 3.30 (yellow)). One subunit is colored in green, the other in blue, CHS in violet and lipids in red. The agonist SGA-111 is highlighted in gold. Dotted lines in the side view are indicating the lipid bilayer. **(b)** Validation report of the TPC2-SGA-111 model (a) gained with the wwPDB Validation System (2.1.2).

The model quality and state were additionally verified by structural alignment with the apo state (Fig. 3.21a; proteins without ligands) resulting in a rmsd of 2.19 Å (Fig. 3.34a). Also, the pore diameter of the two structures was investigated using the `HOLE´ representation tool in Coot (2.1.2). This comparison indicated a more closed selectivity filter of the SGA-111 bound structure at T271/V652 and an identical closed gate (Fig. 3.34b).

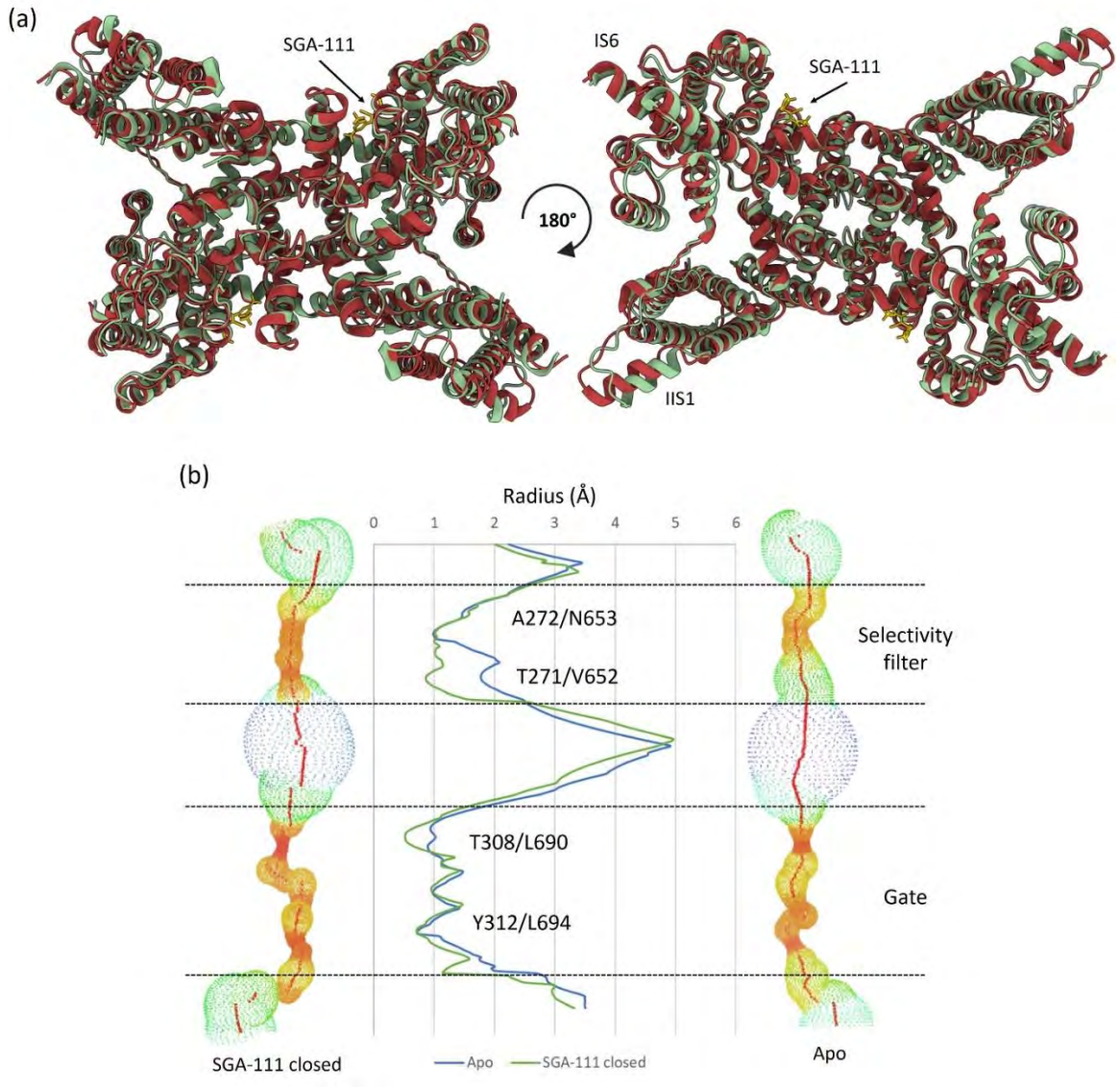

Figure 3.34: Structural alignment of the TPC2 apo and SGA-111 closed state
(a) Luminal view (left) and cytosolic view (right) of the closed TPC2 structure with SGA-111 (Fig. 3.33a; green; only with SAG-111), superimposed with the apo structure (Fig. 3.21a; protein without ligands). SGA-111 is highlighted in gold. **(b)** HOLE profiles of the closed TPC2-SGA-111 structure (left) and the apo state (right) created in Coot (2.1.2). For comparison of the actual pore diameter, the pore radius was plotted against the respective position in the path. Additionally, the position of the selectivity filter and gate residues are denoted.

In the SGA-111-bound closed map, there are no obvious lipid densities between VSD1 and VSD2 of the second subunit, so only GDN-headgroups and no lipids were modelled there (Fig. 3.33a). In the cavity between VSD1 and VSD2 of the same subunit there are two lipids and two GDN-headgroups on the cytosolic side between IIS4 and IS1 (Fig. 3.35b). Compared to the apo state the localization of the GDNs and the lipid interacting with the IP1-IS6 loop is the same (Fig. 3.23c), while in the SGA-111-bound state there is one additional lipid closer to helix IIS4 (Fig. 3.35b). Due to the localization between VSD2 and pore-building domains (IP1 and IS6), these two lipids might play a role in channel opening or stabilization of a certain conformation. In addition, there are lipids located along IIS4-S5 (Fig. 3.35c). The two lipids linking IIS4-S5 (R580) and IS4-S5 (S200) are identical to the apo state (Fig. 3.23d) while the third one is located

along IIS4-S5 like in the PI(3,5)P_2-naringenin-bound state (Fig. 3.28d). The presence of these lipids in ligand-bound states indicates a function in channel opening, which requires further research.

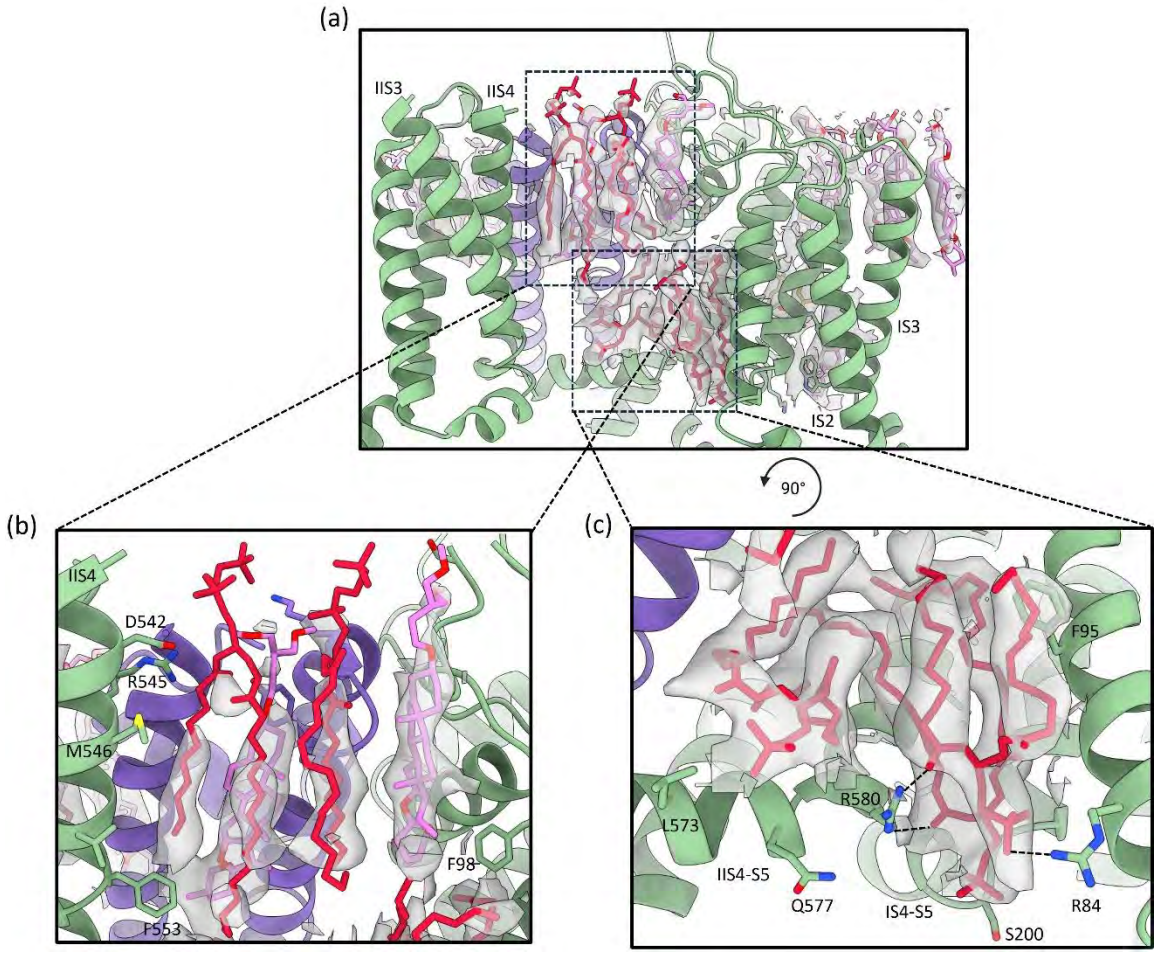

Figure 3.35: Lipids in the closed state of TPC2-SGA-111
(a) Side view of the cavity between VSD1 (IS1-S4) and VSD2 (IIS1-S4) of the same subunit. First subunit is colored in green, the second in blue, GDN-headgroups in violet and lipids in red. **(b)** Two lipids (red) and two GDN-headgroups (violet) between IIS4 and IS1 (F98). Helix IIS3 is removed for better visualization of helix IIS4. **(c)** Three lipids (red) between IS1 (right, F95) and IIS4 linking the IS4-S5 and the IIS4-S5 helix. Interactions with neighboring residues are indicated by dotted lines. Helix IIS3 and IS6 are removed for better visualization of the linker helix IIS4-S5.

For the intermediate map (Fig. 3.30 (purple)), the atomic model (Fig. 3.36a) was built starting from the closed TPC2-SGA-111 state (Fig. 3.33a). Residues 1-38, 108-114, 241-251, 347-353, 408-417, 526-538, 609-619, 702-752 are disordered in the closed map and were not modeled. SGA-111 was placed in a density close to the PI(3,5)P_2-binding site, and detergent and lipids were also added resulting in the similar GDN-belt around the luminal part as in all other models (Fig. 3.21a, Fig. 3.25a; Fig. 3.33a). Validation (Fig. 3.36b; 2.2.7.2.4) showed a twice as high clashscore in comparison to the other models. This drastic increase results from the low resolution of the map in the cytosolic parts (Fig. 3.30) combined with the dense packing of these helices.

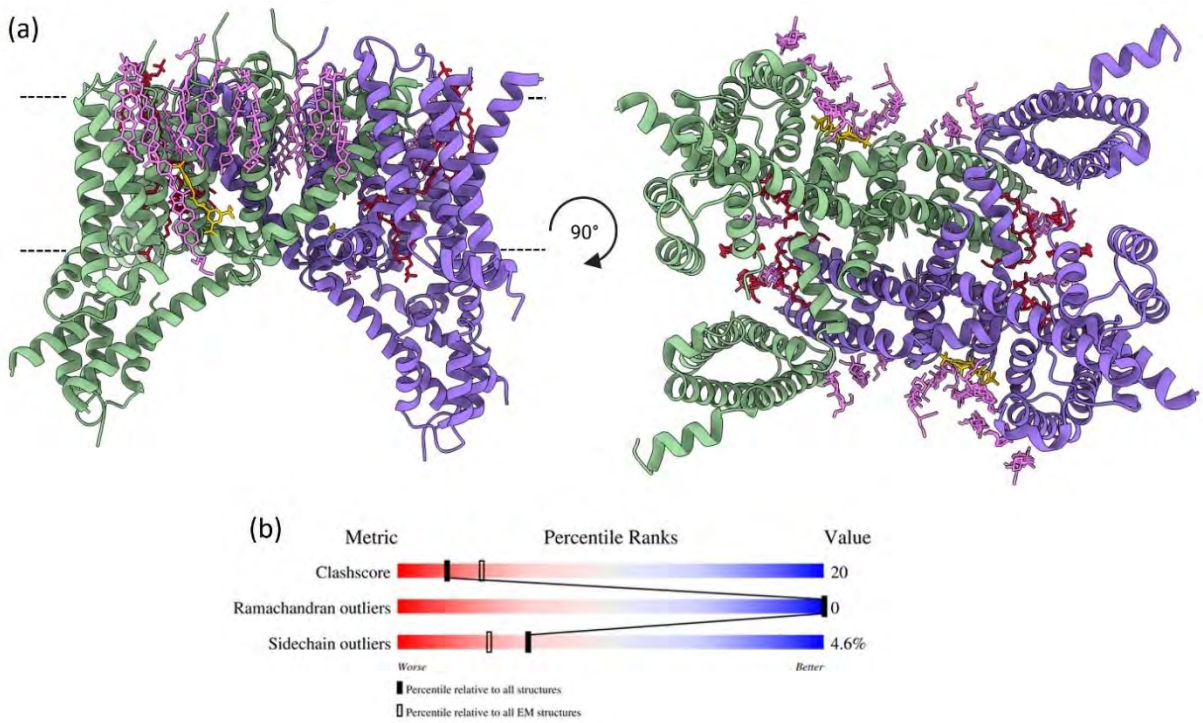

Figure 3.36: SPA cryo-EM intermediate structure of TPC2 with SGA-111
(a) Side view (left) and cytosolic view (right) of the intermediate TPC2-SGA-111 state based on the intermediate SPA cryo-EM map of TPC2-SGA-111 (Fig. 3.30 (purple)). One subunit is colored in green, the other in blue, CHS in violet and lipids in red. The agonist SGA-111 is highlighted in gold. Dotted lines in the side view are indicating the lipid bilayer. **(b)** Validation report of the intermediate TPC2-SGA-111 model (a) from the wwPDB Validation System (2.1.2).

To verify the state, the TPC2-SGA-111 intermediate structure was aligned with the apo state (Fig. 3.21a) and the published PI(3,5)P_2-bound open state (PDB: 6NQ0; She *et al.*, 2019). The rmsd for the TPC2-SGA-111 intermediate state to the apo state is 63.98 Å and 3.22 Å to the PI(3,5)P_2-bound open state. The big deviation from the apo state originates from the conformational changes in the cytosolic domains. Also, the pore diameter of the structures was investigated via the `HOLE´ representation tool in Coot (2.1.2). While the selectivity filter is of similar dimension in all three states, the gate is a slightly more open at position T308/L690 (Fig. 3.37c).

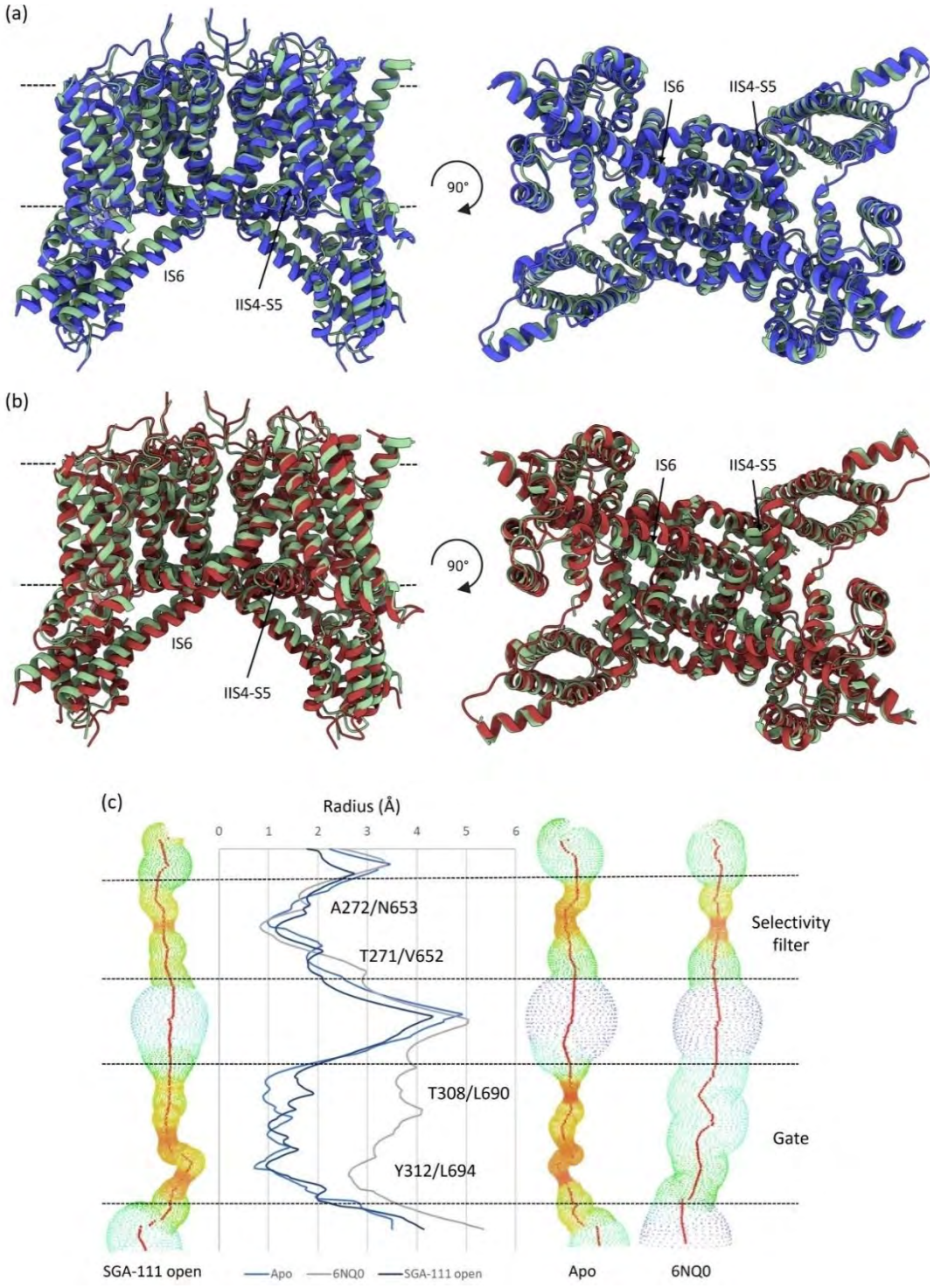

Figure 3.37: SGA-111 intermediate state in comparison to previous TPC2 states

(a) Side view (left) and cytosolic view (right) of the intermediate TPC2 structure with SGA-111 (Fig. 3.36a; green; no ligands) superimposed with the apo structure (Fig. 3.21a; blue; without ligands). **(b)** Side view (left) and cytosolic view (right) of the intermediate TPC2-SGA-111 structure (Fig. 3.36a; green; no ligands) superimposed with the PI(3,5)P_2-bound open state (red; PDB: 6NQ0; She *et al.*, 2019; without ligands). **(c)** HOLE profiles of the intermediate TPC2-SGA-111 structure, the apo state and the PI(3,5)P_2-bound open state created in Coot (2.1.2). For comparison of the actual pore diameter, the pore radius was plotted against the respective position in the path. Additionally, the position of the selectivity filter and gate residues are denoted.

Lipids and detergent were also modeled in the SGA-111 bound intermediate structure (Fig. 3.36a). Lipids between the IP1-IS6 and helix IIS4 (Fig. 3.38b) are identic to the SGA-111 close state (Fig. 3.35b). The main difference is the lack of the cytosolic lipid interacting with R84 in apo (Fig. 3.23d) and the SGA-111 bound closed state (Fig. 3.35c). Due to the created space, the remaining lipid can shift towards R60, thereby interacting with the cytosolic domain (Fig. 3.38c). The second lipid in the SGA-111 intermediate state is located along IIS4-S5 (Fig. 3.38c) like in the SGA-111 closed state (Fig. 3.35c), with the difference that one fatty acid tail is pointing towards IIS4 instead of the bilayer interface.

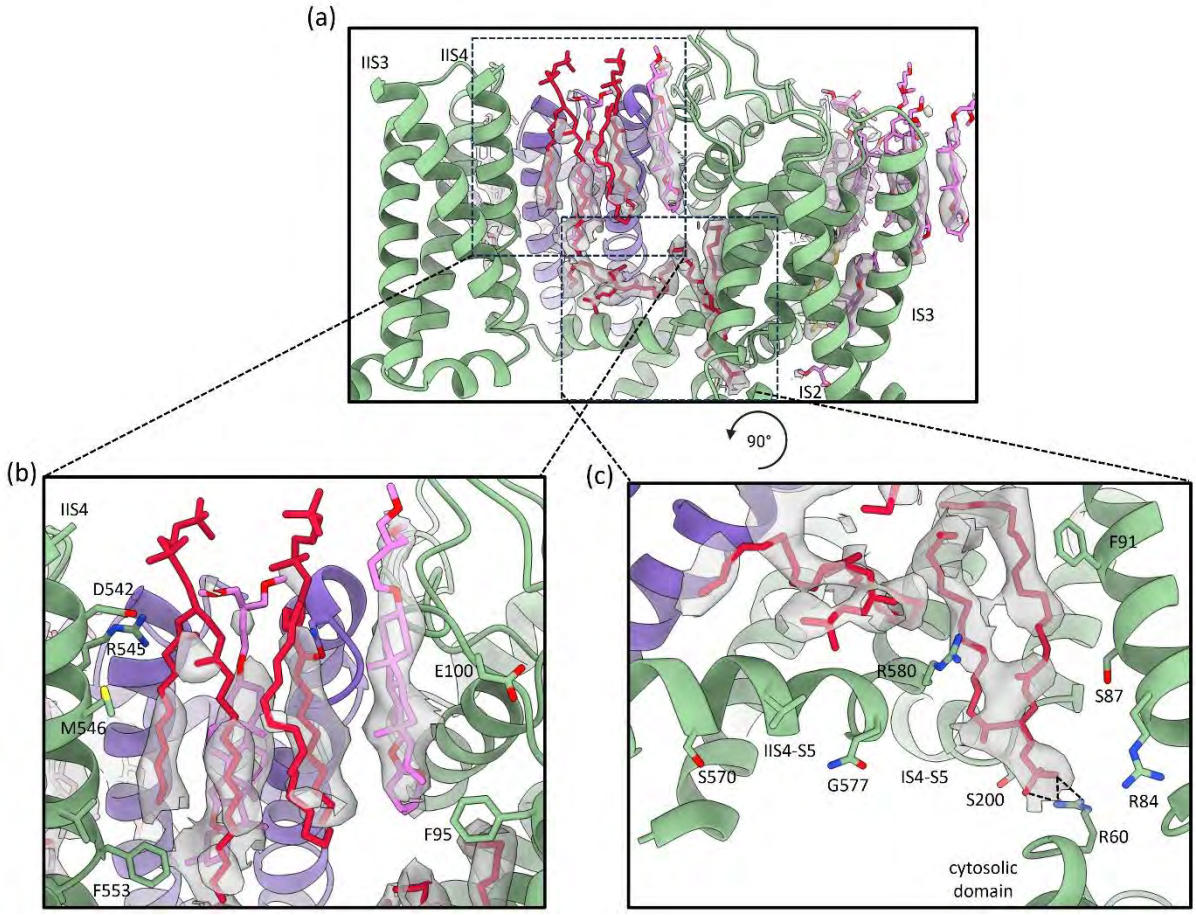

Figure 3.38: Lipids in the intermediate TPC2-SGA-111 state
(a) Side view of the cavity between VSD1 (IS1-S4) and VSD2 (IIS1-S4) of the same subunit. First subunit is colored in green, the second in blue, GDN-headgroups in violet and lipids in red. **(b)** Two lipids (red) and two GDN-headgroups (violet) between IIS4 and IS1 (F98). Helix IIS3 is removed for better visualization of helix IIS4. **(c)** Two lipids (red) between IS1 (right, F91) and IIS4 (left, R557), along the IIS4-S5 linker helix. Interactions with neighboring residues are indicated by dotted lines. Helix IS3 and IS6 are removed for better visualization.

To highlight the differences between both SGA-111 complexed structures their respective pore size and shape was analyzed. The cytosolic domains show major differences (Fig. 3.39a). First, helix IS6 is shifted upwards in the intermediate state to generate more space between the cytosolic domains of the two subunits. In addition, the cytosolic parts are more densely packed and located closer to the membrane. The main chain rmsd of 63.40 Å emphasizes this difference between the two states. Further, the channels pore shows differences in the selectivity filter as well as the gate (Fig. 3.39b). In the intermediate state the lower filter T271/V652 is significantly more open and the upper gate residues T308/L690 have more

distance. In the center however, the pore of the intermediate state is tighter than the closed state. In addition to these protein backbone differences, the deviations in presence and orientation of the lipids at VSD1 and along linker helix IIS-S5 as described beforehand (Fig. 3.35c; Fig. 3.38c) need to be considered.

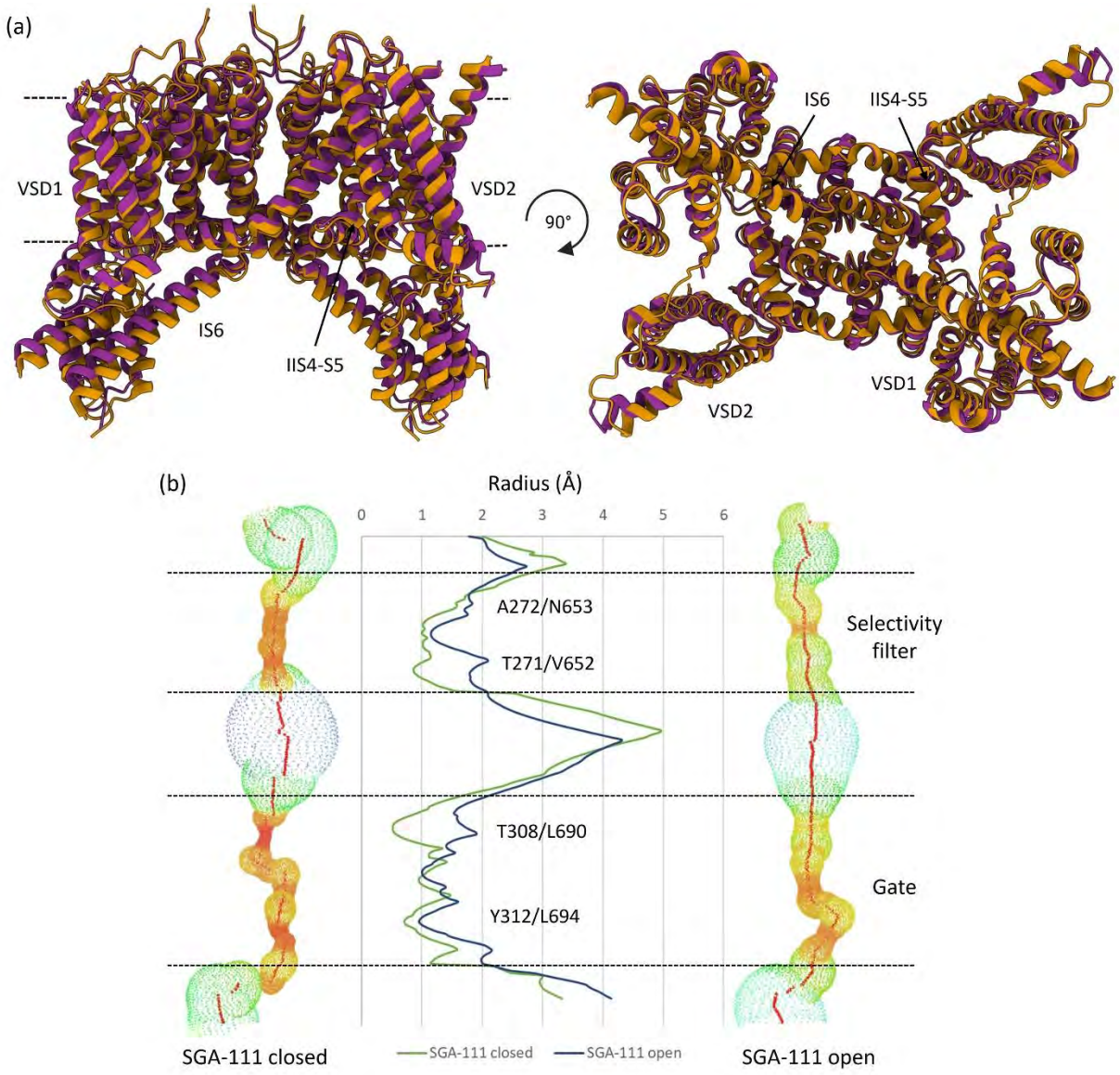

Figure 3.39: SGA-111 intermediate versus closed state
(a) Side view (left) and cytosolic view (right) of the closed SGA-111-bound model (Fig. 3.33a; yellow; no ligands) superimposed with the intermediate SGA-111- bound structure (Fig. 3.36a; purple; without ligands). **(b)** HOLE profiles of the intermediate and closed TPC2-SGA-111 structure created in Coot (2.1.2). The pore radius was plotted against the respective position in the path and the positions of the selectivity filter and gate residues are denoted.

Besides these structural variances, also the binding of SGA-111 is different in the two states. In the closed state (Fig. 3.40a) SGA-111 is present in its enamine-form (Fig. 3.40b) as the intermediate state (Fig. 3.40c) has the keto-form bound (Fig. 3.40d). This influence of the tautomer on the protein state might explain the intermediate to closed ratio of 2:3 and thereby proclaim the efficacy of the ligand in channel activation.

Binding of the SGA-111 enamine-form is coordinated by R210 in helix IS4-S5 and the carboxyl-group of L189 in helix IS4 (Fig. 3.40a). This single interaction with IS4-S5 via R210 is very flexible and by this too modest to influence the protein's structure. The keto-form on the other hand is additionally interacting with IS4-S5 via the carboxyl-groups of L206 and K203 (Fig. 3.40c). This tighter interaction causes a shift of IS4-S5 towards the proteins center and consequently the observed upward shift of IS6 (Fig. 3.39a).

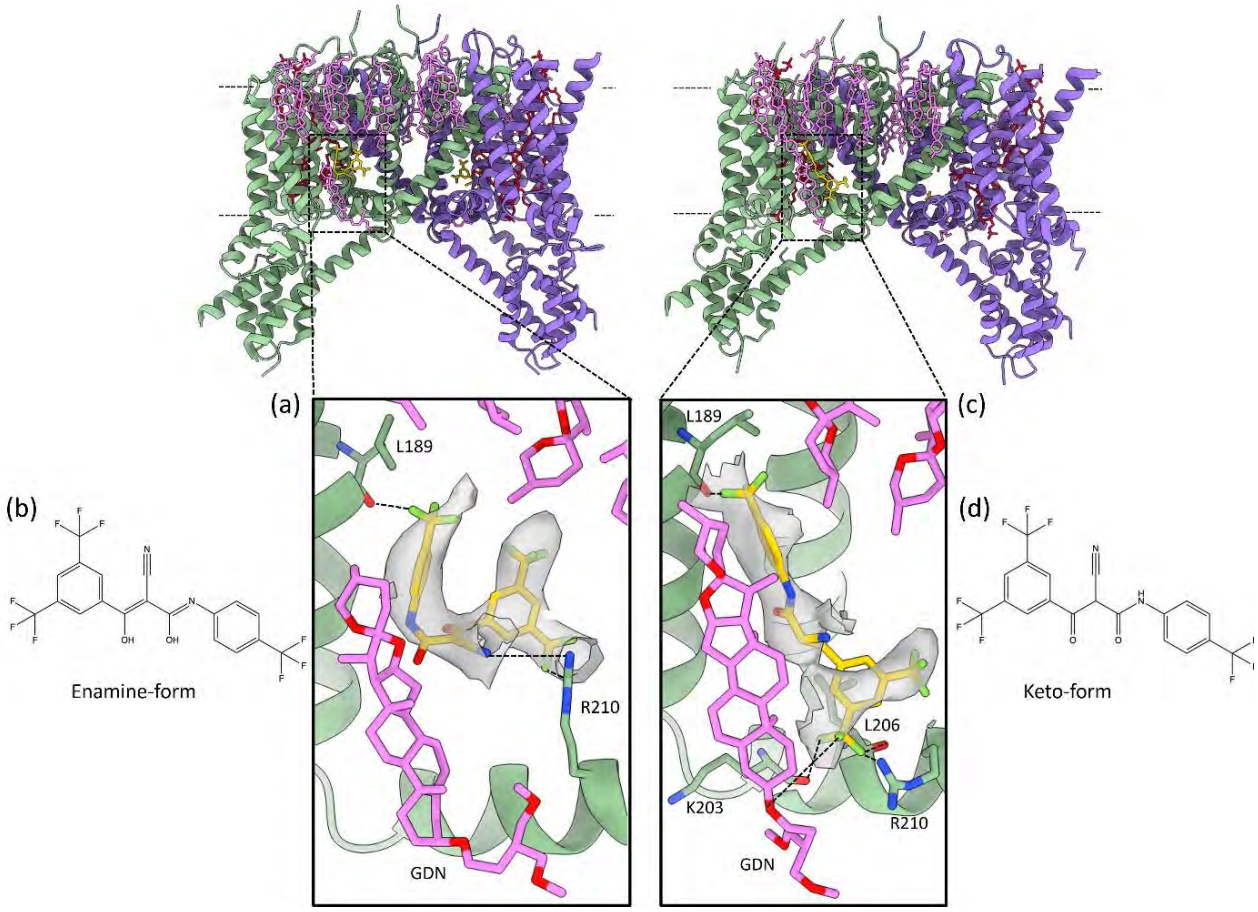

Figure 3.40: SGA-111-binding in the closed and intermediate state
(a) SGA-111 binding site in the closed state. SGA-111 is highlighted in gold and the surrounding GDN-headgroups in violet. Interactions with neighboring residues are indicated by dotted lines. Additionally, the SGA-111-density is indicated in grey. **(b)** Chemical structure of the enamine-form of SGA-111. **(c)** SGA-111 binding site in the intermediate state. SGA-111 is highlighted in gold and the surrounding GDN-headgroups in violet. Interactions with neighboring residues and GDN-headgroups are indicated by dotted lines. **(d)** Chemical structure of the keto-form of SGA-111.

4. Discussion

4.1 SGLT proteins: Dealing with instability

Expressing membrane proteins in HEK cells is a challenge. Different methods were tested, including transient transfection and the Bac-to-Bac® Expression System for the SLC5 family. A stable cell line approach via lentiviral transduction was successful for SGLT3 and later TPC2, resulting in high yields and quality. The expression and purification of SLC5A family members present significant challenges. Initially, the focus was on SGLT2, a key target for Type 2 diabetes mellitus treatment. Different SGLT2 constructs were evaluated for expression, with the C-terminal tagged SGLT2 demonstrating the best expression results (Fig. 3.1a). However, the selected construct exhibited poor protein quality, as most of the protein aggregated either during expression (Fig. 3.2a) or purification (Fig. 3.2b). The problems in expression might result from the use of HEK293S GnT1$^-$ cells, that might not be suitable for SGLTs that are highly glycosylated (Chae *et al.*, 2020). Other potential reasons for this instability include the absence of the interaction partner MAP17 (Coady et al., 2017) or the lack of substrate during expression (Ghezzi C. & Wright E. M., 2012).

A recent publication detailing a SGLT2-MAP17 SPA cryo-EM structure at a resolution of 2.95 Å shed light on the challenges faced with the expression and purification of SGLT2, highlighting similar stability issues. To overcome these challenges, substantial modifications were implemented, including the insertion of a GFP into intracellular loop 6 and a significant truncation of MAP17, which was then fused to a C-terminally attached nanobody against GFP (Fig. 4.1). These adjustments were crucial in obtaining a stable and functional SGLT2 construct, underscoring the considerable difficulties encountered in the expression and purification of SLC5A family members.

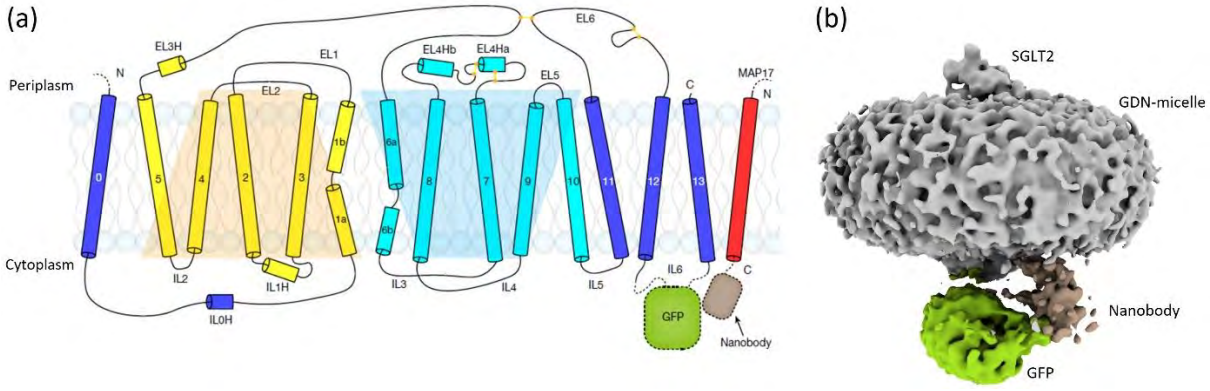

Figure 4.1: The SGLT2–MAP17 complex
Visualization of the complex construct used for SPA cryo-EM structure determination of SGLT2. Both figures are adopted from Niu *et al.*, 2022. **(a)** Topology of the SGLT2–MAP17 complex. Helices are shown as sticks, inverted repeats are indicated as light orange and light blue trapeziums and disulfide bonds are shown as golden sticks. GFP and nanobody fused on the cytoplasmic side are shown as dashed boxes. **(b)** SPA cryo-EM density map of the SGLT2–MAP17 complex with the fused nanobody and GFP. The protein density surrounded by GDN is colored in grey, the nanobody in brown and GFP in green.

SGLT3 was identified as another promising SGLT candidate, with successful establishment of a lentiviral stable cell line for protein expression. Expression of the mutant SGLT3_E457Q also showed promising results. Protein localization in the plasma membrane and quantity were satisfactory. The sodium-coupled

monocarboxylate transporter SMCT2 was also investigated, showing in-cell aggregation but promising results in purification tests. However, further improvements are needed for SMCT2. Additionally, it must be particularly emphasized that the expression and purification established for SGLT3 is without major genetic modifications like for SGLT2 (Niu *et al.*, 2022) and SGLT1 (Han *et al.*, 2022), making it the first native construct of SGLTs showing suitability for SPA cryo-EM.

4.2 Membrane-mimicking systems for SPA cryo-EM

Membrane-mimicking systems are essential to study membrane proteins via SPA cryo-EM. Reconstitution systems frequently used are amphipols and nanodiscs (Fig. 4.2). Here, amphipols (1.2.1) and salipros (1.2.2.2) were tested on GPR from marine γ-proteobacteria, characterized as a light-driven proton pump (Béjà *et al.*, 2000), as a model system.

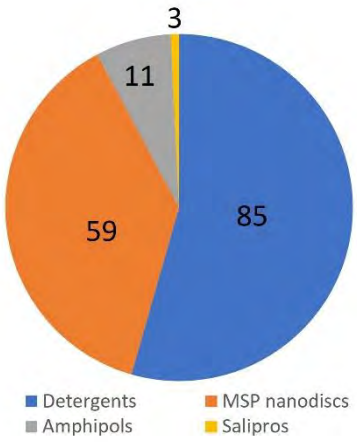

Figure 4.2: Surrounding environment for SPA cryo-EM
Total numbers on the surrounding environments used to solve the structure of membrane proteins via SPA cryo-EM using a 200 keV microscope. Figure is derived from Thangaratnarajah *et al.*, 2022.

GPR in amphipol showed string formation on the SPA cryo-EM grid (Fig. 3.13c), even at high salt concentrations (Fig. 3.13e; Kampjut *et al.*, 2021) and after addition of detergent during vitrification (Fig. 3.13f; Wang *et al.*, 2019). One possible reason therefore can be the negative charge of A8-35 (Fig. 1.6). Reconstitution of GPR in salipros with POPC yielded a good distribution and no preferred orientation of the particles (Fig. 3.14c). This differences in the reconstitution can originate from the addition of lipids (POPC) in salipros. Functional studies showed that GPR is influenced by its lipid environment (Han *et al.*, 2023), and the lack of lipids and detergent in amphipol could lead to aggregation of GPR, visualized as string formation. In addition, the lipid belt in salipros can be beneficial for SPA cryo-EM grid preparation and the accompanying increase of the particle size is also helpful for SPA cryo-EM imaging.
Structurally, a GPR-monomer folds into a seven-transmembrane α-helical bundle containing a covalently bound all-*trans* retinal, which is conjugated to a conserved lysine residue via a characteristic Schiff base (Henderson *et al.*, 1990). Oligomerization of GPR is variable (pentameric: Hirschi *et al.*, 2020; hexameric: Stone *et al.*, 2013; both: Klyszejko *et al.*, 2008) and determines its functionality (Hussain *et al.*, 2015; Idso *et al.*, 2019). Membrane-mimicking systems are reported to have an influence on the oligomerization of the reconstituted protein (Kruip *et al.*, 1999). SPA cryo-EM datasets collected from the salipro sample contained dominantly pentameric GPR (Fig. 4.3) as described by Hirschi *et al.*, 2020 and the final map excellently fits the published pentameric structure (PDB: 7B0; Hirschi *et al.*, 2021). Hexameric oligomers

can be functional, too, as long as the interfaces serve as scaffold for the movement of helices in the neighboring monomer (Hirschi *et al.*, 2021). In addition, functional studies proved that the proton transport by GPR is strongly modulated by its oligomerization (Hussain *et al.*, 2015; Idso *et al.*, 2019).

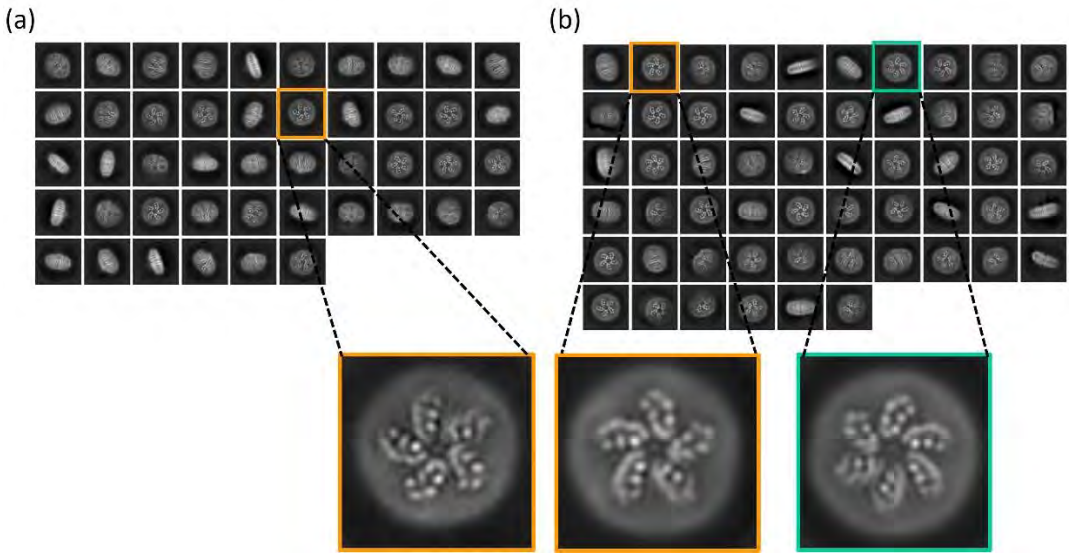

Figure 4.3: Oligomerization of GPR reconstituted in salipros
2D classes of SPA cryo-EM of GPR reconstituted in salipros. **(a)** 2D classes of particles used for final SPA cryo-EM maps of GPR in salipros (3.2). Only pentameric oligomers present. Periplasmic view of one pentamer is enlarged. **(b)** 2D classes of GPR reconstituted in salipros by Konstantin Pierratos, Biophysics II, University of Regensburg, using the same protocol as for the particles in (a) showing a mixture of pentamers and hexamers. 2D classes are sorted by particle number per class from up left to down right, showing an excess of pentamers. Periplasmic views of one pentamer and one hexamer are enlarged.

Proteorhodopsins play a substantial role in the global energy cycle by harnessing solar energy in oceanic environments (Gómez-Consarnau *et al.*, 2019). They are classified according to their spectral properties. GPR, with an absorption maximum at approx. 520 nm, and blue-light absorbing proteorhodopsins (BPR) with an absorption maximum at approx. 490 nm (Man *et al.*, 2003). In GPR, isomerization of all-*trans* retinal to *13-cis* retinal by absorption of green light with a wavelength of approx. 520 nm (Fig. 4.4a), leads to a conformational change and translocation of protons from the intracellular side outside of the cell (Inoue *et al.*, 2015). The isomerization of the retinal is described as unambiguously *all-trans* in the dark sate (Pfleger *et al.*, 2008), but also almost entirely *all-trans* retinal in the light-adapted state (Dioumaev *et al.*, 2002), with only a small increase of *13-cis* retinal (Pfleger *et al.*, 2008). The pentameric SPA cryo-EM structure of GPR combined with MD simulations provides a mechanism for the light-induced structural rearrangements allowing hydration of the intracellular half channel (Hirschi *et al.*, 2021). The central Schiff base is formed by covalent attachment of *all-trans* retinal to the primary amine of K232 (Fig. 4.4b). The two negatively charged residues D98 and D228 are localized on the periplasmic side of the Schiff base, stabilizing the positive charge when protonated, as D98 additionally functions as the primary proton acceptor upon retinal photoisomerization (Fig. 4.4b). The pentameric SPA cryo-EM map (3.64 Å) obtained from the reconstitution in salipros (Fig. 3.15e) has the same entirely *all-trans* isomerization of the retinal as the published 2.95 Å SPA cryo-EM structure in detergent cymal-4 (Fig. 4.4b). The salipro map is also very

similar to the published map in detergent, suggesting that the 7-TM structure of GPR is very stable (Fig. 4.4b).

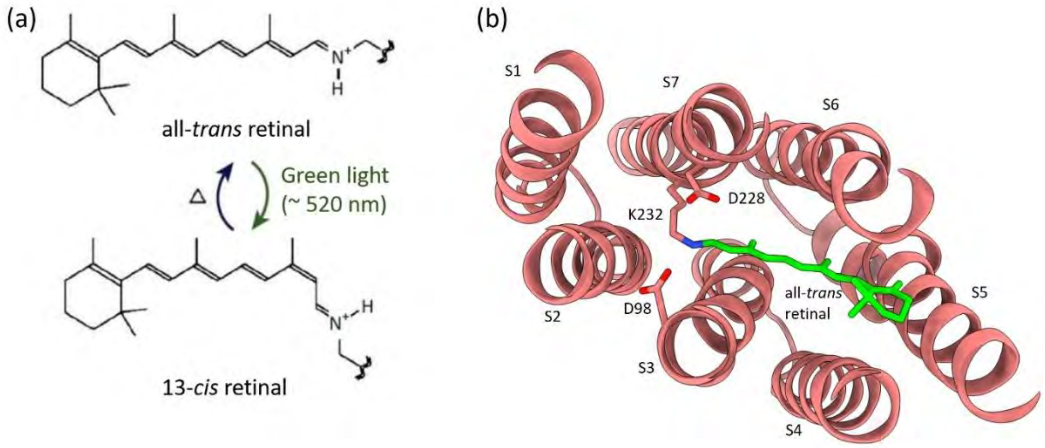

Figure 4.4: Functional und structural characteristics of GPR
(a) Isomerization of all-*trans* retinal by green light (approx. 520 nm) into 13-*cis* retinal. Figure is derived from Inoue *et al.*, 2015. **(b)** Periplasmic view of one GPR subunit bound with all-*trans* retinal (green). Residues building (K232) and stabilizing (D98 and D228) the Schiff base are highlighted. Periplasmic parts of the monomer are removed for better visualization of the Schiff base.

Based on the established SPA cryo-EM protocol an atomic structure of the dark state of GPR is a viable future attempt to obtain more insight into the influence of the light-induced all-*trans* retinal isomerization (Fig. 4.4a) on the GPR-structure. Due to the existing broad knowledge on GPR and other rhodopsins, it has already become a model protein for the development of biophysical techniques (Ritzmann *et al.*, 2017) and for the elucidation of protein structure-function dynamics (Stone *et al.*, 2013; Maciejko *et al.*, 2019), which was demonstrated again in this work. Based on that GPR can be used to adapt physical methods like atomic/scanning force microscopy (AFM) or scanning nearfield optical microscopy (SNOM) on biological samples, which are important components of the new established Regensburg Center for Ultrafast Nanoscopy (RUN).

4.3 TPC2 – Regulation of activity

Mammalian TPCs play a crucial role in various cellular processes such as nutrient sensing linked to the mTOR pathway, viral infections, and cellular autophagy and therefore are potential drug targets for several diseases. Here, the new results elaborated in this work regarding the activation and inhibition investigated by structural analysis via SPA cryo-EM will be discussed in correlation with previous findings.

The regulation of the activity of TPC2 is eminent for the ionic homeostasis of the endolysosome and by this many functions of the cell. Due to this, the flux of different ions through the same pore in TPC2 is tightly regulated by multiple parameters. One interacting protein controlling TPC2 activity is the GTPase Rab7A (Lin-Moshier *et al.*, 2014). However, a direct TPC2-Rab7A interaction could not be demonstrated (3.3.2). As Rab7A most likely binds the N-terminus of TPC2 (Lin-Moshier *et al.*, 2014), the N-terminal His_8-tag or the double mutation L11A/L12A in the N-terminal lysosomal targeting sequence of TPC2 might

prohibit complex formation. The required use of lysozyme for purification of Rab7A possibly destroys parts of the membrane anchored C-terminus (Magee T. and Newman C., 1992), which, along with the presence of GTP, is essential for the ability of Rab7A to interact with other proteins (Ghilarducci *et al.*, 2022). Another possible reason can be a lack of the prenylation in the C-terminus of Rab7A, which is needed to anchor it to the membrane (Khan *et al.*, 2021) and might be important for establishing an interaction of Rab7A with TPC2. The required use of lysozyme for solubilization of Rab7A might even cut parts of the C-terminus and destroy the complex formation ability of Rab7A. In another Rab7A containing complex relevant for the transport of lipids (CLR) between the late endosomes/lysosomes and the endoplasmic reticulum, Rab7A binds the transporter protein via its α3-helix independent from nucleotide binding (Tong *et al.*, 2019). This complex was formed with separately purified proteins equal to this this work (3.3.2). However, for functional analysis revealing that Rab GTPases support NAADP-evoked $Ca2^{+}$ signals via TPC2 the TPC2-Rab7A complex was formed by co-transfection (Lin-Moshier *et al.*, 2014).

Lipids (She *et al.*, 2019) as well as lipophilic agonists (Gerndt *et al.*, 2020a; Gerndt *et al.*, 2020b) are in the center of TPC2 activation. Therefore, possible lipid-densities in all TPC2 SPA cryo-EM maps were modeled and included in the real-space refinement, which was not done in the previous study (She *et al.*, 2019). Best scores were achieved for GDN as ligand in tube-like non-protein densities (Fig. 4.5). GDN surrounds the TPC2 dimer like a belt (Fig. 3.21). Also, on the cytoplasmic side GDN was observed, mostly close to VSD1 (Fig. 3.21). In addition, GDN strongly interacts with the pore helix IP2 (Fig. 3.23c). Reconstitution of GDN-purified TPC2 into salipros with the here established method (3.2) failed, as the protein precipitated when removing the GDN. GDN molecules are even directly interacting with the protein indicating an inhibiting effect, aside of blocking the pore (She *et al.*, 2019), by affecting the flexibility of TPC2.

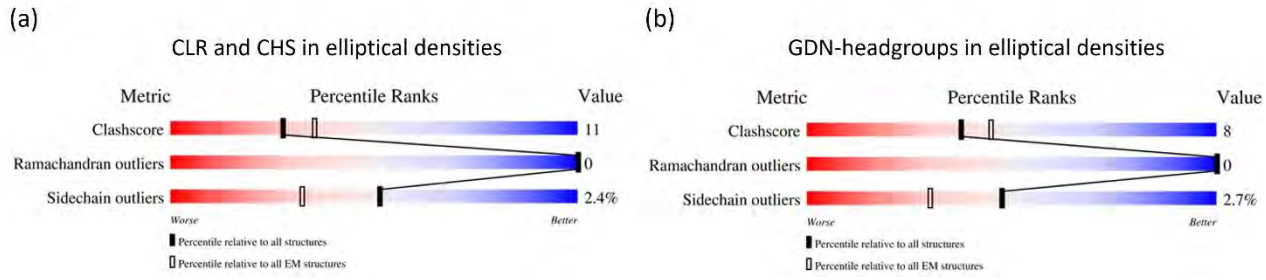

Figure 4.5: Validation of the GDN-belt
Validation report of the TPC2-Apo structure with CLR/CHS (a) or GDN-headgroups (b) modeled in the elliptical densities, gained with the wwPDB Validation System (2.1.2).

Despite the omnipresence of GDN, some few lipids remained associated to TPC2 (Fig. 3.23). Four lipids were identified at the cytoplasmic side, clustered at VSD1. The first lipid is bound to the PI(3,5)P2 site (Fig. 3.23b), the second one next to the GDNs interacting with pore helix IP2 (Fig. 3.23c), and the two remaining ones are located between IS1 and IIS5 forming a tight inter-subunit interaction via R580, IS4-S5 (S200) and R 84 thereby connecting the S4-S5 linker helices from both subunits (Fig. 3.23d). The strong interaction of the lipid that is closest to IS4-S5 is shown by its presence in all solved protein structures (Fig. 3.28d; Fig. 3.35c; Fig. 3.38c) which vividly demonstrates the importance for the function and stability of TPC2. This lipid-interacting represents a missing link in the previously described $PI(3,5)P_2$ activation mechanism (She *et al.*, 2019). Opening of the pore is caused by a rotational movement of IS6 and IIS6 triggered by the conformational changes in the IS4-IS5 linker helix. The conformational changes in both linker helices are key to $PI(3,5)P_2$ activation and contribute to voltage-independent gating of TPC2. However, in the

previously described structure PI(3,5)P_2 is only bound to VSD1, and the additional two lipids might enforce the activation conformational changes in both linker helices.

Inhibition of TPC2 is a promising approach in drug develop against cancer proliferation and growth, as well as virus infections, e.g. SARS-CoV 2 (Clementi *et al.*, 2021). Drug candidates like tetrandrine and naringenin have already proven their effectiveness in functional studies (Favia *et al.*, 2014; Pafumi *et al.*, 2017; Müller *et al.*, 2021; Netcharoensirisuk *et al.*, 2021), however structural investigations of protein-inhibitor interactions are missing. In this work, the focus is on structural analysis of the TPC2-inhibition via naringenin. It is a natural occurring flavonoid present in citruses like oranges, where also the name originates from as they are called “naranja” in Spanish. In this study TPC2 purified in GDN was activated via PI(3,5)P_2, followed by incubation with 0.5 mM naringenin and vitrification for SPA cryo-EM analysis, resulting in a final map of 3.81 Å (Fig. 3.24c). This map shows a PI(3,5)P_2-bound open state (Fig. 3.24e). Model building based on the PI(3,5)P_2-bound open structure (PDB: 6NQ0; She *et al.*, 2019) resulted in an almost equal model (Fig. 3.26a) with identical PI(3,5)P_2 localization (Fig. 3.25b). For naringenin two obvious densities were identified in the lower gate of TPC2 in close contact to the gate residue Y312 (Fig. 3.25d,e). This interaction creates a more closed lower gate in the PI(3,5)P_2-naringenin-bound compared to the solely PI(3,5)P_2-bound state (Fig. 3.26b). Additionally, the presence of naringenin as a pore blocker results in an allover closed channel (Fig. 3.27). Thus, the function of naringenin might be blocking the activity of the channel by inhibiting the diffusion of ions. In previous PI(3,5)P_2-bound open maps (EMD-0477; She et al., 2019) these densities are also present and are postulated as GDN (Fig. 4.6a; She et al., 2019). Validation of the model with GDN-headgroups at the naringenin positions decreased model quality (Fig. 4.6b). Furthermore, the map of GDN-purified TPC2 supplemented with PI(3,5)P_2 and the agonist TPC2-A1-N shows a distinctive open state (Fig. 3.19h) but does not have the blocking densities within the pore (Fig. 4.6c). Molecular docking simulations of naringenin binding in TPC2 propose various possibilities, with the binding site in the pore identified as the most reasonable (Benkerrou *et al.*, 2019). This localization of naringenin is identical to the here observed. The lack of a naringenin density without the presence of a TPC2 agonist (Fig. 3.19j) proclaims that naringenin only binds to an activated channel. This is also the case in the functional studies performed so far, as inhibition via naringenin was examined in presence of PI(3,5)P_2 (Netcharoensirisuk *et al.*, 2021) or NAADP (Pafumi *et al.*, 2017). The potentiating effect of naringenin on the activation of TPC2 via desipramine (Shimomura *et al.*, 2023) however cannot be explained with this model. As there is no structural data on the desipramine-dependent activation of TPC2, these contradictions are not impairing the results shown here. Desipramine related activation might have a completely different mechanism than PI(3,5)P_2 or NAADP, creating other possible binding sites for naringenin. In summary, the structural findings of this work postulate the function of naringenin as a pore blocker inhibiting the ion flux and thus support the previous functional studies.

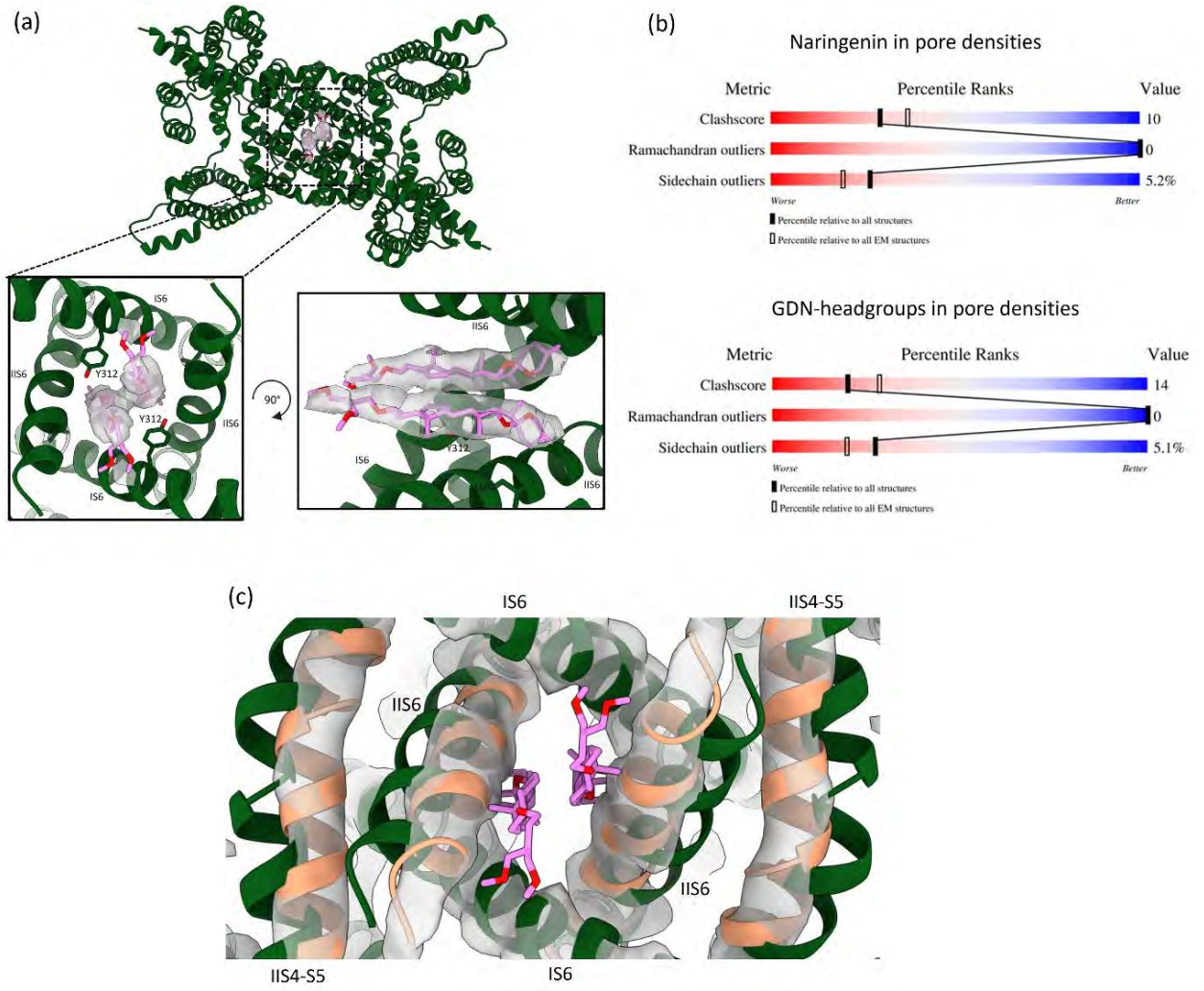

Figure 4.6: Validation of naringenin-binding in TPC2
(a) GDN-headgroups (violet) in the pore densities of the PI(3,5)P_2-bound open map (grey; EMD-0477; She et al., 2019). The PI(3,5)P_2-bound open structure (PDB:6NQ0; She et al., 2019) is shown in green. **(b)** Validation report of the TPC2-PI(3,5)P_2-naringenin structure with naringenin (upper) or GDN-headgroups (down) modeled in the pore densities, gained with the wwPDB Validation System (2.1.2). **(c)** Map of TPC2 supplemented with PI(3,5)P_2 and TPC2-A1-N (grey; 3.3.3) superimposed with the PI(3,5)P_2-bound open structure (green; PDB:6NQ0; She et al., 2019). Parts of the PI(3,5)P_2-TPC2-A1-N map deviating from the PI(3,5)P_2-bound open state are modeled in orange. In the pore there are no densities for GDN-headgroups (violet).

Recently, lipophilic agonists mimicking the NAADP-dependent activation of TPC2 without intermediate NAADP-binding proteins (Saito *et al.*, 2023), leading to a non-selective Na^+- and preferably Ca^{2+}-permeable state, have been developed (Gerndt *et al.*, 2020a). A variety of functional investigations combined with site-directed mutagenesis have been performed to create a first picture on TPC2-A1-N-dependent protein activation (She *et al.*, 2019; Gerndt *et al.*, 2020a; Saito *et al.*, 2023), as structural data of agonist binding and channel opening was missing. Here, structural analysis of TPC2 bound with SGA-111, a derivate of TPC2-A1-N, is reported (3.3.6). In presence of SGA-111 in a molar excess of 40, TPC2 reveals two different states in a 2:3 ratio (Fig. 3.30). The majority of TPC2 is present in a closed state equal to the apo state (Fig. 3.34), while the other 40% show a different conformation, called the SGA-111-bound intermediate state (3.3.6). This intermediate state is different to the existing PI(3,5)P_2-dependent open (PDB: 6NQ0; She *et*

al., 2019) and the apo state (Fig. 3.37a,b), describing a new TPC2 conformation. Analysis of the channel pore indicates an expansion compared to the apo (Fig. 3.37c) and SGA-111 closed state (Fig. 3.39b), but not as widely open as observed via $PI(3,5)P_2$ (Fig. 3.37c). However, changes in the filter residues A271/V652 and slight opening of the upper gate T308/L690 can be observed in comparison to the closed state. An intermediate state was also present in the map of TPC2 supplemented with $PI(3,5)P_2$ and TPC2-A1-N (Fig. 3.19h), where IS6 is in the same orientation as in $PI(3,5)P_2$-bound open, while IIS4-S5 and IIS6 are in a different position. By combining the observations in the two TPC2 states, it can be suggested that the lipophilic, NAADP-mimicking agonists create a new TPC2 conformation, different from the lipid-activated. This assumption is also supported by functional investigations (Saito *et al.*, 2023).

The presence of an intermediate conformation is common in channels and also shown for TPC1 from *Arabidopsis thaliana* (AtTPC1; Kintzer *et al.*, 2018). The four structural states of AtTPC1, reveal the voltage-dependent transition from resting to activated state, and the necessity of cytoplasmic Ca^{2+} ions for channel activation. Based on that, the reason for not adopting an open state of TPC2 with TPC2-A1-N or SGA-111, might be the lack of Ca^{2+} in the protein buffers. Voltage-dependent opening of AtTPC1 is obviously also connected to changes in the VSDs. Even though TPC2 is voltage-independent minor structural changes in the VSDs from the SGA-111 closed to the intermediate state can be observed (Fig. 3.39a). In addition, the mutation R557A in VSD2 abolishes the activation of TPC2 via TPC2-A1-N and $PI(3,5)P_2$ (Saito *et al.*, 2023). Thus, the structural insights affirm the importance of the VSDs for channel opening and its role in the activation via NAADP-mimicking agonists.

The binding site of SGA-111 is located between VSD1 and helix IS4-S5 (Fig. 3.40), close to that of $PI(3,5)P_2$ (Fig. 3.25b). The two observed SGA-111-bound conformations are occupied by different tautomeric states of SGA-111. As the enamine-form is present in the closed state, the intermediate one is bound with the keto-form (Fig. 3.40). Thus, the tautomers influence whether SGA-111 only binds to the channel or creates the intermediate state. Both SGA-111-forms are directly binding to the carboxyl-group of L189 (VSD1) via their 4-trifluormethylgroup. The enamine-form shows flexible binding to R210 via the 3,5-trifluormethylgroup (Fig. 3.40a), while the keto-form binds tightly to the IS4-S5 helix by additional interaction with the carboxyl-groups of K203 and L206 (Fig. 3.40c). Mutations of the neighboring residues K205 and K207 have no influence on TPC2-A1-N-induced activity, while W211A abolishes the activity (Saito *et al.*, 2023). A similar effect of W211A is observed on $PI(3,5)P_2$- and NAADP-activation, indicating the general importance of W211 for channel activation. Functional tests on R210 mutants are not existent, but necessary for deeper understanding of the mechanism.

Besides the actual binding of SGA-111 and structural changes, also deviations in the lipids interacting with TPC2 have been detected. As in the closed state three lipids are present at VSD1 and linker helix IIS4-S5 (Fig. 3.35c) it is only two in the open state (Fig. 3.38c). The absence of the lipid close to IS1 (R84) is likely the result of the lipid close to IS4-S5 (S200) occupying this space in the SGA-111 intermediate state (Fig. 3.38c) and thereby mimicking the Ca^{2+} activation in AtTPC1 (Fig. 4.7). This downward movement, towards R60 of the cytosolic domain, is probably caused by S200 through the binding of SGA-111 to IS4-S5. Thereby, the lipid is shifting the cytosolic domains upwards, closer to VSD1. This movement is supported by the previous described changes in VSD1 also moving upward and pulling the cytosolic domain via the linker in the same direction. The poor local resolution in this area (Fig. 3.30) and the disorder of the linker residues 408-417 in the intermediate map (3.3.6) subsidize this thesis. Finally, the described movements in the cytosolic domain and VSD1 lead to the shift in IS6 characteristic for the observed intermediate state. This mechanism is again underlined by the loss of TPC2-A1-N-function mutation R331A (Saito *et al.*, 2023), as R311 is involved in the interaction of IS6 with the cytosolic domain. In addition, mutation of S322 and R329

essential for PI(3,5)P_2-activation and located away from the interface between IS6 and the cytosolic domains have no influence on activation via TPC2-A1-N.

All in all, the activation of TPC2 via NAADP-mimicking agonists can be described as a mixture of voltage- and lipid-dependent, while more specific descriptions of the mechanism need further studies of site directed mutagenesis combined with functional investigations based on the here described results.

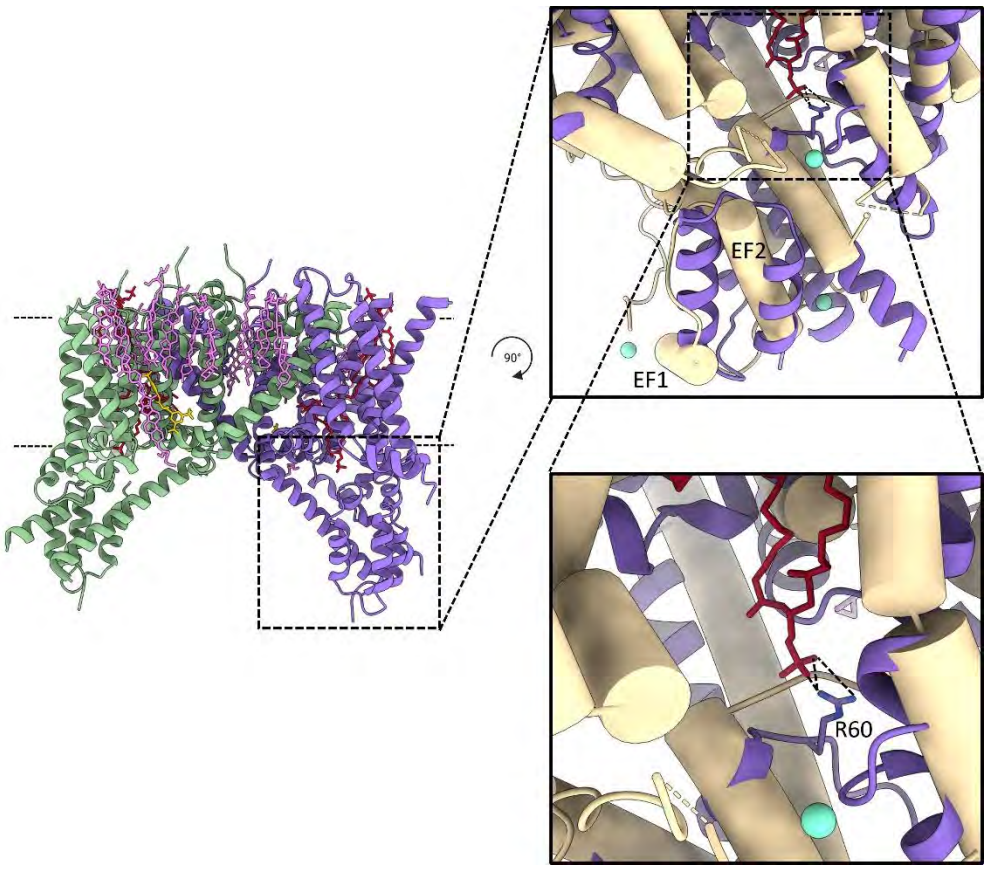

Figure 4.7: Lipid-binding in TPC2 mimics the Ca^{2+} activation in AtTPC1
Side view of the intermediate TPC2-SGA-111 state (Fig. 3.36a), with one cytosolic domain enlarged and superimposed with the EF-hand domains of AtTPC1 (sand colored; PDB: 5DQQ; Kintzer *et al.*, 2018). In TPC2 one subunit is colored in green, the other in blue, CHS in violet and lipids in red. The agonist SGA-111 is highlighted in gold. In the enlarged pictures the lipid of the intermediate TPC2-SGA-111 state, interacting with R60 from the cytosolic domain, is shown in red. Ca^{2+} present at the EF-hand of AtTPC1 is represented as cyan balls.

5. Concluding remarks and future perspectives

Investigation of druggable membrane proteins such has nutrient transporters or ion channels via SPA cryo-EM has increased in the last years. Here, the structures of SLC5A transporters and the cation channel TPC2 should be determined in complex with activators and inhibitors. Hereby, expression in HEK 293 cells, detergent reconstitution as well as reconstitution into membrane mimicking systems was successfully applied. SGLT3 reconstitution in salipros showed good preliminary results and can be replicated in higher quantities necessary for high-resolution structure determination. Hereby, an extramembrane feature like a nanobody, being successfully used for SMCT1 (Han *et al.*, 2022) and SGLT2 (Niu *et al.*, 2022) might be beneficial. The resulting structure model, using a construct without major genetic modifications, will enable a critical discussion on sodium binding and substrate specificity of this glucose sensor together with the already solved transporter structures (SGLT1 and SMCT1: Han *et al.*, 2022; SGLT2: Niu *et al.*, 2022). In addition, atomic structures of the produced mutant SGLT3_E457Q, claimed to function as a transporter similar to SGLT1, can give detailed insight into activation and regulation of these transporter family. Functional studies of SGLT3, tested in this work via SSM-based electrophysiology, together with SGLT3-E457Q can expose important features of sugar transport and binding in SGLTs. Combined with the structural results a huge step into developing new SLC5A transporter drugs can be made. Thereby, the focus for SGLTs will be on inhibition as treatment for Type II diabetes mellitus and cardiovascular diseases, while the activation of SMCTs is of interest for tumor suppression.

Recent scientific attention has increasingly focused on TPC2, particularly in relation to its role in immunology and pharmacology. Especially the potential role in the SARS-CoV-2 pandemic, with inhibitors targeting the endolysosomal pathway to prevent viral genome release (Ou *et al.*, 2020; Clementi *et al.*, 2021) are promising. Thereby, the here presented results of naringenin inhibition can be instrumental. For verification of these results a GDN-free structure is necessary to exclude the possibility of this known TPC2-inhibitor influencing the final confirmation. A possible attempt can be the use of a different detergent with larger headgroups that cannot insert the pore. In addition, successful reconstitution of TPC2 can be useful, to study protein-lipid interactions. However, reconstitution always creates a non-native lipid environment. To tackle these problems establishing the production of SMALPs (1.2.2.3) is the next required step, with GPR being identified as well-suited model system. Furthermore, complex formation with Rab7A, that might rely on the presence of a membrane, could be addressed with this approach. The observation of a closed and an intermediate state of SGA-111-bound TPC2 with an open state missing, gives the assumption that the channel opening in answer to the ion-selective agonists is dependent on the presence of the respective ion. As in all gained structures only Na^+ is present, addition of Ca^{2+} might be necessary to obtain truly open states with TPC2-A1-N, SGA85 and SGA-111. However, the closed state of TPC2 in presence of TPC2-A1-P and Na^+ speaks against this thesis. Interactions of TCP2 with organelles at the membrane level and its precise intracellular localization are underexplored but important for deeper understanding of the channel's physiological functions. EM-techniques like 3D tomography offer powerful tools for exploring the localization of TPC2 and by this expand the understanding of its role in Ca^{2+} homeostasis and signaling. The established SPA cryo-EM workflow enables the investigation of the structural effects of various agonists and inhibitors on TPC2, which can help to improve the drug-protein interaction and specificity. Hereby, the interplay between two agonists (TPC2-A1-P and TPC2-A1-N), or agonist and inhibitor (desipramine and naringenin) are potential future projects that give deeper insights into TPC2 function. The SPA cryo-EM maps and structures gained in this work, already give new insights into the activation and inhibition of TPC2. New perspectives on the importance of lipids for the channels stability and function were obtained and first answers towards the mimicking of the complex NAADP-activation by a single

lipophilic agonist are made. Also, the first structure of interaction of synthetic agonists with TPC2 are important step towards future drug development. Hereby, especially the tautomeric-specificity is significant and should be pursued further. The integration of these structural studies with electrophysiological and molecular biological approaches could provide comprehensive insights into the physiological and pathophysiological roles of TPC2.

6. References

Adelman J. L., Ghezzi C., Bisignano P., Loo D. D., Choe S., Abramson J., Rosenberg J. M., Wright E. M., Grabe M., Stochastic steps in secondary active sugar transport. Proc Natl Acad Sci USA, **2016**, 113(27): E3960-6.

Afonine P. V., Poon B. K., Read R. J., Sobolev O. V., Terwilliger T. C., Urzhumtsev A., Adams P. D., Real-space refinement in PHENIX for cryo-EM and crystallography. Acta Crystallogr D Struct Biol., **2018a**, 74(Pt 6): 531-544.

Afonine P. V., Klaholz B. P., Moriarty N. W., Poon B. K., Sobolev O. V., Terwilliger T. C., Adams P. D., Urzhumtsev A., New tools for the analysis and validation of cryo-EM maps and atomic models. Acta Crystallogr D Struct Biol., **2018b**, 74(Pt 9): 814-840.

Ahn V. E., Leyko P., Alattia J. R., Chen L., Privé G. G., Crystal structures of saposins A and C. Protein Sci., **2006**, 15(8): 1849-57.

Alam M. A., Subhan N., Rahman M. M., Uddin S. J., Reza H. M., Sarker S. D., Effect of citrus flavonoids, naringin and naringenin, on metabolic syndrome and their mechanisms of action. Adv Nutr., **2014**, 5(4): 404-17.

Alami M., Dalal K., Lelj-Garolla B., Sligar S. G., Duong F., Nanodiscs unravel the interaction between the SecYEG channel and its cytosolic partner SecA. EMBO J., **2007**, 26(8): 1995-2004.

Allen T. M., Romans A. Y., Kercret H., Segrest J. P., Detergent removal during membrane reconstitution. Biochim Biophys Acta., **1980**, 601(2): 328-42.

Ambrosio A. L., Boyle J. A., Aradi A. E., Christian K. A., Di Pietro S. M., TPC2 controls pigmentation by regulating melanosome pH and size. Proc Natl Acad Sci USA, **2016**, 113(20): 5622-7.

Amporndanai K., Johnson R. M., O'Neill P. M., Fishwick C. W. G., Jamson A. H., Rawson S., Muench S. P., Hasnain S. S., Antonyuk S. V., X-ray and cryo-EM structures of inhibitor-bound cytochrome bc1 complexes for structure-based drug discovery. IUCrJ., **2018**, 5(Pt 2): 200-210.

Antoine T., Ott D., Ebell K., Hansen K., Henry L., Becker F., Hannus S., Homogeneous time-resolved G protein-coupled receptor-ligand binding assay based on fluorescence cross-correlation spectroscopy. Anal Biochem., **2016**, 502: 24-35.

Autzen H. E., Myasnikov A. G., Campbell M. G., Asarnow D., Julius D., Cheng Y., Structure of the human TRPM4 ion channel in a lipid nanodisc. Science, **2018**, 359(6372): 228-232.

Autzen H. E., Julius D., Cheng Y., Membrane mimetic systems in CryoEM: keeping membrane proteins in their native environment. Curr Opin Struct Biol., **2019**, 58: 259-268.

Bai X. C., McMullan G., Scheres S. H., How cryo-EM is revolutionizing structural biology. Trends Biochem Sci., **2015**, 40(1): 49-57.

Barrueto F., Foxglove. Encyclopedia of Toxicology (Second Edition), **2005**, p. 380-382

Bayburt T. H., Carlson J. W., Sligar S. G., Reconstitution and imaging of a membrane protein in a nanometer-size phospholipid bilayer. J Struct Biol., **1998**, 123(1): 37-44.

Bayburt T. H., Grinkova Y. V., Sligar S. G., Self-Assembly of Discoidal Phospholipid Bilayer Nanoparticles with Membrane Scaffold Proteins. Nano Letters, **2002**, 2 (8): 853–856

Bazzone A., Körner A., Meincke M., Bhatt M., Dondapati S., Barthmes M., Kubick S., Fertig N., SSM-based electrophysiology, a label-free real-time method reveals sugar binding & transport events in SGLT1, Biosensors and Bioelectronics, **2022**, 197: 113763

Béjà O., Aravind L., Koonin E. V., Suzuki M. T., Hadd A., Nguyen L. P., Jovanovich S. B., Gates C. M., Feldman R. A., Spudich J. L., Spudich E. N., DeLong E. F., Bacterial rhodopsin: evidence for a new type of phototrophy in the sea. Science, **2000**, 289(5486): 1902-6.

Benkerrou D., Minicozzi V., Gradogna A., Milenkovic S., Bodrenko I. V., Festa M., Lagostena L., Cornara L., D'Amore A., Ceccarelli M., Filippini A., Carpaneto A., A perspective on the modulation of plant and animal two pore channels (TPCs) by the flavonoid naringenin. Biophys Chem., **2019**, 254:106246.

Berman H. M., Westbrook J., Feng Z., Gilliland G., Bhat T. N., Weissig H., Shindyalov I. N., Bourne P. E., The Protein Data Bank. Nucleic Acids Res., **2000**, 28(1):235-42.

Berman H., Henrick K., Nakamura H., Announcing the worldwide Protein Data Bank. Nat Struct Biol., **2003**, 10(12): 980.

Bertani G., Studies on lysogenisis I.: The mode of phage liberation by lysogenic Escherichia coli. J Bacteriol, **1951**, 62: 293-300.

Bianchi L. & Díez-Sampedro A., A single amino acid change converts the sugar sensor SGLT3 into a sugar transporter. PLoS One, **2010**, 5(4):e10241.

Blake M. S., Johnston K. H., Russell-Jones G. J., Gotschlich E. C., A rapid, sensitive method for detection of alkaline phosphatase-conjugated anti-antibody on Western blots. Anal Biochem, **1984**, 136: 175-179.

Boussambe G. N. M., Guillet P., Mahler F., Marconnet A., Vargas C., Cornut D., Soulié M., Ebel C., Le Roy A., Jawhari A., Bonneté F., Keller S., Durand G., Fluorinated diglucose detergents for membrane-protein extraction. Methods, **2018**, 147: 84-94.

Bradford M. M., A rapid and sensitive method for the quantitation of microgram quantities of protein utilizing the principle of protein-dye binding. Anal. Biochem., **1976**, 72: 248–254.

Brailoiu E., Churamani D., Cai X., Schrlau M. G., Brailoiu G. C., Gao X., Hooper R., Boulware M. J., Dun N. J., Marchant J. S., Patel S., Essential requirement for two-pore channel 1 in NAADP-mediated calcium signaling. J Cell Biol., **2009**, 186(2): 201-9.

Brailoiu E., Rahman T., Churamani D., Prole D. L., Brailoiu G. C., Hooper R., Taylor C. W., Patel S., An NAADP-gated two-pore channel targeted to the plasma membrane uncouples triggering from amplifying Ca^{2+} signals. J Biol Chem., **2010**, 285(49): 38511-6.

Brunelle J. L. and Green R., One-dimensional SDS-polyacrylamide gel electrophoresis (1D SDS-PAGE). Methods Enzymol., **2014**, 541: 151-9.

Böck J., Krogsaeter E., Passon M., Chao Y. K., Sharma S., Grallert H., Peters A., Grimm C., Human genome diversity data reveal that L564P is the predominant TPC2 variant and a prerequisite for the blond hair associated M484L gain-of-function effect. PLoS Genet., **2021**, 17(1): e1009236.

Calcraft P. J., Ruas M., Pan Z., Cheng X., Arredouani A., Hao X., Tang J., Rietdorf K., Teboul L., Chuang K. T., Lin P., Xiao R., Wang C., Zhu Y., Lin Y., Wyatt C. N., Parrington J., Ma J., Evans A. M., Galione A., Zhu M. X., NAADP mobilizes calcium from acidic organelles through two-pore channels. Nature, **2009**, 459(7246): 596-600.

Cang C., Zhou Y., Navarro B., Seo Y. J., Aranda K., Shi L., Battaglia-Hsu S., Nissim I., Clapham D. E., Ren D., mTOR regulates lysosomal ATP-sensitive two-pore Na(+) channels to adapt to metabolic state. Cell, **2013**, 152(4): 778-790.

Cang C., Aranda K., Ren D., A non-inactivating high-voltage-activated two-pore Na^+ channel that supports ultra-long action potentials and membrane bistability. Nat Commun., **2014a**, 5: 5015.

Cang C., Bekele B., Ren D., The voltage-gated sodium channel TPC1 confers endolysosomal excitability. Nat Chem Biol., **2014b**, 10(6): 463-9.

Carlson M. L., Young J. W., Zhao Z., Fabre L., Jun D., Li J., Li J., Dhupar H. S., Wason I., Mills A. T., Beatty J. T., Klassen J. S., Rouiller I., Duong F., The Peptidisc, a simple method for stabilizing membrane proteins in detergent-free solution. Elife, **2018**, 7: e34085.

Castells-Graells R., Meador K., Arbing M. A., Sawaya M. R., Gee M., Cascio D., Gleave E., Debreczeni J. É., Breed J., Leopold K., Patel A., Jahagirdar D., Lyons B., Subramaniam S., Phillips C., Yeates T. O., Cryo-EM structure determination of small therapeutic protein targets at 3 Å-resolution using a rigid imaging scaffold. Proc Natl Acad Sci USA, **2023**, 120(37): e2305494120.

Chae P. S., Rasmussen S. G., Rana R. R., Gotfryd K., Kruse A. C., Manglik A., Cho K. H., Nurva S., Gether U., Guan L., Loland C. J., Byrne B., Kobilka B. K., Gellman S. H., A new class of amphiphiles bearing rigid hydrophobic groups for solubilization and stabilization of membrane proteins. Chemistry, **2012**, 18(31):9485-90.

Chae H., Augustin R., Gatineau E., Mayoux E., Bensellam M., Antoine N., Khattab F., Lai B. K., Brusa D., Stierstorfer B., Klein H., Singh B., Ruiz L., Pieper M., Mark M., Herrera P. L., Gribble F. M., Reimann F., Wojtusciszyn A., Broca C., Rita N., Piemonti L., Gilon P., SGLT2 is not expressed in pancreatic α- and β-cells, and its inhibition does not directly affect glucagon and insulin secretion in rodents and humans. Mol Metab., **2020**, 42: 101071.

Chan G. C. W. & Tang S. C. W., SGLT2 inhibitor empagliflozin: Finally at the latter stage of understanding? Kidney International, **2018**, 93: 22-24.

Chao Y. K., Schludi V., Chen C. C., Butz E., Nguyen O. N. P., Müller M., Krüger J., Kammerbauer C., Ben-Johny M., Vollmar A. M., Berking C., Biel M., Wahl-Schott C. A., Grimm C., TPC2 polymorphisms associated with a hair pigmentation phenotype in humans result in gain of channel function by independent mechanisms. Proc Natl Acad Sci USA, **2017**, 114(41): E8595-E8602.

Chen X. Z., Coady M. J., Jackson F., Berteloot A., Lapointe J. Y., Thermodynamic determination of the Na^+: glucose coupling ratio for the human SGLT1 cotransporter. Biophys J., **1995**, 69: 2405–2414.

Chen J. S., Faller D. V., Spanjaard R. A., Short-chain fatty acid inhibitors of histone deacetylases: promising anticancer therapeutics? Curr Cancer Drug Targets, **2003**, 3(3):219-36.

Chen J., Williams S., Ho S., Loraine H., Hagan D., Whaley J. M., Feder J. N., Quantitative PCR tissue expression profiling of the human SGLT2 gene and related family members. Diabetes Ther., **2010**, 1: 57-92.

Chen Y., Clarke O. B., Kim J., Stowe S., Kim Y. K., Assur Z., Cavalier M., Godoy-Ruiz R., von Alpen D. C., Manzini C., Blaner W. S., Frank J., Quadro L., Weber D. J., Shapiro L., Hendrickson W. A., Mancia F., Structure of the STRA6 receptor for retinol uptake. Science, **2016**, 353(6302): aad8266.

Chen W. & Kudryashev M., Structure of RyR1 in native membranes. EMBO Rep., **2020**, 21(5): e49891.

Chevallet M., Luche S., Rabilloud T., Silver staining of proteins in polyacrylamide gels. Nat Protoc., **2006**, 1(4): 1852-8.

Choy B. C., Cater R. J., Mancia F., Pryor Jr. E. E., A 10-year meta-analysis of membrane protein structural biology: Detergents, membrane mimetics, and structure determination techniques. Biochim Biophys Acta Biomembr., **2021**, 1863(3): 183533.

Clementi N., Scagnolari C., D'Amore A., Palombi F., Criscuolo E., Frasca F., Pierangeli A., Mancini N., Antonelli G., Clementi M., Carpaneto A., Filippini A., Naringenin is a powerful inhibitor of SARS-CoV-2 infection in vitro. Pharmacol Res., **2021**, 163: 105255.

Coady M. J., El Tarazi A., Santer R., Bissonnette P., Sasseville L. J., Calado J., Lussier Y., Dumayne C., Bichet D. G., Lapointe J. Y., MAP17 Is a Necessary Activator of Renal Na^+/Glucose Cotransporter SGLT2. J Am Soc Nephrol., **2017**, 28(1):85-93.

Cymer F., von Heijne G., White S. H., Mechanisms of integral membrane protein insertion and folding. J Mol Biol., **2015**, 427(5): 999-1022.

Dahmane T., Giusti F., Catoire L. J., Popot J.-L., Sulfonated amphipols: synthesis, properties, and applications. Biopolymers, **2011**, (12): 811-23.

Danev R., Buijsse B., Khoshouei M., Plitzko J. M., Baumeister W., Volta potential phase plate for in-focus phase contrast transmission electron microscopy. Proc Natl Acad Sci USA, **2014**, 111(44): 15635-40.

Danev R., Belousoff M., Liang Y. L., Zhang X., Eisenstein F., Wootten D., Sexton P. M., Routine sub-2.5 Å cryo-EM structure determination of GPCRs. Nat Commun., **2021**, 12(1): 4333.

Danielczak B., Meister A., Keller S., Influence of Mg^{2+} and Ca^{2+} on nanodisc formation by diisobutylene/maleic acid (DIBMA) copolymer. Chem Phys Lipids, **2019**, 221: 30-38.

Das M., Du Y., Mortensen J. S., Hariharan P., Lee H. S., Byrne B., Loland C. J., Guan L., Kobilka B. K., Chae P. S., Rationally Engineered Tandem Facial Amphiphiles for Improved Membrane Protein Stabilization Efficacy. Chembiochem., **2018**, 19(20): 2225-2232.

Davie J. R., Inhibition of histone deacetylase activity by butyrate. J Nutr., **2003**, 133(7 Suppl):2485S-2493S.

Denisov I. G., Grinkova Y. V., Lazarides A. A., Sligar S. G., Directed self-assembly of monodisperse phospholipid bilayer Nanodiscs with controlled size. J Am Chem Soc., **2004**, 126(11): 3477-87.

Denisov I. G. & Sligar S. G., Nanodiscs in Membrane Biochemistry and Biophysics. Chem Rev., **2017**, 117(6): 4669-4713.

Diab C., Tribet C., Gohon Y., Popot J.-L., Winnik F.M., Complexation of integral membrane proteins by phosphorylcholine-based amphipols. Biochim Biophys Acta., **2007**, 1768(11): 2737-47.

Dickinson M. S., Myasnikov A., Eriksen J., Poweleit N., Stroud R. M., Resting state structure of the hyperdepolarization activated two-pore channel 3. Proc Natl Acad Sci USA, **2020**, 117(4): 1988-1993.

Diez-Sampedro A., Hirayama B. A., Osswald C., Gorboulev V., Baumgarten K., Volk C., Wright E. M., Koepsell H., A glucose sensor hiding in a family of transporters. Proc Natl Acad Sci USA, **2003**, 100(20):11753-8.

Dioumaev A. K., Brown L. S., Shih J., Spudich E. N., Spudich J. L., Lanyi J. K., Proton transfers in the photochemical reaction cycle of proteorhodopsin. Biochemistry, **2002**, 41(17): 5348-58.

Dodd R., Schofield D. J., Wilkinson T., Britton Z. T., Generating therapeutic monoclonal antibodies to complex multi-spanning membrane targets: Overcoming the antigen challenge and enabling discovery strategies. Methods, **2020**, 180: 111-126.

Dong L., Feng R., Bi J., Shen S., Lu H., Zhang J., Insight into the interaction mechanism of human SGLT2 with its inhibitors: 3D-QSAR studies, homology modeling, and molecular docking and molecular dynamics simulations. J Mol Model., **2018**, 24(4): 86.

Drulyte I., Gutgsell A. R., Lloris-Garcerá P., Liss M., Geschwindner S., Radjainia M., Frauenfeld J., Löving R., Direct cell extraction of membrane proteins for structure-function analysis. Sci Rep., **2023**, 13(1): 1420.

Du D., Neuberger A., Orr M. W., Newman C. E., Hsu P. C., Samsudin F., Szewczak-Harris A., Ramos L. M., Debela M., Khalid S., Storz G., Luisi B. F., Interactions of a Bacterial RND Transporter with a Transmembrane Small Protein in a Lipid Environment. Structure, **2020**, 28(6): 625-634.e6.

Dubochet J., Adrian M., Chang J. J., Homo J. C., Lepault J., McDowall A. W., Schultz P., Cryo-electron microscopy of vitrified specimens. Q Rev Biophys., **1988**, 21(2): 129-228.

Dörr J. M., Koorengevel M. C., Schäfer M., Prokofyev A. V., Scheidelaar S., van der Cruijsen E. A., Dafforn T. R., Baldus M., Killian J. A., Detergent-free isolation, characterization, and functional reconstitution of a tetrameric K^+ channel: the power of native nanodiscs. Proc Natl Acad Sci USA, **2014**, 111(52): 18607-12.

Dörr J. M., Scheidelaar S., Koorengevel M. C., Dominguez J. J., Schäfer M., van Walree C. A., Killian J. A., The styrene-maleic acid copolymer: a versatile tool in membrane research. Eur Biophys J., **2016**, 45(1): 3-21.

Efremov R. G., Gatsogiannis C., Raunser S., Lipid Nanodiscs as a Tool for High-Resolution Structure Determination of Membrane Proteins by Single-Particle Cryo-EM. Methods Enzymol., **2017**, 594: 1-30.

Ehsan M., Das M., Stern V., Du Y., Mortensen J. S., Hariharan P., Byrne B., Loland C. J., Kobilka B. K., Guan L., Chae P. S., Steroid-Based Amphiphiles for Membrane Protein Study: The Importance of Alkyl Spacers for Protein Stability. Chembiochem., **2018**, 19(13): 1433-1443.

Ehsan M., Katsube S., Cecchetti C., Du Y., Mortensen J. S., Wang H., Nygaard A., Ghani L., Loland C. J., Kobilka B. K., Byrne B., Guan L., Chae P. S., New Malonate-Derived Tetraglucoside Detergents for Membrane Protein Stability. ACS Chem Biol., **2020**, 15(6): 1697-1707.

Elegheert J., Behiels E., Bishop B., Scott S., Woolley R. E., Griffiths S. C., Byrne E. F. X., Chang V. T., Stuart D. I., Jones E. Y., Siebold C., Aricescu A. R., Lentiviral transduction of mammalian cells for fast, scalable and high-level production of soluble and membrane proteins. Nat Protoc., **2018**, 13(12): 2991-3017.

Emsley P., Lohkamp B., Scott W. G., Cowtan K., Features and development of Coot. Acta Crystallogr D Biol Crystallogr., **2010**, 66(Pt 4): 486-501.

Faham S., Watanabe A., Besserer G. M., Cascio D., Specht A., Hirayama B. A., Wright E. M., Abramson J., The crystal structure of a sodium galactose transporter reveals mechanistic insights into Na+/sugar symport, Science, **2008**, 321(5890): 810-4.

Favia A., Desideri M., Gambara G., D'Alessio A., Ruas M., Esposito B., Del Bufalo D., Parrington J., Ziparo E., Palombi F., Galione A., Filippini A., VEGF-induced neoangiogenesis is mediated by NAADP and two-pore channel-2-dependent Ca2+ signaling. Proc Natl Acad Sci USA, **2014**, 111(44): E4706-15.

Flayhan A., Mertens H. D. T., Ural-Blimke Y., Martinez Molledo M., Svergun D. I., Löw C., Saposin Lipid Nanoparticles: A Highly Versatile and Modular Tool for Membrane Protein Research. Structure, **2018**, 26(2): 345-355.e5.

Frauenfeld J., Löving R., Armache J.-P., Sonnen A. F.-P., Guettou F., Moberg P., Zhu L., Jegerschöld C., Flayhan A., Briggs J. A. G., Garoff H., Löw C., Cheng Y., Nordlund P., A saposin-lipoprotein nanoparticle system for membrane proteins. Nature Methods, **2016**, 13: 345–351.

Freeman S. L., Bohan D., Darcel N., Raybould H. E. Luminal glucose sensing in the rat intestine has characteristics of a sodium-glucose cotransporter. Am J Physiol Gastrointest Liver Physiol., **2006**, 291(3): G439-45.

Gallo L. A., Wright E. M., and Vallon V., Probing SGLT2 as a therapeutic target for diabetes: Basic physiology and consequences. Diabetes & Vascular Disease Research, **2015**, 12: 78-89.

Ganapathy V., Thangaraju M., Gopal E., Martin P. M., Itagaki S., Miyauchi S., Prasad P. D., Sodium-coupled monocarboxylate transporters in normal tissues and in cancer. AAPS J, **2008**, 10:193–199.

Gao Y., Cao E., Julius D., Cheng Y., TRPV1 structures in nanodiscs reveal mechanisms of ligand and lipid action. Nature, **2016**, 534(7607): 347-51.

Genazzani A. A. & Debidda M., Intracellular Calcium Channels: NAADP+-Modulated. Encyclopedia of Biological Chemistry (Second Edition), Academic Press, **2013**, p. 637-639.

Gerndt S., Chen C. C., Chao Y. K., Yuan Y., Burgstaller S., Scotto Rosato A., Krogsaeter E., Urban N., Jacob K., Nguyen O. N. P., Miller M. T., Keller M., Vollmar A. M., Gudermann T., Zierler S., Schredelseker J., Schaefer M., Biel M., Malli R., Wahl-Schott C., Bracher F., Patel S., Grimm C., Agonist-mediated switching of ion selectivity in TPC2 differentially promotes lysosomal function. Elife, **2020a**, 9: e54712.

Gerndt S., Krogsaeter E., Patel S., Bracher F., Grimm C., Discovery of lipophilic two-pore channel agonists. FEBS J., **2020b**, 287(24): 5284-5293.

Ghezzi C. & Wright E. M., Regulation of the human Na^+-dependent glucose cotransporter hSGLT2. Am J Physiol Cell Physiol., **2012**, 303(3):C348-54.

Ghilarducci K., Cabana V. C., Harake A., Cappadocia L., Lussier M. P., Membrane Targeting and GTPase Activity of Rab7 Are Required for Its Ubiquitination by RNF167. Int J Mol Sci., **2022**, 23(14): 7847.

Giovannucci E., Tomatoes, tomato-based products, lycopene, and cancer: review of the epidemiologic literature. J Natl Cancer Inst., **1999**, 91(4): 317-31.

Goehring A., Lee C. H., Wang K. H., Michel J. C., Claxton D. P., Baconguis I., Gouaux E., Screening and large-scale expression of membrane proteins in mammalian cells for structural studies. Nature Protocols, **2014**, 9: 2574-2585.

Gohon Y., Giusti F., Prata C., Charvolin D., Timmins P., Ebel C., Tribet C., Popot J.-L., Well-defined nanoparticles formed by hydrophobic assembly of a short and polydisperse random terpolymer, amphipol A8-35. Langmuir, **2006**, 22(3): 1281-90.

Gohon Y., Dahmane T., Ruigrok R. W., Schuck P., Charvolin D., Rappaport F., Timmins P., Engelman D. M., Tribet C., Popot J. L., Ebel C., Bacteriorhodopsin/amphipol complexes: structural and functional properties. Biophys J., **2008**, 94(9): 3523-37.

Gómez-Consarnau L., Raven J. A., Levine N. M., Cutter L. S., Wang D., Seegers B., Arístegui J., Fuhrman J. A., Gasol J. M., Sañudo-Wilhelmy S. A., Microbial rhodopsins are major contributors to the solar energy captured in the sea. Sci Adv., **2019**, 5(8): eaaw8855.

Gopal E., Umapathy N. S., Martin P. M., Ananth S., Gnana-Prakasam J. P., Becker H., Wagner C. A., Ganapathy V., Prasad P. D., Cloning and functional characterization of human SMCT2 (SLC5A12) and expression pattern of the transporter in kidney. Biochim Biophys Acta., **2007**, 1768(11):2690-7.

Goth C. K., Petäjä-Repo U. E., Rosenkilde M. M., G Protein-Coupled Receptors in the Sweet Spot: Glycosylation and other Post-translational Modifications. ACS Pharmacol Transl Sci., **2020**, 3(2): 237-245.

Grimm C., Holdt L. M., Chen C. C., Hassan S., Müller C., Jörs S., Cuny H., Kissing S., Schröder B., Butz E., Northoff B., Castonguay J., Luber C. A., Moser M., Spahn S., Lüllmann-Rauch R., Fendel C., Klugbauer N., Griesbeck O., Haas A., Mann M., Bracher F., Teupser D., Saftig P., Biel M., Wahl-Schott C., High susceptibility to fatty liver disease in two-pore channel 2-deficient mice. Nat Commun., **2014**, 5: 4699.

Gubbens A., Barfels M., Trevor C., Twesten R., Mooney P., Thomas P., Menon N., Kraus B., Mao C., McGinn B., The GIF Quantum, a next generation post-column imaging energy filter, Ultramicroscopy, **2010**, 110(8): 962-970

Gulamhussein A. A., Uddin R., Tighe B. J., Poyner D. R., Rothnie A. J., A comparison of SMA (styrene maleic acid) and DIBMA (di-isobutylene maleic acid) for membrane protein purification. Biochim Biophys Acta Biomembr., **2020**, 1862(7): 183281.

Gulezian E., Crivello C., Bednenko J., Zafra C., Zhang Y., Colussi P., Hussain S., Membrane protein production and formulation for drug discovery. Trends Pharmacol Sci., **2021**, 42(8):657-674.

Gunaratne G. S., Brailoiu E., Kumar S., Yuan Y., Slama J. T., Walseth T. F., Patel S., Marchant J. S., Convergent activation of two-pore channels mediated by the NAADP-binding proteins JPT2 and LSM12. Sci Signal., **2023**, 16(799): eadg0485.

Hall S. C. L., Tognoloni C., Charlton J., Bragginton É. C., Rothnie A. J., Sridhar P., Wheatley M., Knowles T. J., Arnold T., Edler K. J., Dafforn T. R., An acid-compatible co-polymer for the solubilization of membranes and proteins into lipid bilayer-containing nanoparticles. Nanoscale, **2018**, 10(22): 10609-10619.

Han Y., Fan X., Wang H., Zhao F., Tully C. G., Kong J., Yao N., Yan N., High-yield monolayer graphene grids for near-atomic resolution cryoelectron microscopy. Proc Natl Acad Sci USA, **2020**, 117(2): 1009-1014.

Han L., Qu Q., Aydin D., Panova O., Robertson M. J., Xu Y., Dror R. O., Skiniotis G., Feng L., Structure and mechanism of the SGLT family of glucose transporters, Nature, **2022**, 601: 274-279.

Han C. T., Nguyen K. D. Q., Berkow M. W., Hussain S., Kiani A., Kinnebrew M., Idso M. N., Baxter N., Chang E., Aye E., Winslow E., Rahman M., Seppälä S., O'Malley M. A., Chmelka B. F., Mertz B., Han S., Lipid membrane mimetics and oligomerization tune functional properties of proteorhodopsin. Biophys J., **2023**, 122(1): 168-179.

Hanahan D., Studies on transformation of Escherichia coli with plasmids. J Mol Biol, **1983**, 166: 557-580.

Hedrich R. & Marten I., TPC1-SV channels gain shape. Mol Plant, **2011**, 4(3): 428-41.

Helenius A. & Simons K., Solubilization of membranes by detergents. Biochim Biophys Acta., **1975**, 415(1): 29-79.

Hemsley A., Arnheim N., Toney M. D., Cortopassi G., Galas D. J., A simple method for site-directed mutagenesis using the polymerase chain reaction. Nucleic Acids Res., **1989**, 17(16): 6545-51.

Henderson R., Baldwin J. M., Ceska T. A., Zemlin F., Beckmann E., Downing K. H., Model for the structure of bacteriorhodopsin based on high-resolution electron cryo-microscopy. J Mol Biol., **1990**, 213(4): 899-929.

Hidaka Y., Kurokawa K., Hashimoto A., Matsui K., Absorption and Fluorescence Characteristics of Pyranine Molecules Embedded in Anodic Porous Alumina. Journal of The Surface Finishing Society of Japan, **2013**, 64: 253-257.

Higgins A. J., Flynn A. J., Marconnet A., Musgrove L. J., Postis V. L. G., Lippiat J. D., Chung C. W., Ceska T., Zoonens M., Sobott F., Muench S. P., Cycloalkane-modified amphiphilic polymers provide direct extraction of membrane proteins for CryoEM analysis. Commun Biol., **2021**, 4(1): 1337.

Hirschi S., Kalbermatter D., Ucurum Z., Fotiadis D., Cryo-electron microscopic and X-ray crystallographic analysis of the light-driven proton pump proteorhodopsin reveals a pentameric assembly. J Struct Biol X., **2020**, 4: 100024.

Hirschi S., Kalbermatter D., Ucurum Z., Lemmin T., Fotiadis D., Cryo-EM structure and dynamics of the green-light absorbing proteorhodopsin. Nat Commun., **2021**, 12(1): 4107.

Hockey L. N., Kilpatrick B. S., Eden E. R., Lin-Moshier Y., Brailoiu G. C., Brailoiu E., Futter C. E., Schapira A. H., Marchant J. S., Patel S., Dysregulation of lysosomal morphology by pathogenic LRRK2 is corrected by TPC2 inhibition. J Cell Sci., **2015**, 128(2): 232-8.

Hummel C. S., Lu C., Loo D. D., Hirayama B. A., Voss A. A., Wright E. M., Glucose transport by human renal Na^+/D-glucose cotransporters SGLT1 and SGLT2. Am J Phys Cell Physiol., **2011**, 300:C14–C21.

Hussain S., Kinnebrew M., Schonenbach N. S., Aye E., Han S., Functional consequences of the oligomeric assembly of proteorhodopsin. J Mol Biol., **2015**, 427(6 Pt B): 1278-1290.

Idso M. N., Baxter N. R., Narayanan S., Chang E., Fisher J., Chmelka B. F., Han S., Proteorhodopsin Function Is Primarily Mediated by Oligomerization in Different Micellar Surfactant Solutions. J Phys Chem B., **2019**, 123(19): 4180-4192.

Inoue H., Nojima H., Okayama H., High efficiency transformation of Escherichia coli with plasmids. Gene, **1990**, 96 (1): 23-28.

Inoue K., Kato Y., Kandori H., Light-driven ion-translocating rhodopsins in marine bacteria. Trends Microbiol., **2015**, 23(2): 91-8.

Itagaki S., Gopal E., Zhuang L., Fei Y. J., Miyauchi S., Prasad P. D., Ganapathy V., Interaction of ibuprofen and other structurally related NSAIDs with the sodium-coupled monocarboxylate transporter SMCT1 (SLC5A8). Pharm Res., **2006**, 23(6):1209-16.

Jha A., Ahuja M., Patel S., Brailoiu E., Muallem S., Convergent regulation of the lysosomal two-pore channel-2 by Mg^{2+}, NAADP, $PI(3,5)P_2$ and multiple protein kinases. EMBO J., **2014**, 33(5): 501-11.

Kamitori K., Shirota M., Fujiwara Y., Structural Basis of the Selective Sugar Transport in Sodium-Glucose Cotransporters. J Mol Biol., **2022**, 434(5):167464.

Kampjut D., Steiner J., Sazanov L. A., Cryo-EM grid optimization for membrane proteins. iScience, **2021**, 24(3): 102139.

Kavran J. M. and Leahy D. J., Silver staining of SDS-polyacrylamide gel. Methods Enzymol., **2014**, 541: 169-76.

Kehlenbeck D. M., Traore D. A. K., Josts I., Sander S., Moulin M., Haertlein M., Prevost S., Forsyth V. T., Tidow H., Cryo-EM structure of MsbA in saposin-lipid nanoparticles (Salipro) provides insights into nucleotide coordination. FEBS J., **2022**, 289(10): 2959-2970.

Khan H., Chen L., Tan L., Im Y.J., Structural basis of human PDZD8-Rab7 interaction for the ER-late endosome tethering. Sci Rep., **2021**, 11(1): 18859.

Kim J., Tan Y. Z., Wicht K. J., Erramilli S. K., Dhingra S. K., Okombo J., Vendome J., Hagenah L. M., Giacometti S. I., Warren A. L., Nosol K., Roepe P. D., Potter C. S., Carragher B., Kossiakoff A. A., Quick M., Fidock D. A., Mancia F., Structure and drug resistance of the Plasmodium falciparum transporter PfCRT. Nature, **2019**, 576(7786): 315-320.

Kimanius D., Dong L., Sharov G., Nakane T., Scheres S. H. W., New tools for automated cryo-EM single-particle analysis in RELION-4.0. Biochem J., **2021**, 478(24): 4169-4185.

Kintzer A. F., Green E. M., Dominik P. K., Bridges M., Armache J. P., Deneka D., Kim S. S., Hubbell W., Kossiakoff A. A., Cheng Y., Stroud R. M., Structural basis for activation of voltage sensor domains in an ion channel TPC1. Proc Natl Acad Sci USA, **2018**, 115(39): E9095-E9104.

Klyszejko A. L., Shastri S., Mari S. A., Grubmüller H., Muller D. J., Glaubitz C., Folding and assembly of proteorhodopsin. J Mol Biol., **2008**, 376(1): 35-41.

Knowles T. J., Finka R., Smith C., Lin Y. P., Dafforn T., Overduin M., Membrane proteins solubilized intact in lipid containing nanoparticles bounded by styrene maleic acid copolymer. J Am Chem Soc., **2009**, 131(22): 7484-5.

Kostelic M. M., Zak C. K., Jayasekera H. S., Marty M. T., Assembly of Model Membrane Nanodiscs for Native Mass Spectrometry. Anal Chem, **2021**, 93(14): 5972-5979.

Kothinti R. K., Blodgett A. B., North P. E., Roman R. J., Tabatabai N. M., A novel SGLT is expressed in the human kidney. Eur J Pharmacol., **2012**, 690(1-3):77-83.

Kotov V., Bartels K., Veith K., Josts I., Subhramanyam U. K. T., Günther C., Labahn J., Marlovits T. C., Moraes I., Tidow H., Löw C., Garcia-Alai M. M., High-throughput stability screening for detergent-solubilized membrane proteins. Sci Rep., **2019**, 9(1): 10379.

Kruip J., Karapetyan N. V., Terekhova I. V., Rögner M., In vitro oligomerization of a membrane protein complex. Liposome-based reconstitution of trimeric photosystem I from isolated monomers. J Biol Chem., **1999**, 274(26): 18181-8.

Kumar P., Cymes G. D., Grosman C., Structure and function at the lipid-protein interface of a pentameric ligand-gated ion channel. Proc Natl Acad Sci USA, **2021**, 118(23): e2100164118.

Kögler L. M., Stichel J., Kaiser A., Beck-Sickinger A. G., Cell-Free Expression and Photo-Crosslinking of the Human Neuropeptide Y_2 Receptor. Front Pharmacol., **2019**, 10: 176.

Kühlbrandt W., The resolution revolution. Science, **2014**, 343(6178): 1443-4.

Laemmli U. K., Cleavage of structural proteins during the assembly of the head of bacteriophage T4. Nature, **1970**, 227: 680-685.

Lau F. W., Nauli S., Zhou Y., Bowie J. U., Changing single side-chains can greatly enhance the resistance of a membrane protein to irreversible inactivation. J Mol Biol., **1999**, 290(2): 559-64.

Le Bon C., Marconnet A., Masscheleyn S., Popot J.-L., Zoonens M., Folding and stabilizing membrane proteins in amphipol A8-35. Methods, **2018**, 147: 95-105.

Lee H. J., Lee H. S., Yoon T., Byrne B., Chae P. S., Impact of novel detergents on membrane protein studies. Chem, **2022**, 8: 980–1013

Li H., Myeroff L., Smiraglia D., Romero M. F., Pretlow T. P., Kasturi L., Lutterbaugh J., Rerko R. M., Casey G., Issa J.-P., Willis J., Willson J. K. V., Plass C., Markowitz S. D., SLC5A8, a sodium transporter, is a tumor suppressor gene silenced by methylation in human colon aberrant crypt foci and cancers. Proc. Natl. Acad. Sci. USA, **2003**, 100:8412–8417.

Li X., Mooney P., Zheng S., Booth C. R., Braunfeld M. B., Gubbens S., Agard D. A., Cheng Y., Electron counting and beam-induced motion correction enable near-atomic-resolution single-particle cryo-EM. Nat Methods, **2013**, 10(6): 584-90.

Liang Y. L., Belousoff M. J., Zhao P., Koole C., Fletcher M. M., Truong T. T., Julita V., Christopoulos G., Xu H. E., Zhang Y., Khoshouei M., Christopoulos A., Danev R., Sexton P. M., Wootten D., Toward a Structural Understanding of Class B GPCR Peptide Binding and Activation. Mol Cell, **2020**, 77(3): 656-668.e5.

Liao M., Cao E., Julius D., Cheng Y., Structure of the TRPV1 ion channel determined by electron cryo-microscopy. Nature, **2013**, 504(7478): 107-12.

Lin-Moshier Y., Keebler M. V., Hooper R., Boulware M. J., Liu X., Churamani D., Abood M. E., Walseth T. F., Brailoiu E., Patel S., Marchant J. S., The Two-pore channel (TPC) interactome unmasks isoform-specific roles for TPCs in endolysosomal morphology and cell pigmentation. Proc Natl Acad Sci USA, **2014**, 111(36): 13087-92.

Lloris-Garcerá P., Klinter S., Chen L., Skynner M. J., Löving R., Frauenfeld J., DirectMX - One-Step Reconstitution of Membrane Proteins from Crude Cell Membranes Into Salipro Nanoparticles. Front. Bioeng. Biotechnol., **2020**, 8: 215.

Lyons J. A., Bøggild A., Nissen P., Frauenfeld J., Saposin-Lipoprotein Scaffolds for Structure Determination of Membrane Transporters. Methods Enzymol., **2017**, 594: 85-99.

Lyumkis D., Challenges and opportunities in cryo-EM single-particle analysis. J Biol Chem., **2019**, 294(13): 5181-5197.

Maciejko J., Kaur J., Becker-Baldus J., Glaubitz C., Photocycle-dependent conformational changes in the proteorhodopsin cross-protomer Asp-His-Trp triad revealed by DNP-enhanced MAS-NMR. Proc Natl Acad Sci USA, **2019**, 116(17): 8342-8349.

Madej M. G., Sun L., Yan N., Kaback H. R., Functional architecture of MFS D-glucose transporters. Proc Natl Acad Sci USA, **2014**, 111(7): E719-27.

Magee T. and Newman C., The role of lipid anchors for small G proteins in membrane trafficking. Trends Cell Biol., **1992**, 2(11): 318-23.

Man D., Wang W., Sabehi G., Aravind L., Post A. F., Massana R., Spudich E. N., Spudich J. L., Béjà O., Diversification and spectral tuning in marine proteorhodopsins. The EMBO Journal, **2003**, 22: 1725-1731.

Marconnet A., Michon B., Le Bon C., Giusti F., Tribet C., Zoonens M., Solubilization and Stabilization of Membrane Proteins by Cycloalkane-Modified Amphiphilic Polymers. Biomacromolecules, **2020**, 21(8): 3459-3467.

Mastronarde D. N., Automated electron microscope tomography using robust prediction of specimen movements. J Struct Biol., **2005**, 152(1): 36-51.

Matar-Merheb R., Rhimi M., Leydier A., Huché F., Galián C., Desuzinges-Mandon E., Ficheux D., Flot D., Aghajari N., Kahn R., Di Pietro A., Jault J. M., Coleman A. W., Falson P., Structuring detergents for extracting and stabilizing functional membrane proteins. PLoS One, **2011**, 6(3): e18036.

Milenkovic S., Bodrenko I. V., Carpaneto A., Ceccarelli M., The key role of the central cavity in sodium transport through ligand-gated two-pore channels. Phys Chem Chem Phys., **2021**, 23(34): 18461-18474.

McMullan G., Chen S., Henderson R., Faruqi A. R., Detective quantum efficiency of electron area detectors in electron microscopy. Ultramicroscopy, **2009**, 109(9): 1126-43.

Miyauchi S., Gopal E., Fei Y. J., Ganapathy V., Functional identification of SLC5A8, a tumor suppressor down-regulated in colon cancer, as a Na^+-coupled transporter for short-chain fatty acids. J Biol Chem., **2004**, 279: 13293–13296.

Mobbs J. I., Belousoff M. J., Harikumar K. G., Piper S. J., Xu X., Furness S. G. B., Venugopal H., Christopoulos A., Danev R., Wootten D., Thal D. M., Miller L. J., Sexton P. M., Structures of the human cholecystokinin 1 (CCK1) receptor bound to Gs and Gq mimetic proteins provide insight into mechanisms of G protein selectivity. PLoS Biol., **2021**, 19(6): e3001295.

Moriarty N. W., Grosse-Kunstleve R. W., Adams P. D., electronic Ligand Builder and Optimization Workbench (eLBOW): a tool for ligand coordinate and restraint generation. Acta Crystallogr D Biol Crystallogr., **2009**, 65(Pt 10): 1074-80.

Mueckler M., Facilitative glucose transporters. Eur J Biochem, **1994**, 219: 713–725.

Myzak M. C. & Dashwood R. H., Histone deacetylases as targets for dietary cancer preventive agents: lessons learned with butyrate, diallyl disulfide, and sulforaphane. Curr Drug Targets, **2006**, 7(4): 443-52.

Müller M., Gerndt S., Chao Y. K., Zisis T., Nguyen O. N. P., Gerwien A., Urban N., Müller C., Gegenfurtner F. A., Geisslinger F., Ortler C., Chen C. C., Zahler S., Biel M., Schaefer M., Grimm C., Bracher F., Vollmar A. M., Bartel K., Gene editing and synthetically accessible inhibitors reveal role for TPC2 in HCC cell proliferation and tumor growth. Cell Chem Biol., **2021**, 28(8): 1119-1131.e27.

Nasr M. L., Baptista D., Strauss M., Sun Z. J., Grigoriu S., Huser S., Plückthun A., Hagn F., Walz T., Hogle J. M., Wagner G., Covalently circularized nanodiscs for studying membrane proteins and viral entry. Nat Methods, **2017**, 14(1): 49-52.

Netcharoensirisuk P., Abrahamian C., Tang R., Chen C. C., Rosato A. S., Beyers W., Chao Y. K., Filippini A., Di Pietro S., Bartel K., Biel M., Vollmar A. M., Umehara K., De-Eknamkul W., Grimm C., Flavonoids increase melanin production and reduce proliferation, migration and invasion of melanoma cells by blocking endolysosomal/melanosomal TPC2. Sci Rep., **2021**, 11(1): 8515.

Newport T. D., Sansom M. S. P., Stansfeld P. J., The MemProtMD database: a resource for membrane-embedded protein structures and their lipid interactions. Nucleic Acids Res., **2019**, 47(D1): D390-D397.

Nguyen N. X., Armache J. P., Lee C., Yang Y., Zeng W., Mootha V. K., Cheng Y., Bai X. C., Jiang Y., Cryo-EM structure of a fungal mitochondrial calcium uniporter. Nature, **2018**, 559(7715): 570-574.

Nishimura M. & Naito S., Tissue-specific mRNA expression profiles of human ATP-binding cassette and solute carrier transporter superfamilies. Drug Metab Pharmacokinet., **2005**, 20(6):452-77.

Niu Y., Liu R., Guan C., Zhang Y., Chen Z., Hoerer S., Nar H., Chen L., Structural basis of inhibition of the human SGLT2-MAP17 glucose transporter. Nature, **2022**, 601(7892): 280-284.

Noble A. J., Wei H., Dandey V. P., Zhang Z., Tan Y. Z., Potter C. S., Carragher B., Reducing effects of particle adsorption to the air-water interface in cryo-EM. Nat Methods, **2018**, 15(10): 793-795.

Okuda T. & Haga T., Functional characterization of the human high-affinity choline transporter. FEBS Lett., **2000**, 484(2):92-7.

Oluwole A. O., Danielczak B., Meister A., Babalola J. O., Vargas C., Keller S., Solubilization of Membrane Proteins into Functional Lipid-Bilayer Nanodiscs Using a Diisobutylene/Maleic Acid Copolymer. Angew Chem Int Ed Engl., **2017**, 56(7): 1919-1924.

Ooi A., Wong A., Esau L., Lemtiri-Chlieh F., Gehring C., A Guide to Transient Expression of Membrane Proteins in HEK-293 Cells for Functional Characterization. Front Physiol., **2016**, 7: 300.

Ou X., Liu Y., Lei X., Li P., Mi D., Ren L., Guo L., Guo R., Chen T., Hu J., Xiang Z., Mu Z., Chen X., Chen J., Hu K., Jin Q., Wang J., Qian Z., Characterization of spike glycoprotein of SARS-CoV-2 on virus entry and its immune cross-reactivity with SARS-CoV. Nat Commun., **2020**, 11(1): 1620.

Owji A. P., Zhao Q., Ji C., Kittredge A., Hopiavuori A., Fu Z., Ward N., Clarke O. B., Shen Y., Zhang Y., Hendrickson W. A., Yang T., Structural and functional characterization of the bestrophin-2 anion channel. Nat Struct Mol Biol., **2020**, 27(4): 382-391.

Pafumi I., Festa M., Papacci F., Lagostena L., Giunta C., Gutla V., Cornara L., Favia A., Palombi F., Gambale F., Filippini A., Carpaneto A., Naringenin Impairs Two-Pore Channel 2 Activity And Inhibits VEGF-Induced Angiogenesis. Sci Rep., **2017**, 7(1): 5121.

Panayotova-Heiermann M., Loo D. D., Wright E. M., Kinetics of steady-state currents and charge movements associated with the rat Na^+/glucose cotransporter. J Biol Chem., **1995**, 270(45):27099-105.

Pang S. S., Bayly-Jones C., Radjainia M., Spicer B. A., Law R. H. P., Hodel A. W., Parsons E. S., Ekkel S. M., Conroy P. J., Ramm G., Venugopal H., Bird P. I., Hoogenboom B. W., Voskoboinik I., Gambin Y., Sierecki E., Dunstone M. A., Whisstock J. C., The cryo-EM structure of the acid activatable pore-forming immune effector Macrophage-expressed gene 1. Nat Commun., **2019**, 10(1): 4288.

Paulsen C. E., Armache J. P., Gao Y., Cheng Y., Julius D., Structure of the TRPA1 ion channel suggests regulatory mechanisms. Nature, **2015**, 520(7548): 511-7.

Penny C. J., Vassileva K., Jha A., Yuan Y., Chee X., Yates E., Mazzon M., Kilpatrick B. S., Muallem S., Marsh M., Rahman T., Patel S., Mining of Ebola virus entry inhibitors identifies approved drugs as two-pore channel pore blockers. Biochim Biophys Acta Mol Cell Res., **2019**, 1866(7): 1151-1161.

Pettersen E. F., Goddard T. D., Huang C. C., Meng E. C., Couch G. S., Croll T. I., Morris J. H., Ferrin T. E., UCSF ChimeraX: Structure visualization for researchers, educators, and developers. Protein Sci., **2021**, 30(1): 70-82.

Pfleger N., Lorch M., Woerner A. C., Shastri S., Glaubitz C., Characterisation of Schiff base and chromophore in green proteorhodopsin by solid-state NMR. J Biomol NMR, **2008**, 40(1): 15-21.

Picard M., Dahmane T., Garrigos M., Gauron C., Giusti F., le Maire M., Popot J.-L., Champeil P., Protective and inhibitory effects of various types of amphipols on the Ca2+-ATPase from sarcoplasmic reticulum: a comparative study. Biochemistry, **2006**, 45(6): 1861-9.

Piper S. J., Johnson R. M., Wootten D., Sexton P. M., Membranes under the Magnetic Lens: A Dive into the Diverse World of Membrane Protein Structures Using Cryo-EM. Chem Rev., **2022**, 122(17): 13989-14017.

Plenge P., Yang D., Salomon K., Laursen L., Kalenderoglou I. E., Newman A. H., Gouaux E., Coleman J. A., Loland C. J., The antidepressant drug vilazodone is an allosteric inhibitor of the serotonin transporter. Nature Commun., **2021**, 12(1):5063.

Pollock N. L., Lee S. C., Patel J. H., Gulamhussein A. A., Rothnie A. J., Structure and function of membrane proteins encapsulated in a polymer-bound lipid bilayer. Biochim Biophys Acta Biomembr., **2018**, 1860(4): 809-817.

Popot J.-L., Berry E. A., Charvolin D., Creuzenet C., Ebel C., Engelman D. M., Flötenmeyer M., Giusti F., Gohon Y., Hong Q., Lakey J. H., Leonard K., Shuman H. A., Timmins P., Warschawski D. E., Zito F., Zoonens M., Pucci B., Tribet C., Amphipols: polymeric surfactants for membrane biology research. Cell Mol Life Sci., **2003**, 60(8): 1559-74.

Pos K. M., Bott M., Dimroth P., Purification of two active fusion proteins of the Na(+)-dependent citrate carrier of Klebsiella pneumoniae. FEBS Lett., **1994**, 347(1): 37-41.

Punjani A., Rubinstein J. L., Fleet D. J., Brubaker M. A., cryoSPARC: algorithms for rapid unsupervised cryo-EM structure determination. Nat Methods., **2017**, 14(3): 290-296.

Rahman M. M., Basta T., Teng J., Lee M., Worrell B. T., Stowell M. H. B., Hibbs R. E., Structural mechanism of muscle nicotinic receptor desensitization and block by curare. Nat Struct Mol Biol., **2022**, 29(4): 386-394.

Rapisarda C., Cherrak Y., Kooger R., Schmidt V., Pellarin R., Logger L., Cascales E., Pilhofer M., Durand E., Fronzes R.**,** In situ and high-resolution cryo-EM structure of a bacterial type VI secretion system membrane complex. EMBO J., **2019**, 38(10): e100886.

Rasmussen S. G., DeVree B. T., Zou Y., Kruse A. C., Chung K. Y., Kobilka T. S., Thian F. S., Chae P. S., Pardon E., Calinski D., Mathiesen J. M., Shah S. T., Lyons J. A., Caffrey M., Gellman S. H., Steyaert J., Skiniotis G., Weis W. I., Sunahara R. K., Kobilka B. K., Crystal structure of the β2 adrenergic receptor-Gs protein complex. Nature, **2011**, 477(7366): 549-55.

Ratkeviciute G., Cooper B. F., Knowles T. J., Methods for the solubilisation of membrane proteins: the micelle-aneous world of membrane protein solubilisation. Biochem Soc Trans., **2021**, 49(4): 1763-1777.

Ravula T., Hardin N. Z., Ramadugu S. K., Ramamoorthy A., pH Tunable and Divalent Metal Ion Tolerant Polymer Lipid Nanodiscs. Langmuir, **2017**, 33(40): 10655-10662.

Ravula T., Hardin N. Z., Di Mauro G. M., Ramamoorthy A., Styrene maleic acid derivates to enhance the applications of bio-inspired polymer based lipid-nanodiscs. Eur Polym J., **2018**, 108: 597-602.

Reeves P. J., Thurmond R. L., Khorana H. G., Structure and function in rhodopsin: high level expression of a synthetic bovine opsin gene and its mutants in stable mammalian cell lines. Proc Natl Acad Sci USA, **1996**, 93(21): 11487-92.

Reid M. S., Kern D. M., Brohawn S. G., Cryo-EM structure of the potassium-chloride cotransporter KCC4 in lipid nanodiscs. Elife, **2020**, 9: e52505.

Ritzmann N., Thoma J., Hirschi S., Kalbermatter D., Fotiadis D., Müller D. J., Fusion Domains Guide the Oriented Insertion of Light-Driven Proton Pumps into Liposomes. Biophys J., **2017**, 113(6): 1181-1186.

Robertson M. J., Meyerowitz J. G., Skiniotis G., Drug discovery in the era of cryo-electron microscopy. Trends Biochem Sci., **2022**, 47(2): 124-135.

Rossmann M., Schultz-Heienbrok R., Behlke J., Remmel N., Alings C., Sandhoff K., Saenger W., Maier T., Crystal structures of human saposins C and D: implications for lipid recognition and membrane interactions. Structure, **2008**, 16(5): 809-17.

Ruas M., Davis L. C., Chen C. C., Morgan A. J., Chuang K. T., Walseth T. F., Grimm C., Garnham C., Powell T., Platt N., Platt F. M., Biel M., Wahl-Schott C., Parrington J., Galione A., Expression of Ca^{2+}-permeable two-pore channels rescues NAADP signalling in TPC-deficient cells. EMBO J., **2015**, 34(13): 1743-58.

Saito R., Mu Q., Yuan Y., Rubio-Alarcón M., Eznarriaga M., Zhao P., Gunaratne G., Kumar S., Keller M., Bracher F., Grimm C., Brailoiu E., Marchant J. S., Rahman T., Patel S., Convergent activation of Ca2+ permeability in two-pore channel 2 through distinct molecular routes. Sci Signal., **2023**, 16(799): eadg0661.

Sakurai Y., Kolokoltsov A. A., Chen C. C., Tidwell M. W., Bauta W. E., Klugbauer N., Grimm C., Wahl-Schott C., Biel M., Davey R. A., Ebola virus. Two-pore channels control Ebola virus host cell entry and are drug targets for disease treatment. Science, **2015**, 347(6225): 995-8.

Santos R., Ursu O., Gaulton A., Bento A. P., Donadi R. S., Bologa C. G., Karlsson A., Al-Lazikani B., Hersey A., Oprea T. I., Overington J. P., A comprehensive map of molecular drug targets. Nat Rev Drug Discov., **2017**, 16: 19–34.

Saponaro A., Bauer D., Giese M. H., Swuec P., Porro A., Gasparri F., Sharifzadeh A. S., Chaves-Sanjuan A., Alberio L., Parisi G., Cerutti G., Clarke O. B., Hamacher K., Colecraft H. M., Mancia F., Hendrickson W. A., Siegelbaum S. A., DiFrancesco D., Bolognesi M., Thiel G., Santoro B., Moroni A., Gating movements and ion permeation in HCN4 pacemaker channels. Mol. Cell, **2021**, 81(14): 2929-2943.e6.

Scheres S. H., RELION: implementation of a Bayesian approach to cryo-EM structure determination. J Struct Biol., **2012**, 180(3): 519-30.

Schmidt-Krey I. & Rubinstein J. L., Electron cryomicroscopy of membrane proteins: specimen preparation for two-dimensional crystals and single particles. Micron, **2011**, 42(2): 107-16.

Schultz S. G., Ion-coupled transport of organic solutes across biological membranes, Physiology of Membrane Disorders, **1985**, p. 283–294.

Schulz P., Garcia-Celma J. J., Fendler K., SSM-based electrophysiology. Methods., **2008**, 46(2): 97-103.

Seddon A. M., Curnow P., Booth P. J., Membrane proteins, lipids and detergents: not just a soap opera. Biochim Biophys Acta., **2004**, 1666(1-2): 105-17.

Sharma K. S., Durand G., Gabel F., Bazzacco P., Le Bon C., Billon-Denis E., Catoire L. J., Popot J.-L., Ebel C., Pucci B., Non-ionic amphiphilic homopolymers: synthesis, solution properties, and biochemical validation. Langmuir, **2012**, 28(10): 4625-39.

Sharma S. & Wilkens S., Biolayer interferometry of lipid nanodisc-reconstituted yeast vacuolar H^+-ATPase. Protein Sci., **2017**, 26(5): 1070-1079.

She J., Guo J., Chen Q., Zeng W., Jiang Y., Bai X. C., Structural insights into the voltage and phospholipid activation of the mammalian TPC1 channel. Nature, **2018**, 556(7699): 130-134.

She J., Zeng W., Guo J., Chen Q., Bai X. C., Jiang Y., Structural mechanisms of phospholipid activation of the human TPC2 channel. Elife, **2019**, 8: e45222.

Shimomura T., Hirazawa K., Kubo Y., Conformational rearrangements in the second voltage sensor domain switch PIP2- and voltage-gating modes in two-pore channels. Proc Natl Acad Sci USA, **2023**, 120(6): e2209569120.

Singh A. K., McGoldrick L. L., Sobolevsky A. I., Structure and gating mechanism of the transient receptor potential channel TRPV3. Nature Structural & Molecular Biology, **2018**, 25(9): 805-813.

Sivaprakasam S., Bhutia Y. D., Yang S., Ganapathy V., Short-chain fatty acid transporters: role in colonic homeostasis. Compr. Physiol., **2017**, 8: 299–314.

Skelding K. A., Barry D. L., Theron D. Z., Lincz L. F., Targeting the two-pore channel 2 in cancer progression and metastasis. Explor Target Antitumor Ther., **2022**, 3(1): 62-89.

Srinivas S. R., Gopal E., Zhuang L., Itagaki S., Martin P. M., Fei Y. J., Ganapathy V., Prasad P. D., Cloning and functional identification of slc5a12 as a sodium-coupled low-affinity transporter for monocarboxylates (SMCT2). Biochem J, **2005**, 392: 655–664.

Steen O. & Goldenberg R. M., The Role of Sodium-Glucose Cotransporter 2 Inhibitors in the Management of Type 2 Diabetes. Canadian Journal of Diabetes, **2017**, 41: 517-523.

Stone K. M., Voska J., Kinnebrew M., Pavlova A., Junk M. J., Han S., Structural insight into proteorhodopsin oligomers. Biophys J., **2013**, 104(2): 472-81.

Sun C., Benlekbir S., Venkatakrishnan P., Wang Y., Hong S., Hosler J., Tajkhorshid E., Rubinstein J. L., Gennis R. B., Structure of the alternative complex III in a supercomplex with cytochrome oxidase. Nature, **2018**, 557(7703): 123-126.

Swainsbury D. J. K., Hawkings F. R., Martin E. C., Musiał S., Salisbury J. H., Jackson P. J., Farmer D. A., Johnson M. P., Siebert C. A., Hitchcock A., Hunter C. N., Cryo-EM structure of the four-subunit Rhodobacter sphaeroides cytochrome bc1 complex in styrene maleic acid nanodiscs. Proc Natl Acad Sci USA, **2023**, 120(12): e2217922120.

Takasuga S. & Sasaki T., Phosphatidylinositol-3,5-bisphosphate: metabolism and physiological functions. J Biochem., **2013**, 154(3): 211-8.

Tartoff K. & Hobbs C., Improved media for growing plasmid and cosmid clones. Bethesda Research Laboratories Focus, **1987**, 9: 12.

Thangaratnarajah C., Rheinberger J., Paulino C., Cryo-EM studies of membrane proteins at 200 keV. Curr Opin Struct Biol., **2022**, 76: 102440.

Tocilj A., Munger C., Proteau A., Morona R., Purins L., Ajamian E., Wagner J., Papadopoulos M., Van Den Bosch L., Rubinstein J. L., Féthière J., Matte A., Cygler M., Bacterial polysaccharide co-polymerases share a common framework for control of polymer length. Nat Struct Mol Biol., **2008**, 15(2): 130-8.

Tong J., Tan L., Chun C., Im Y. J., Structural basis of human ORP1-Rab7 interaction for the late-endosome and lysosome targeting. PLoS ONE, **2019**, 14(2): e0211724.

Tribet C., Audebert R., Popot J. L., Amphipols: polymers that keep membrane proteins soluble in aqueous solutions. Proc Natl Acad Sci USA, **1996**, 93(26): 15047-50.

Turk E. & Wright E. M., Membrane topology motifs in the SGLT cotransporter family. J Membr Biol., **1997**, 159(1):1-20.

Turk E., Kim O., le Coutre J., Whitelegge J. P., Eskandari S., Lam J. T., Kreman M., Zampighi G., Faull K. F., Wright E. M., Molecular characterization of Vibrio parhaemolyticus vSGLT: a model for sodium-coupled sugar transport. J Biol Chem., **2000**, 275: 25711-25716.

Uchański T., Masiulis S., Fischer B., Kalichuk V., López-Sánchez U., Zarkadas E., Weckener M., Sente A., Ward P., Wohlkönig A., Zögg T., Remaut H., Naismith J. H., Nury H., Vranken W., Aricescu A. R., Pardon E., Steyaert J.**,** Megabodies expand the nanobody toolkit for protein structure determination by single-particle cryo-EM. Nat Methods, **2021**, 18(1): 60-68.

Uhlén M., Fagerberg L., Hallström B. M., Lindskog C., Oksvold P., Mardinoglu A., Sivertsson Å., Kampf C., Sjöstedt E., Asplund A., Olsson I., Edlund K., Lundberg E., Navani S., Szigyarto C. A., Odeberg J., Djureinovic D., Takanen J. O., Hober S., Alm T., Edqvist P. H., Berling H., Tegel H., Mulder J., Rockberg J., Nilsson P., Schwenk J. M., Hamsten M., von Feilitzen K., Forsberg M., Persson L., Johansson F., Zwahlen M., von Heijne G., Nielsen J., Pontén F., Tissue-based map of the human proteome. Science, **2015**, 347(6220): 1260419.

Urner L. H., Liko I., Yen H. Y., Hoi K. K., Bolla J. R., Gault J., Almeida F. G., Schweder M. P., Shutin D., Ehrmann S., Haag R., Robinson C. V., Pagel K., Modular detergents tailor the purification and structural analysis of membrane proteins including G-protein coupled receptors. Nat Commun., **2020**, 11(1): 564.

Vénien-Bryan C. & Fernandes C. A. H., Overview of Membrane Protein Sample Preparation for Single-Particle Cryo-Electron Microscopy Analysis. International Journal of Molecular Sciences, **2023**, 24(19): 14785.

Voss A. A., Díez-Sampedro A., Hirayama B. A., Loo D. D., Wright E. M., Imino sugars are potent agonists of the human glucose sensor SGLT3. Mol Pharmacol., **2007**, 71(2):628-34.

Wahlgren W. Y., Dunevall E., North R. A., Paz A., Scalise M., Bisignano P., Bengtsson-Palme J., Goyal P., Claesson E., Caing-Carlsson R., Andersson R., Beis K., Nilsson U. J., Farewell A., Pochini L., Indiveri C., Grabe M., Dobson R. C. J., Abramson J., Ramaswamy S., Friemann R., Substrate-bound outward-open structure of a Na^+-coupled sialic acid symporter reveals a new Na^+ site. Nat Commun, **2018**, 9: 1753.

Wang X., Zhang X., Dong X. P., Samie M., Li X., Cheng X., Goschka A., Shen D., Zhou Y., Harlow J., Zhu M. X., Clapham D. E., Ren D., Xu H., TPC proteins are phosphoinositide- activated sodium-selective ion channels in endosomes and lysosomes. Cell, **2012**, 151(2): 372-83.

Wang Y., Zhang Y., Li N., Chen L., Zhang D., Sun D., Li S., Guo X., Ma X., Stirring rate regulates the proliferation and metabolism of microencapsulated recombinant CHO cells. Biotechnol Appl Biochem., **2015**, 62(6): 833-9.

Wang K., Preisler S. S., Zhang L., Cui Y., Missel J. W., Grønberg C., Gotfryd K., Lindahl E., Andersson M., Calloe K., Egea P. F., Klaerke D. A., Pusch M., Pedersen P. A., Zhou Z. H., Gourdon P., Structure of the human ClC-1 chloride channel. PLoS Biol., **2019**, 17(4): e3000218

Wang Q. & Zhu M. X., NAADP-Dependent TPC Current. Handb Exp Pharmacol., **2023**, 278: 35-56.

Wehbie M., Onyia K. K., Mahler F., Le Roy A., Deletraz A., Bouchemal I., Vargas C., Babalola J. O., Breyton C., Ebel C., Keller S., Durand G., Maltose-Based Fluorinated Surfactants for Membrane-Protein Extraction and Stabilization. Langmuir, **2021**, 37(6): 2111-2122.

Wright E. M., Renal Na^+-glucose cotransporters. Am J Physiol Renal Physio, **2001**, 280: F10–F18.

Wright E. M., Glucose transport families SLC5 and SLC50. Molecular Aspects of Medicine, **2013**, 34(2-3): 183-196.

Wu M., Wang T., Loh E., Hong W., Song H., Structural basis for recruitment of RILP by small GTPase Rab7. EMBO J., **2005**, 24(8): 1491-501.

Wu S., Avila-Sakar A., Kim J., Booth D. S., Greenberg C. H., Rossi A., Liao M., Li X., Alian A., Griner S. L., Juge N., Yu Y., Mergel C. M., Chaparro-Riggers J., Strop P., Tampé R., Edwards R. H., Stroud R. M., Craik C. S., Cheng Y., Fabs enable single particle cryoEM studies of small proteins. Structure, **2012**, 20(4): 582-92.

Wu X. & Rapoport T. A., Cryo-EM structure determination of small proteins by nanobody-binding scaffolds (Legobodies). Proc. Natl. Acad. Sci. USA, **2021**, 118(41):e2115001118.

Xue D., Xu T., Wang H., Wu M., Yuan Y., Wang W., Tan Q., Zhao F., Zhou F., Hu T., Jiang Z., Liu Z. J., Zhao S., Liu D., Wüthrich K., Tao H., Disulfide-Containing Detergents (DCDs) for the Structural Biology of Membrane Proteins. Chemistry, **2019**, 25(50): 11635-11640.

Yamashita A., Singh S. K., Kawate T., Jin Y., Gouaux E., Crystal structure of a bacterial homologue of Na^+/Cl^--dependent neurotransmitter transporters. Nature, **2005**, 437(7056):215-23.

Yao X., Fan X., Yan N., Cryo-EM analysis of a membrane protein embedded in the liposome. Proc Natl Acad Sci USA, **2020**, 117(31): 18497-18503.

Yip K. M., Fischer N., Paknia E., Chari A., Stark H., Atomic-resolution protein structure determination by cryo-EM. Nature, **2020**, 587(7832): 157-161.

Yoder N. & Gouaux E., The His-Gly motif of acid-sensing ion channels resides in a reentrant 'loop' implicated in gating and ion selectivity. Elife, **2020**, 9: e56527.

Young J. W., Wason I. S., Zhao Z., Kim S., Aoki H., Phanse S., Rattray D. G., Foster L. J., Babu M., van Hoa D. F., Development of a Method Combining Peptidiscs and Proteomics to identify, stabilize, and purify a Detergent-Sensitive Membrane Protein Assembly. J. Proteome Res., **2022**, 21(7): 1748-1758.

Yu F. H. & Catterall W. A., The VGL-chanome: a protein superfamily specialized for electrical signaling and ionic homeostasis. Sci STKE, **2004**, 253:re15.

Yuan Y., Jaślan D., Rahman T., Bolsover S. R., Arige V., Wagner L. E. 2nd, Abrahamian C., Tang R., Keller M., Hartmann J., Rosato A. S., Weiden E. M., Bracher F., Yule D. I., Grimm C., Patel S., Segregated cation flux by TPC2 biases Ca2+ signaling through lysosomes. Nat Commun., **2022**, 13(1): 4481.

Zampieri V., Gobet A., Robert X., Falson P., Chaptal V., CryoEM reconstructions of membrane proteins solved in several amphipathic solvents, nanodisc, amphipol and detergents, yield amphipathic belts of similar sizes corresponding to a common ordered solvent layer. Biochim Biophys Acta Biomembr., **2021**, 1863(11): 183693.

Zhang J.-H., Wang F., Wang T.-Y., A simple and effective SuperBuffer for DNA agarose electrophoresis. Gene, **2011**, 487(1): 72-74.

Zhang Z. & Chen J., Atomic Structure of the Cystic Fibrosis Transmembrane Conductance Regulator. Cell, **2016**, 167(6): 1586-1597.e9.

Zhang X., Chen W., Li P., Calvo R., Southall N., Hu X., Bryant-Genevier M., Feng X., Geng Q., Gao C., Yang M., Tang K., Ferrer M., Marugan J. J., Xu H., Agonist-specific voltage-dependent gating of lysosomal two-pore Na^+ channels. Elife, **2019**, 8: e51423.

Zhang X., Belousoff M. J., Zhao P., Kooistra A. J., Truong T. T., Ang S. Y., Underwood C. R., Egebjerg T., Šenel P., Stewart G. D., Liang Y. L., Glukhova A., Venugopal H., Christopoulos A., Furness S. G. B., Miller L. J., Reedtz-Runge S., Langmead C. J., Gloriam D. E., Danev R., Sexton P. M., Wootten D., Differential GLP-1R Binding and Activation by Peptide and Non-peptide Agonists. Mol Cell, **2020**, 80(3): 485-500.e7.

Zhang H., Huang C. S., Yu X., Lee J., Vaish A., Chen Q., Zhou M., Wang Z., Min X., Cryo-EM structure of ABCG5/G8 in complex with modulating antibodies. Commun Biol., **2021**, 4(1): 526.

Zhang M., Gui M., Wang Z. F., Gorgulla C., Yu J. J., Wu H., Sun Z. J., Klenk C., Merklinger L., Morstein L., Hagn F., Plückthun A., Brown A., Nasr M. L., Wagner G., Cryo-EM structure of an activated GPCR-G protein complex in lipid nanodiscs. Nat Struct Mol Biol., **2021**, 28(3):258-267.

Zhang X. X., Young J. W., Foster L. J., Duong F., Nanodisc-Based Proteomics Identify Caj1 as an Hsp40 with Affinity for Phosphatidic Acid Lipids. J Proteome Res., **2021**, 20(10): 4831-4839.

Zhang Y., Dijkman P. M., Zou R., Zandl-Lang M., Sanchez R. M., Eckhardt-Strelau L., Köfeler H., Vogel H., Yuan S., Kudryashev M., Asymmetric opening of the homopentameric 5-HT3A serotonin receptor in lipid bilayers. Nat Commun., **2021**, 12(1): 1074.

Zhu K. F., Yuan C., Du Y. M., Sun K. L., Zhang X. K., Vogel H., Jia X. D., Gao Y. Z., Zhang Q. F., Wang D. P., Zhang H. W., Applications and prospects of cryo-EM in drug discovery. Mil Med Res., **2023**, 10(1): 10.

Zong X., Schieder M., Cuny H., Fenske S., Gruner C., Rötzer K., Griesbeck O., Harz H., Biel M., Wahl-Schott C., The two-pore channel TPCN2 mediates NAADP-dependent Ca(2+)-release from lysosomal stores. Pflugers Arch., **2009**, 458(5): 891-9.

7. Supplements

7.1 SLC5A family

7.1.1 SGLT2 plasmids

Table 7.1: pEGBacMam_SGLT2 constructs

Name	Characteristics
pEGBacMam_8xHis_mEGFP_3C_SGLT2	**N-term. His_8-Tag** N-term. mEGFP-Tag 3C cleavage site
pEGBacMam_Myc_mEGFP_3C_SGLT2	**N-term. Myc-Tag** N-term. mEGFP-Tag 3C cleavage site
pEGBacMam_SGLT2_3C_mEGFP_8xHis (Fig. 7.1)	**C-term. His_8-Tag** C-term. mEGFP-Tag 3C cleavage site
pEGBacMam_SGLT2_3C_mEGFP_Myc	**C-term. Myc-Tag** C-term. mEGFP-Tag 3C cleavage site
pEGBacMam_SGLT2_3C_mEGFP_StrepII	**C-term. StrepII-Tag** C-term. mEGFP-Tag 3C cleavage site

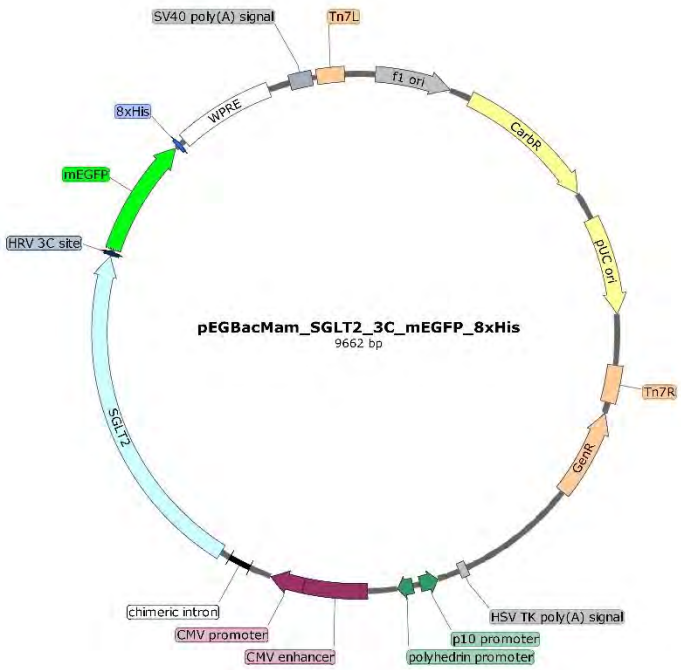

Figure 7.1: Expression vector pEGBacMam_SGLT2_3C_mEGFP_8xHis
Composition of the pEGBacMam_SGLT2 expression vector on the example of the C-term. His_8-tagged constructpEGBacMam_SGLT2_3C_ mEGFP_8xHis.

7.1.2 Gateway cloning

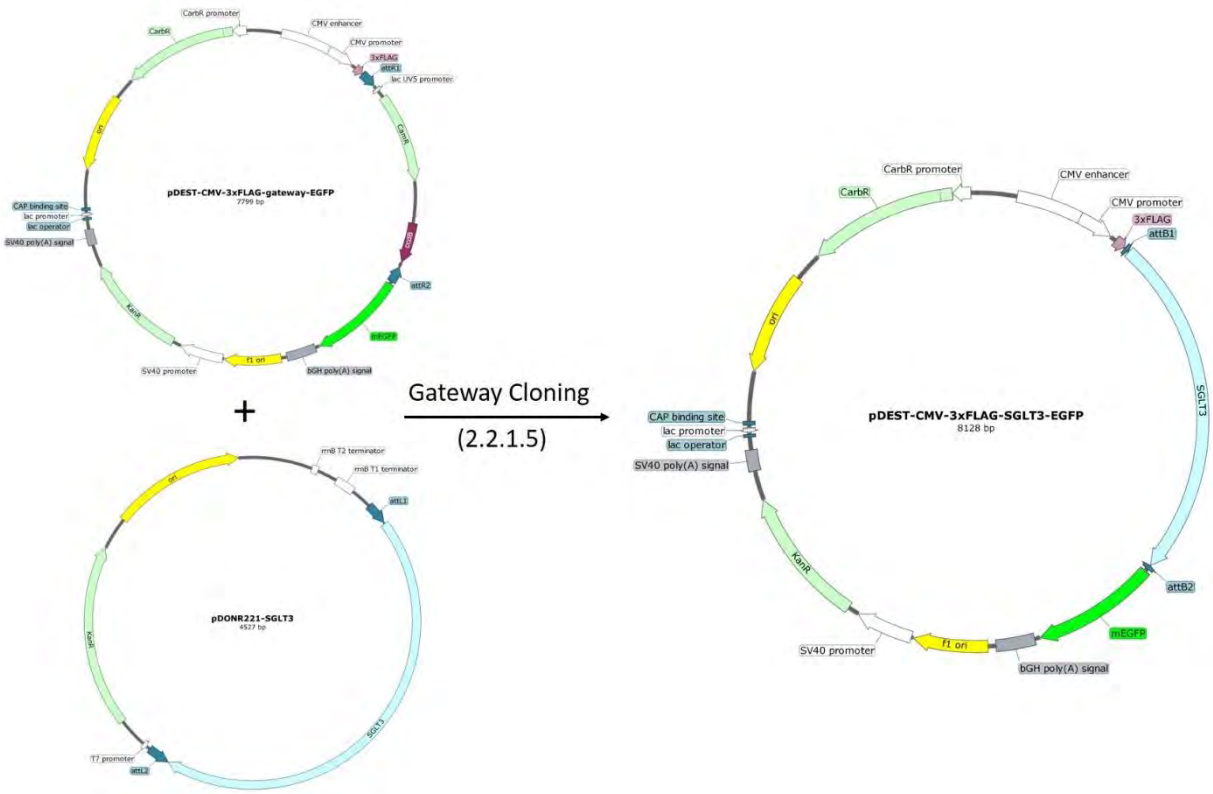

Figure 7.2: Gateway cloning on the example of SGLT3
Generation of the SGLT3 expression vector pDEST-CMV-3xFLAG-SGLT3-EGFP (2.1.14.2.2) via Gateway cloning (2.2.1.5) from the destination vector pDEST-CMV-3xFLAG-gateway-EGFP (2.1.14.2.2) and the entry vector pDONR221-SGLT3 (2.1.14.2.2). The image was created with BioRender (2.1.2).

7.1.3 AA sequence of SGLT3 construct for stable cell line

Start**WSHPQFEK**GGGGSMVSKGEELFTGVVPILVELDGDVNGHKFSVSGEGEGDATYGKLTLKFICTTGKLPVPWPTLV
TTLTYGVQCFSRYPDHMKQHDFFKSAMPEGYVQERTIFFKDDGNYKTRAEVKFEGDTLVNRIELKGIDFKEDGNILGHKL
EYNYNSHNVYIMADKQKNGIKVNFKIRHNIEDGSVQLADHYQQNTPIGDGPVLLPDNHYLSTQSALSKDPNEKRDHMV
LLEFVTAAGITLGMDELYKPRELVPRGSPREMASTVSPSTIAETPEPPPLSDHIRNAADISVIVIYFLVVMAVGLWAMLKT
NRGTIGGFFLAGRDMAWWPMGASLFASNIGSNHYVGLAGTGAASGVATVTFEWTSSVMLLILGWIFVPIYIKSGVMT
MPEYLKKRFGGERLQVYLSILSLFICVVLLISADIFAGAIFIKLALGLDLYLAIFILLAMTAVYTTTGGLASVIYTDTLQTIIMLIG
SFILMGFAFNEVGGYESFTEKYVNATPSVVEGDNLTISASCYTPRADSFHIFRDAVTGDIPWPGIIFGMPITALWYWCTN
QVIVQRCLCGKDMSHVKAACIMCAYLKLLPMFLMVMPGMISRILYTDMVACVVPSECVKHCGVDVGCTNYAYPTMV
LELMPQGLRGLMLSVMLASLMSSLTSIFNSASTLFTIDLYTKMRKQASEKELLIAGRIFVLLLTVVSIVWVPLVQVSQNGQ
LIHYTESISSYLGPPIAAVFVLAIFCKRVNEQGAFWGLMVGLAMGLIRMITEFAYGTGSCLAPSNCPKIICGVHYLYFSIVLF
FGSMLVTLGISLLTKPIPDVHLYRLCWVLRNSTEERIDIDAEEKSQEETDDGVEEDYPEKSRGCLKKAYDLFCGLQKGPKLT
KEEEEALSKKLTDTSERPSWRTIVNINAILLLAVVVFIHGYYAStop

StrepII-Tag; mEGFP; Thrombin cleavage site; SGLT3

7.1.4 SPA cryo-EM data processing of SGLT3 in DDM/CHS

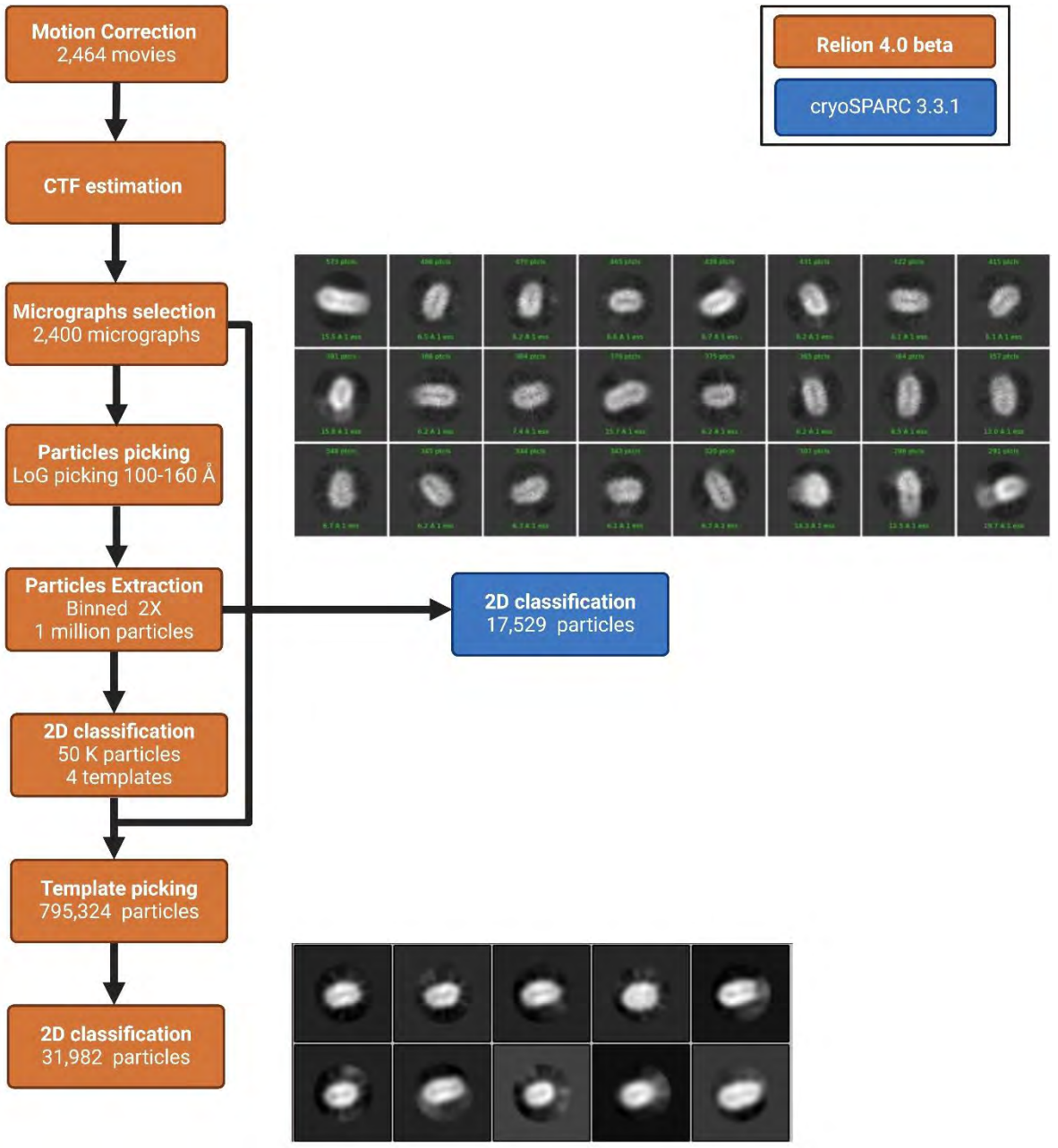

Figure 7.3: Processing workflow of SGLT3 in DDM/CHS

SPA cryo-EM image processing workflow for SGLT3 in DDM/CHS. 2,464 movies were collected on a CRYO ARM™ 200 (2.2.7.2.3), motion corrected and CTF was estimated. Afterwards micrographs with resolution below 8 Å were excluded (2,400 micrographs left), particles with a size of 100 – 160 Å got picked and manually 2D classified to generate 4 templates. Those were used for template picking from the 2,400 micrographs, resulting in 795,324 particles, manually classified to 10 2D-classes with a total of 31,982 particles. All these steps were performed with RELION (2.1.2). Additionally, the auto-picked (LoG) particles were exported in to cryoSPARC (2.1.2) and classified into 24 2D-classes with a total of 17,529 particles. The image was created with BioRender (2.1.2).

7.2 GPR

7.2.1 SPA cryo-EM data processing of GPR in salipros

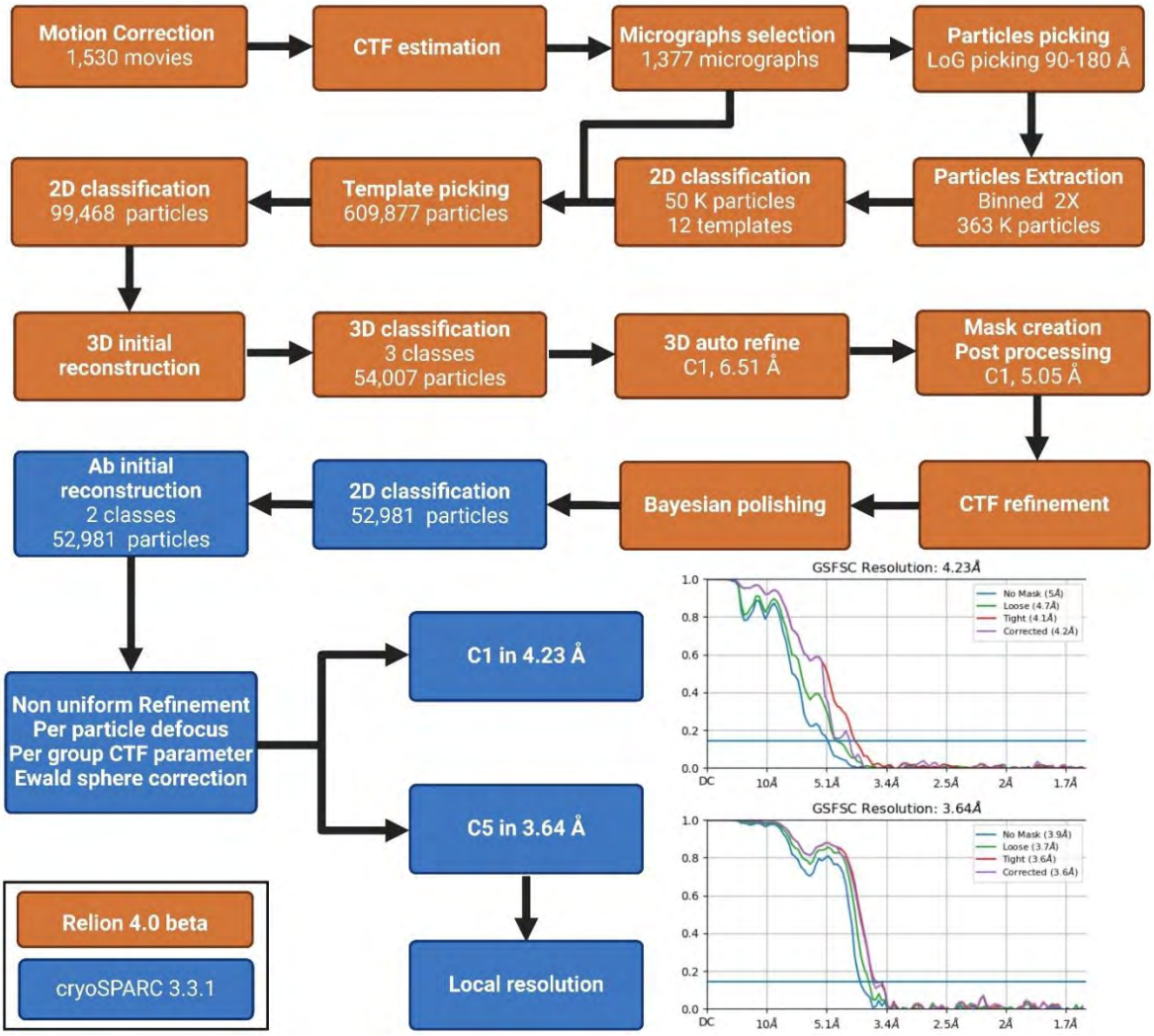

Figure 7.4: Processing workflow of GPR in salipros

SPA cryo-EM image processing workflow for GPR reconstituted in salipros together with POPC (2.2.6.2). 1,530 movies were collected on a CRYO ARM™ 200 (2.2.7.2.3), motion corrected and CTF was estimated. Afterwards micrographs with resolution below 8 Å were excluded (1,377 micrographs left), particles with a size of 90 – 180 Å got picked and manually 2D classified to generate 12 templates. Those were used for template picking from the 1,377 micrographs, resulting in 609,877 particles, manually classified to 99,468 particles. After creating an initial 3D model, three 3D classes were generated, the best 3D class, containing 54,007 particles, was picked and 3D auto refined in C1 symmetry (6.51 Å). Then a mask was created, the model was post-processed in C1 (5.05 Å), CTF was refined followed by Bayesian polishing. All these steps were performed with RELION (2.1.2). Afterwards, the polished particles were exported in to cryoSPARC (2.1.2) and classified to 52,981 particles (Fig.3.15b). Ab initial reconstruction in two classes resulted in two similar classes, so it was decided to run the final step of non-uniform refinement with all 52,981 particles. This resulted in a C1 map with a final resolution of 4.23 Å and a C5 map with 3.64 Å (Fig.3.15c). Additionally, the local resolution of the C5 map was determined (Fig.3.15d). The image was created with BioRender (2.1.2).

7.3 TPC2

7.3.1 TPC2 plasmid

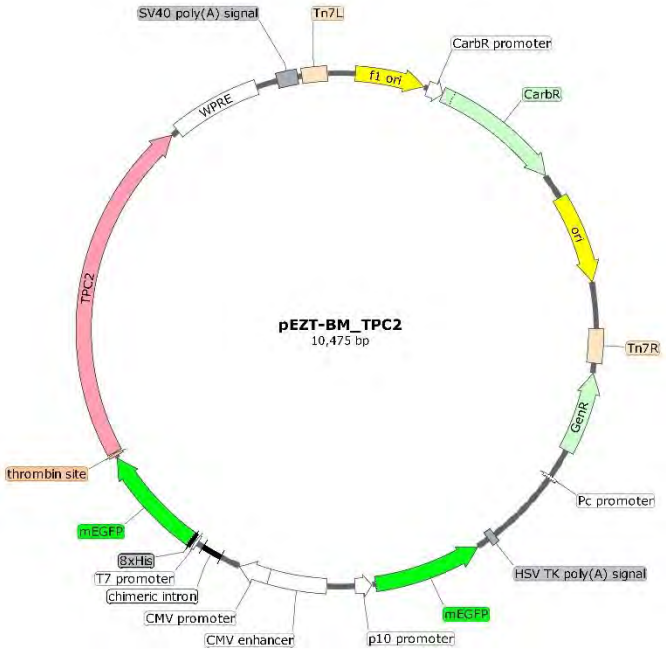

Figure 7.5: Expression vector pEZT-BM_TPC2
Composition of the pEZT-BM_TPC2 expression vector containing C-term. His_8-mEGFP-tagged TPC2. Additionally, the construct contains a T7 for transient expression and a p10 promotor making it feasible for the Bac-to-Bac® Expression System (Fig. 3.2).

7.3.2 AA sequence of TPC2 construct for stable cell line

Start**HHHHHHHH**MAEPQAESEP**AA**GGARGGGGDWPAGLTTYRSIQVGPGAAARWDLCIDQAVVFIEDAIQYRSINH
RVDASSMWLYRRYYSNVCQRTLSFTIFLILFLAFIETPSSLTSTADVRYRAAPWEPPCGLTESVEVLCLLVFAADLSVKGYLF
GWAHFQKNLWLLGYLVVLVVSLVDWTVSLSLVCHEPLRIRRLLRPFFLLQNSSMMKKTLKCIRWSLPEMASVGLLLAIHL
CLFTMFGMLLFAGGKQDDGQDRERLTYFQNLPESLTSLLVLLTTANNPDVMIPAYSKNRAYAIFFIVFTVIGSLFLMNLLT
AIIYSQFRGYLMKSLQTSLFRRRLGTRAAFEVLSSMVGEGGAFPQAVGVKPQNLLQVLQKVQLDSSHKQAMMEKVRSY
GSVLLSAEEFQKLFNELDRSVVKEHPPRPEYQSPFLQSAQFLFGHYYFDYLGNLIALANLVSICVFLVLDADVLPAERDDFIL
GILNCVFIVYYLLEMLLKVFALGLRGYLSYPSNVFDGLLTVVLLVLEISTLAVYRLPHPGWRPEMVGLLSLWDMTRMLNM
LIVFRFLRIIPSMK**P**MAVVASTVLGLVQNMRAFGGILVVVYYVFAIIGINLFRGVIVALPGNSSLAPANGSAPCGSFEQLEY
WANNFDDFAAALVTLWNLMVVNNWQVFLDAYRRYSGPWSKIYFVLWWLVSSVIWVNLFLALILENFLHKWDPRSHL
QPLAGTPEATYQMTVELLFRDILEEP**E**EDELTERLSQHPHLWLCRStop

His_8-Tag; TPC2 (**mutations**)

7.3.3 SPA cryo-EM data processing of TPC2

7.3.3.1 TPC2 Apo

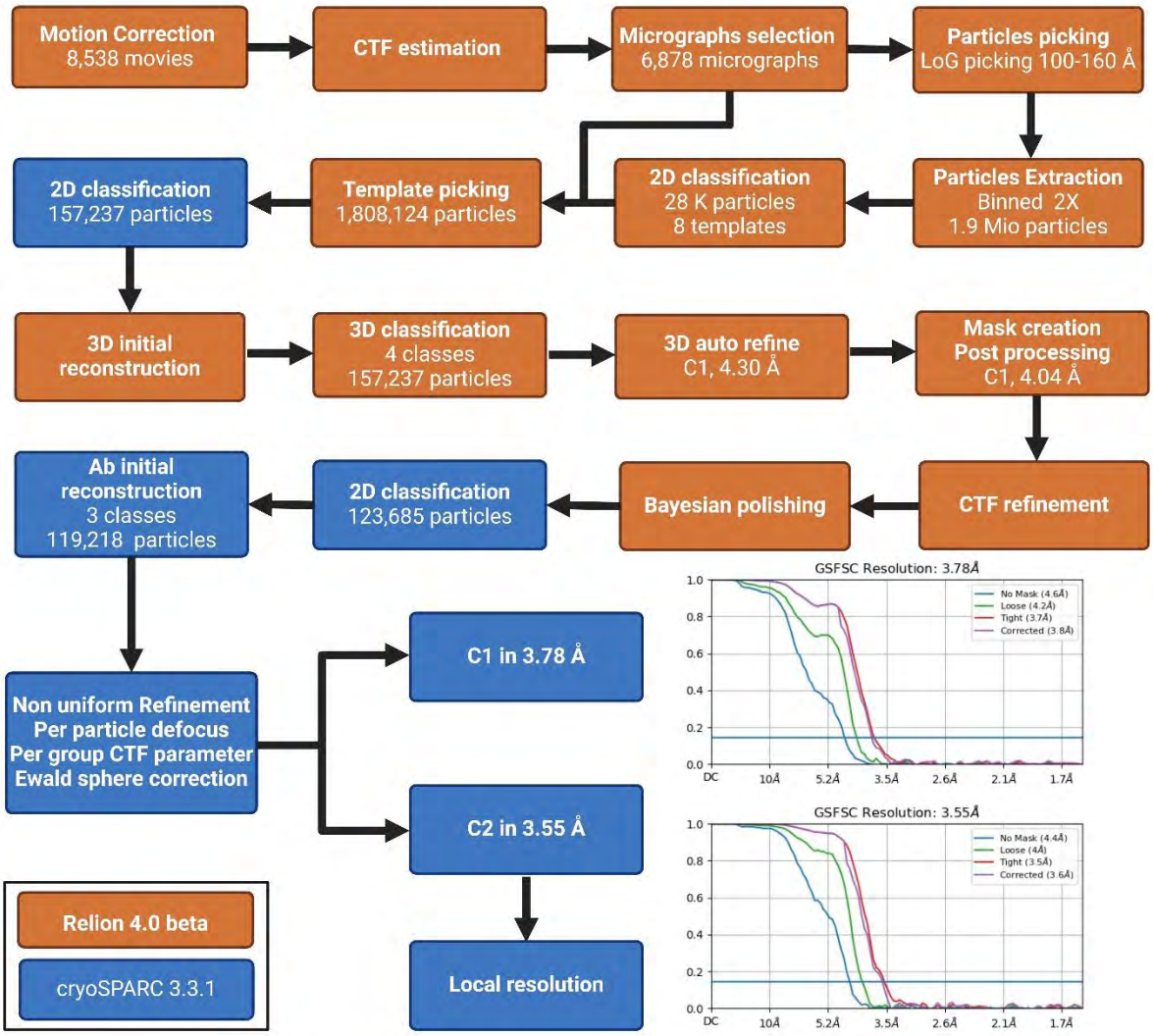

Figure 7.6: Processing workflow of TPC2 Apo

SPA cryo-EM image processing workflow of TPC2. 8,538 movies were collected on a CRYO ARM™ 200 (2.2.7.2.3), motion corrected and CTF was estimated. Afterwards micrographs with resolution below 8 Å were excluded (6,878 micrographs left), particles with a size of 100 – 160 Å got picked and manually 2D classified to generate 8 templates. Those were used for template picking from the 6,878 micrographs, resulting in 1,808,124 particles, manually classified to 157,237 particles. After creating an initial 3D model, four 3D classes were generated. As all four classes looked similar, so all of them were used for 3D auto refine in C1 symmetry (4.30 Å). Then a mask was created, the model was post-processed in C1 (4.04 Å) and CTF was refined followed by Bayesian polishing. All these steps were performed with RELION (2.1.2), except 2D classification after template picking, which was done in cryoSPARC (2.1.2), as well as the following steps. The polished particles were classified to 123,685 particles. Ab initial reconstruction in three classes resulted in two good classes, so it was decided to exclude one 3D class (4,467 particles) and run the final step of non-uniform refinement with the remaining 119,218 particles (Fig.3.20b). This resulted in a C1 map with a final resolution of 3.78 Å and a C2 map with 3.55 Å (Fig.3.20c). Additionally, the local resolution of the C2 map was determined (Fig.3.20d). The image was created with BioRender (2.1.2).

7.3.3.2 TPC2-A1-P

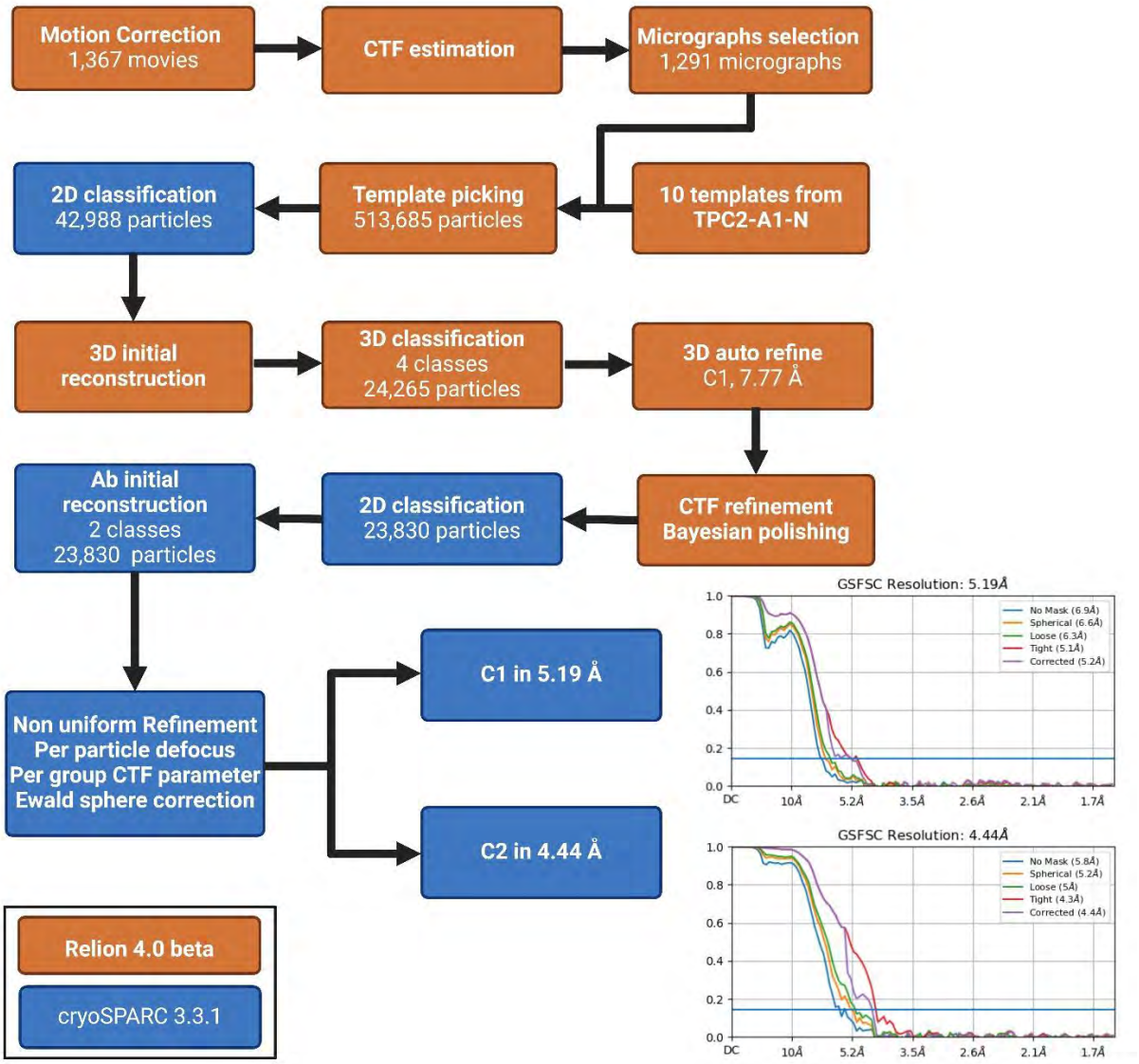

Figure 7.7: Processing workflow of TPC2 with TPC2-A1-P

SPA cryo-EM image processing workflow of TPC2 supplemented with TPC2-A1-P (Table 3.8). 1,367 movies were collected on a CRYO ARM™ 200 (2.2.7.2.3), motion corrected and CTF was estimated. Afterwards micrographs with resolution below 8 Å were excluded (1,291 micrographs left). 10 templates from TPC2-A1-N (7.3.3.3) were used for template picking from the 1,367 micrographs, resulting in 513,685 particles, manually classified to 42,988 particles. After creating an initial 3D model, four 3D classes were generated. Two out of the four classes looked promising (24,265 particles), so those were used for 3D auto refine in C1 symmetry (7.77 Å) and CTF was refined followed by Bayesian polishing. All these steps were performed with RELION (2.1.2), except 2D classification after template picking, which was done in cryoSPARC (2.1.2), as well as the following steps. The polished particles were classified to 23,830 particles (Fig.3.19a). Ab initial reconstruction in two classes resulted in two similar classes, so it was decided to run the final step of non-uniform refinement with all 23,830 particles. This resulted in a C1 map with a final resolution of 5.19 Å and a C2 map with 4.44 Å (Fig.3.19b). The image was created with BioRender (2.1.2).

7.3.3.3 TPC2-A1-N

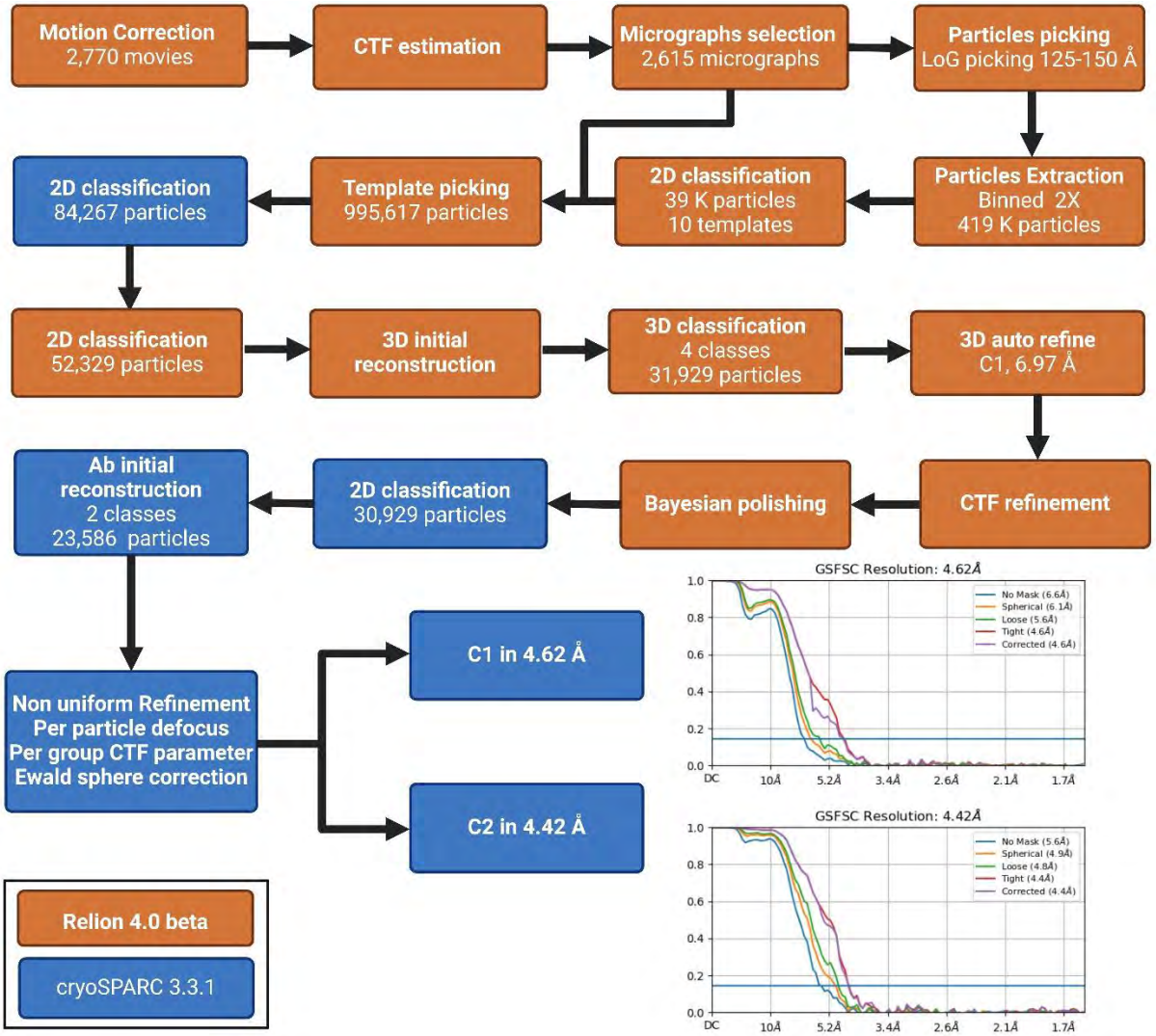

Figure 7.8: Processing workflow of TPC2 with TPC2-A1-N

SPA cryo-EM image processing workflow of TPC2 supplemented with TPC2-A1-N (Table 3.8). 2,770 movies were collected on a CRYO ARM™ 200 (2.2.7.2.3), motion corrected and CTF was estimated. Afterwards micrographs with resolution below 8 Å were excluded (2,615 micrographs left), particles with a size of 125 – 150 Å got picked and manually 2D classified to generate 10 templates. Those were used for template picking from the 2,615 micrographs, resulting in 995,617 particles, manually classified to 52,329 particles. After creating an initial 3D model, four 3D classes were generated. Two out of the four classes looked promising (31,292 particles), so those were used for 3D auto refine in C1 symmetry (6.97 Å) and CTF was refined followed by Bayesian polishing. All these steps were performed with RELION (2.1.2), except 2D classification after template picking, which was done in cryoSPARC (2.1.2), as well as the following steps. The polished particles were classified to 30,929 particles. Ab initial reconstruction in two classes resulted in one good class (23,586 particles), so it was decided to run the final step of non-uniform refinement with those 23,586 particles (Fig.3.19c). This resulted in a C1 map with a final resolution of 4.62 Å and a C2 map with 4.42 Å (Fig.3.19d). The image was created with BioRender (2.1.2).

7.3.3.4 SGA-85

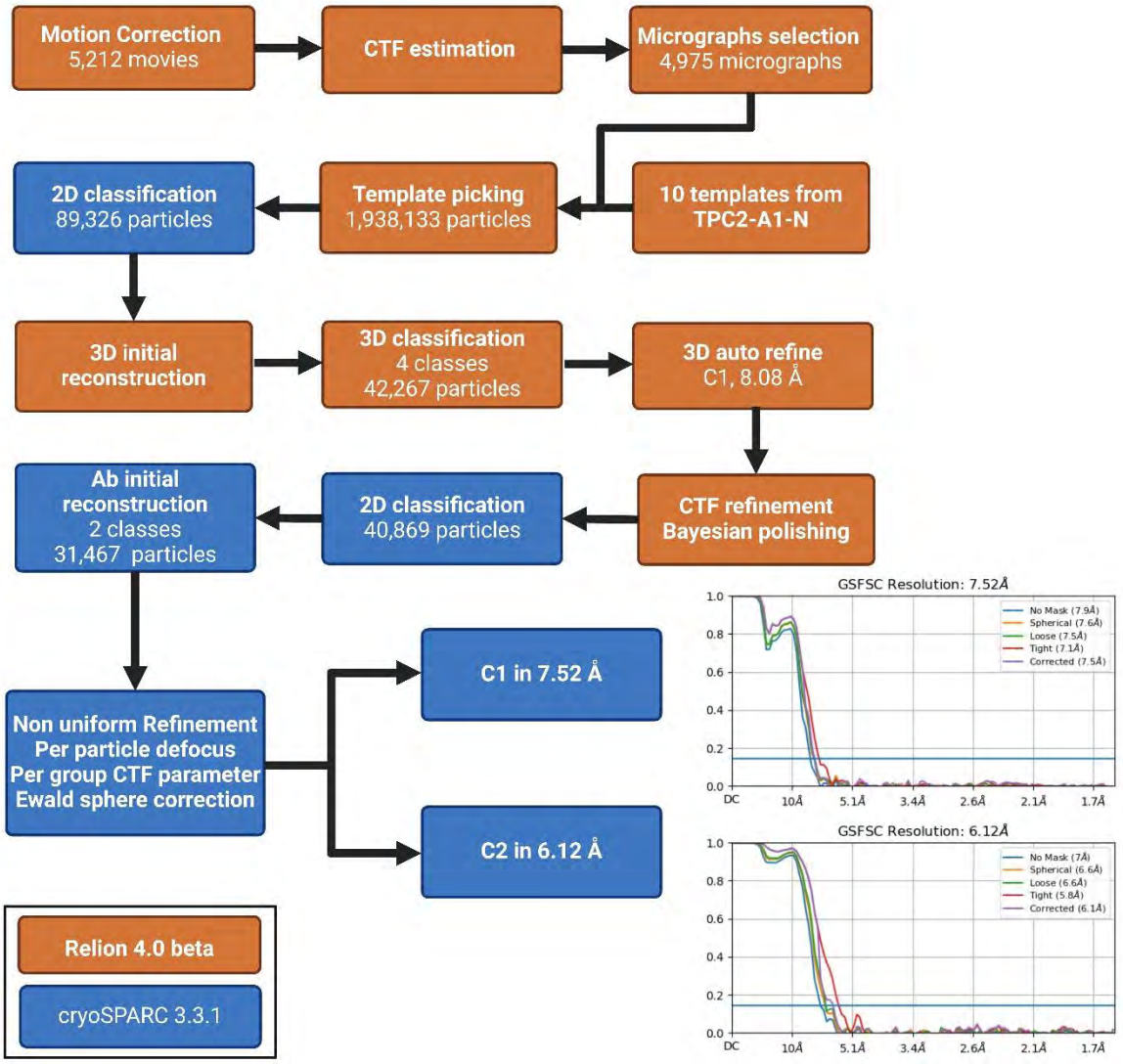

Figure 7.9: Processing workflow of TPC2 with SGA-85

SPA cryo-EM image processing workflow of TPC2 supplemented with SGA-85 (Table 3.8). 5,212 movies were collected on a CRYO ARM™ 200 (2.2.7.2.3), motion corrected and CTF was estimated. Afterwards micrographs with resolution below 8 Å were excluded (4,975 micrographs left). 10 templates from TPC2-A1-N (7.3.3.3) were used for template picking from the 4,975 micrographs, resulting in 1,938,133 particles, manually classified to 89,326 particles. After creating an initial 3D model, four 3D classes were generated. Two out of the four classes looked promising (42,267 particles), so those were used for 3D auto refine in C1 symmetry (8.08 Å) and CTF was refined followed by Bayesian polishing. All these steps were performed with RELION (2.1.2), except 2D classification after template picking, which was done in cryoSPARC (2.1.2), as well as the following steps. The polished particles were classified to 40,869 particles. Ab initial reconstruction in two classes resulted in one good class (31,476 particles), so it was decided to run the final step of non-uniform refinement with those 31,476 particles (Fig.3.19e). This resulted in a C1 map with a final resolution of 7.52 Å and a C2 map with 6.12 Å (Fig.3.19f). The image was created with BioRender (2.1.2).

7.3.3.5 SGA-111

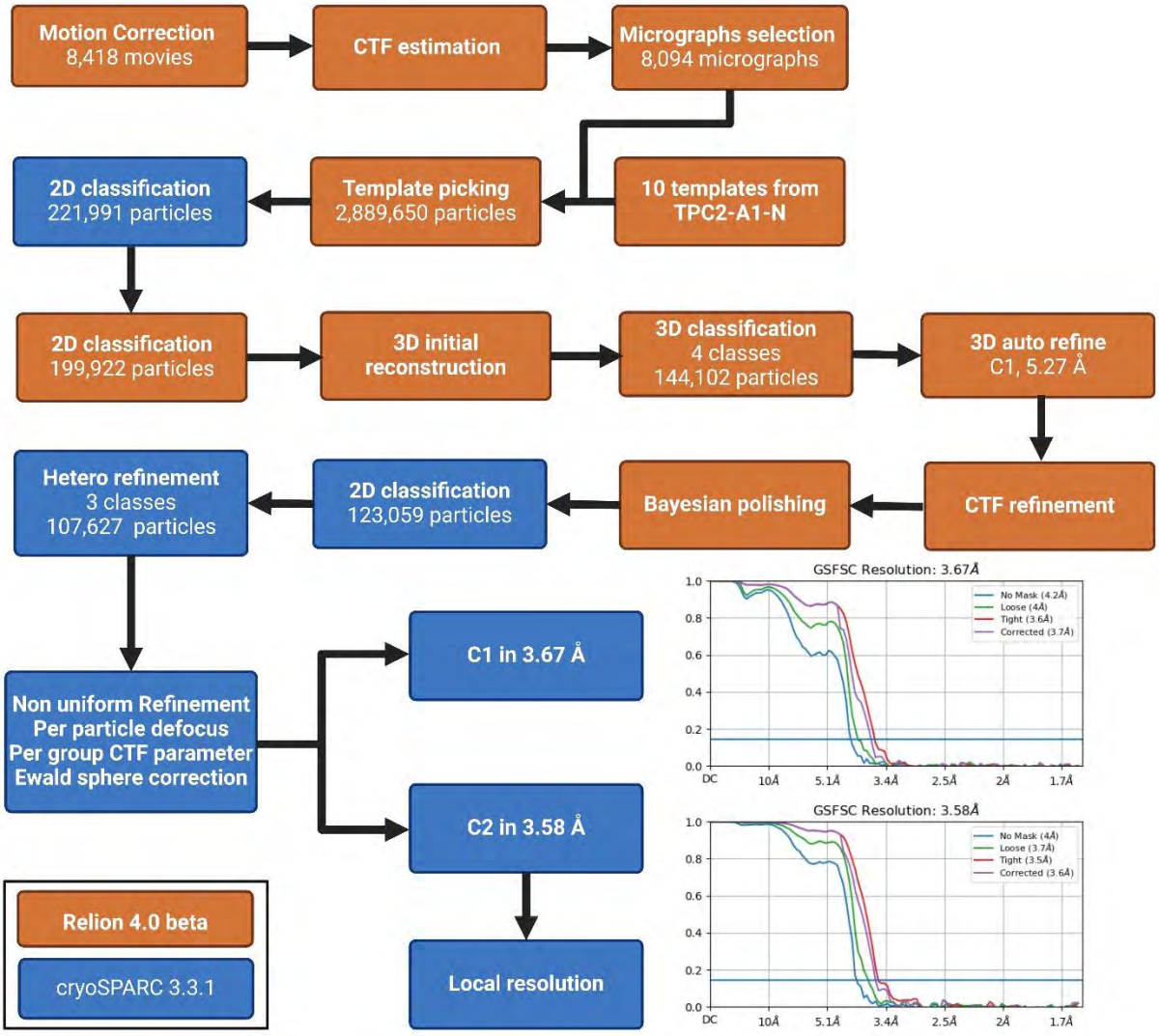

Figure 7.10: Processing workflow of TPC2 with SGA-111

SPA cryo-EM image processing workflow of TPC2 supplemented with SGA-111 (Table 3.8). 8,418 movies were collected on a CRYO ARM™ 200 (2.2.7.2.3), motion corrected and CTF was estimated. Afterwards micrographs with resolution below 8 Å were excluded (8,094 micrographs left). 10 templates from TPC2-A1-N (7.3.3.3) were used for template picking from the 8,094 micrographs, resulting in 2,889,650 particles, manually classified to 199,992 particles. After creating an initial 3D model, four 3D classes were generated. Three out of the four classes looked promising (144,102 particles), so those were used for 3D auto refine in C1 symmetry (5.27 Å) and CTF was refined followed by Bayesian polishing. All these steps were performed with RELION (2.1.2), except 2D classification after template picking, which was done in cryoSPARC (2.1,2), as well as the following steps. The polished particles were classified to 123,059 particles. Hetero refinement in three classes resulted in two good classes (total 107,627 particles), so it was decided to run the final step of non-uniform refinement with those 107,627 particles (Fig.3.29b). This resulted in a C1 map with a final resolution of 3.67 Å and a C2 map with 3.58 Å (Fig.3.29c). Additionally, the local resolution of the C2 map was determined (Fig.3.29d). The image was created with BioRender (2.1.2).

7.3.3.6 TPC2-A1-N + PI(3,5)P_2

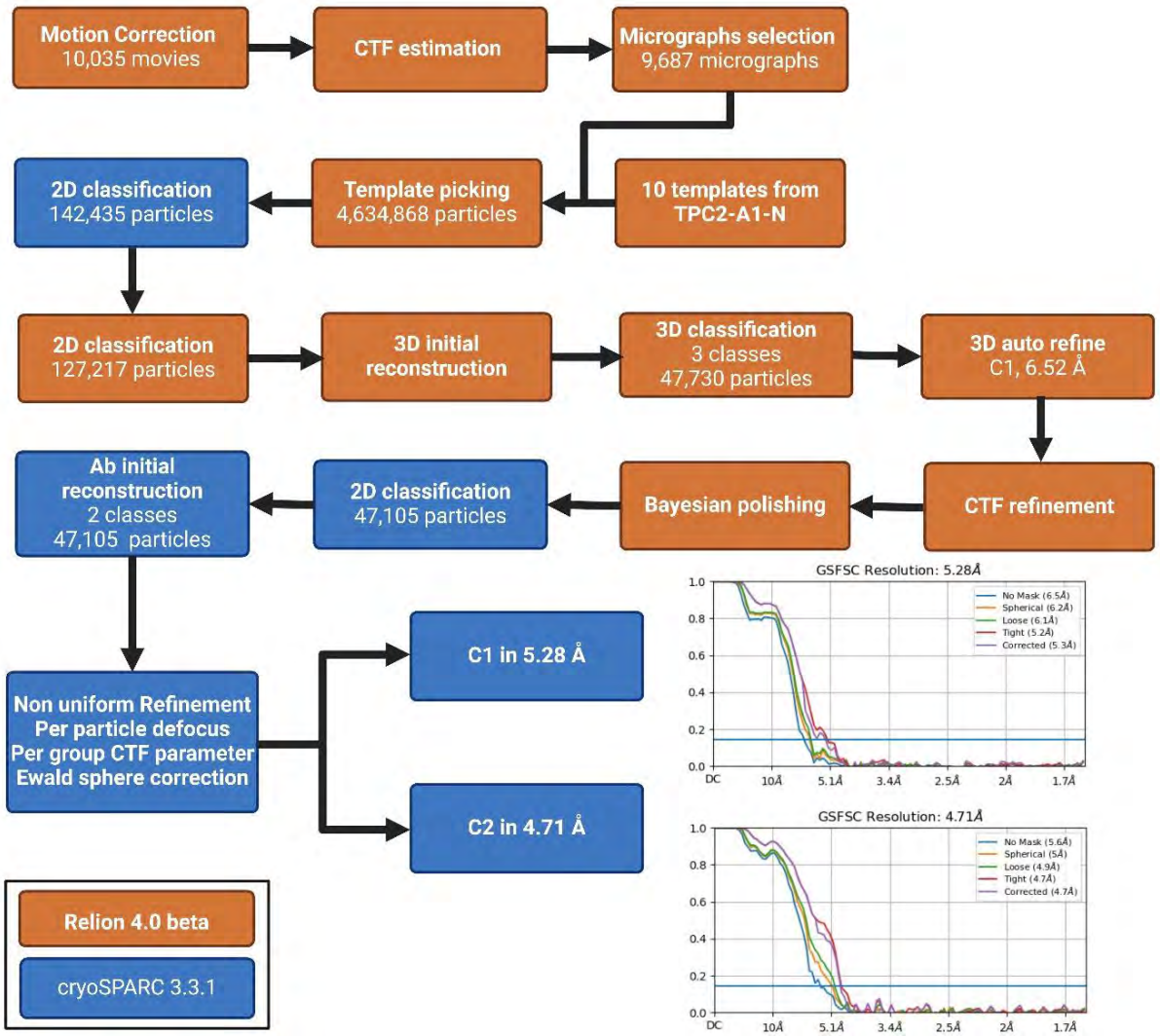

Figure 7.11: Processing workflow of TPC2 with TPC2-A1-N + PI(3,5)P_2

SPA cryo-EM image processing workflow of TPC2 supplemented with TPC2-A1-N + PI(3,5)P_2 (Table 3.8). 10,035 movies were collected on a CRYO ARM™ 200 (2.2.7.2.3), motion corrected and CTF was estimated. Afterwards micrographs with resolution below 8 Å were excluded (9,687 micrographs left). 10 templates from TPC2-A1-N (7.3.3.3) were used for template picking from the 9,687 micrographs, resulting in 4,634,868 particles, manually classified to 127,217 particles. After creating an initial 3D model, three 3D classes were generated. One class out of the three looked promising (47,730 particles), so those were used for 3D auto refine in C1 symmetry (6.52 Å) and CTF was refined followed by Bayesian polishing. All these steps were performed with RELION (2.1.2), except 2D classification after template picking, which was done in cryoSPARC (2.1.2), as well as the following steps. The polished particles were classified to 47,105 particles (Fig.3.19g). Ab initial reconstruction in two classes resulted in two similar classes, so it was decided to run the final step of non-uniform refinement with all 47,105 particles. This resulted in a C1 map with a final resolution of 5.28 Å and a C2 map with 4.71 Å (Fig.3. 19h). The image was created with BioRender (2.1.2).

7.3.3.7 Naringenin

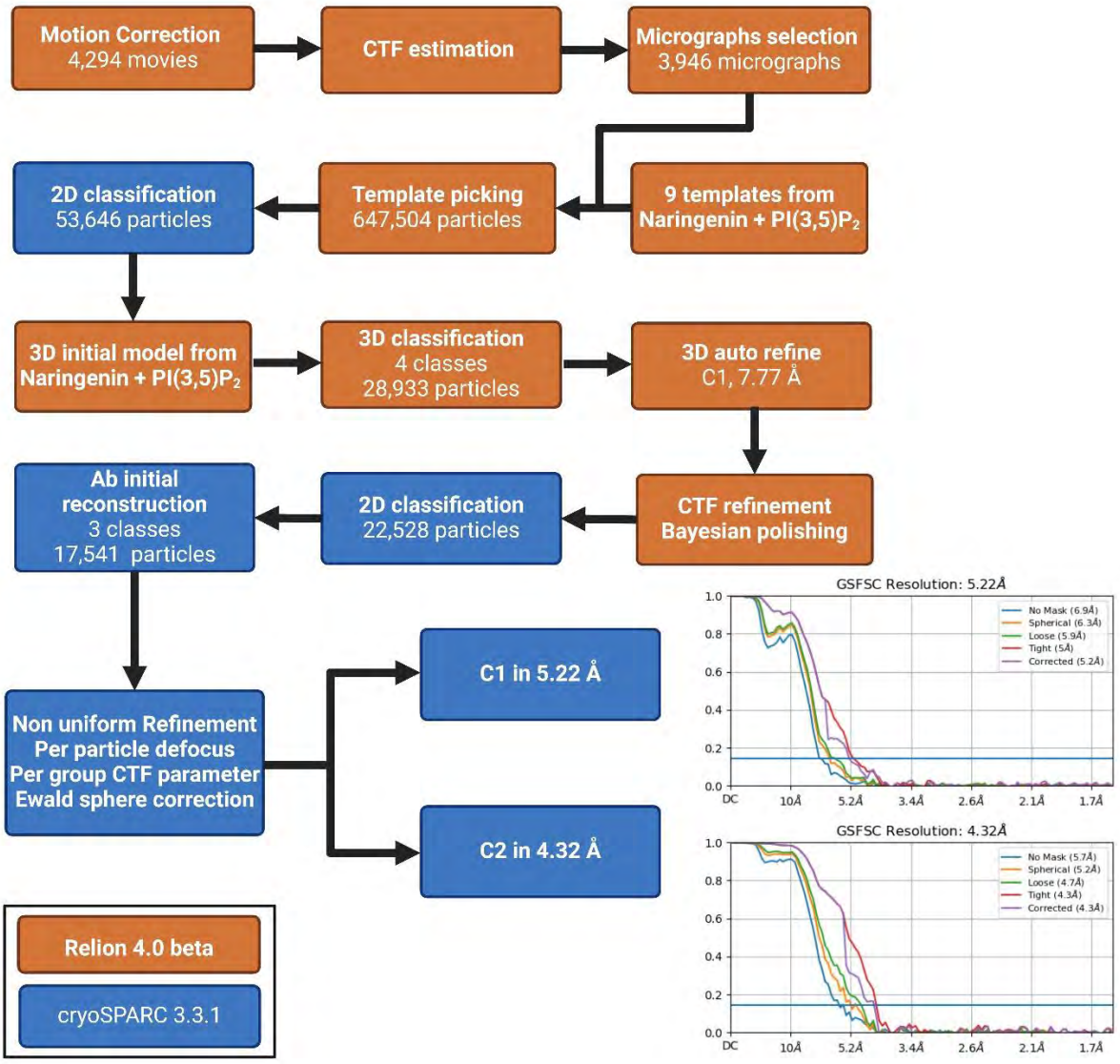

Figure 7.12: Processing workflow of TPC2 with Naringenin

SPA cryo-EM image processing workflow of TPC2 supplemented with Naringenin (Table 3.8). 4,294 movies were collected on a CRYO ARM™ 200 (2.2.7.2.3), motion corrected and CTF was estimated. Afterwards micrographs with resolution below 8 Å were excluded (3,946 micrographs left). 9 templates from Naringenin + PI(3,5)P_2 (7.3.3.8) were used for template picking from the 3,946 micrographs, resulting in 647,504 particles, manually classified to 53,646 particles. Four 3D classes were generated, using the initial 3D model from Naringenin + PI(3,5)P_2 (7.3.3.8). One out of the four classes looked good (28,933 particles), so this one was used for 3D auto refine in C1 symmetry (7.77 Å) and CTF was refined followed by Bayesian polishing. All these steps were performed with RELION (2.1.2), except 2D classification after template picking, which was done in cryoSPARC (2.1.2), as well as the following steps. The polished particles were classified to 22,528 particles. Ab initial reconstruction in three classes resulted in one good class (17,541 particles), so it was decided to run the final step of non-uniform refinement with those 17,541 particles (Fig.3. 19i). This resulted in a final C1 map with a resolution of 5.22 Å and a C2 map with 4.32 Å (Fig.3.19j). The image was created with BioRender (2.1.2).

7.3.3.8 Naringenin + PI(3,5)P_2

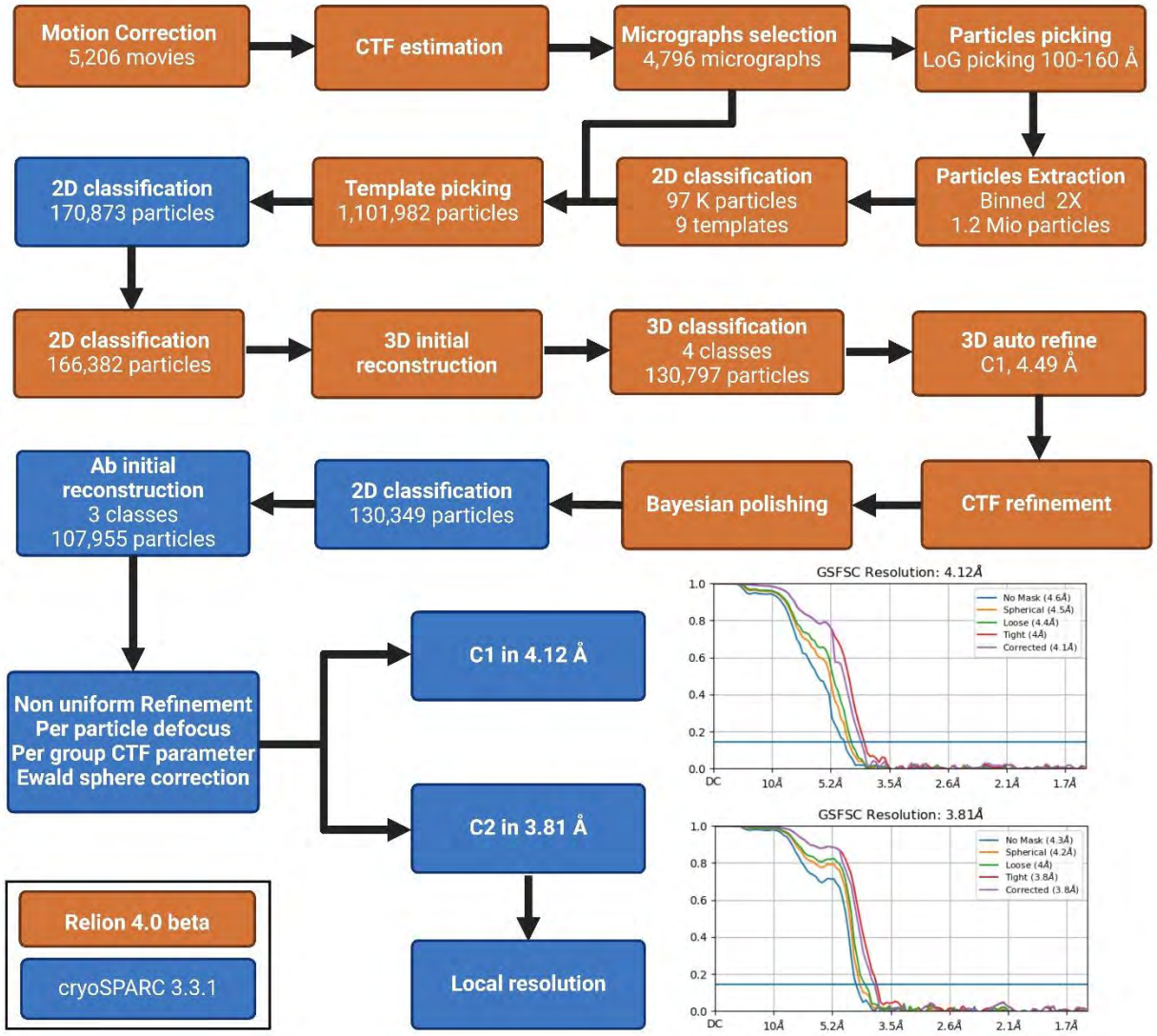

Figure 7.13: Processing workflow of TPC2 with Naringenin + PI(3,5)P_2

SPA cryo-EM image processing workflow of TPC2 supplemented with Naringenin + PI(3,5)P_2 (Table 3.8). 5,206 movies were collected on a CRYO ARM™ 200 (2.2.7.2.3), motion corrected and CTF was estimated. Afterwards micrographs with resolution below 8 Å were excluded (4,796 micrographs left), particles with a size of 100 – 160 Å got picked and manually 2D classified to generate 9 templates. Those were used for template picking from the 4,796 micrographs, resulting in 1,101,982 particles, manually classified to 166,382 particles. After creating an initial 3D model, four 3D classes were generated. Two out of the four classes looked good (130,797 particles), so those were used for 3D auto refine in C1 symmetry (4.49 Å) and CTF was refined followed by Bayesian polishing. All these steps were performed with RELION (2.1.2), except 2D classification after template picking, which was done in cryoSPARC (2.1.2), as well as the following steps. The polished particles were classified to 130,349 particles. Ab initial reconstruction in three classes resulted in one good class (107,955 particles), so it was decided to run the final step of non-uniform refinement with those 107,955 particles (Fig. 3.24b). This resulted in a C1 map with a final resolution of 4.12 Å and a C2 map with 3.81 Å (Fig. 3.24c). Additionally, the local resolution of the C2 map was determined (Fig. 3.24d). The image was created with BioRender (2.1.2).

7.4 Rab7A

7.4.1 AA sequence of the Rab7A construct

StartTSRKKVLLKVIILGDSGVGKTSLMNQYVNKKFSNQYKATIGADFLTKEVMVDDRLVTMQIWDTAGQERFQSLGVA
FYRGADCCVLVFDVTAPNTFKTLDSWRDEFLIQASPRDPENFPFVVLGNKIDLENRQVATKRAQAWCYSKNNIPFETSA
KEAINVEQAFQTIARNALKQETEVELYNEFPEPIKLDKNDRAKASAESCSCKLAAALE**HHHHHH**Stop

Rab7A; **His_6-Tag**

7.4.2 Cloning of the Rab7A expression vector

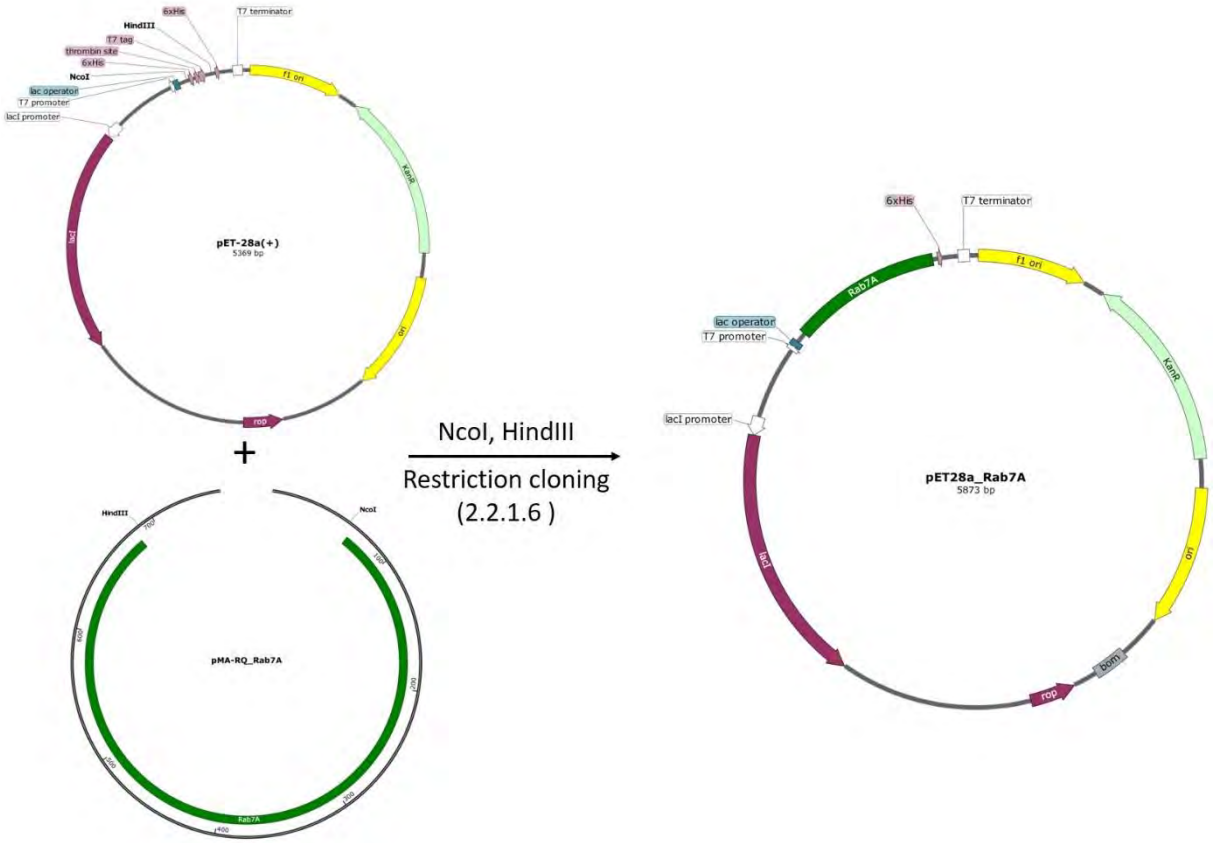

Figure 7.14: Restriction cloning of pET28a_Rab7A
The Rab7A construct (7.4.1) was located in a pMA-RQ vector (2.1.14.1.2) flanked by NcoI-site at the N-terminus and HindII at the C-terminus. The destination vector pET-28a(+) also contained these two restriction sites, while cutting the vector with these enzymes leads to a loss of the N-term. His_6-tag, the thrombin cleavage site and the T7-tag. For restriction cloning both vectors are cut with NcoI and HindIII, the fragments separated via preparative agarose gel electrophoresis, the pET-28a(+) backbone and the Rab7A construct purified and finally ligated via T4 DNA Ligase (2.1.10) to the final construct pET28a-Rab7A containing C-term. His_6-tagged Rab7A. The image was created with BioRender (2.1.2).

7.4.3 Absorbance of pyranine

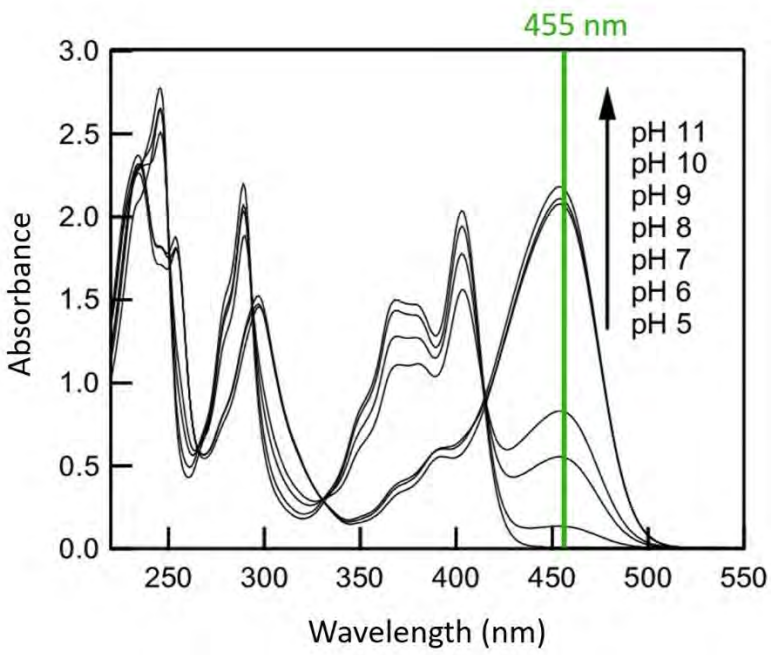

Figure 7.15: Absorption spectra of pyranine in water at various pH
The absorbance of pyranine solved in an aqueous solution with various pH (5-11) at a wavelength from 200-550 nm. The wavelength used in this work (455 nm) is marked in green. Here pyranine has the biggest deviations regarding absorbance related to pH, making it the preferred wavelength to measure pH dependent pyranine absorbance. The figure is derived from Hidaka *et al.*, 2013.

8. Acknowledgements

This thesis would not have been possible without the amazing help and support of many people. Naming everybody would certainly exceed this page. Form the bottom of my heart, 'thank you very much' to everyone who jointly went part of this journey with me.

First, I want to thank my supervisor Christine Ziegler for the opportunity to do this PhD and to work on those nice topics. Her continuous personal and professional support was essential for me to succeed.

In addition, I want to thank my RIGeL-mentor and cooperation partner Prof. Dr. Dr. Christian Grimm from Munich for his patience and sharing his broad knowledge of TPC2. On this occasion I also want to thank Prof. Sandip Patel from London for the fruitful discussions.

I warmly thank Dr. Gregor Madej for the SPA cryo-EM data collection, his help regarding protein modelling and the open door for the many questions I had in the last years. You are the engine of this lab!

Thanks to Prof. Dr. Reinhard Rachel for the care and support regarding electron microscopy.

Many thanks to Marko Roblek from Vienna for producing the lentiviral stable cell lines and the helpful discussion that helped to establish a good working human cell culture.

Infinite gratitude goes to my colleague Lifei Fu, for his help regarding IT and SPA cryo-EM data processing. You were always kind, answered my questions and solved problems whenever needed and your cooking skills are amazing! I cannot thank you enough!

Big thanks to all my colleagues, especially Georg Horn, Felix Fischer, Laure Gauthier-Manuel and Veronika Heinz for the pleasant atmosphere, the assistance, the discussions, and the instructive time. It was amazing to work with you and wish you all the best for the future!

Many thanks also to the technical assistants Sabine Ruppel and Maria Kolodziejczyk for all the help in the lab, and Robert Bobardt for the data collection at the CM12 electron microscope.

I would also like to thank all the unnamed and previous employees as well as all the students that were present during my time at the chair of Biophysics II. It was always nice with you.

Lastly, I would like to thank my fiancée Celine, my family, and my friends for their love and endless support. Without you this would not have been possible. I love you all!

Eigenständigkeitserklärung

Ich erkläre hiermit, dass ich die vorliegende Arbeit selbständig verfasst und keine anderen als die angegebenen Quellen und Hilfsmittel benutzt habe. Die aus anderen Quellen direkt oder indirekt übernommenen Daten und Konzepte sind unter Angabe des Literaturzitats gekennzeichnet.

Weitere Personen waren an der inhaltlich-materiellen Herstellung der vorliegenden Arbeit nicht beteiligt. Insbesondere habe ich hierfür nicht die entgeltliche Hilfe eines Promotionsberaters oder anderer Personen in Anspruch genommen. Niemand hat von mir weder unmittelbar noch mittelbar geldwerte Leistungen für Arbeiten erhalten, die im Zusammenhang mit dem Inhalt der vorgelegten Dissertation stehen.

Die Arbeit wurde bisher weder im In- noch im Ausland in gleicher oder ähnlicher Form einer anderen Prüfungsbehörde vorgelegt.

Regensburg, Benedikt Mayer